UNIVERSITY OF SOUTHAMPTON

DEPOSITION OF ELECTRONIC AND PLASMONIC MATERIALS INSIDE MICROSTRUCTURED OPTICAL FIBRES

by

Adrian Amezcua Correa

A thesis submitted in partial fulfillment for the
degree of Doctor of Philosophy

in the
Faculty of Engineering, Science and Mathematics
Optoelectronics Research Centre

November 2007

UNIVERSITY OF SOUTHAMPTON

ABSTRACT

FACULTY OF ENGINEERING, SCIENCE AND MATHEMATICS
OPTOELECTRONICS RESEARCH CENTRE

Doctor of Philosophy

DEPOSITION OF ELECTRONIC AND PLASMONIC MATERIALS INSIDE MICROSTRUCTURED OPTICAL FIBRES

by Adrian Amezcua Correa

Optical fibres are the transport medium of today's digital information. Nowadays, modern optical telecommunication systems make use of semiconductor optoelectronic devices to generate, control and detect light. The union of the two technologies, namely fibre photonics and semiconductor electronics is expected to have a major impact on next generation of optoelectronic devices, exploiting both the guiding capabilities of optical fibres and the signal processing properties of semiconductors devices. Only recently, with the advent of microstructured optical fibres and templating material processing methods, it has been possible to create optical fibres with solid-state material inclusions.

This thesis describes the development of various high-pressure chemical deposition methods for the formation of extreme aspect ratio tubes and wires of semiconductors, metals and other functional materials within the capillary holes of microstructured optical fibres. Fabrication of composite structures in this way provides optical fibres with a number of new electronic, photonic and plasmonic degrees of freedom.

An in-depth study into the material, optical and electrical properties of these new composite fibres is presented. TEM, SEM and micro-Raman analysis was used to determine the structural characteristics of silicon and germanium-modified microstructured optical fibres. These studies demonstrate that single crystal, poly-crystalline and amorphous semiconductors can be conformally deposited within the capillary voids of microstructured optical fibres. As a step towards fibre-integrated optoelectronic devices, it is demonstrated that in-fibre silicon and germanium wires and tubes can function as field effect transistors and light waveguides.

An experimental investigation on the optical transmission properties of microstructured optical fibres impregnated with silver nanoparticles is also presented. These fibres are shown to be an excellent way of coupling optical guided modes into surface plasmons. As a result, they represent a promising platform technology for fully integrated photonic-plasmonic devices. These fibres have demonstrated the enhancement of Raman signals from molecules adsorbed onto the inner metal surfaces and thus ideally suited for Surface Enhance Raman Scattering molecular detection.

Declaration of Authorship

I, Adrian Amezcua Correa, declare that this thesis entitled:

DEPOSITION OF ELECTRONIC AND PLASMONIC MATERIALS INSIDE MICROSTRUCTURED OPTICAL FIBRES

and the work presented in it are my own. I confirm that:

- This work was done wholly or mainly while in candidature for a research degree at this University
- Where any part of this thesis has previously been submitted for a degree or any other qualification at this University or any other institution, this has been clearly stated
- Where I have consulted the published work of others, this is always clearly attributed
- Where I have quoted from the work of others, the source is always given. With the exception of such quotations, this thesis is entirely my own work
- I have acknowledged all main sources of help
- Where the thesis is based on work done by myself jointly with others, I have made clear exactly what was done by others and what I have contributed myself

Adrian Amezcua Correa

November 2007

Contents

List of Figures

List of Tables

Nomenclature and Abbreviations

e	Electron charge, $e = 1.602 \times 10^{-19}\,\mathrm{C}$
c	Speed of light, $c = 2.998 \times 10^{8}\,\mathrm{m/s}$
h	Planck constant, $h = 6.626 \times 10^{-34}\,\mathrm{J \cdot s}$
$\hbar$	Reduced Planck constant, $\hbar \equiv h/2\pi$
i	Imaginary unit number, $i = \sqrt{-1}$
μ_0	Vacuum magnetic permeability, $\mu_0 = 4\pi \times 10^{-7}\,\mathrm{H/m}$
ε_0	Vacuum dielectric permittivity, $\varepsilon_0 = 8.85 \times 10^{-12}\,\mathrm{F/m}$
$\vec{E}$	Electric field
$\vec{H}$	Magnetic field
$\vec{D}$	Electric flux density
$\vec{B}$	Magnetic flux density
$\vec{J}$	Current density
$\vec{r}$	Spatial vector
t	Time
ρ	Charge density
σ	Conductivity
τ	Electron relaxation time
m	Electron mass
υ	Frequency
ω	Angular frequency, $\omega = 2\pi\upsilon$
λ	Wavelength
ε	Dielectric permittivity, $\varepsilon = \varepsilon_1 + i\varepsilon_2$
ϵ	Relative dielectric permittivity, $\epsilon = \epsilon_1 + i\epsilon_2$
n	Refractive index, $n = n_1 + in_2$
k	Wave vector, $k = k_1 + ik_2$
TE	Transverse Electric
TM	Transverse Magnetic
ACS grade	American Chemical Society grade
CVD	Chemical Vapour Deposition
FET	Field Effect Transistor

FIB	Focused Ion Beam
HOMO	Higher Occupied Molecular Orbital
HPCVD	High-Pressure Chemical Vapour Deposition
IC	Integrated Circuit
QD	Semiconductor Quantum Dot
LSP	Localized Surface Plasmon
LUMO	Lower Unoccupied Molecular Orbital
MBE	Molecular Beam Epitaxy
MOF	Microstructured Optical Fibre
PBG	Photonic Bandgap
PBGF	Photonic Bandgap Fibre
PC	Photonic Crystal
PCF	Photonic Crystal Fibre
PVD	Physical Vapour Deposition
TEM	Transmission Electron Micrsocopy
TOP	Trictylposphine
RRS	Resonant Raman Scattering
SAD	Selected Area of Diffraction
SC	Supercritical
SCF	Supercritical Fluid
SP	Surface Plasmon
SPP	Surface Plasmon Polariton
SERS	Surface Enhanced Raman Scattering
SEM	Scanning Electron Microscopy
VLS	Vapour-Liquid-Solid

Acknowledgements

Firstly, I would like to thank my supervisor, Pier Sazio for introducing me to the field of solid state physics, for all his effort put into this project, his continual guidance, advice and for his friendship during the four years I have spent in Southampton. Further thanks are given to my colleagues and friends, Anna Peacock and Chris Finlayson because working close to them I have learned so many things from quantum dot's fabrication to plasmons physics. Both have played an important role in this work and have shared with me many experimental challenges encountered in this exciting project. Thanks to David Richardson for giving me advise and encouragement throughout my PhD.

My special thank to our outstanding research collaborators at Penn State: John Badding, Venkat Gopalan, Don-Jin Won, Neil Baril, Jacob Calkins and Bryan Jackson who I had the pleasure to work with, discuss so many aspects of this project and spent a great time in State College! Their remarkable knowledge in high-pressure chemistry have made possible the fabrication of the exciting fibres analyzed in this thesis. My thank also extend to our collaborators from the University of Nottingham, Jixin Yang and Steve Howdle for producing the silver fibres I have used during this work.

I wish to thank Lencho, Anna, Pier and Eleanor who have had the "great pleasure" of proof reading this thesis. Thanks for all your constructive suggestions and corrections!

I would also like to extend my gratitude to my officemates and other members of the Optoelectronics Research Centre, especially to Naveed, Symos, Francesca, Lionel, Everardo, Rodrigo and Laura, for sharing their equipment with me and for many interesting discussions on optoelectronics and the PhD life...

I want to express my gratitude to my sponsor, CONACyT (National Council for Science and Technology of Mexico) who made it possible for me to spend these four years in the Optoelectronics Research Centre with all its advantages, excellent laboratories, traveling to conferences, interesting lectures, great people, etc.

Many friends in Southampton should be thanked for providing me the essential laugh, support and the entertainment needed to reach this point: Catia, Arturo, Vladis, Jorge,

Andy, Steve, Maria & Rob, David & Rocio, Eli, Nav, Symos and Greg thanks to you all !!

28 years ago, Paty and Miguel gave the first step in this story... A very especial thanks go to you for giving me love, trust, friendship and teaching me good values that have helped me to fulfil this and many other goals... you have always been my best teachers! I cannot forget my twin brother, Rodrigo who I know since time before I was born... and some years after Mariano was there... thanks to you both for sharing this story with me.

To all my family, thanks for your love, support and encouragement!

As well a big "thank you!" to my friends Lencho, Mad, Mauricio, Gustavo, Joaquin, Rogelio, Andres for many years of unbroken friendship.

Finally, my sincerely thank to you Hélène, my biggest happiness was to meet you and share this time with you.

A Paty y Miguel

"The known is finite, the unknown infinite; intellectually we stand on an islet in the midst of an illimitable ocean of inexplicability. Our business in every generation is to reclaim a little more land..."

Thomas H. Huxley

Chapter 1

Introduction

21st Century global telecommunications systems have been made possible thanks to optical fibre technology. Optical fibres are the internet and telephone communications backbone, interconnecting buildings, cities and continents. Around the world, lie more than 300 million [1] kilometres of fibre that can carry millions of simultaneous phone calls and the Internet's information. A significant portion of the development of optical fibres for telecommunications took place at the University of Southampton, with its origins going back as far as the 1960's. These innovations led directly to the data communications revolution of the late 20th century and have now impacted many other technologies from remote sensing to biomedicine. In addition, the invention of the transistor in 1947 at Bell Labs gave birth to the last century's semiconductor revolution which has marked a new technological age in human history. As a result, electronic and optoelectronics planar devices based on silicon, germanium and compound semiconductors have had a profound effect on our way of living.

Currently, optical telecommunication systems combine silica optical fibres as signal carriers with external optoelectronics semiconductor circuits that are capable of generating, detecting, and manipulating the light. However, the process of converting the photons to electrons requires coupling optics, alignment structures and packaging. These conversion processes consume enormous amounts of power, require costly technology and have limited the overall bandwidth of optical systems. Therefore, it would be ideal not to transform in-fibre photonic signals to chip-based electronic signals, due to the complexity of having to use heterogeneous and discrete optoelectronic components. Indeed, the ultimate vision would be purely fibre based devices in which photons do not need to leave the fibre. One example of such a device is the erbium-doped-fibre-amplifier (EDFA) which replaced old heterogeneous optoelectronic amplifiers composed of photo-detectors, filters, electronic amplifiers and lasers diodes to reconvert the amplified electronic signal back again into photons, with a single all-optical amplifier. Due to the amplifier's *in-fibre*

nature they allow optical systems to operate with a broad bandwidth. These systems were commercialized in the late 80's and have become widely used in the telecommunications industry and for laser machining applications.

Although, the EDFA has solved the problem of how to amplify optical signals, the signal processing involved in the transmission system is still carried out in the electronic domain, which limits the overall bandwidth and raises the costs of the optical networks. The ability of solid-state devices to manipulate electrons and photons relies on the microelectronics industry's exceptional capability of integrating semiconductor, dielectric and conductive materials in a single device. However, until now, fibre technology has not been able to integrate crystalline semiconductors and metals with anywhere near their level of sophistication.

It has been well known for many years that the periodic organization of atoms within a crystalline medium gives rise to different electronic bands in which the conduction of electrons is forbidden. Electrons with energy in between the valence band and the conduction band are not allowed to exist in semiconductor crystals. Utilizing these electronic bandgaps to control the propagation of electrons led to the microelectronics revolution of the last century and is now giving birth to the nanosciences and integrated photonics. However, it was not until 1987, when Eli Yablonovitch [2] and Sajeev John [3] proposed, independently, that the fabrication of materials with periodic dielectric structures on a scale comparable to the wavelength of light, offers the possibility of tailoring the way light propagates within materials, in the same manner that ordered arrangement of atoms do for electron waves. These novel structures are known as photonic crystals (PCs). In photonic crystals, the periodic index difference can give rise to photonic band gaps (PBGs) where propagation of electromagnetic waves would be prohibited for certain wavelengths [4] even though the constituent (bulk) dielectrics are intrinsically transparent. Such periodic dielectric structures have numerous potential applications in the development of photonics devices which offer control over the electromagnetic fields and the possibility of manipulating photons with unprecedented optical degrees of freedom [5, 6, 7].

Standard optical fibre's operation usually relies on a physical mechanism named total internal reflection or index guiding, where light propagates within a higher refractive index core surrounded by a lower index cladding. During more than 40 years of research on index guiding optical fibres, the full capabilities of silica-doped fibres have almost been reached. Most of the development over this time was mainly focused on reducing the fibre propagation loss. The discovery of photonic crystals has been very promising for optical fibre technology. In 1995 Russell [8] proposed the concept of a novel class of optical fibres with a photonic crystal cladding to confine the light within the fibre core. A year later, a photonic crystal fibre (PCF), single material fibre that has a

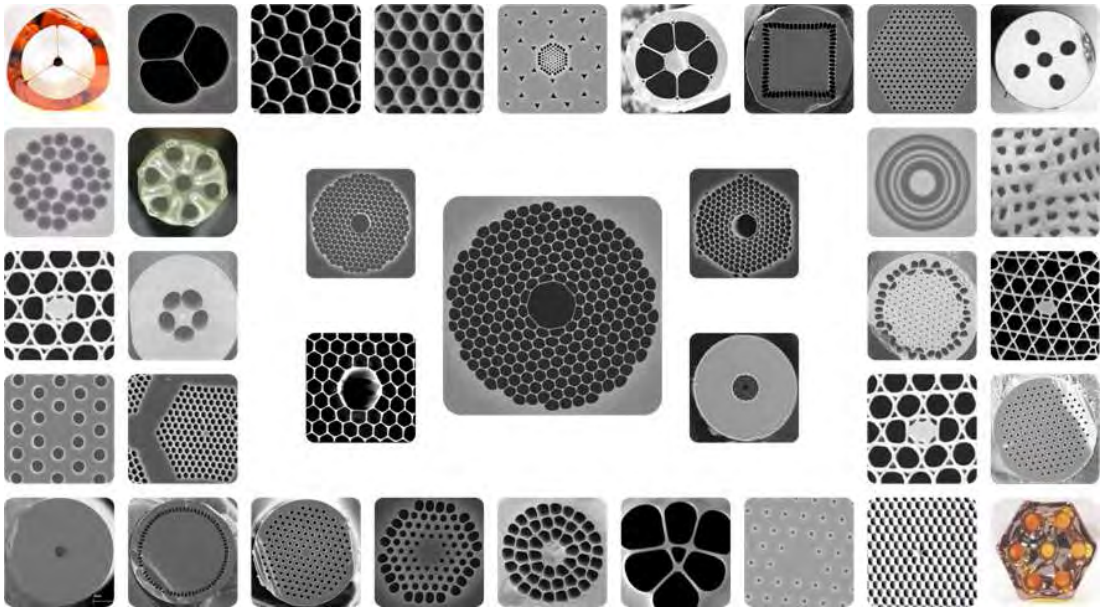

FIGURE 1.1: SEM cross sectional micrographs of different microstructured optical fibres fabricated at the ORC. The central fibres are among the most advanced kind of MOFs as they can guide light in their hollow core by photonic band gap mechanisms.

silica core surrounded by a cladding with a periodical arrangement of air holes running down its length was fabricated [9]. This fibre guided light by a modified total internal reflection mechanism [10]. However, it was not until 1998 that the first true photonic bandgap fibre (PBGF) was created [11]. Both kinds of fibres can be considered as microstructured optical fibres (MOFs). MOFs are usually single material optical fibres with air-holes that define their transverse profile. Their capillary voids can be precisely configured in a variety of structures and with diameters ranging from tens of nanometres to a few microns (Figure 1.1). Solid MOFs in which the air holes are replaced by different kind of glasses can also be fabricated. MOFs had already demonstrated advantages over conventional silica-doped fibres due to their novel optical properties such as broad band single mode guidance, widely engineerable dispersion, nonlinear properties, mode area tailoring and photonic band gap guidance in air [12, 13, 14, 15].

The most interesting property of MOFs, for the research presented here, is that they have holes which provide a way to infiltrate other materials into the fibre. Our research group has recently demonstrated that silica fibres combining dielectrics, metals and crystalline semiconductors can be fabricated by new material deposition processes similar to those used in the planar microelectronics industry [16, 17]. This technology may lead to novel multifunctional optical fibres capable of not only guide light but also able to generate, manipulate and process optical and electronic signals. Furthermore the formation of semiconductor tubes and wires within nanoscale holes of MOFs will bring together fibre optics technology with the growing field of ultra small semiconductor

nanowires [18, 19, 20, 21, 22]. Figure 1.2 is an artistic vision of the integration of solid-state and fibre technologies.

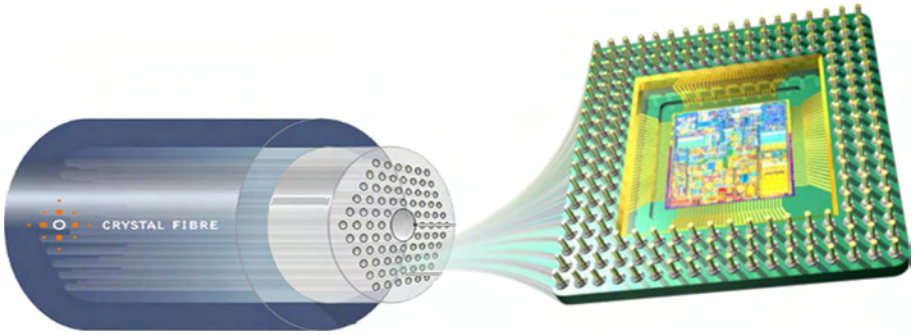

FIGURE 1.2: The deposition of semiconductors and metals within the capillary holes of microstructured optical allow for the fusion of two powerful technologies: semiconductor and microstructured optical fibres technologies for the creation of a new class of metamaterials. This gives room for the development of interesting in-fibre electronic, optoelectronic and plasmonic devices.

1.1 Past and Current Work

Although the flow of light using micro/nanoscale structures was mastered by nature many millions of years ago (Figure 1.3), it was not until the past two decades when the refinement of micro/nano materials fabrication techniques allowed the development of artificial photonic crystal structures. The first photonic crystal was fabricated by mechanically drilling millimetre sized holes into a dielectric material [23]. It presented a complete 3D photonic band gap for microwave frequencies. The realisation of this first photonic crystal gave rise to increasing scientific and technological interest especially in the optical regime. Photonic crystal technology has matured at a surprising pace and research has gradually shifted focus from the fundamental physics of the properties of these materials to more application driven research and devices. Nowadays, photonic crystal technology is thought to be one of the future platform technologies to create optical microcircuits capable of processing speeds potentially much faster than today's microelectronic circuits.

The precise periodic nature of these mesoporous structures readily lends them to the concept of embedding functional materials into the void lattice spaces. This enables them to combine the optical properties of the original structure with the optical or electronic functionality of the embedded materials. In this section the significant advances on depositing materials inside photonic crystals are reviewed. One can start by mentioning the work by Vlasov and colleagues, who embedded CdS quantum dots (QDs) into the lattice voids of an inverse opal [24]. A drastic change in the QDs emission spectra was

observed due to the heavily modified photonic density of states in the opal. To deposit the quantum dots, the PC matrix was exposed to a vapour of Cd and S followed by a thermal annealing process. Later, Busch and John in search of a certain degree of electrical tuneability of photonic band structures, proposed the first marriage of liquid crystals and photonic crystals [25]. They calculated what would happen if the spherical voids of an inverse silicon opal were partially filled with a low refractive index liquid crystal. The resulting composite material exhibits an electrically tuneable PBG thanks to the electrical dependence on the refractive index of the liquid crystal. This experiment opened up a broad range of technological interests [26].

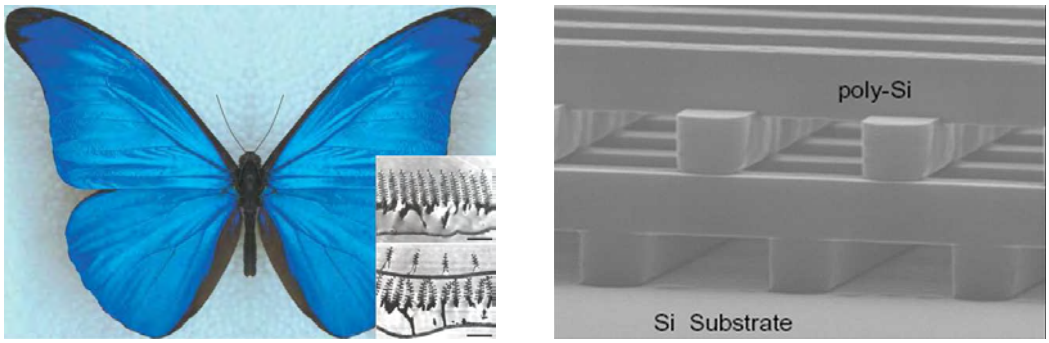

FIGURE 1.3: This butterfly is an example of how the micro-scale architecture of a dielectric medium gives rise to fantastic optical effects. Its wings prohibit the transmission of blue light which produces a striking blue coloration, adapted from reference [27]. Right: first 3D human-made photonic crystal operating at infrared wavelengths, from reference [28].

Due to the excellent mechanical properties of MOFs, their flexible geometric design and their relatively low fabrication cost, they are exceptional templates for the inclusion of materials inside their air channels. There are some examples in this direction which have until now focused on infusing the capillary holes with materials in liquid or gas phase. Filling the capillaries with liquid crystals, gases, polymers, and colloids has found applications in many diverse technological areas. For example, electrically stimulated light-induced second harmonic generation in Ge-doped silica core holey fibre was reported [29]. In this experiment, two 25 μm diameter metal wires were manually introduced into the holes of a MOF to generate a high electrostatic field in the core. Due to the micro dimensions of the structure the electric field generated in this experiment was probably the highest achieved in silica.

A similar technique was used to trap and guide atoms in a holey fibre [30], as previously, conductive wires were introduced into four holes of a hollow core fibre. A cloud of laser cooled Rb atoms was then coupled to this structure allowing them to propagate over several centimetres inside the hollow core. More recently, the cladding-mode properties of a polymer-silica MOF using a fibre grating UV written into the Ge-doped core were examined [31]. For this experiment acrylate-based polymer, with a refractive index close

to that of silica, was introduced into the air regions (six 40 μm diameter air holes) by placing one end of the fibre into low viscosity uncured polymer, and connecting the other end of the fibre to low vacuum. Once the polymer was inside the fibre holes, it was cured with UV light. Using the thermo-optical response of the polymer the authors demonstrated a reduction of the cladding-modes. Later Kerbage *et al.* used the same procedure to incorporate polymer into the air hole regions of a tapered air-silica MOF [32]. By taking advantage of the refractive index temperature response of the polymer and the high interaction between the light and the polymer in the tapered length, they demonstrated an integrated all-fibre variable attenuator. Another inventive example took advantage of the existence of air holes in MOFs to fabricate an in-fibre Mach-Zehnder interferometer [33]. For this trial, an eutectic metal alloy, with low melting temperature, was introduced under 8 atm pressure into a twin core optical fibre which also had two parallel 20 μm holes running next to one core. The high interaction between light and the electric field generated between the electrodes achieved a 1.4 kV switching voltage from the weak intrinsic Kerr nonlinearity of silica, this fibre is shown in Figure 1.4a. Soon after, Larsen and collaborators demonstrated thermo-optic switching of visible light propagating in a photonic bandgap fibre whose holes were impregnated with liquid crystal. In this experiment the 3.5 μm diameter holes of a photonic crystal fibre were filled with high refractive index liquid crystal [34]. To access the potential of controllability, the fibre was coated with a thin conductive layer that worked as a resistive micro-heater to thermally change the optical properties of the liquid crystals. The resulting photonic crystal structure has narrow photonic bandgaps crossing the silica line, thus the PBG allows for certain frequencies to propagate in the low-index silica core. By changing the temperature of the liquid crystal, the photonic bandgap may be tuned from green to blue, and in this way the authors fabricated the first thermo-optic fibre switch based on PBG effects. More recently, gas-filled hollow core photonic bandgap fibres were used as compact and high performance Raman lasers [35, 36]. The stable performance of these compact fibre devices may find applications in high-precision frequency measurements, quantum optics and nonlinear optics. Several other device applications including fibre sensors have been demonstrated by filling MOF capillaries with different fluids and colloids.

The most noteworthy example of a MOF combining different materials was recently demonstrated by Bayindir and colleagues, who fabricated MOFs that combine solid state materials [37]. Their approach entails the drawing of fibre preforms which include low melting temperature metals, amorphous semiconductors, and a high-glass-transition-temperature polymeric insulator. The resulting fibre can be used to construct detectors which are sensitive to illumination along the entire fibre length. Figure 1.4b shows a SEM micrograph of one of these hybrid fibres. These kinds of MOFs were drawn with all components present in the fibre preform, therefore the technique requires all materials

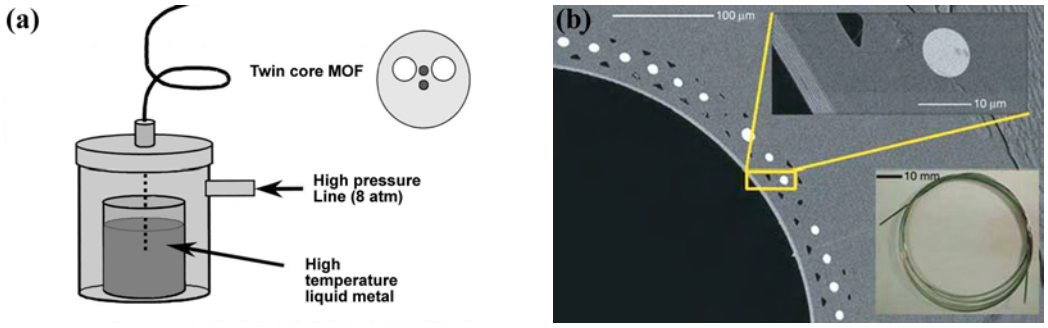

FIGURE 1.4: (a) Example of a MOF filled with Bi and Sn metal eutectic. The melting temperature of the eutectic is 137 °C and the pressure used to introduce the liquid metal into the 20 μm fibre holes was 8 atm. The resulting fibre was used as a Mach-Zehnder amplitude modulator, from reference [33]. (b) Cross-sectional SEM micrograph of a hollow-core metal-semiconductor-insulator fibre. The upper inset shows the omnidirectional mirror which is formed by an array of quarter-wave As_2Se_3 and PEI layers. Also a metallic, Sn, filament which is used as the conductive medium of the in-fibre detector is shown in the inset. The lower inset is a picture of 1 m long, 1 mm thick hybrid fibre, taken from reference [37].

to have similar melting temperatures and thermal expansion coefficients. Thus the number of possible materials that can be used to construct dielectric, semiconductor and conductor impregnated MOFs using this technique is limited. In addition, there have been some experiments demonstrating the deposition of solid-state materials inside capillaries using conventional chemical deposition processes [38]. But because of mass transport constraints along high aspect ratio structures these studies have been restricted to capillaries bigger than 10 μm.

All the previous experiments exemplify the advantages of introducing functional materials within MOFs capillaries. Especially, the inclusion of semiconductors and metals into the air channels of MOFs lead to a number of exciting in-fibre device applications, such as the fibre fabricated by Bayindir *et al.* [37]. This could also generate a brand new class of fibre devices capable of generating light, controlling it and also able to create fibre sensors with a high sensitivity. Clearly, however, the methods that have until now been used to deposit materials into holey fibres, suffer from disadvantages such as materials inflexibility, they can only be applied to fluids and are restricted to large holes.

Supercritical fluid (SCF) deposition and high pressure synthesis techniques have been successfully addressed to deposit high melting temperature semiconductors such as: silicon [39] and germanium [40] nanowires within mesoporous silica templates. Also, metal deposition from organometallic compounds in supercritical carbon dioxide ($scCO_2$) has also been widely used to generate homogeneous metal films into mesoporous substrates (e.g. gold [41], copper, nickel [42] and platinum [43]). Because of the deposition flexibility of high pressure methods and supercritical fluids, our research group has investigated

these new deposition techniques to enable the impregnation of solid state materials inside optical fibres using pressures in the range of $2 - 100$ MPa, which are well sustained by the intrinsic strength of fused silica fibres (which is greater than 1 GPa [44]). For those who are not familiar with high pressure systems is interesting to mention that the pressure used in the experiments is equivalent to the water pressure hundreds to 10 thousand metres below sea level!

Figure 1.5 shows an example of an empty MOF impregnated with silicon via a high pressure method that was developed in this work. Our research group has also demonstrated the deposition of amorphous and crystalline germanium, single crystal silicon, metals: silver, gold, inside silica MOFs [16] with capillaries as small as 100 nm in diameter and for tens of centimetres length. The number of materials that can be deposited by these techniques is thus not limited by their melting temperature and so complex fibre based devices can be envisioned.

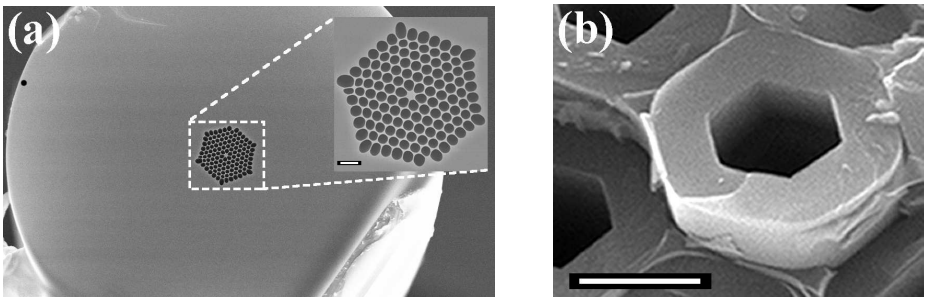

FIGURE 1.5: (a) Empty air silica MOF template, the scale bar in the inset is 2 μm. Despite the fragile appearance of the thin (< 100 nm) capillary walls, this figure illustrates how robust these fibres are. MOF are able to support the high precursor pressure required for the deposition process. (b) Conformal deposition of polycrystalline silicon within the MOF holes using a high pressure material deposition technique, the scale bar is 1 μm.

1.2 Thesis Structure

As described in this chapter, the work in this thesis is related to the use of microstructured optical fibres as templates for micro/nano materials fabrication. It comprises a collection of experiments involving the deposition of semiconductors, metals and polymers within the capillary holes of MOFs. The resulting fibres have proved optical guidance and relevance as molecular sensors. This research is part of a joint research effort between the Optoelectronics Research Centre at the University Southampton, the Pennsylvania State University Materials Research Institute and the University of Nottingham Supercritical Chemistry group. This close multidisciplinary effort shares expertise in fibre design and fabrication, together with high pressure chemistry for the deposition

of functional materials, including semiconductors, metals and polymers, into the structures; as well optical, material and chemical characterization studies of the resulting fibres. Silica MOFs are first fabricated in the ORC, then the deposition of materials inside the fibres holes is done in PSU and in Nottingham Universities. Finally, most of the fibre characterisation presented in this thesis was done here in Southampton.

Chapter 2 provides an introduction to MOFs including their optical properties and current computational methods used for their calculation. It also shows a description of the stack-draw technique used for the fabrication of silica MOFs. During the first year of his PhD studies the author was involved in the drawing of silica capillaries and MOFs. Effort was put on the characterisation of the fibre structure via SEM studies and on the fabrication of fibres with nanoscale features. After the fire in the ORC clean rooms in November 2005 no further fibre fabrication was carried out by the author. In this chapter, the author uses a commercial software based on full-wave plane-wave expansion method to theoretically study the bandgap structure of semiconductor-modified MOFs. Unfortunately the programs developed for this task and most of the results obtained were lost in the fire.

Chapter 3 introduces the different methods currently used in microelectronics and nanofabrication for the deposition of semiconductors, metals and dielectrics within planar and 3D substrates. Their experimental advantages, disadvantages and possible extension to MOF deposition are discussed. The chapter closes with a description of novel high pressure deposition techniques developed during this project for the formation of crystalline semiconductor, metal and polymeric tubes within MOFs templates. The material deposition is carried out by our research collaborators in PSU and Nottingham. The Southampton team visited the PSU team in two occasions and during these visits the author fabricated several silicon and germanium fibres. The author carried out SEM studies of the impregnated fibres in order to characterise their deposition profile.

Chapter 4 details the characterisation methods used to obtain the structural, optical and electrical properties of silicon and germanium-filled MOFs. A key requirement for the characterisation of semiconductor modified MOFs is to expose the semiconductor material from the silica cladding. The author designed and made the tools required for the HF etching and investigated the experimental conditions required to achieve a precise control over the etching process. The samples used for the first TEM studies presented in this chapter were fabricated and prepared by the author in PSU. Afterwards, the second and more advanced TEM analysis presented in this chapter was done by our collaborators in PSU. This chapter also show Raman studies of silicon and germanium MOFs, the majority of the semiconductor fibres and Raman experiments were carried out by the author. The demonstration of the first electronic device inside an optical fibre is presented in this chapter. Some of the semiconductor fibres used for electrical

measurements were fabricated by the author. The electrical measurements presented in this chapter were done in collaboration with other members of the group. As the etching process was done in the ORC clean rooms, the fire also affected this part of the project and it was not possible to fabricate new devices after November 2005.

Chapter 5 describes the field of plasmonics. It concentrates on details of the optical properties of metals and provides a theoretical background to the following two chapters.

Metallo/dielectric nanostructures, which allow the excitation of plasmons, have opened up new possibilities for Raman scattering as a powerful spectroscopy technique, and are described in Chapter 6. In the search for an application of metal-modified MOFs, this chapter explains the nature of the Raman effect and provides the theoretical background of Surface Enhanced Raman Scattering (SERS).

The experimental SERS results obtained using silver modified MOFs are presented in Chapter 7. MOFs SERS substrates provide an interesting method for the fabrication of inexpensive and powerful molecular sensors. The silver-modified MOFs used in these experiments were fabricated by our collaborators in Nottingham and all the experiments presented in this chapter were done by the author.

Chapter 8 begins by outlining the synthesis of PbSe quantum dots performed by a team consisting of members of the Southampton Chemistry department, as well as the author and other members of the group. The following section will then present the optical properties of semiconductor quantum dots. The absorption and photoluminescence experiments presented in this chapter were carried out by the author and other members of the group.

Chapter 9 is a summary of results and discusses the future directions that will follow from the research presented in this thesis.

Chapter 2

Microstructured Optical Fibres

Firstly, in order to avoid confusion, it is important to point out that *microstructured optical fibres* are also referred as *photonic crystal fibres* (PCF) and *holey fibres*. Since the original motivation for developing these fibres was the creation of structures that able to guide light by means of a 2D photonic bandgap the term *photonic crystal fibre* was introduced. In a large part of literature this term is used to refer to all types of fibres with microscale features defining their transverse profile. However, as these fibres not necessarily have a periodic arrangement of holes and can guide light by both photonic bandgap effects and modified internal reflection, the more general term *microstructured optical fibre* is preferred in this thesis. The following chapter presents a comprehensive review of the optical properties, guidance mechanisms, modelling methods and fabrication methods of MOFs.

2.1 History of MOFs

A remarkable property of microstructured optical fibre (MOF) manufacture, is that the continuity of air channels running along the length of a glass preform are preserved when drawn down to the micro-scale. This property was investigated back in the early 70s by Kaiser *et al.* [45, 46]. They fabricated a single-material fibre consisting of a small diameter rod supported by thin glass struts inside a larger tube (Figure 2.1a). In 1977, Yariv *et al.* [47] theoretically proposed a fibre with a periodically structured cross-section which could guide light in a low refractive index core due to Bragg reflections that prevent light dissipation in the cladding. However, most of the research in fibre technology in those years was focused in reducing transmission loss. With the implementation of chemical vapour deposition (CVD) techniques to fibre fabrication, in the late 70's the loss of conventional step-index fibres was reduced to lower values [48] than those

achieved with MOF technology, and so, MOF research was left aside for many years. It was not until the seminal work of Russell and co-workers [9], in 1996, that the interest in microstructured optical fibres was renewed. They fabricated a single material fibre which contained a periodic arrangement of air holes that ran along the fibre length and the fibre core was formed by replacing the central hole with a solid region, (Figure 2.1b). As the purpose of this fibre was to confine and guide light due to photonic bandgap effects, they introduced the term photonic crystal fibre. However, the fibre structure was not regular enough and the holes were not large enough to support photonic bandgap guidance [10].

Since then photonic crystal fibres (PCF), with a periodic or aperiodic transverse microstructure, have been used as practical fibre waveguides. After the success of PCF technology, many kinds of structures with periodically structured cross-section have been fabricated. For example, the Bragg fibres proposed in the 70s are currently produced by many different methods. In 2000, Brechet *et al.* [49, 50] made a solid core Bragg fibre using modified-CVD. In addition, employing a combination of polymer and chalcogenide glass, Joannopoulos' group at MIT in the US has realized a hollow-core version of Bragg fibres [51, 52, 53].

In a conventional optical fibre the light propagation is due to total internal reflection at the core/cladding interface and light is confined in the core due to its higher refractive index than that of the cladding. In contrast to this, MOFs are able to guide light by means of two different mechanisms: *Modified total internal reflection*, in which light is guided in a solid core, surrounded by a (not necessarily periodic) structured cladding. In this case the average refractive index of the cladding is decreased because of the air holes (low refractive index). This ensures that light incident at certain angles propagates in the high refractive index core by modified total internal reflections at the core/cladding interface, as in conventional optical fibres [9]. On the other hand, *photonic bandgap fibres* are an especial category of MOFs which exploit the photonic bandgap effects as the mechanism of light guidance therefore they can guide light in a low refractive index medium [11]. In photonic bandgap fibres (PBGFs) the air holes that define the cladding region are arranged on a periodic lattice which presents a photonic band gap that does not allow light to propagate in the cladding region. By breaking the order of the cladding i.e. adding a defect in the structure it is possible to introduce localized modes within the defect. This is typically done by introducing a hollow core in the centre of the structure. If light can propagate in the defect but its frequency lies within a bandgap it will not be allowed to propagate in the cladding and therefore the optical energy will be concentrated in the defect. Hollow-core PBGF are a special class of bandgap fibres that guide light in a central air core [54]. The design freedom of MOFs has allowed new opportunities in optical fibre technology. Over the past few years they have shown potential for many applications and have permitted progress in several areas such

as medical sciences, nonlinear optics, telecommunications, supercontinuum generation, high power delivery and sensors.

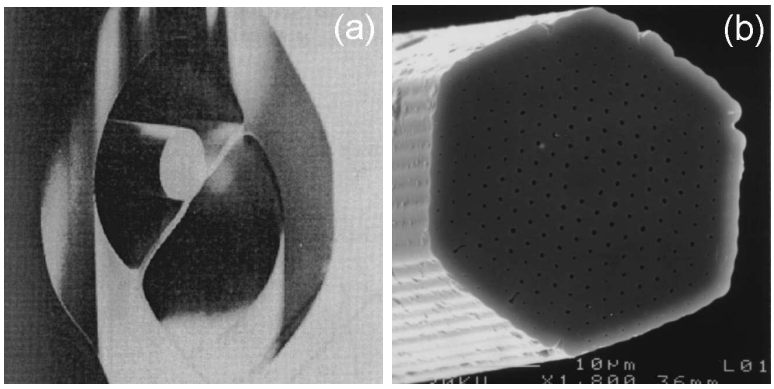

FIGURE 2.1: (a) First demonstration of a MOF, taken from reference [45]. (b) First MOF with a silica core surrounded by a periodic array of air holes in silica, from reference [9].

2.2 Fabrication of MOFs

Microstructured optical fibre fabrication typically involves two stages: preform fabrication and fibre drawing. A preform is a centimetre-scale replica of the fibre normally $\sim 50\,\text{cm}$ in length and $\sim 20\,\text{mm}$ in diameter. After fabricating the MOF preform it is drawn down to micro-scale dimensions on a fibre drawing tower. Figure 2.2 shows the schematic preforms of a solid and hollow core MOFs. During the relatively short history of MOF technology various preform synthesis methods have been developed to allow the fabrication of a variety of fibre structures. There are many examples of preform fabrication including stacking of capillaries and rods, sol-gel casting, direct drilling, extrusion from bulk glass with low softening temperature and rolling flexible material sheets into tubes, each of which has advantages and disadvantages depending on the glass used and the desired fibre geometry. The most commonly used technique is capillary stacking which is especially flexible for silica MOFs fabrication. This method involves stacking glass capillaries and rods of $\sim 1\,\text{mm}$ diameter inside a silica tube with an internal diameter of $\sim 20\,\text{mm}$. These capillaries are drawn from a starting tube of high-purity silica with an outer diameter of $10 - 20\,\text{mm}$. The inner/outer diameter of the starting tube determines the ratio between the hole diameter and the lattice pitch in the drawn fibre. All the silica MOFs preforms used in the present work have been fabricated by this method. The resulting preform is then drawn into either a fibre or cane. If very small features ($< 2\,\mu\text{m}$) are required then a two step drawing process is used. The microstructured cane from the first draw is introduced into a silica tube and is then drawn into a fibre.

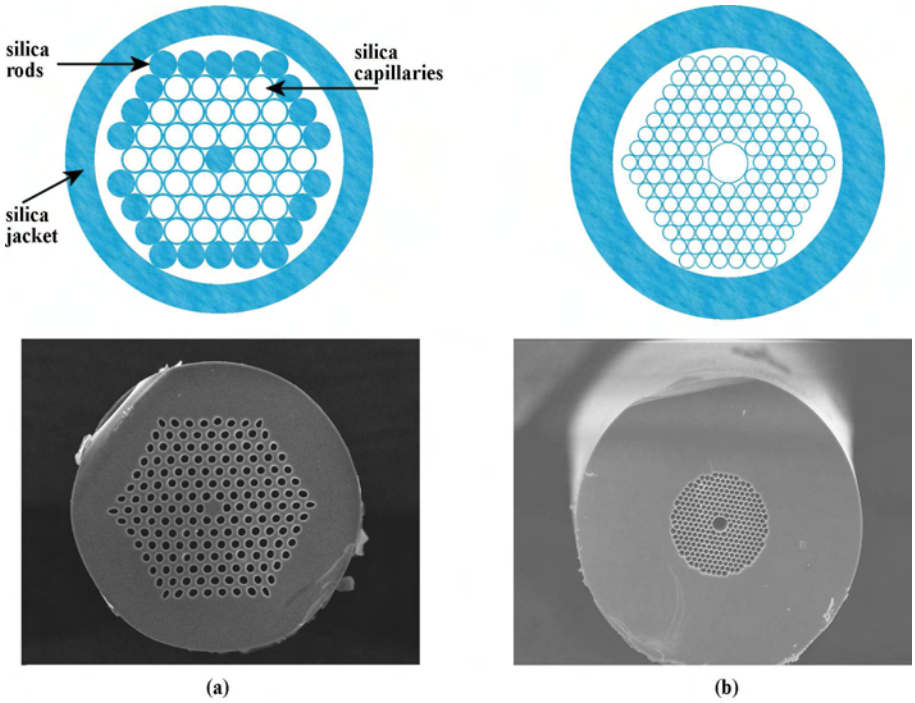

FIGURE 2.2: Top, examples of (a) solid core and (b) air core MOFs preforms fabricated by stacking silica capillaries and rods. Bottom, SEM micrographs of the MOFs which have the same geometry as their preform.

A 5 m fibre tower, whose schematic is shown in Figure 2.3, was used for MOF drawing. The preform is mounted in a holding chuck attached to a feed mechanism that lowers the preform into a furnace at the feeding speed (V_p). The furnace temperature is raised to 1900° C – 2000° C and the drawn fibre is taken up by the capstan which controls the draw speed (V_f). In order to maintain a uniform fibre outer diameter, the drawing process includes a diameter monitor which is located at the furnace exit. Before the fibre reaches the capstan it is coated with a protective polymer. Coating is required to protect the pristine silica surface from scratches and abrasion and it preserves the intrinsic strength of silica. The acrylate coating is applied in liquid phase and is solidified by UV-curing. Silica MOF fibres fabricated by this method have extremely high tensile strength (more than 1 GPa [44]) which makes them excellent reaction vessels for high pressure deposition experiments.

Due to the potential importance of having MOFs and silica capillaries with nanoscale dimensions for nanomaterial templates, several experiments were carried out in order to control the fibre's hole size in the nanoscale regime. The preform feed speed, V_p, the furnace temperature and the drawing speed, V_f are the main parameters in determining the fibre structure. In these experiments the diameter monitor was used to measure the external diameter, which for our experiments is not necessarily 125 μm as it is for standard fibres. The dimensions of the fibre channels were measured under an optical microscope as the fibre was drawn. Although the desired subwavelength features could

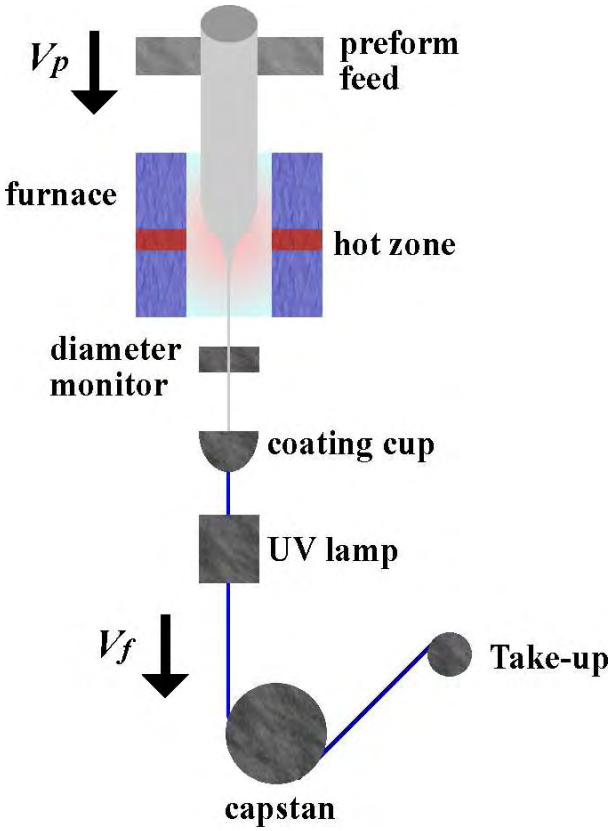

FIGURE 2.3: Schematic diagram for a drawing tower.

not be resolved using the optical microscope, in most of the cases it was possible to determine whether the holes had collapsed or the subwavelength capillary holes were preserved. The drawing parameters were then varied and new fibre samples were taken. SEM micrographs indicated that it was possible to fabricate MOF with internal dimensions $< 500\,\text{nm}$ as well as silica capillaries with an inner diameter as small as 100 nm. Figure 2.4 shows a honey-comb fibre which was drawn down to the nanoscale, it is possible to appreciate that by changing the drawing conditions the holes size was changed from $\sim 450\,\text{nm}$ to 250 nm. It is important to note how precisely the hole size can be controlled. These results have shed light onto the application of MOFs in nanotechnology which has been hardly explored before. In the next chapter we move forward into the formation of semiconductor nanotubes within the nanoholes of MOFs.

2.3 Fundamentals of Photonic Crystals

Photonic bandgap (PBG) materials give new opportunities in quantum optics, nonlinear optics and optoelectronics. These structures were predicted theoretically to describe two new optical principles, the localization and trapping of light in a PC [3, 55] and the complete inhibition of spontaneous emission [2]. Maxwells' equations are the fundamental

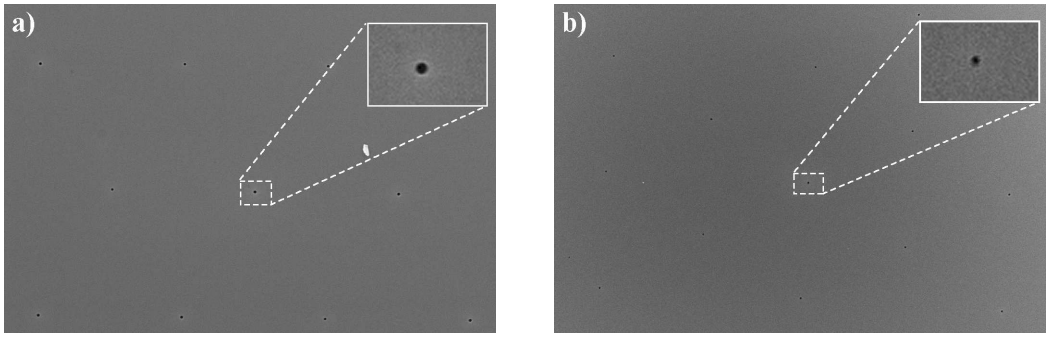

FIGURE 2.4: SEM micrographs of MOFs with periodic arrangement of nanoscale holes (a) the diameter of the holes is ∼450 nm. (b) The diameter of the holes is ∼ 250 nm.

relations that govern the behavior of the electromagnetic fields and the propagation of light in a MOF can be described by them. For a loss-less medium and one that is free of charges or currents, i.e. ε_m is real and $\rho = 0,\ \vec{J} = 0$, the Maxwell equations may be expressed in their differential form as:

$$\nabla \times \vec{E}(\vec{r},t) = -\frac{\partial \vec{B}(\vec{r},t)}{\partial t}\,, \tag{2.1a}$$

$$\nabla \times \vec{H}(\vec{r},t) = \frac{\partial \vec{D}(\vec{r},t)}{\partial t}\,, \tag{2.1b}$$

$$\nabla \cdot \vec{H}(\vec{r},t) = 0\,, \tag{2.1c}$$

$$\nabla \cdot \vec{D}(\vec{r},t) = 0\,. \tag{2.1d}$$

According to this notation, $\vec{E}$ and $\vec{H}$ are the electric and magnetic fields respectively, $\vec{B}$ is the magnetic flux density and $\vec{D}$ is the electric displacement vector. In a photonic crystal the structuring of the dielectric medium may be represented by the space dependence of the dielectric permittivity $\varepsilon_m(\vec{r})$. For this study neither nonlinear effects nor material dispersion are taken into account. Then, the constitutive equations of the material, are given by

$$\vec{D}(\vec{r},t) = \varepsilon_m(\vec{r})\vec{E}(\vec{r},t) = \varepsilon_0\epsilon_m(\vec{r})\vec{E}(\vec{r},t)\,, \tag{2.2a}$$

$$\vec{B}(\vec{r},t) = \mu_0\vec{H}(\vec{r},t)\,, \tag{2.2b}$$

where μ_0 is the vacuum's magnetic permeability. If we assume harmonic time dependence of the electromagnetic fields,

$$\begin{aligned}\vec{E}(\vec{r},t) &= \vec{E}(\vec{r})e^{i\omega t}\,,\\ \vec{H}(\vec{r},t) &= \vec{H}(\vec{r})e^{i\omega t}\,.\end{aligned} \tag{2.3}$$

By the substitution of equations (2.2) into equations (2.1) the following system is obtained

$$\nabla \times \vec{E}(\vec{r}) = -i\omega\mu_0\vec{H}(\vec{r})\,, \tag{2.4a}$$

$$\nabla \times \vec{H}(\vec{r}) = i\omega\varepsilon_m(\vec{r})\vec{E}(\vec{r})\,, \tag{2.4b}$$

$$\nabla \cdot \vec{H}(\vec{r}) = 0\,, \tag{2.4c}$$

$$\nabla \cdot (\varepsilon_m(\vec{r})\vec{E}(\vec{r}) = 0\,. \tag{2.4d}$$

Now, the first two Maxwell's relations, equation (2.4a) and equation (2.4b) can be rearranged into a single vectorial expression satisfied by the magnetic field

$$\nabla \times \frac{1}{\varepsilon_m(\vec{r})}\left(\nabla \times \vec{H}(\vec{r})\right) = \omega^2\mu_0\vec{H}(\vec{r})\,. \tag{2.5}$$

Equation (2.5) is the master equation that represents an eigenvalue problem and together with the divergence equation (2.4c) describes completely the properties of an optical wave in a structured material whose dielectric constant distribution is given by $\varepsilon_m(\vec{r})$. The left side of the master equation can be formulated as an operator Θ acting on $\vec{H}(\vec{r})$ so that it looks explicitly as an eigenvalue problem,

$$\begin{aligned}\Theta\vec{H}(\vec{r}) &= \omega^2\mu_o\vec{H}(\vec{r})\,,\\ \Theta &\equiv \nabla \times \left(\tfrac{1}{\varepsilon_m(\vec{r})}\nabla\times\right)\,.\end{aligned} \tag{2.6}$$

Although the master equation could have also been formulated in terms of $\vec{E}(r)$, it is more convenient to express the problem in terms of $\vec{H}(\vec{r})$. This is because the operator Θ is *Hermitian* which makes it possible to simplified the computational problem [4]. Once the modes $\vec{H}(\vec{r})$ for a given frequency are found then equation (2.4b) is used to obtain the electric field,

$$\vec{E}(\vec{r}) = \left(\frac{-i}{\omega\varepsilon(\vec{r})}\right)\nabla \times \vec{H}(\vec{r}). \tag{2.7}$$

It is important to note that all the previous discussion did not assume a periodic medium, therefore it can be applied for any dielectric distribution. For example, in the case of a wave propagating in a homogeneous medium ($\varepsilon_m(\vec{r}) = \varepsilon_m$) equation (2.5) reduces to the Heltmholtz equation, which for certain structures can be solved in a closed form. This is the case of conventional step-index fibres. However, in the case of photonic crystals and MOFs the eigenvalue problems is more complicated and an analytical solution is usually impossible to obtain. Nevertheless, the periodic nature of a photonic crystal allows the simplification of the electromagnetic problem of all the structure to a small region of the photonic crystal.

A photonic crystal might be described in terms of a periodic array of points in a space called *lattice*, and a unit cell which is repeated identically at every point of the lattice. A unit cell is defined as the smallest area, which by mere translations may fully represent the structure. Every point of the lattice can be defined in terms of the *lattice vectors* ($\vec{u_1}, \vec{u_2}, \vec{u_3}$), which are the smallest vectors that can connect one lattice point with another. All crystals have an associated lattice in Fourier space called a *reciprocal lattice* which consists of the set of all the allowed terms in the Fourier expansion of the periodic structure. This lattice is defined in terms of the *primitive reciprocal lattice vectors* ($\vec{g_1}, \vec{g_2}, \vec{g_3}$) [56, 57, 4].

To examine the way a photonic crystal affects the propagation of light through it, the dielectric constant of the structure must be expressed in terms of the lattice vector $\vec{R}$. The periodic dielectric function of a photonic crystal satisfies $\varepsilon_m(\vec{r}) = \varepsilon_m(\vec{r} + \vec{R})$. According to the Bloch's theorem, the eigenfunctions solutions of the the magnetic field can be expressed as Bloch's states consisting of a plane wave modulated by a periodic function with the same periodicity as the photonic crystal.

$$\vec{H}_k(\vec{r}) = \vec{U}_k(\vec{r}) e^{i\vec{k}\cdot\vec{r}}, \tag{2.8}$$

where $\vec{U}_k(\vec{r})$ has the same periodicity as the lattice, i.e. $\vec{U}_k(\vec{r}) = \vec{U}_k(\vec{r} + \vec{R})$. Therefore, knowing the values of the magnetic field $\vec{H}_k$ in a unit cell, the magnetic field in all the structure can be inferred from equation 2.8. In other words, the electromagnetic problem in photonic crystals is reduced to find the values of the magnetic field (2.5) in a small area. In the same way, in the reciprocal lattice, a Bloch states for a wave vector $\vec{k}$ is equal to the Bloch state $\vec{k} + \vec{G}$, where $\vec{G}$ is any vector of the reciprocal lattice. This gives rise to a periodicity of the dispersion curve in the reciprocal space (or $\vec{k}$-space), expressed as $\omega(\vec{k}) = \omega(\vec{k} + \vec{G})$. Consequently, the dispersion information of the modes is contained in a region of the reciprocal space called the *Brillouin zone* and only wave vectors $\vec{k}$ lying inside the Brillouin zone identify an independent mode. Therefore the dispersion curves of a photonic crystal are normally presented as plots of

frequency versus wavevectors in the first Brillouin zone. In the subsequent sections a description of the distinctive optical properties of MOFs is provided.

2.4 Step-Index Optical Fibres

To get a qualitative understanding of some of the basic optical properties of MOFs, it is convenient to describe some properties of step-index optical fibres. The simplest form of silica optical fibre has a step-index geometry which consists of a central core, surrounded by cladding layer whose refractive index n_{clad} is slightly lower than that of the core n_{core}. Light is guided in the core by means of total internal reflection (TIR) at the core/cladding interface, as in Figure 2.5.

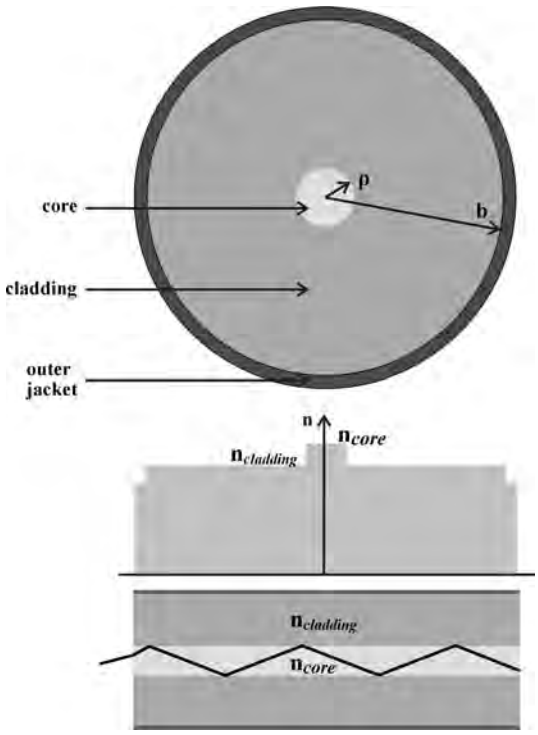

FIGURE 2.5: Schematic illustration of the cross-section and refractive-index profile of a SMF. The bottom image shows guidance by TIR.

The solution of electromagnetic problem (equation 2.5) for the step-index fibres results in an analytical solution. In this solution there are two parameters that provide important information of the optical guiding properties of these fibres. The first one is the relative core-cladding index difference

$$\Delta = \frac{n_{core} - n_{clad}}{n_{core}} \tag{2.9}$$

and secondly the normalized frequency

$$V = k_0 \rho \sqrt{n_{core}^2 - n_{clad}^2}\,, \tag{2.10}$$

where $k_0 = 2\pi/\lambda$, ρ is the core radius, and λ_0 is the wavelength of the transmitted light [58]. In a optical ray picture, the relative difference in refractive index Δ gives rise to total internal reflection that will confine light in the core for certain incidence angles. The parameter V determines the number of transverse optical modes supported by the structure. These fibres support a single transverse mode if $V < 2.405$. Because $\Delta \approx 0.003$ for most fibres, the main parameter that determines whether a fibre is single mode or multimode at λ_0 is the core radius ρ. Single mode fibres at $1.5\,\mu$m require ρ to be $\sim 7\,\mu$m and the cladding radius b is not that important as long as it is large enough to confine the optical mode.

2.5 Index-Guiding MOFs

A MOF usually consists of a periodic array of air holes on a silica background. The cladding may form a two-dimensional photonic crystal. The most common structure of MOFs is a pattern of circular holes arranged in a hexagonal lattice. Figure 2.6 presents a schematic representation of a MOFs in which the structural parameters are Λ, the pitch and d, the hole diameter.

If the core is made of silica, the fibre may guide light by TIR, just like the step-index fibre described above. In this case TIR takes place at the interface between the silica core and the structured cladding, which is made of air and silica and has an "effective" refractive index lower than that of the solid core.

To obtain a qualitative description of the optical properties of index guiding MOFs, Birks *et al.*[10] proposed the now known effective index method. This method consists of interpreting the structured cladding as a solid medium with a properly chosen effective refractive index, n_{eff}. The effective index method uses a scalar model to evaluate the periodic structure of the cladding in order to calculate n_{eff}. The resulting waveguide consists of a solid core and a solid cladding with refractive indices n_{core} and n_{eff} respectively. As a result, some modeling elements for standard optical fibres can be applied for MOFs. The first step of the effective index method is to determine the fundamental mode or fundamental space-filling mode of the photonic crystal cladding. This is done by solving the wave (equation 2.5) within a cell centred at one of the holes in the periodical lattice. The propagation constant of the resulting fundamental space-filling mode, β_{FSM}, is the maximum propagation constant allowed in the cladding, and is used to

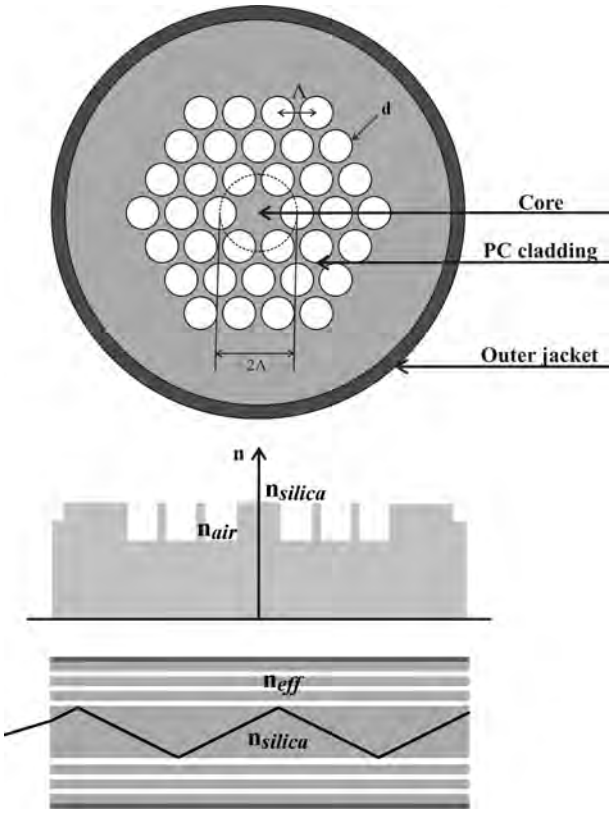

FIGURE 2.6: Top: Transverse cross-section of a solid core MOFs. The white and grey regions are air and silica respectively. The photonic crystal cladding is an ideal hexagonal lattice with parameters: pitch Λ and hole diameter d. The refractive index profile of fibre the is shown in the middle. The bottom images illustrate the modified TIR guidance mechanisms.

define the effective index $n_{eff} = \beta_{FSM}/k$. Similarly to conventional fibres, the propagation constant of any mode supported in the core needs to be $k_{core} > \beta > \beta_{FSM}$. This method can only be applied to index guiding MOFs and provides a good qualitative description of their optical properties [59].

2.6 Optical Properties of MOFs

2.6.1 Endlessly Single Mode Operation

Although the guidance in solid core MOFs is in some respects similar to conventional total internal reflection, it becomes apparent that it has a particulary interesting property; MOFs with relative small air filling fraction and large core areas exhibit single-transverse mode behavior from the UV to the near infrared wavelengths [10]. This behavior is related to the strong wavelength dependence of the cladding refractive index $n_{eff}(\lambda)$. In a conventional step-index fibre the number of guided modes is determined by the value

of the normalized frequency V (equation (2.10)), which must be less than 2.405 for the core to be single mode. In the case of MOFs the normalized frequency may be defined as an effective value,

$$V_{eff}(\lambda) = k_0 a \sqrt{n_{glass}^2 - n_{eff}^2(\lambda)}\,. \tag{2.11}$$

Numerical modeling shows that, by choosing an appropriate design ($d/\Lambda \leq 0.4$), the normalized frequency remains smaller than 2.405 for any wavelength and the fibre never supports any higher order modes [60]. Endlessly single-mode guidance in MOF originates from the fact that when long wavelength light travels in the fibre its electromagnetic field will penetrate into the cladding region and part of its energy will be concentrated in the air regions, whereas, shorter wavelengths concentrate more energy in the silica core which forces the core/cladding index difference to fall as the wavelength gets shorter. This counteracts the usual trend towards multimode behavior and $V_{eff}(\lambda)$ is almost kept constant. The endlessly single mode operation does not depend upon the core size but only on the air filling fraction [60] permitting single mode fibre cores with large areas. For example, a single-mode MOF with core diameter of 22 μm at 458nm was reported in 1998 [61], in a conventional step index fibre this would require the core to be ~ 10 times smaller. It has been demonstrated that by simply modifying the air filling fraction, the fibre's mode area can be tailored over three orders of magnitude [62].

Fibres providing large mode areas allow higher power to be transmitted before nonlinearities affect the beam quality or damage the fibre. Indeed, these fibres are desirable when high power is transmitted [63] and for fibre lasers/amplifier applications [64, 65, 66]. Moreover, the ability to transmit high power in a single mode has a major impact in the field of laser machining, while, small core fibres are convenient for nonlinear applications [67].

2.6.2 Group Velocity Dispersion

Group velocity dispersion (GVD) causes different frequencies of light to travel at different group velocities. This is an important factor in the design of optical communication systems and nonlinear experiments. It is well know that GVD is one of the major limitations for high speed communications and for any optical system supporting ultrashort pulses, hence, the importance of tailoring the dispersion properties of optical fibres. The total dispersion in a optical fibre depends on both the material dispersion and the waveguide dispersion and, as most fibres are made of silica, the material dispersion cannot be changed. Small core MOFs with high air filling fraction offer a great advantage in comparison to standard fibres in that the tight mode confinement leads to a very strong

waveguide contribution which is extremely sensitive to the fibre's geometrical structure. As the holes get larger the small core becomes more and more isolated, and dispersion properties resemble those of an isolated silica rod. These fibres can present interesting dispersion properties that are impossible to obtain with standard step-index structures [68, 69]. For example, if the whole structure is made very small, the zero dispersion wavelength (ZDW) can be moved below 1.28 μm which is the ZDW of conventional single-mode fibres [70]. In wavelength-division multiplexing (WDM) communication systems it is essential to maintain a uniform time delay of the different channels, which requires that the transmission line approaches the ideal state of constant dispersion. Therefore, MOFs with flat dispersion, covering wavelengths across the telecommunications window, have been a hot topic of research during the last couple of years. Such fibres have been fabricated covering both the 1.3 μm and 1.5 μm bands [71, 72] showing great relevance for high speed communications. In addition, hollow-core PBGFs are even more flexible than index guiding MOFs in terms of dispersion control. Their ZDW is always present within its operational band thus they offer many opportunities for dispersion compensation at any wavelength.

2.6.3 Nonlinear Optics

Nonlinear processes in optical fibres are essential for various all-optical functions required in communications systems. Although many all-optical communications systems based on soliton interactions have been developed during the last two decades, it was not until the advent of MOF technology that the behavior of solitons and other nonlinear effects were engineered. The fibre's effective nonlinearity per unit length is defined by [58]

$$\gamma = \frac{2\pi \mathrm{n}_2}{A_{eff}\lambda}\,, \tag{2.12}$$

where n_2 is the nonlinear refractive index of silica and A_{eff} is the effective cross-sectional area of the guided mode. Since the fibre nonlinearity is inversely proportional to A_{eff}, which may be tailored by modifying the cladding structure, MOFs offer the possibility to make fibres with either very high or low nonlinearity. Nonlinear MOFs have high air filling fraction leading to strong confinement of the mode (small A_{eff}) and therefore high nonlinearity. Although small core MOFs with high air filling fraction are not necessarily single mode, they are robust to excitation of higher order modes which is essential for stable nonlinear effects.

Silica MOFs with tight modal confinement can present 10-50 times greater nonlinearity than that of conventional fibres [73] which allows ready access to various nonlinear optical functions. For example optical switching [74, 75, 76], wavelength conversion, Raman

amplification [77], parametric processes [78], soliton generation squeezing [79, 80], and supercontinuum generation [81, 82, 83, 84, 85] have been explored with MOFs. When high-energy short pulses (picosecond or femtosecond) travel through a material, their frequency spectrum can be broadened by the combination of various nonlinear effects [86]. The possibility of tailoring the dispersion characteristics of small core MOFs combined with their high nonlinearity has led to perhaps one of the most exciting applications of MOFs, supercontinuum generation spanning from 400 nm to 2000 nm. The first demonstration of a supercontinuum in a PCF used a fibre whose core was small enough to give zero dispersion at 800 nm, which is near the emission wavelength of a Ti:sapphire femtosecond pump laser [81]. Supercontinuum lasers find applications in medicine [87], metrology, spectroscopy, and many other areas [86]. Figure 2.7 shows a supercontinuum fibre laser that is used to study photon/plasmon interactions in metal-filled MOFs in Chapter 7.

FIGURE 2.7: Supercontinuum laser generation using a high nonlinear MOF. Nanosecond infrared pulses are coupled into the fibre core where visible light is generated due to nonlinear processes. The photograph shows the nonlinear fibre and a prism used as a diffraction medium. This laser has been used for plasmon experiments in Chapter 7.

In order to further increase the effective nonlinearity per unit length, fibres made of high index and high nonlinearity glasses have been fabricated [88, 89]. Using our technology the deposition of material with even higher nonlinearity than glasses, such as semiconductors, into the holes of MOFs is possible and may offer new opportunities in nonlinear optics. For example, it is difficult to generate laser light at wavelengths beyond those offered by the small window of available lasers. The efficient transfer of laser energy to new wavelengths, by stimulated Raman conversion, is therefore a very attractive way of generating light.

Spontaneous Raman scattering is caused by molecular vibrations, that interact spontaneously with the incident light, shifting its frequency both up (anti-Stokes) and down (Stokes). The Stokes signal is stronger than the anti-Stokes, due to Boltzmann distribution of occupying molecular states, and at high laser intensities is the predominant molecular oscillation. Ultimately, above a certain threshold power, the process becomes stimulated and the major fraction of the pump power is converted to the Stokes frequency. Semiconductors such as silicon and germanium have much larger Raman coefficients than silica which make them a good prospect for Raman wavelength conversion. A fibre which guides light in a silicon or germanium core, may be useful to generate Stokes wavelengths in very short fibre lengths and with low threshold. Moreover, because these semiconductors are transparent in the infrared, outside silica's transmission window, they have excellent prospects for MID-IR light generation.

2.7 Modelling Microstructured Optical Fibres

Having reviewed the fabrication, properties and applications of existing MOFs and the exciting possibilities offered by material deposition within their capillaries, it is necessary to understand the optical properties of these material-modified MOFs. This section provides a short discussion of the most extensively used numerical methods for analysing MOF. As mentioned, when complex fibre geometries are to be analyzed, the solution of equation 2.5 in a close form is not usually possible and powerful computational tools are required. This is the case when the goal is to provide a solution to the optical modes in microstructured optical fibres. Various parameters including the size, pitch, shape of the holes, number of holes, etc. affect the properties of MOFs. As it has been shown in the previous sections, the proper choice of these parameters permits the design of particular fibres for an intended application. Furthermore, due to the relatively high-refractive index difference of MOFs, it is necessary to apply full-vector methods and prevents us from employing scalar approximations that lead, for example, to the definition of LP modes of step-index fibres.

In recent years a significant amount of work has been devoted to the formulation of full-vector numerical methods for the modelling of MOFs. Methods such as Beam Propagation, Plane Wave Expansion, localized function, multipole method, Finite-Difference Time and Frequency domains, as well as Finite Element Method have been adapted/developed for the accurate description of both index-guiding and photonic bandgap fibres.

It is worth briefly describing some of these methods because the deposition of submicron layers of semiconductor and/or metals within the fibre holes makes the computational task even more complicated, and a good understanding of the possibilities of each method

has been useful to predict the behavior of material modified fibres. The next section provides an overview of the main methods that have been applied for the solution of the eigenproblem (equation (2.5)) in MOFs.

2.7.1 Full-vector Plane-wave Expansion Method (FVPWE)

This was the first theoretical approach proposed to find the photonic bandgaps of photonic crystals. FVPWE is based on the methods used to obtain electronic bandgaps in semiconductor crystals. It is particularly well-suited to calculate the bandgap of periodic structures, and the modes allowed within the photonic bandgap by defects. For a full periodic structure, according to the Bloch theorem, the solution to the vectorial wave equation may be expressed as a plane wave modulated by a periodic function with the same periodicity as the photonic crystal (equation (2.8)). As the solutions to the problem are periodic, it is convenient to operate in the reciprocal space. Thus, the solutions and the periodic dielectric constant distribution are expressed as a Fourier-series expansion in terms of the reciprocal lattice vectors [4]. FVPWE has been one of the major tools for the analysis of MOFs with periodic dielectric perturbations [90].

2.7.2 Orthogonal Basis Functions Techniques

Orthogonal basis techniques are based on the direct solution of Maxwell equations, using a representation of the refractive index and the field distributions as a sum of orthogonal functions. Because guided modes of PCFs are localized in the core vicinity, it is possible to calculate them by representing the electromagnetic field as sums of localized functions in the core vicinity. The expansion coefficients are obtained by overlapping integrals between the localized basis functions and the fibre refractive index distribution. Using this, Maxwell's equations are reformulated as an eigenvalue problem for the propagation constant of the modes. The first scalar localized functions method was developed by Mogilevtsev *et al.*, using a Hermite-Gaussian basis [70]. Since then, the orthogonal basis functions technique has been extended and further developed by other scientists. For example, in the work by Monro and co-workers the transverse refractive index profile is represented with two orthogonal basis functions [62]. The periodic lattice of holes is described using periodic functions (e.g. as a Fourier series) and the central defect is described using Hermite-Gaussian functions. Because of the reduced number of terms needed to accurately represent the refractive index profile, this method allows for a fast and efficient computation. Although orthogonal basis function techniques were very useful to obtain a good description of the optical properties of MOFs during their early years, they are not very flexible in terms of calculating aperiodic fibre structures [24].

2.7.3 Beam Propagation Method

The beam propagation method (BPM) is a well-established tool of analysis for field distribution in integrated photonic devices. BPM uses numerical algorithms to simulate the propagation of a coherent beam along any arbitrary structure and obtain its field distribution [91, 92, 93, 94]. In BPM an initial field distribution propagates step by step in the longitudinally direction of the photonic structure. Although a paraxial approximation is usually employed in order to reduce the computational time, BPM can easily be extended to wide-angle problems. It is also possible to take into account the vectorial nature of the electromagnetic wave making it suitable for the analysis of MOFs. BPM it is not designed to calculate the optical modes of a structure; however there are some expansions of BPM which make it possible to provide mode-solving capability. For example, imaginary-distance BPM [95] the fundamental mode is obtained by propagating an initial mode profile along an imaginary distance direction (iz). Then the oscillating term $e^{i\beta z}$ becomes a gain term $e^{i\beta z}$. As the fundamental mode is characterised by the largest propagation constant, its intensity will increase at the higher growth rate and its profile will dominate all other modes after a short distance, higher order modes can be sequentially obtained. This method is suitable for the modeling of semiconductor and polymer optical fibres many optical properties of filled MOFs such as, mode structure and optical loss.

Finally, it is worth noting that many numerical methods have been used to efficiently predict the optical properties of photonic crystals, and in particular, the multipole method and finite element method (FEM) are of great interest for this research.

2.8 Semiconductor Photonic Bandgap Fibres

The spectral position and extent of bandgaps are highly dependent on the optical properties of the material which form a photonic crystal. Therefore, the inclusion of materials, whose optical properties can be easily modified, within the capillary voids of PBGF offer opportunities to developing tuneable photonic devices such as filters, modulators and variable attenuators based on bandgap effects. Bise and colleagues demonstrated a solid silica core tuneable PBGF [96]. For this experiment the cladding holes were filled with high refractive index oil and, by thermally modifying its refractive index, they were able to tune the band gap structure of the fibre, and therefore its transmission properties. Subsequently, tuneable photonic bandgap fibres based on the thermo-optic response of liquid crystals (LCs) were demonstrated [34]. In this work, Larsen *et al.* filled LCs into the circular voids of a triangular structured MOFs. The relatively high, and controllable refractive index of the LC, together with the periodic arrangement of

holes in the MOF, gave rise to a fibre cladding with photonic bandgaps. The bandgap properties of the filled fibre, thus, depend on the original structured cladding and on the refractive index of the LC which can be thermally tuned by a resistive heater. In this way the photonic band gaps of the cladding could be shifted to different wavelengths. This might change the transmission loss of the guided modes to create in-fibre amplitude modulators, filters, attenuator. Due to the strong sensitivity of the optical properties of semiconductors to electrical and optical fields, they are ideal candidates for control of light by very small external influences. Therefore, the deposition of semiconductors within photonic bandgap fibres can be employed for the development of a new class of high speed tuneable PBGFs that, in contrast with previous demonstrations might be more stable, faster and be either tuned by electronic or optical effects. In this section the the bandgap structure of MOF with annular deposition of semiconductors is theoretically investigated. The resulting semiconductor photonic crystal fibres resembles PCs fabricated in macroporous silicon [97]. Fibre structures have the advantages that they can be easily fabricated and the pores can be much longer than those currently fabricated in porous silicon. A commercially available FVPWE software (BandSolve®, RSoft) has been utilized to calculate the band structure of MOFs whose holes have been covered with a thin layer of silicon. Figure 2.8 is a schematic of the cross section of a PBGF used in the numerical simulations, this fibre has a triangular arrangement of holes in the cladding, and a thin silicon layer is deposited onto the hole walls.

The optical modes supported by the periodic cladding of the fibre shown in Figure 2.8 were calculated by solving the master equation (equation 2.5) in the unit cell. The fibre parameters pitch, hole radius and silicon wall thickness were changed. As an example, Figure 2.9 is the bandgap map of a fibre whose parameters are $\Lambda = 2\,\mu$m, $a = 1\,\mu$m and $t = 150\,$nm.

The green regions of Figure 2.9 are the bandgaps of the periodic cladding (no light can propagate in the cladding for this region). The red line is the silica line (propagating modes in silica are only allowed to the left of the silica line) and the blue line is the silicon line. It is clear that the silica line crosses some bandgaps, and hence there can be modes that can propagate within silica but not within the periodic cladding. By changing the refractive index of the silicon by means of optical or electrical fields [98] it is possible to modify the bandgap structure of the fibre, which will affect the propagation properties of a guided mode in the silica core. These results suggest that it is possible to create fibres with silicon inclusions, that can guide light in a silica core due to photonic bandgap effects. However more extensive analysis of these fibres must need to be carried out to confirm this behavior.

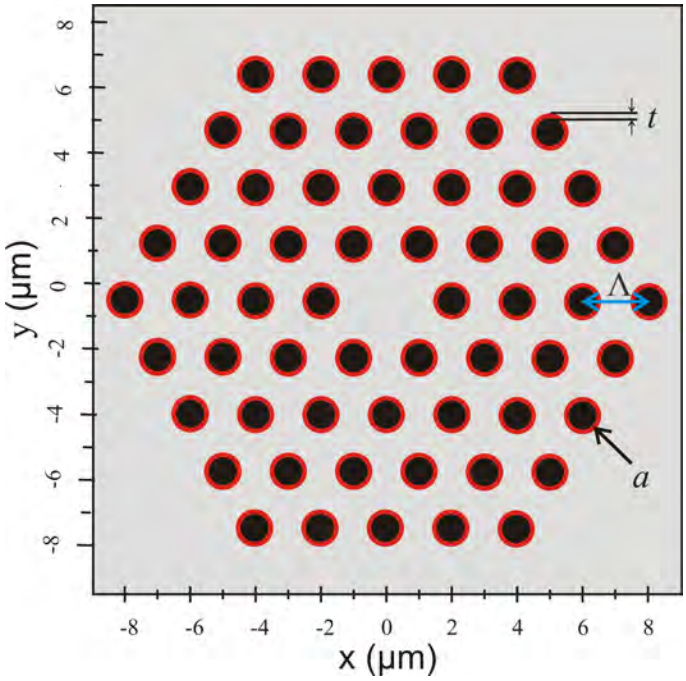

FIGURE 2.8: Transverse index profile of a MOF with triangular lattice. A thin silicon layer is deposited on the hole walls. The silicon is represented by red colour, silica by gray and the black region is air. A missing hole in the centre forms its silica core. The pitch Λ, silicon thickness t and hole radius a can be modified for the simulations.

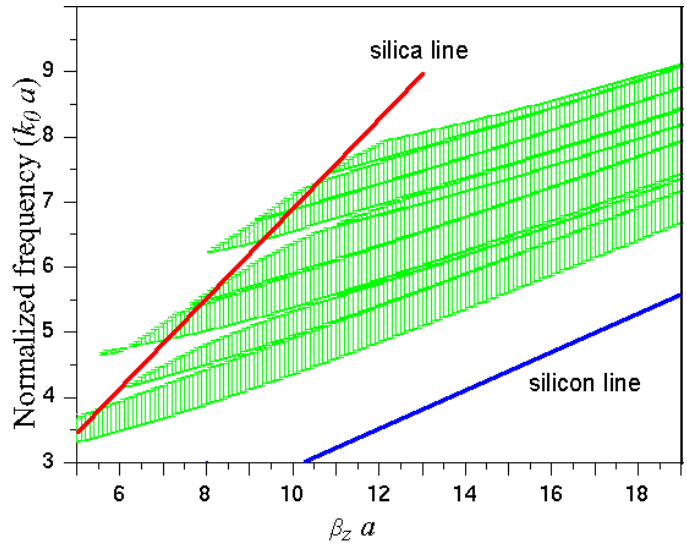

FIGURE 2.9: Bandgap map for the 16 lowest-frequency modes of a the fibre show in Figure 2.8. The parameters used in the simulation were $\Lambda = 2\,\mu$m, $a = 1\,\mu$m and $t = 150\,$nm.

Chapter 3

Materials Deposition inside Microstructured Optical Fibres

The fibres studied in this thesis are fabricated in what can be considered to be a two step process: first silica/air MOFs are made using the stacking and drawing method. Afterwards, in an *independent* process, materials are deposited inside MOFs capillaries, to give maximum design flexibility over both structural and compositional parameter space. The deposition within MOFs presents considerable challenges to achieve sufficient mass transport of the precursors within the high aspect ratio fibre channels, due to the fact that the flow is restricted by the small capillary dimensions and the deposited material itself. Thus the use of traditional deposition methods, such as those used for integrated circuit (IC) fabrication, are limited by the fibre structure and more appropriate techniques are required.

This chapter gives an insight into the conventional material processing methods used for the deposition of semiconductors and metals onto planar substrates and into nanostructures. The advantages of these deposition methods are discussed and their applicability within MOFs is analyzed. Finally, this chapter describes the high-pressure chemical deposition methods that our research team has developed and implemented for the deposition of crystalline semiconductors, metals and polymers inside the long air channels of silica MOFs.

The silica MOFs used in this work were fabricated in the ORC and the deposition process has been carried out in collaboration with Penn State University, in the case of semiconductors and with the University of Nottingham for PMMA and silver impregnated fibres.

3.1 Micro/Nanomaterials Synthesis

What is the smallest possible device with optical, electronic, or magnetic functionality?

Questions like this and the demands of present and future microelectronic, photonic, data storage and lab-in-a-chip systems for genomics, combined with ideas from great visionaries such as Richard Feynman -who predicted the possibility of tailoring the properties of matter in the sub-micronscale- [99] are fueling interest in the field of nanotechnology. At the present time the word *nanotechnology* is becoming more and more familiar to scientific and engineering communities because of the numerous opportunities that this field might open, including building circuits for a new kinds of computers, supercapacitors, ultra-sensitive molecular sensors, and fabricating the perfect molecular-scale machines and information systems of living organisms. However, nanotechnology, as all other technologies, is strongly dependent on its platform materials. Therefore, before having devices such as those proposed by Feynman more that 40 years ago, stringent requirements on nanomaterials and nanostructure fabrication methods must be satisfied.

Figure 3.1 is a cartoon of the two main approaches for micro/nanomaterial fabrication: top-down and bottom-up. Top-down, which is commonly used to produce microchips, makes use of photolithography, etching and deposition from the vapour phase to carve out material and create tiny features on substrates. Although this technology allows complex structures to be made in well-defined positions, it requires substantial effort when extended to scales below 100 nm. It is intrinsically planar and its extension to 3D is limited to the stacking of planar structures.

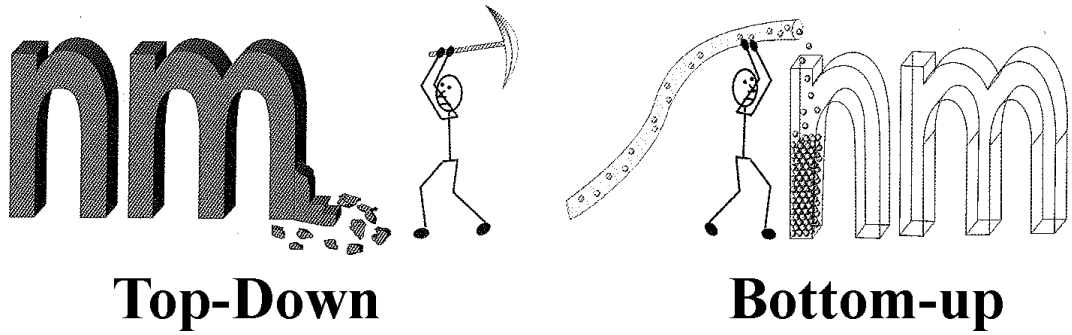

FIGURE 3.1: Cartoon of top-down and bottom-up nanofabrication techniques. From reference [100].

The second nanomaterial fabrication method is known as templating or bottom-up. It entails synthesizing the desired material within the holes of a preordered template. The material deposited within the holes will follow the structure of the template. Because the template and the deposited material are formed in discrete processes, many different materials can be deposited inside the structure. Porous templates can be made of

several materials and with a variety of geometries. A major advantage of bottom-up is that complex 3D structures and topologies can be fabricated so this technique is not restricted to planar geometries.

Nature has applied bottom-up fabrication routes to provide animals and plants with superior multifunctional structures [101, 102]. Some examples of nature's ability to create complex structures are illustrated in Figure 3.2. The templates used by nature are commonly formed by self assembly of molecules or minerals. Maybe the most obvious example to humans are our bones which grow on ordered macromolecular templates [103, 104]. The materials experts in the Iron Age recognized bottom-up as the straightforward method of replicating objects, it is much easier to cast a mold than to carve out the same device over and over again. However, this idea was not applied to the nanoworld until the beginning of the 70s [105] and recently the template method has proved to be a powerful approach for micro/nanomaterials' processing [106, 107, 108]. Many materials such as metals, semiconductors, dielectrics and magnetic materials have been deposited within mesoporous templates. If desired, the template can be dissolved away after deposition, leaving behind free standing 3D structures.

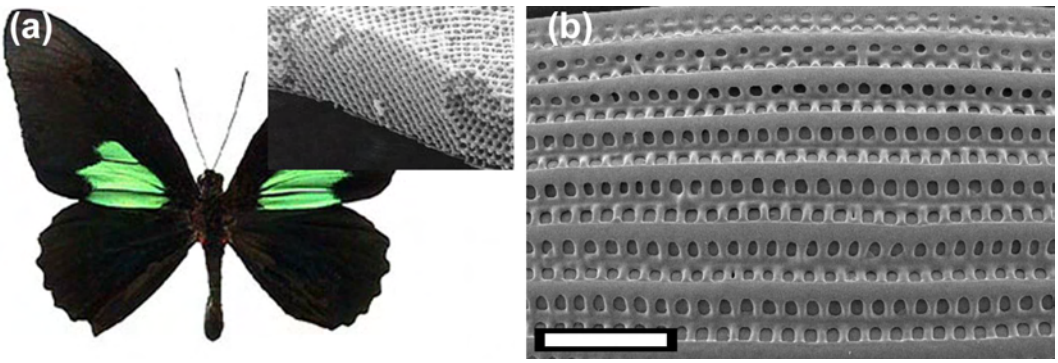

FIGURE 3.2: The green colour of *Parides sesostris* is created by an "inverse opal" photonic crystal which is made by templating and self-assembly methods [27]. Nanostructures in nature do not only have optical functionalities but also mechanical purposes, as has the glasshouse of marine diatoms. (b) SEM micrograph of the silica wall of the marine benthic diatom *Amphora coffeaformis*, the scale bar is 5 μm. This ordered silica nanostructure is made by the deposition of silica in organic matrices [101].

The most common templates currently used in bottom-up are mesoporous alumina [109, 110], self-assembled nanoscale spheres [111, 112, 108, 113, 114, 115] and polymeric membranes [105]. There are many examples of microfabrication of 3D photonic crystals based on self-organizing sphere templates. A template of close-packed spheres can be converted into photonic crystals by depositing a high refractive index semiconductor such as Si, Ge, GaP and subsequently removing the template. The resulting "inverse opal" structure may exhibit photonic band gaps [116].

The range of template structures that can be formed, and their extent and perfection restricts the possibilities of bottom-up [117] fabrication. Therefore, the search for new templates with highly controlled geometry is essential for bottom-up and micro/-nanosciences. The merit of a particular template structure, if it is to find wide practical application, will be defined by its robustness, temporal and mechanical stability, and its ability to be easily integrated within existing technological infrastructures. With these criteria in mind, one can conclude that MOFs present a number of attractive properties, such as very large internal surface areas, high aspect ratios and outstanding mechanical properties, making them excellent lithography free, robust and inexpensive 3D templates for materials deposition.

A limitation of using MOFs as templates is that the material deposition methods currently applied in microelectronics and nanofabrication do not allow conformal coverage and/or complete filling of MOFs narrow high aspect capillary holes. Therefore, our research group has explored new high pressure deposition methods for achieving this task.

3.2 Vapour Phase Deposition

Material deposition methods fall into two broad categories: vapour and liquid phase techniques depending on the physical state of the carrying medium which is used to transport the precursor to the substrate.

This section describes the main characteristics of vapour phase deposition (VPD) which is the process whereby gas phase species are condensed, chemically reacted or converted into solid deposits. Vapour deposition techniques are divided into two main categories: physical vapour deposition and chemical vapour deposition. Due to the absence of surface tension in gases, they can completely wet complex topologies. Therefore, vapour precursors provide a powerful medium for the conformal deposition within mesoporous substrates [118]. During the last decades the deposition of high quality thin films, free standing structures and mesoporous materials by vapour deposition methods have been demonstrated. As will be described in the following sections, our research group has developed high-pressure vapour phase techniques for growing amorphous and crystalline silicon and germanium wire/tubes within MOFs [16].

3.2.1 Physical Vapour Deposition

Physical Vapour Deposition (PVD)is typically a direct line-of-sight technique in which the gaseous precursor is produced by either evaporating or ablating the target material.

The evaporated atoms or molecules solidify onto a substrate and form films. In order to obtain high quality deposits and to allow the particles to travel as freely as possible, the whole process takes place in a vacuum chamber. Many PVD techniques can produce high purity films and have found increased use in the microelectronics and optoelectronics industries, especially for the fabrication of film resistors and filters. The most common PVD methods are: thermal vapour deposition, sputtering, laser ablation deposition and molecular beam epitaxy (MBE) which is particulary useful for top-down micro/nano fabrication, where device quality is at a premium.

3.2.1.1 Thermal Vapour Deposition (TVD)

Thermal evaporation represents one of the oldest of the thin film deposition techniques and, at present, many different kinds of films in integrated circuits are deposited by evaporation. The material to be deposited is heated to its melting temperature in a vacuum, which allows its vapour to reach the substrate surface and grow thin films [119]. The material is usually evaporated by passing current through a high melting temperature metal (e.g., a tungsten boat or filament). In industrial applications, resistive heating has been replaced by electron beam and RF induction evaporation [118]. TVD is suitable for film growth of materials with simple stoichiometry, making it very common for metal deposition. Indeed, a wide range of metals and alloy thin films such as Au, Al, Ag, Ni, Ni-Cr [120], Ti-Al-V, Ni-Cr-Al [121] have been effectively deposited. This technique is not suitable for compound materials or materials with complex stoichiometries because the different vapour pressures of their constituents would lead to deposits with incorrect compositions. TVD offers almost no control over the path taken by the evaporated atoms, with consequent slow growth rates, and inefficient use of the source material. Some variations of TVD, such as MBE, offer great control of the deposition process even down to the level of atomic monolayer precision. However, because the process has to take place in a vacuum chamber, the vapour cannot wet the internal walls of mesoporous templates. A representation of a TVD chamber is illustrated in Figure 3.3.

3.2.1.2 Sputtering

A schematic of a sputtering chamber is shown in Figure 3.4. During the deposition process, the solid coating material (target), at a high negative potential, is converted into vapour phase by ion bombardment (Ar^+). The vaporized material is condensed onto the substrate placed on the anode [119]. Although sputtering coating always takes place in the presence of plasma, the pressure in the vacuum chamber is always kept very low and the evaporated atoms follow a more or less collision-less path to the substrate. Sputtering is preferred over evaporation in many applications due to the fact that virtually any

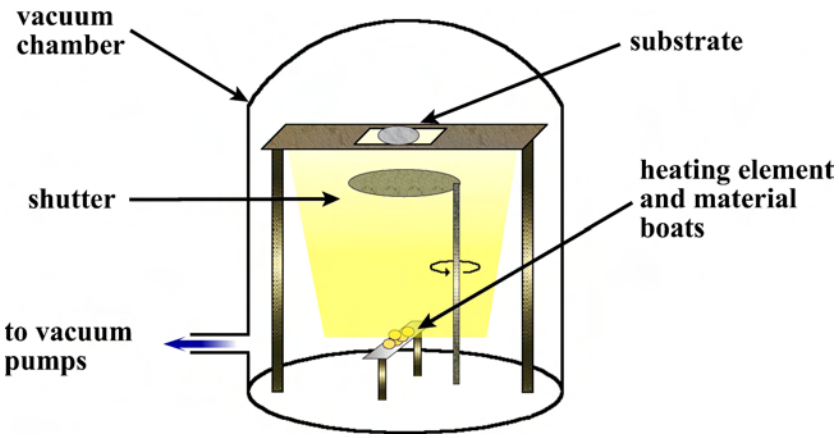

FIGURE 3.3: Illustration of a typical TVD deposition chamber. Only materials with a much higher vapor pressure than the heating element can be deposited without contamination of the film. TVD requires good vacuum during evaporation, and pressures lower than 10^{-6} Pa are normally used.

material can be sputtered and has better adhesion to the substrate. This technique is commonly used for the deposition of metals, semiconductors and dielectrics onto integrated circuit wafers. An important advantage of the sputtering process is its capacity to convert the material into gas phase without changing its chemical composition, resulting in high purity deposits.

PVD methods have many features which have permitted them to be widely used at laboratory and industrial levels. In PVD, the starting materials are chemically pure and the deposition takes place in a vacuum chamber, thus these methods usually have fewer contamination problems than other deposition techniques. However, since the evaporated particles tend to follow a straight path (line-of-sight), films deposited by physical means are commonly directional rather than conformal which prohibits them from forming homogeneous films within mesoporous structures. Moreover, since PVD are vacuum deposition processes, there is limited mass transport down the extreme aspect-ratio capillaries of MOFs. Thus, PVD techniques cannot be applied to our purposes and chemical methods are must be considered.

3.2.2 Chemical Vapour Deposition

Chemical Vapour Deposition (CVD) is a non-line-of-sight deposition process whereby chemical reactions produce solid material from gaseous reagents on or near the surface of a heated substrate. The constituents in the vapour phase are typically diluted with an inert carrier gas and react at the surface of hot substrates [122]. CVD has developed into one of the most versatile and important methods for material synthesis and today has application to a wide spectrum of compounds. CVD plays a central role in the synthesis

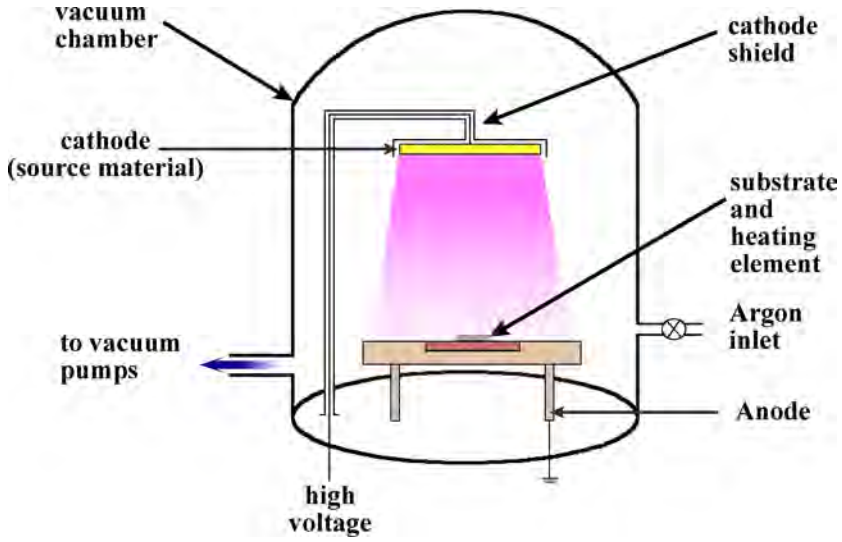

FIGURE 3.4: Schematic diagram of a simple sputtering deposition chamber.

of amorphous, polycrystalline and epitaxial single crystal films which are used in almost every semiconductor device. Moreover, CVD techniques are used for the fabrication of conventional step index optical fibres [123].

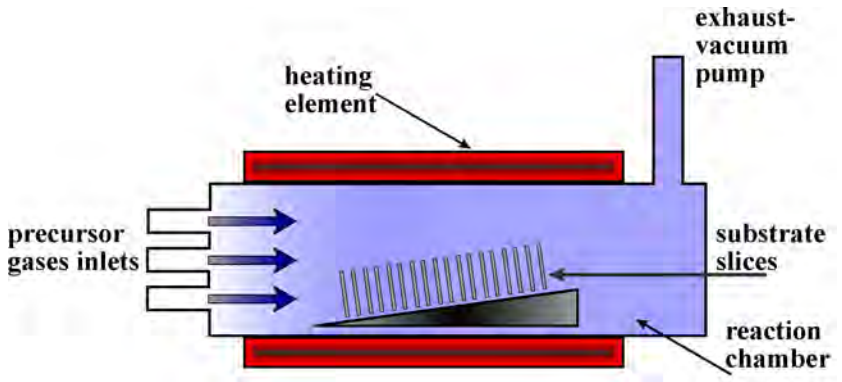

FIGURE 3.5: A schematic diagram of a hot wall open flow CVD system. All substrates can be covered homogeneously because of the low surface reaction rate of the growth process. The total pressure in the chamber is usually less than 60 kPa.

A simple CVD system apparatus is illustrated in Figure 3.5. The deposition process involves a dynamic flow, in which gaseous precursors enter to the reaction chamber and pass over the heated substrates. If the substrate temperature is high enough, the vapour precursors heterogeneous chemical react to produce a solid coating (deposit) plus by-product gases. The by-products are desorbed and, together with any remaining reactant gas, exit from the hot reaction zone through the exhaust tube. Heterogeneous CVD reaction take place on the substrate surface and have reactants in two or more phases and lead to thin coating. However, the reactions may not always take place on or close to the substrates but also can occur in the gas phase. These second kind of

CVD reactions, in which the reactants are only in the gas phase are called homogeneous reaction and take place via direct chemical decomposition of the precursors in the gas phase. Homogeneous reactions lead to powders, low density and poorly consolidated films and thus, are not usually desirable [124]. The various transport and reaction processes underlying CVD can be summarized as follows [118]:

- Mass transport of reactants and diluent gases, from the reactor inlet to the deposition zone.
- Homogeneous gas phase reactions, leading to film precursors and by-products. These reactions are undesirable.
- Mass transport of reactants to the hot substrate.
- Adsorption of film precursors and reactants on the surface.
- Heterogeneous surface reactions occurring selectively on the heated surface.
- Formation of film nucleation points and film growth.
- Desorption of by-products of the surface reactions.
- Mass transport of by-products in the gas flow away from the reaction chamber.

In CVD there are several factors which determine the rate, kind of deposition and the compound deposited, these include gas pressure, precursor concentration, substrate chemistry and temperature, gas precursor flow rate, etc. Because of the many variables involved in CVD and the complicated chemical, thermodynamic and physical phenomena involved, most reaction chambers are designed empirically and the parameters of the deposition are experimentally optimized specifically for each chamber and the desired deposition characteristics. When the CVD parameters are controlled in the correct manner, CVD can lead to the formation of high purity materials with structural control at an atomic or nanometre scale level.

The most popular CVD method uses thermal energy to drive the chemical reactions. However, there exist many diverse low temperature CVD techniques which require an additional energy source to initiate the reaction. Some examples of these CVD variants include: Laser-assisted (LACVD) and plasma-enhanced CVD (PECVD). Metallo-organic CVD (MOCVD) [125] and aerosol assisted CVD (AACVD) [126] are other important CVD methods.

In LACVD, photons are used either to locally heat (pyrolytic mechanisms) the substrate and initiate the CVD reactions or to decompose (photolytic mechanisms) the precursors in the gas phase. The energy provided by the photons can accelerate the reaction, increase the deposition rate in particular areas of the substrate and lower the deposition

temperature. The key attraction of this method is direct writing of 3D structures without lithography and extremely low temperature deposition [127]. The LACVD process can be performed at atmospheric or reduced pressure and has been described for a number of materials [128].

In PECVD, an RF-induced plasma transfers energy to the reactant gases. The vapour precursors are ionized and dissociated by electron impacts. The extra energy, provided by the plasma, permits the substrate to remain at a lower temperature, than in thermal CVD, and enhances the deposition rate. PECVD enables dielectric films such as nitrides, oxides, and oxynitrides to be deposited on wafers with small feature sizes which has led to wide use of PECVD in very large scale integration (VLSI).

MOCVD is variation of CVD which relies on the flow of organometallic or hydride gases to deposit materials with complex stoichiometries. MOCVD produces pure films and provides control within one atomic layer. Therefore it has commonly been used to epitaxially grow metallic, III-V and II-VI thin films [129, 125, 130]. This technique plays a key role in the manufacture of many III-V optoelectronic devices, such as, lasers, photodiodes and quantum wells.

Despite the considerable advantages and material flexibility of traditional CVD, the synthesis process takes place in reaction chambers at low ($\sim 1\,\text{Pa}$-$\sim 10\,\text{Pa}$) or atmospheric pressures ($\sim 100\,\text{Pa} - 10\,\text{kPa}$), making the precursors transport inside the long MOFs not feasible. However, as will be described later, there is no restriction to CVD being extended to higher pressures.

3.3 Liquid Phase Deposition

Liquid solutions or suspensions using water or other solvents (organic, ionic liquids, molten salts) represent an alternative method to PVD for the growth of materials either in bulk form or as thin films. Liquid phase deposition (LPD), as the name implies, involves the formation of solid deposits on a substrate from a liquid solution. The material precursors are either dissolved or suspended in a liquid medium and the deposition may occur by either chemical or physical mechanisms. Over time, LPD has developed into various important methods for material processing and synthesis. LPD techniques have certain advantages over vapour phase methods including the lower processing temperatures involved, high deposition rates and the lower cost of the precursors. Furthermore, LPD methods have recently found applications for the preparation of nanoscale structures by deposition within mesoporous templates.

3.3.1 Electrochemical Deposition

Electrochemical deposition refers to the growth of a material or alloys from a conductive solution (electrolyte) containing ions of the material to be deposited. The deposition occurs on the cathode's surface, by the flow of an electric current between two electrodes immersed in the solution. Many metals have been deposited within the holes of porous alumina, polycarbonate and polymer templates by the electrochemical reduction of metals ions [131, 132, 133]. Figure 3.6 shows examples of gold wires formed by electrodeposition within alumina templates. The membrane employed has cylindrical pore geometry, with monodisperse diameters that extend through the entire thickness of the membrane. The deposition is done by simply coating one end of the template with a metal layer and using this film as a cathode. The deposition is initiated on the cathode and the material grows following the geometry of the pores. It usually results in well-defined, high aspect ratio, nanowires or nanotubes. If desired, after the deposition the template can be dissolved away leaving behind the resulting metal structures. Nanowires and nanotubes of metals like gold, silver, platinum, copper, nickel have been prepared by electrochemistry. This technique has been prefered for the deposition of metals however many researchers have applied it for the deposition of semiconductor films on planar [134] and porous [135, 136] substrates.

Although electrochemistry has shown to be an excellent bottom-up template processing technique, the deposition conditions required in this method make it difficult to use for the impregnation of materials within MOFs templates. The main problem is that electrodeposition needs a conductive layer onto which the materials are grown. Because of this, materials could only be deposited at one end of a very long fibre but not in the central part of it. Another limitation of electrochemical deposition is the need for liquid precursors solutions, which can not easily diffuse inside centimetre long optical fibres and would thus prohibit the sufficient mass transport of precursors.

3.3.2 Electroless Deposition

Electroless deposition involves catalytic reactions in an aqueous solution which, in contrast to electrodeposition, occur without an external electric current. This technique has been used to fabricate metal nanotubes within nanoporous templates [137, 138, 139]. Figure 3.7 shows a very interesting experiment by Monk and Walt [38], in which millimetre long gold tubes are grown within microscale capillaries of an optical fibre.

The electroless deposition process can be briefly described as follows, a catalyst is first applied to all surfaces of the porous membrane, which is afterwards immersed into a solution containing metal ions and a chemical reduction agent (usually hydrogen). The

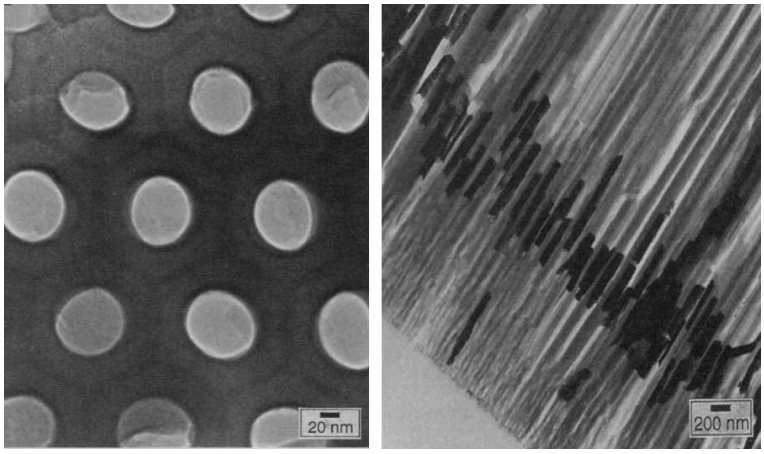

FIGURE 3.6: Synthesis of gold nanowires in porous alumina template by electrochemical deposition. Left: TEM image of a microtomed[1] section of alumina membrane. Right: TEM of Au nanotubes that are 70 nm in diameter within the pores of a membrane, from reference [131].

reduction of the metal solution to solid metal only occurs on the surface (where the catalyst was previously deposited) and metal films are formed on the walls. This technique has resulted in the preparation of gold nanotubes ensembles whose wall thickness can be controlled from a few nanometres to some micrometres. Nanotubes with inside diameters of less than 1 nm, made by electroless deposition of gold, have shown interesting applications for molecular filtering [137].

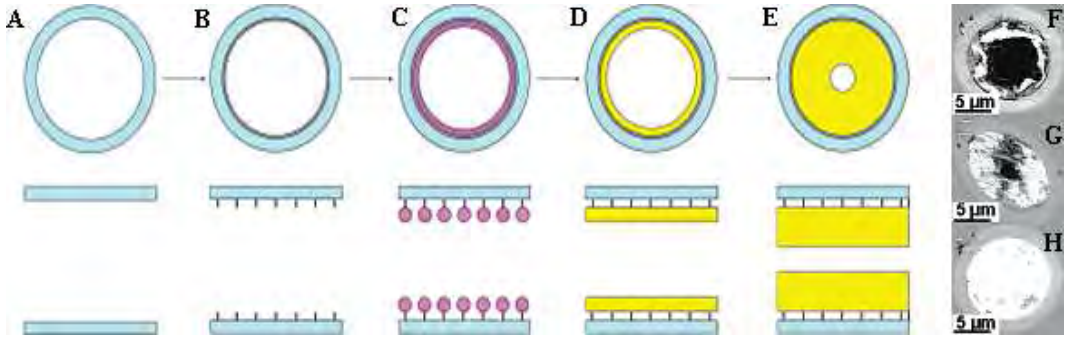

FIGURE 3.7: Synthesis of gold micro-tubes in a 5 μm silica capillary by electroless deposition (end and side views). Silica capillaries (A) are modified with a monolayer of bifunctional silane for gold adhesion (B), deposition of a monolayer of colloidal gold (C). Deposition of bulk gold from solution increases the size of the gold layer, eventually forming a uniform layer (D). As deposition progresses, the gold thickness approaches the radius of the capillary (E), microscope images of the resulting gold tubes (F G H). Taken from reference [38]

Both LPD methods, electrochemical and electroless deposition, require the diffusion of the precursor solutions through the template pores. Thus, these techniques are usually

[1]A microtome is a mechanical instrument used to cut samples into thin segments for microscopic examination, usually 1 to 20 μm thick.

limited to thin substrates ($\simeq 100\mu$m), or else deposition must be conducted over long periods of time (days) or cannot be achieved due to insufficient mass transport of the precursor far into the capillaries [38]. More than likely, this would be an inherently time consuming process for high aspect ratio features like MOFs capillaries. Furthermore,the removal of the liquid precursor solution and reaction by-products from the fibre holes would be a difficult task after the deposition inside long MOFs.

3.4 Supercritical Fluid Deposition

In order to develop a flexible method for the deposition within mesoporous templates, it is necessary to think of a technique that combines characteristics of both vapour and liquid phase methods. This method should present the desirable attributes of both vapour and aqueous techniques while minimizing the disadvantages of each. Evidently, such a deposition technique would make use of a solvent whose physicochemical properties resemble those of gases and liquids at the same time!

Fortunately, supercritical fluids (SCF) are gas/liquid hybrids and present exceptional solvent and transport properties. "Liquid-like" supercritical fluid will dissolve precursors and will be transported by the "gas-like" supercritical fluid. A fluid is defined to be supercritical when its temperature and pressure are higher than their critical values, while it is not far from its critical state. Figure 3.8 depicts the phase diagram of a pure substance with the critical point labeled (C). When a fluid is in supercritical state, the difference between coexisting liquid and vapour phases disappears. Liquid and gas join to form an intermediate state, known as supercritical fluid, that possesses properties of both.

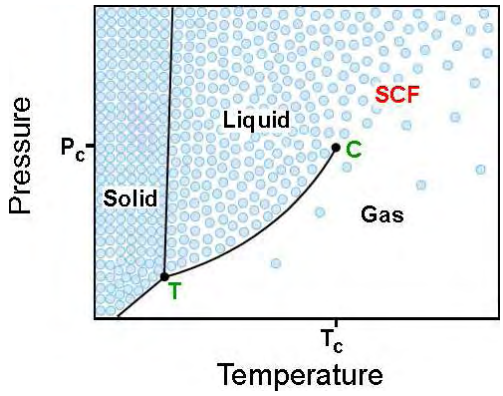

FIGURE 3.8: Pressure-temperature phase diagram for a pure substance. The blue circles illustrate the variation in the substance density. The triple point (T), critical point (C) and the SCF state are all displayed (adapted from reference [140]).

The key characteristics of SCFs are the strong temperature and pressure dependence of their physicochemical properties (density, dielectric constant, viscosity) [141]. By tuning the temperature or the pressure of a SCF, a state of liquid-like properties can rapidly transform into one of gas-like properties without the appearance of an interface. These unusual and intriguing properties can lead to a new branch chemistry including green chemistry [142] and, in particular, a variety of material processing methods [143].

Supercritical fluid deposition (SCFD) has been extensively used for the deposition of metals but can also be applied to semiconductors and dielectrics. In the case of metals, it involves the chemical decomposition of soluble organometallic compounds in a supercritical fluid such as carbon dioxide ($scCO_2$) to yield high-purity deposits. In the SC regime, increasing pressure leads only to an increase in fluid density and SCFs' densities can approach those of liquids. Since the solubility of fluids directly depends on their density, various SCFs (including $scCO_2$) are very good solvents. Moreover, the tuning of the solubility in SCFs can be exploited to control the composition and morphology of the materials to deposit. Despite near-liquid densities, the transport properties of SCFs are more akin to those of gases than liquids: in SCFs viscosities are orders of magnitude lower and diffusivities orders of magnitude higher than in liquids and SCFs do not present surface tension (see Table 3.1). Given, the solvating properties near those of liquids, in combination with viscosities resembling gases, facilitate the dissolution of desired precursor chemicals in a SCF and enables the flow into high aspect ratio channels, completely wetting the surface. In addition, the low deposition temperature inherent to solution based techniques, makes SCFD compatible with thermally sensitive substrates such as polymers.

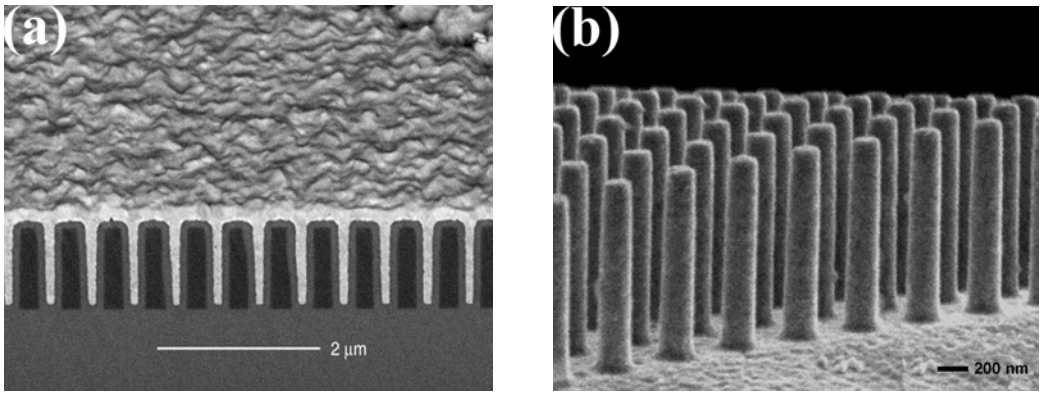

FIGURE 3.9: (a) SEM micrograph of SCF deposition of copper films into features as narrow as 45 nm on a silicon wafer, from reference [42]. (b) SEM micrograph of self-supporting gold arrays deposited by SCFD onto mesoporous silicon. The micrograph was obtained after removing the substrate, from reference [144].

SCFs have been shown to be ideal for metal deposition within micro/nano porous substrates including high aspect ratio structures. The use of supercritical fluids to advance

Parameter	Phase		
	Liquid	SCF	Gas
Density (g/cm^3)	1	0.1-1	10^{-3}
Viscosity (Pa · s)	10^{-3}	10^{-4}-10^{-5}	10^{-5}
Diffusivity (cm^2/s)	10^{-5}	10^{-3}	10^{-1}
Surface Tension (dynes/cm)	20-50	0	0
Precursor conc. (M/cm^3)	10^{-3}	10^{-5}	10^{-8}
Deposition Temp. (°C)	25-80	40-250	250+

TABLE 3.1: Comparison of the physicochemical properties of liquids, supercritical fluids and gases.

micro/nano material processing has been admirably demonstrated by Blackburn *et al.* who used $scCO_2$ to deposit copper and nickel from organometallic precursors, within narrow trenches (100 nm by 800 nm) on a silicon wafer, using low deposition temperatures [42]. SCFD has also been successfully demonstrated for the formation of thin metal films and nanoparticles on smooth and mesoporous substrates (see Figure 3.9). Almost any precursor reagent which is soluble in a SCF can be deposited onto a substrate. Metals like: gold [41, 144], palladium [41, 145, 146], rhodium [41], platinum [41, 43], copper [42, 147, 144], cobalt[148] and nickel [42, 148], have been successfully deposited from different organometallic precursors in $scCO_2$.

As the critical point of most fluids is typically less than 70 MPa and 1000°C which are below the maximum pressure and temperature sustainable by microstructured silica fibres, it is possible to take advantage of the unusual properties SCF to deposit materials within the capillary voids.

3.5 High-Pressure Chemical Vapour Deposition inside MOFs

The deposition techniques described in the previous sections gave an insight into the conditions necessary to deposit materials within MOFs capillaries. For this process it is necessary to develop schemes which allow for conformal coverage of complex surfaces, complete filling of high aspect ratio pores, the capacity for the impregnation of different materials ranging from dielectrics to conductors is, in addition, important to be able to achieve fully integrated in-fibre devices. The following sections of this chapter describe the methods implemented by our research group for the deposition of materials within MOFs.

Mainly because of the material flexibility of CVD and the possibility of depositing semiconductors of any phase structure, they have been widely used in top-down fabrication of integrated circuits. Unfortunately, CVD into the walls of long, extremely narrow capillary holes of MOF templates does not seem feasible using any of the conventional techniques described before. It is not difficult to imagine that, due to the low pressure involved in these CVD techniques, mass transport of the reactants and by-products along such confined spaces would be impossible or too slow. Also, any deviation from conformal deposition anywhere along the length of the pore would totally arrest deposition.

However due to the diffusion properties of gases at high-pressure, CVD methods could be extended towards the impregnation of functional materials within MOFs holes. For this purpose our research team has developed a new variation of CVD, known as high-pressure CVD (HP-CVD), where the precursor gases are flowed inside the MOF channels at very high pressure ($2-100\,\mathrm{MPa}$) [16], allowing for transport of reactants into the extreme aspect ratio holes and enabling the CVD process to occur inside the MOF "micro-reaction chamber". Flow at very high pressure in MOFs can be sustained because of the very high mechanical strength of optical fibres. High-pressure CVD permits the fabrication of uniform, dense and conformal annular deposition of high quality amorphous and polycrystalline semiconductor structures within the fibre micro/nanoscale pores [16].

As in any other CVD method, in HP-CVD some steps must occur in order to achieve semiconductor deposition. The process involves the flow of a high-pressure gas mixture, containing a small concentration, C_{in}, of a precursor in an inert carrier gas such as argon, into a silica MOF at constant inlet temperature, T_{in}, and inlet pressure, P_{in}. The reacting vapour species are transported far into the fibre capillaries. The fibre reactor is heated within a furnace which causes adsorption of film precursors and reactants on the internal silica walls. Heterogeneous surface reactions initiate the annular film growth. Finally, the high-pressure flow permits the reaction by-products and desorbed reactants to flow out from the fibre. A schematic diagram of the transport and reaction processes underlying HPCVD inside MOFs is shown in Figure 3.10.

In a typical deposition experiment the fibre is heated in either a L=15 or 75 cm long tube furnace while the precursor and inert gas mixture flows. In the heated region a thin semiconductor film grows on the silica wall. Considerations of the deposition process reveal that there is a complex interplay between all of the experimental parameters which vary along the length of the fibre:

a) The concentration of the precursor $C(z,t)$, which decreases along the fibre length.

b) The gas pressure, $P(z,t)$, which decreases along the fibre length.

c) The temperature, which is determined by the temperature profile of the furnace.

d) The gas density and precursor viscosity, which depend on the temperature, pressure and concentration.

e) The gas stream velocity, which depends on the viscosity, pressure and gas density. The gas stream velocity parallel to the substrate is laminar inside MOFs capillaries, as the Reynolds number is small[2]. Therefore the gas flow rate inside the holes is higher at the centre of the holes than near the capillary walls.

f) The rate of deposition, which is a function of the above parameters.

g) The hole diameter, which is determined by the rate of deposition at a certain position and time. This clearly influences the film growth, for example, if the deposition is very fast at the beginning of the furnace, then the hole diameter being made smaller will restrict the rate of flow of the precursor mixture through the rest of the fibre.

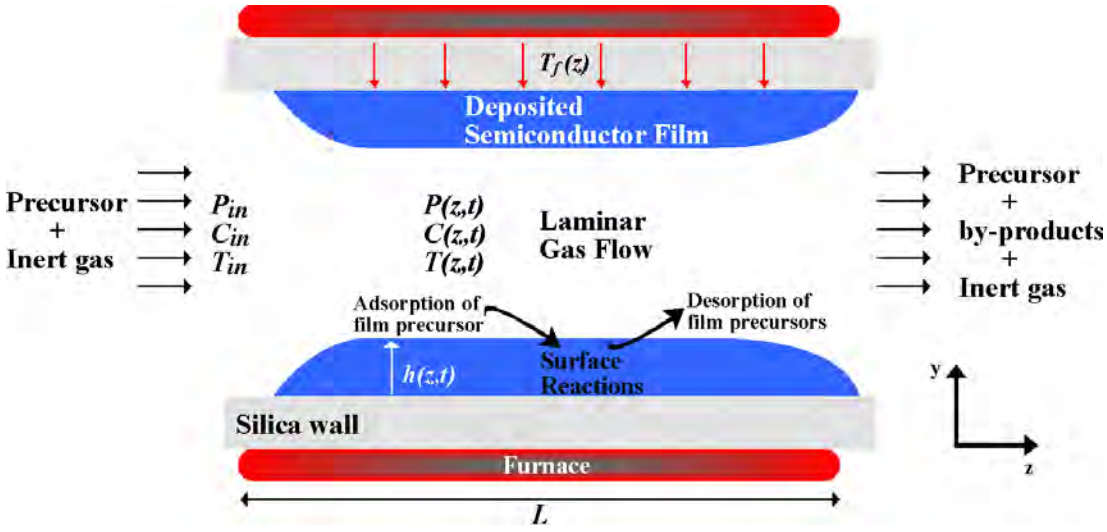

FIGURE 3.10: High-pressure chemical deposition process for fabricating semiconductor structures within micro/nanoscale pores of MOFs. The process occurs over lengths of tens of centimeters inside capillary holes as small as 100 nm.

Traditionally, CVD experimental conditions are experimentally optimized. Modeling of the flow and thermodynamics of HPCVD process inside the fibre reaction chambers results in an even more complicated task, thus it has been more convenient to turn into trial and error experimental search of the desired deposition conditions. It seems probable that the wide range of deposition chemistries developed for fabricating planar

[2]Laminar flow occurs at low Reynolds numbers, and is characterised by smooth constant fluid motion, whilst turbulent flow occurs at high Reynolds numbers and is characterised by flow fluctuations and vortices.

structures can be adopted for HPCVD [149], allowing the incorporation of many different materials inside optical fibres. At the present time we have demonstrated the deposition of amorphous and polycrystalline silicon, germanium and GeS_2 by this method.

Finally, the danger associated with the very high pressure used in the process and the toxic and explosive precursors is negligible in view of the small volume of the capillary holes, which makes the process safe, practical and convenient.

3.5.1 High-Pressure CVD of Silicon inside MOFs

In the last century silicon has become the most important material in microelectronics and a large number of different CVD methods have been explored for the deposition of silicon layers onto planar substrates. CVD plays the important role of providing the thin silicon film in which the active devices, ranging from complicated IC to cheap solar cells, are patterned by lithography and etching methods. Two CVD techniques have emerged as being the most useful and both have achieved a massive commercial impact. These are the pyrolysis of silane (SiH_4) and the hydrogen reduction of silicon tetrachloride ($SiCl_4$) [122]. From these two techniques the one involving $SiCl_4$ is advantageous for top-down fabrication because it allows the growth of very high quality silicon at convenient rates (μm/min). However, for the purposes of this thesis, where we require to grow silicon micro/nanowires inside MOF templates, it is more convenient to use the direct pyrolysis of silane. This is because the reactions involving ($SiCl_4$) occur at higher temperatures and silane reactions are more simple as they produce only one light by-product (hydrogen).

In a typical HP-CVD experiment a high pressure gas mixture of 5% silicon precursor SiH_4 and 95% carrier gas, argon, at a pressure of approximately 40 MPa is contained in a high-pressure stainless steel reservoir. The gas is configured to flow through MOFs whose hole diameters may range from $\sim$ 50 nm to 50 μm. Even though a very small amount of silane precursor is used, the gas mixtures used in these experiment are very toxic and explosive, so are always handled with extreme care.

The fibre is fed through a 75 cm long tube furnace which is heated from room temperature to 750 °C at a rate of 4 °C/min. The polymer coating of the fibres is either stripped before heating or burned off during heating. When a silane molecule strikes the internal silica surface, it can either bounce off or be absorbed. If it is absorbed, and the temperature is high enough to initiate its decomposition, it may decompose into Si and H_2 with the later going back into the gas phase and being carried away from the reaction zone by the fresh gas flow. Alternatively, H_2 can diffuse out through the silica walls [150]. The silicon left behind can build up as a thin amorphous silicon film on the MOF's inner

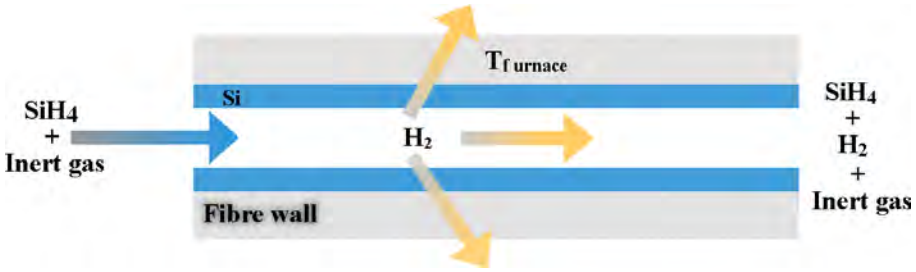

FIGURE 3.11: HP-CVD process for deposition of silicon wires inside micro/-nanoscale capillaries of MOFs using silane precursor. The high-pressure flow allows for transport of reactants deep inside the extreme aspect holes and enables uniform, dense and conformal annular deposition of silicon.

silica walls (see Figure 3.11). As growth proceeds, a remarkably uniform tube forms. As the temperature exceeds the crystallisation point of $\sim 700\,^{\circ}\mathrm{C}$, crystalline grains then nucleate and grow. The gas flow during the deposition can be monitored by placing the fibre output into a mineral spirits liquid and examining the rate of bubble formation.

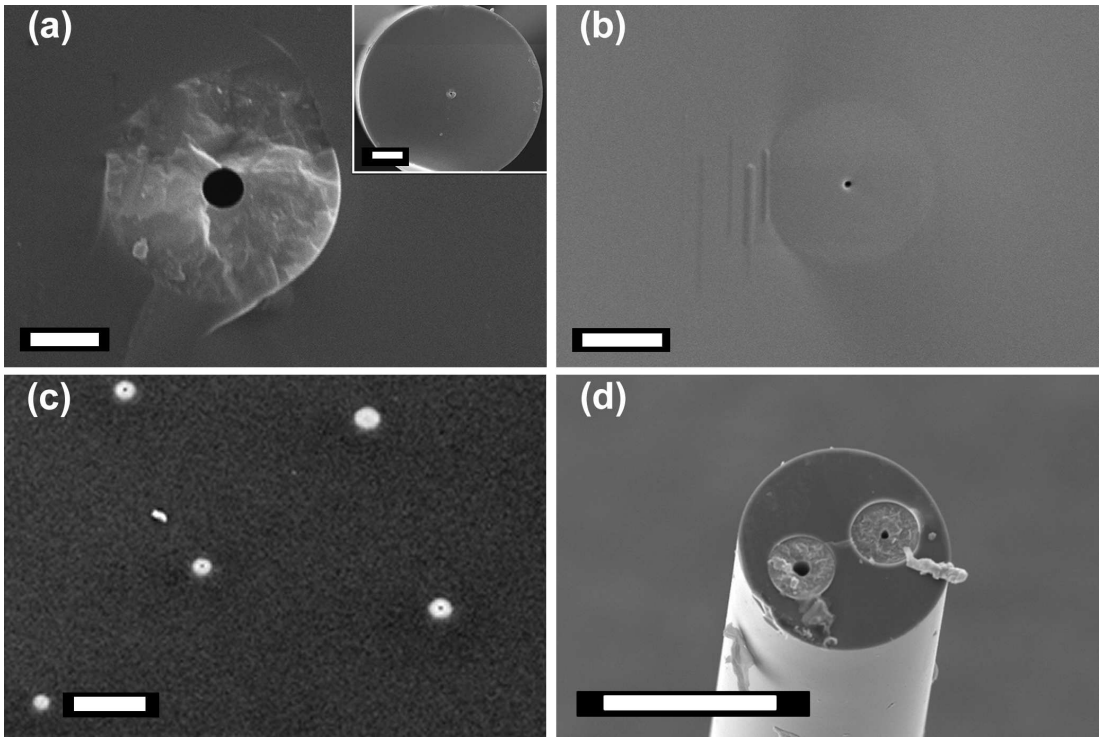

FIGURE 3.12: SEM micrographs of silicon annular deposition by HP-CVD method within micro/nano sized MOFs. a) $6\,\mu$m diameter silica capillary filled with silicon. The internal hole diameter after the deposition is only $1\,\mu$m. The inset shows the whole structure for clarity, scale bars are $2\,\mu$m and $20\,\mu$m respectively. b) silicon within a $2\,\mu$m silica capillary, scale bar $1\,\mu$m. c) Array of filled nanoscale holes, scale bar is $3\,\mu$m (see Figure 2.4 for fibre template). d) Twin hole MOF with $30\,\mu$m diameter lateral holes, scale bar is $100\,\mu$m

Scanning electron microscopy cross-sections, every centimetre along the length of capillaries filled with silicon, have been collected. It is observed that deposition is achieved

even in sub 10 nm holes, indicating that substantive fluid flow must have occurred through centimetres long nanoscale channels. Figure 3.12 shows SEM cross-sections of different silicon-filled MOFs whose capillary holes range from ~ 400 nm to $\sim 30\,\mu$m.

Deposition within MOF with a honeycomb pattern, as shown in Figure 3.13, results in several high aspect ratio silicon wires that can be released from the silica template by HF etching. To our knowledge, the silicon wires fabricated in this way are the highest aspect ratio silicon structure fabricated by any method.

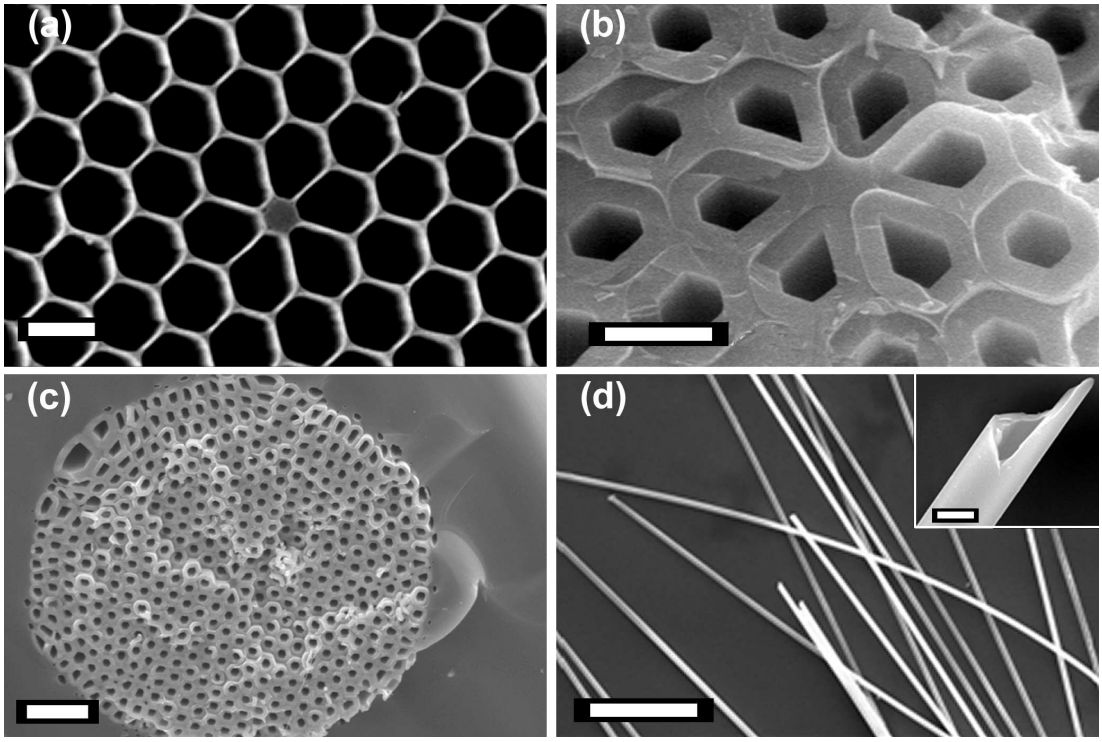

FIGURE 3.13: SEM micrographs of silicon annular deposition by the HP-CVD method within a honeycomb MOF. a) MOF template before silicon deposition, scale bars is $2\,\mu$m. b) silicon deposition inside a honeycomb MOF, scale bar is $2\,\mu$m c) Another example of silicon deposition within the holes of a honeycomb fibre, scale bar is $5\,\mu$m. d) The resulting tubes are released by etching the silica template, scale bar is $50\,\mu$m and inset is $1\,\mu$m

The key issue to obtain conformal and homogeneous deposition is that silicon must be deposited in the amorphous phase and then, by a post deposition thermal process, crystallization is achieved. This allows the thin amorphous layer to follow the complex geometry of the template which cannot be done by crystal grains. To investigate this, two fibres attached to independent reservoirs were fed through a furnace. The pressure and concentration of both precursor reservoirs was the same. The furnace temperature was increased from room temperature to 750 °C and the precursor was allowed to flow through one fibre whereas the other other reservoir was not opened until the furnace temperature was 550 °C. It can be seen in Figure 3.14, that the deposition in the

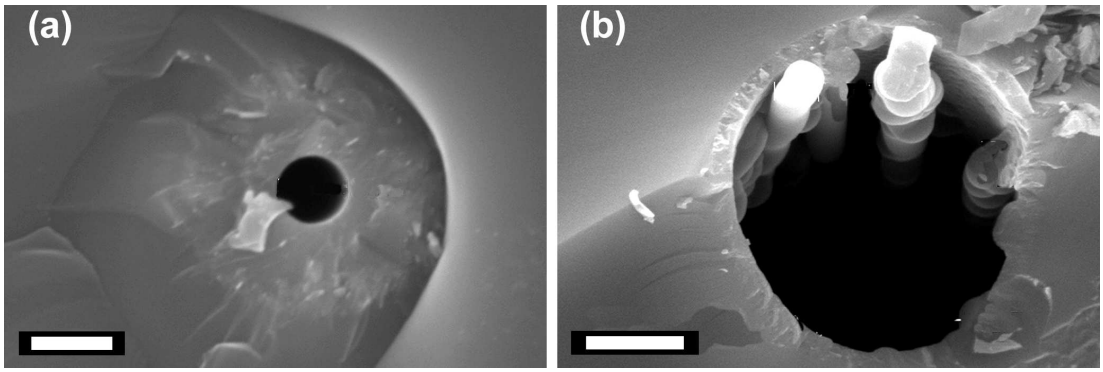

FIGURE 3.14: 6 μm silica capillary filled with silicon using same experimental conditions but different deposition temperature. a) The deposition obtained is homogeneous and follows the cylindrical geometry of the silica wall while in b) the deposition process is irregular and big crystals of silicon are formed. The deposition in (b) was initiated at higher temperatures.

first fibre was homogeneous and conformal whereas the deposition in the second fibre was irregular. For the first fibre most of the deposition occurred when the furnace temperature was below the crystallization point. Thus amorphous silicon was deposited and, as the temperature increased, crystallization occurred (as confirmed by TEM and Raman structural studies presented in the next chapter). In contrast, in the second fibre the deposition was initiated at temperatures high enough to immediately form silicon crystals. These grains are formed in random nucleation points and do not follow the capillary geometry.

3.5.2 High-Pressure CVD of Germanium inside MOFs

For the formation of germanium tubes/wires a precursor of GeH_4 (germane) is heated at similar partial and total pressures as those used for silicon deposition, up to a temperature of 500 °C. A smooth layer of amorphous germanium begins to deposit on the pore walls as the temperature is ramped up past 300 °C, Figure 3.15.

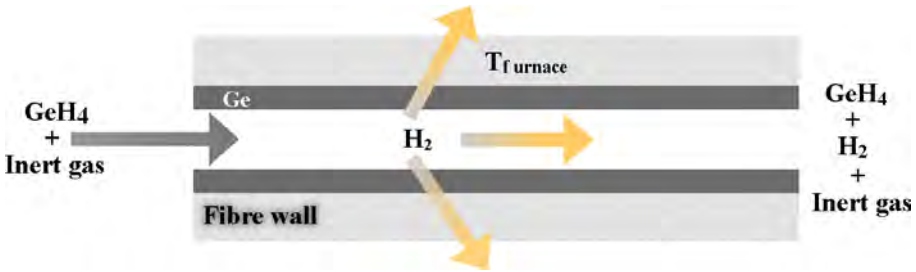

FIGURE 3.15: HP-CVD process for deposition of germanium inside MOFs.

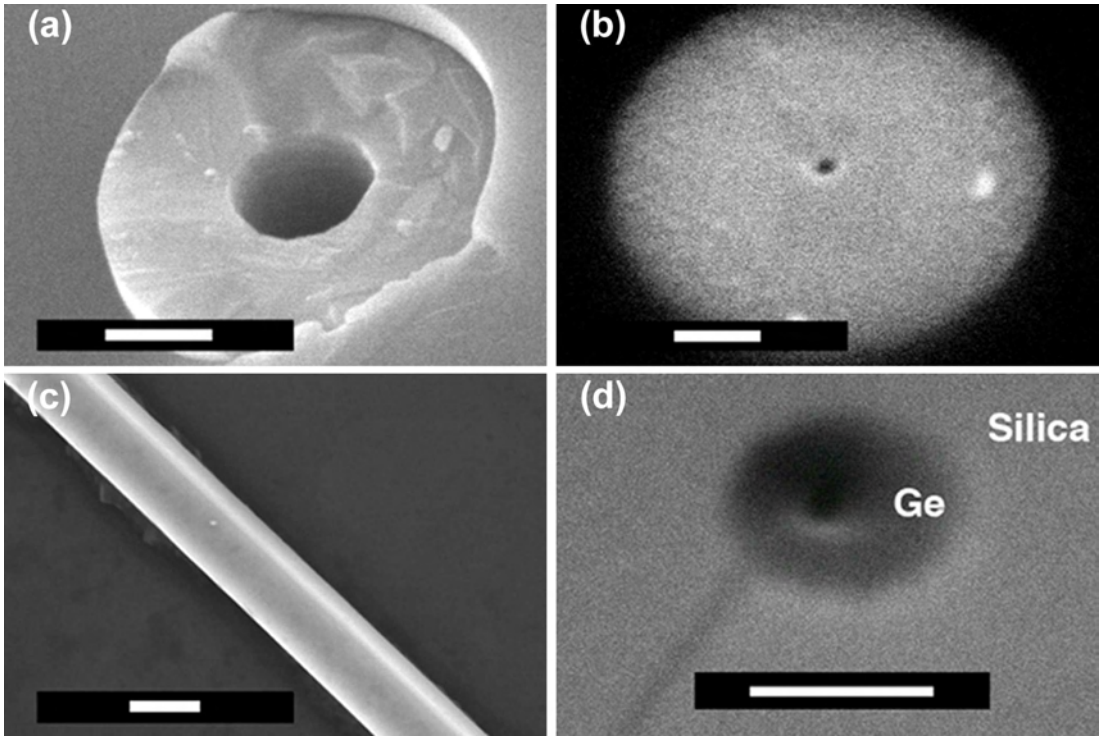

FIGURE 3.16: Germanium integrated into MOFs. (a) SEM cross-section of a germanium tube in a 2 μm silica capillary, scale bar is 500 nm (b) Germanium deposited in a 1 μm pore, the central hole is $\sim$ 25 nm in diameter, scale bar is 200 nm. (c) A germanium wire etched out of silica MOF template, scale bar is 2 μm. (d) Field emission SEM cross section of a germanium nanotube within a MOF nanotemplate, scale bar is 100 nm, from [16].

Crystalline grains then nucleate and grow as the temperature exceeds the crystallization point of 375 °C, which is much lower than that of silicon $\sim$ 700 °C. As growth proceeds, again, a remarkably uniform tube forms (see Figure 3.16); as it fills with germanium, a 1 μm diameter pore can be narrowed by a factor of 100 down to 25 nm or smaller, tapering open gradually over a deposition length of 70 cm. Silica capillaries drawn to a 100 nm diameter were also successfully filled with germanium to form nanotubes over macroscopic lengths of up to 30 cm, with an inner diameter of less than 10 nm (Figure 3.16).

Deposition into more highly structured pores reveals additional information about this conformal filling. When a large-air-fraction fibre with a honeycomb pattern of holes is filled, a spatially ordered array of hexagonal germanium tubes is formed (Figure 3.17). The interior vertices of the hexagonal holes, originally defined by the rounded silica template, actually sharpen as growth proceeds. If uniform inward motion of the surface, along the normal, during deposition is assumed, then the rounded corners of a polygon will become sharp as the thickness of the deposited layer exceeds the radius of curvature of the corner, as illustrated in Figure 3.17c. The resulting faceted tubes resemble

lithographically patterned micro and nanostructures but are formed in a simple single-stage deposition. This uniform annular growth, down to very small inner diameters, with sharp geometric features, is particularly striking when one considers that the germanium is polycrystalline, with a grain size much larger than the dimensions of these features.

The remarkably simple fabrication of 3D semiconductor structures via the HP-CVD deposition of semiconductors within holey fibres templates introduces a new class of optically and electronically controllable in-fibre metamaterials. The following chapter explores the exciting optical and electrical properties of these new semiconductor modified optical fibres.

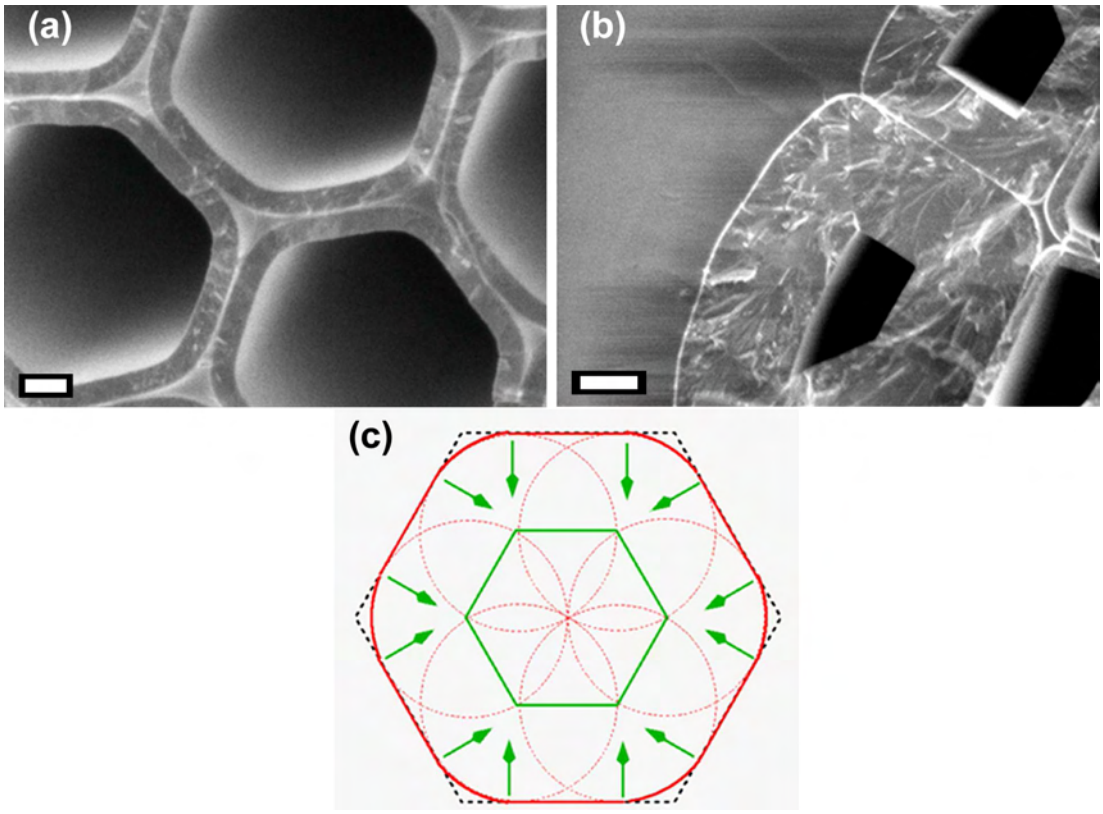

FIGURE 3.17: SEM micrographs showing of a 2 μm honeycomb MOF filled wit (a) thin homogeneous layer of germanium, scale bar is 300 nm (b) thick conformal layer of germanium, scale bar is 1 μm. (c) Schematic showing surfaces growing inward in a direction perpendicular to the silica walls (green arrows). When the deposition reaches the thickness indicated by the green hexagon, the rounded corners have vanished and the cross-section is a perfect hexagon [16].

3.6 Vapor Liquid Solid Growth of Single-Crystal Silicon inside MOFs

Single crystal semiconductors have superior photonic and electronic properties compared with poly-crystalline and amorphous semiconductors, which makes them the base materials for electronic and optoelectronic devices. During the last decades, several single crystal growth methods have been investigated and today epitaxial growth constitutes the primary process toward the construction of most microelectronic circuits and MEMS. Epitaxial techniques arrange atoms in single-crystal fashion upon a seed crystal substrate so that the lattice of the newly grown film duplicates that of the substrate. Epitaxial growth of silicon occurs on a substrate with a closely matched lattice constant and thermal expansion coefficient [118].

Although CVD has been used for the deposition of epitaxial single crystal silicon, the use of HP-CVD is not successful in growing single crystal silicon inside MOFs. This is mainly because of the lattice mismatch between the silica template and silicon. An alternative method, Vapour-Liquid-Solid (VLS) growth has been investigated for monocrystal formation inside MOFs. VLS requires the presence of a metal catalyst which has a low eutectic temperature with silicon. Since the first demonstration of VLS growth of silicon [151], gold has commonly been used as the VLS seed. Moreover the Si-Au eutectic temperature is ~ 360 °C, this can be easily supported by silica fibres, making it possible to carry out the process inside MOFs. Recently VLS has been applied for growing single crystal silicon, germanium and compound semiconductor nanowires which have found many applications as building blocks for nanoscale electronic, optoelectronic and NEMS devices [18, 152, 153, 154, 155, 156, 157]. The extension of this technique to the templated growth of semiconductor wires within MOFs could result in many interesting applications.

VLS growth of silicon wires from a gold seed can be described as a four-step process. (1) A gold particle is deposited onto a surface and heated above the eutectic temperature. The seed will define the dimensions and geometry of the silicon wire. (2) A silicon vapour precursor (SiH_4) interacts with the gold seed which acts as a catalyst to decompose the precursor. The reaction produces Si and H_2 gas as a by-product on the gold surface. The silicon diffuses into the gold particle and forms a Si-Au alloy. As the silicon concentration increases, the melting temperature of the alloy decreases. The silicon concentration increases and the alloy particle is saturated. (3) At the saturation point no more silicon can diffuse into the gold and instead a solid silicon particle nucleates on the substrate. (4) Finally single crystal wire grows from the nucleation point with a liquid Si-Au droplet at the tip [150].

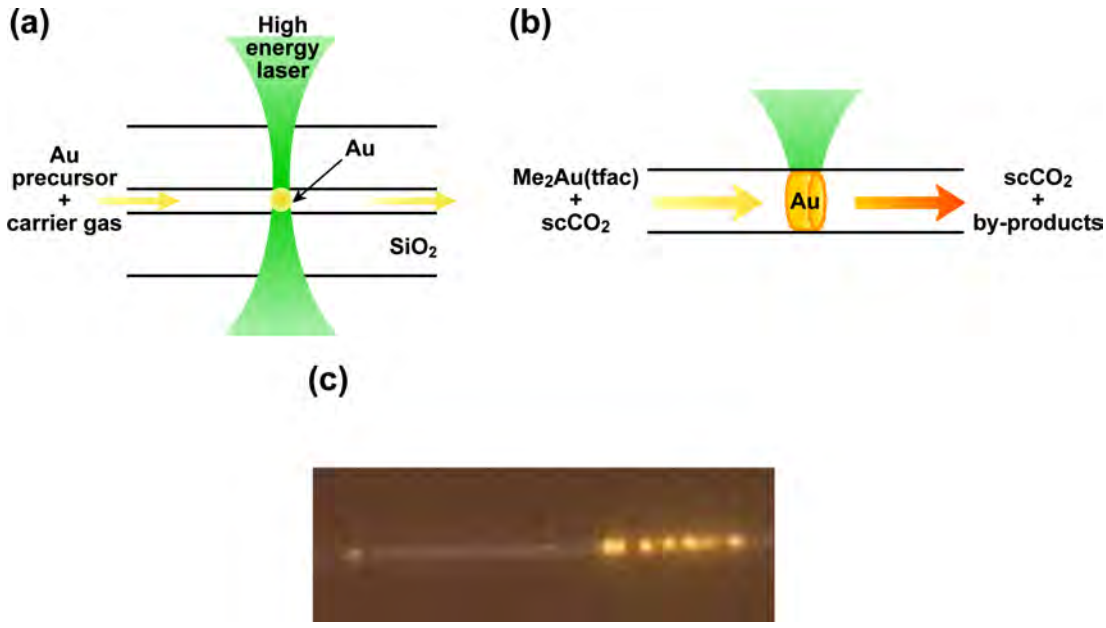

FIGURE 3.18: Schematic of laser-assisted supercritical fluid deposition of gold particles inside MOF capillaries (a,b). Focused laser radiation enables the deposition of gold from a flowing supercritical fluid precursor at precise locations along the fibre. (b) Microscope image of gold particles deposited in a 2 μm capillary. [150, 16]

The principle of template-directed VLS requires the deposition of gold particles inside the MOF template and then the flow of silicon precursor inside the pores. The transparency of silica MOFs permits gold deposition inside MOFs by laser assisted decomposition of a gold organometallic precursor ($Me_2Au(tfac)$) which is dissolved in $scCO_2$. Laser-Assisted Supercritical Fluid Deposition (LASCFD) provides the ability to create gold particles at specific locations in the fibre, which is extremely important to achieve VLS growth. If the case where a gold seed is deposited within a large area is consider, then the silicon wires would grow at any location which will easily block the precursor flow and arrest the deposition. A diagram of the LASCFD process of gold particles is shown in Figure 3.18a,b. Radiation from an argon-ion laser, operating at 514 nm, is focused with a 100× objective at the desired position inside the capillary holes. As the gold precursor passes through the illuminated region it is photolytically decomposed and forms solid gold, plus by-products which are carried out of the fibre by the high pressure flow. Figure 3.18c shows a 1.6 μm capillary fibre which has been patterned with gold particles at different positions.

Once a gold seed is deposited inside the capillary the VLS process takes place by heating up the capillary above 360 °C while flowing high-pressure silane in a helium carrier gas. The high-pressure VLS process is shown in Figure 3.19. During the growth process is extremely important to remove the reaction by-products away from the gold seed. Although most of the reaction by-products are carried out of the fibre by the gas flow,

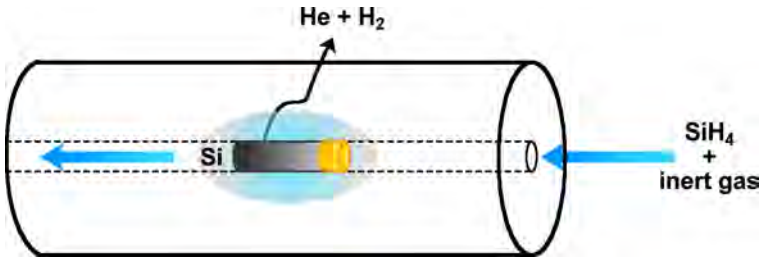

FIGURE 3.19: Schematic of high-pressure VLS growth of silicon single crystal [150].

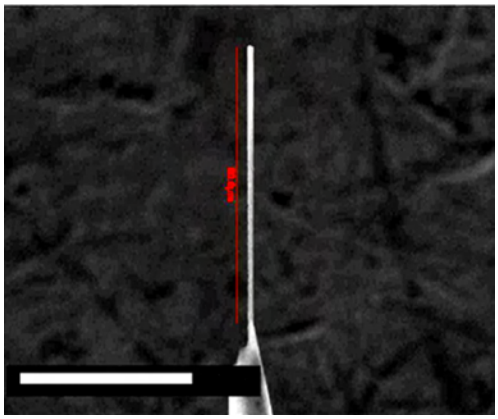

FIGURE 3.20: SEM micrograph of a single crystal silicon growth by VLS after removing the silica template by HF etching, scale bar is 50 μm [150, 16]. VLS growth experiments were done by Brian Jackson.

H_2 and helium may diffuse through the silica walls which certainly makes an important contribution to the success of the process. Figure 3.20 is a SEM micrograph of a single crystal silicon wire that was grown inside a 1.6 μm silica capillary. As it is described in the following chapter, the single crystal nature of this wire has been verified by FIB sectioning and TEM analysis along the fibre length.

3.7 SCFD of Silver Nanoparticles inside MOFs

Due to the solvating and transport properties of SCF, they can be employed as the carrier medium of metal precursors within the high aspect ratio holes of MOFs. The empty capillary pores of MOFs can be treated as microscale reaction chambers and, by flowing a silver organometallic precursor solution through the fibre, the deposition of compact metal films along the fibre walls has been achieved to create a new class of metallo-dielectric optical fibre devices. The high-pressure flow of the precursor and the SCF carrier medium is followed by a pyrolytic (thermal) reduction of the precursor to form an annular deposition of silver nanoparticles inside the capillary holes.

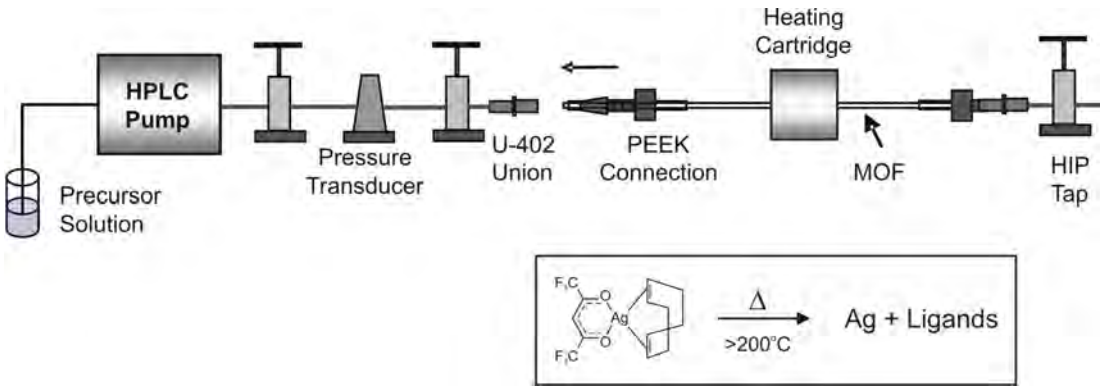

FIGURE 3.21: Schematic (not to scale) of the experimental set-up for the deposition of silver nanoparticles inside microstructured optical fibres. The decomposition of the organometallic precursor to form a compact silver film on the silica walls takes place within the heated area. The chemical structure of the organometallic silver precursor together with the decomposition process is shown in the inset.

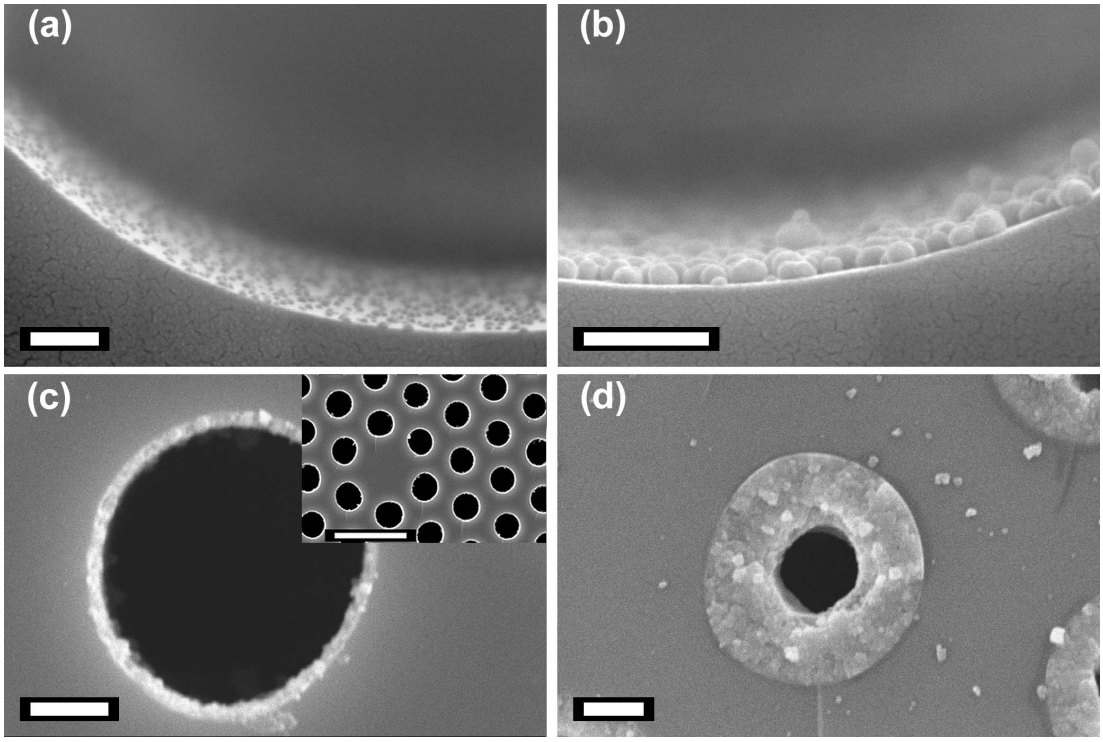

FIGURE 3.22: SEM micrographs showing a range of silver deposition profiles obtained by tuning the experimental parameters. (A) Deposition time = 0.5 hrs with a precursor concentration of 5 mg/ml; 1 μm scale bar. (B) Deposition time = 0.5 hrs with a precursor concentration of 10 mg/ml; scale bar is 1 μm. (C) Deposition time = 2 hrs with a precursor concentration of 10 mg/ml; scale bars are 2 μm and 20 μm on the inset. (D) Deposition time = 3 hrs with a precursor concentration of 15 mg/ml; 2 μm scale bar.

The chosen precursor for the formation of silver films is Ag(hfac)(1, 5-COD) (hfac=

1, 1, 1, 5, 5, 5-hexafluoroacetylacetonato, COD = cyclo-octadiene) due to its high solubility in organic solvents, such as n-heptane and $scCO_2$, and also due to the desirable low decomposition temperature (200°C) of this complex. The experimental chemicals, Ag(hfac)(1, 5-COD) and n-heptane (HPLC grade), are purchased from Sigma-Aldrich and used as received. Figure 3.21 shows a schematic of the experimental set-up used in SCF deposition inside MOFs. Ag(hfac)(1, 5-COD) is dissolved in n-heptane (typically up to 15 mg/ml) and the solution is flowed through the optical fibre at around 17 MPa by a high performance liquid-chromatography pump (HPLCP). Once again, due to the small volume contained in the fibres, the amount of precursor required for the deposition is tiny making the process safe even at the high pressures used in the experiments. The optical fibre is then fed through a 10 cm long heating cartridge with temperature control and HiP taps (High Pressure Equipment Company, USA) are used to control the precursor solution flow rate. As the precursor flows through the fibre, the furnace is heated up to 200°C to initiate the decomposition of the precursor into pure silver and by-products. During the first few minutes of the process, metal begins to deposit as small islands onto the capillary walls. As the deposition time increases, the nanoparticles serve as nucleation points allowing the formation of thin granular films along the heated length. Run times for this process range between $0.5 - 3$ hours depending on the desired deposition profile and on the fibre structure.

After the deposition, any decomposed ligands can be easily removed by the same solvent, leaving high purity silver grains inside the fibre. If required, supercritical CO_2 can be flowed through the optical fibre to remove any trace of precursor (or any other unwanted by-products) left inside the holes. Figure 3.22 displays different silver coatings achieved by tuning the experimental parameters such as the deposition time, temperature, precursor concentration and flow rate. The silver nanoparticles diameter can be finely controlled from tens of nanometres to hundred nanometres, and the silver coating thickness up to a few micrometres. In all cases we observed a uniform filling of the holes across the fibre structure, as illustrated by the inset of Figure 3.22c.

The optical characterisation of silver-modified MOFs is presented in Chapter 7, they have proven to be excellent substrates for surface enhanced Raman scattering.

3.8 SCFD of Polymers inside MOFs

Holey fibres filled with polymers present some attractive tuneable optical properties [158]. SCF deposition of polymer inside MOFs is advantageous, compared to other low pressure polymer impregnation methods previously used by other research groups, in

that it allows for fast impregnation of very small holes. In contrast, simply filling the fibre pores by capillary action is restricted to large holes.

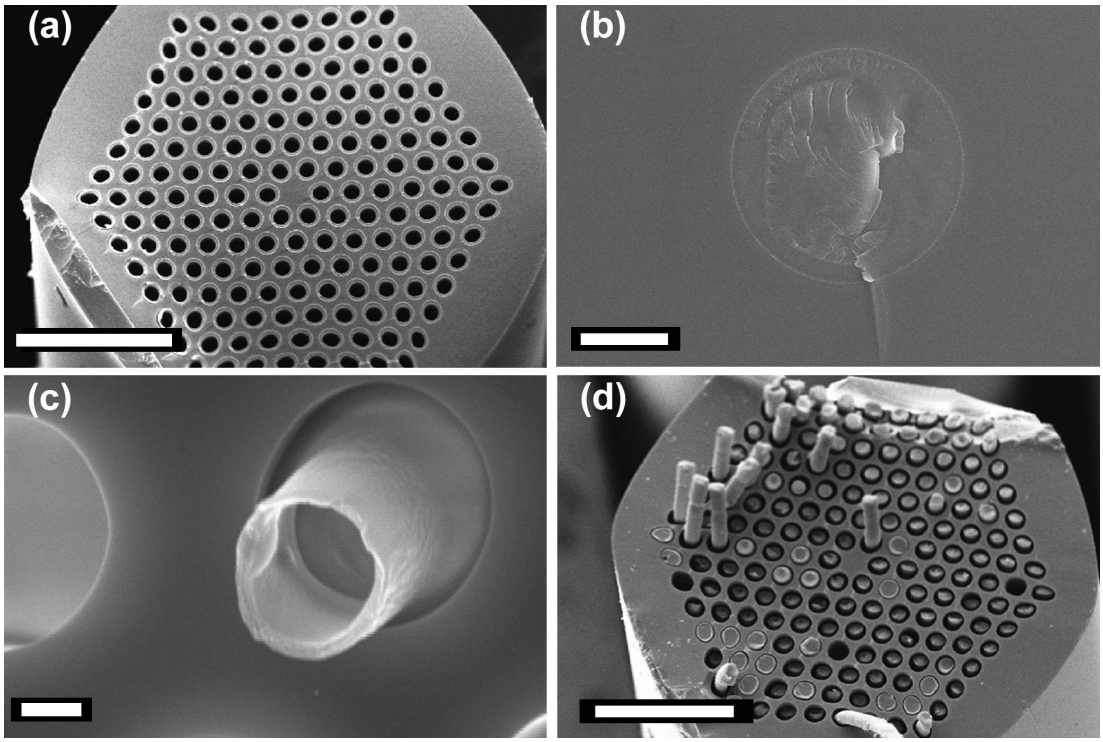

FIGURE 3.23: SEM micrographs showing a range of polymer modified MOFs. Different deposition profiles can be obtained by tuning the experimental parameters. (A) 8 μm honeycomb fibre with a thin layer of polymer, scale bar is 100 μm. (B) 50 μm capillary, 20 μm scale bar. (C) Thin layer of polymer deposited in a 8μm honeycomb fibre, scale bar are 2 μm. (D) Same silica fibre with thick polymer deposition, scale bar corresponds to 100 μm

The same SCF set-up utilized for the deposition of silver, can be used to deposit polymers (Figure 3.21). For example, for the deposition of PMMA (poly methyl methacrylate) the chemical precursors MMA (methyl methacrylate) and AIBN (azobis isobutyronitrile) are dissolved in $scCO_2$ and are flown inside the holes of MOFs. The deposition is achieved by a thermal polymerisation process. The chemicals MMA and AIBN are purchased from Aldrich and used without further purification. In a typical deposition experiment, 5 g of MMA and 75 mg of AIBN are dissolved in $scCO_2$ (usually at 21 MPa) at room temperature. The solution is then flowed through the MOF, which is heated in a furnace at 90 °C. The polymerisation processes take place within the heating area, whose length is between 10 cm and 5 cm. As with the deposition of Ag nanoparticles, the flow rate and experimental time can be controlled for different polymer coating thicknesses. In addition, the solvating properties of $scCO_2$ are strongly pressure-dependent in the vicinity of the critical point, making $scCO_2$ a highly tunable solvent for a multitude of precursors.

The SEM micrographs in Figure 3.23 show some examples of the deposition profiles that can be obtained. Holes ranging from $2-50\,\mu$m have been successfully impregnated with thin polymer coating or completely filled.

Chapter 4

Semiconductor Modified Optical Fibres

As described in Chapter 3, using HP-CVD we have for the first time to our knowledge, achieved the fabrication of optical fibres with bulk crystalline semiconductor inclusions. A critical issue of this research has been to characterise the physical properties of silicon and germanium deposited inside by HP-CVD. In this chapter the crystalline structure of resulting semiconductor tubes/wires are studied with TEM and Raman spectroscopy. Electrical transport and optical transmission measurements are used to gather information on the material quality and the prospects of their use. Semiconductor-filled MOFs provide the opportunity to exploit various optical and electronic processes to control and manipulate guided light. The first results in this direction are presented in this chapter, with a FET and waveguides being the main devices which have at the time of writing been demonstrated.

4.1 Structural Characterisation of Semiconductor MOFs

This section describes the theoretical and experimental background of two techniques used to characterise the crystalline structure of semiconductor-filled MOFs. These techniques are transmission electron microscopy (TEM) and Raman spectroscopy. The characterisation of silicon and germanium in-fibre wires/tubes requires the removal of the semiconductor structures from the silica MOF/template to have access to the deposited material itself. For this purpose it has been important to develop an etching method by which only a small length of the semiconductor wire protrudes from the silica template.

The silica template is selectively etched with 48% hydrofluoric acid (HF). For the etching process, semiconductor-filled fibres are mounted on a Teflon® holder with 125 μm v-grooves. The holder is then attached to a container and a short section of the fibre is then in contact with HF acid. Figure 4.1 is an illustration of the fibre holder and the acid container.

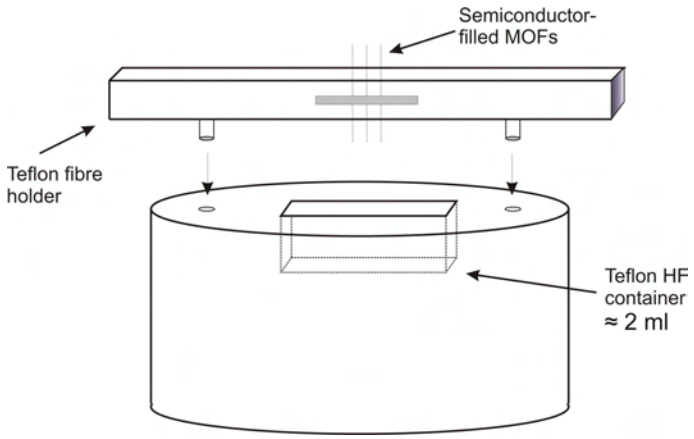

FIGURE 4.1: Schematic diagram (not to scale) of the experimental etching set up. The etching procedure only requires around 2 ml of HF acid, and it lasts for approximately 30 minutes. Because of the small amount of HF used, the process is safe, however, care must be taken.

Once the fibres are introduced into the HF acid the process, is continuously monitored under a microscope and etching is finished when the desired length of silica has been removed. Finally the fibres are washed with distilled water, to remove any acid residue, and are mounted onto glass slides for further characterisation. Figure 4.2 shows some etched fibres, illustrating the precise control that has been obtained over the etching process.

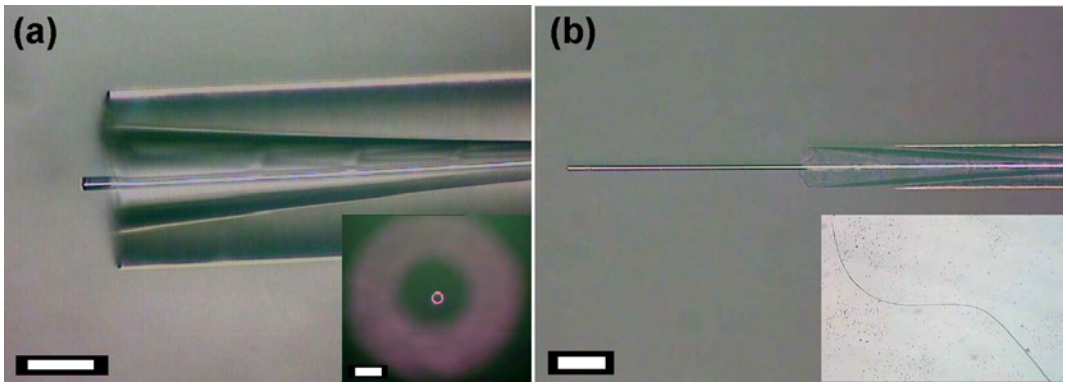

FIGURE 4.2: Microscope images of etched MOFs. (a) 5 μm silica capillary filled with germanium, the germanium tube sticks out $\approx$ 10 μm from the silica template, scale bar is 20 μm. Inset: cross-sectional view of the etched tube, scale bar 10 μm. (b) 2 μm silicon tube, scale bar is 20 μm. The inset is the same capillary fibre after etching a longer length.

4.1.1 Transmission Electron Microscopy (TEM)

In electron microscopes samples are imaged by electron beams that are used as "illumination sources". An electron beam has a wavelength many orders of magnitude shorter (for example, 100 keV electrons $\lambda = 3.7$ pm) than that of light, which gives much higher spatial resolution than that achieved by optical microscopes. Instead of optical lenses, electron microscopes rely on magnetic and electrostatic fields which act as electron lenses to focus the electron beam and form images. When a high energy electron beam hits a sample various interactions between the electrons and the atoms take place, as can be appreciated from Figure 4.3. These interactions give important information about the structure of matter.

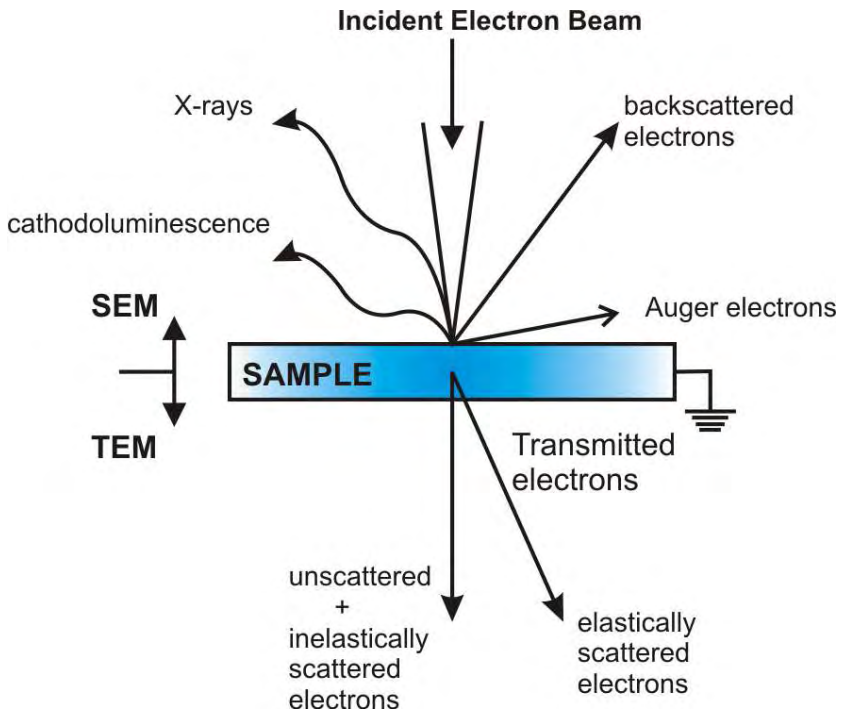

FIGURE 4.3: Schematic representation of interactions that result as an electron beam hits a sample in an electron microscope. The TEM related interactions are below the sample, [159].

Figure 4.3 shows that, for thin enough samples, some incident electrons are transmitted through it. In a TEM the transmitted electrons are focused into an enlarged image on a sensitive screen. Depending on the interactions that occur within the specimen the transmitted electrons can be identify in three groups; unscattered, inelastically scattered and elastically scattered electrons. Unscattered electrons pass the sample without any interaction occurring. They do not change either their trajectory or their energy. Inelastically scattered electrons interact with the sample atoms, losing energy due to collisions within the specimen, but the process occurs with very little deviation. Finally

elastically scattered electrons interact with the heavy atoms and their trajectory is affected without losing any, or very little, energy. They are deflected through wide angles (typically 0.6-3 degree) by the interaction [159].

As described by Bragg's Diffraction Law, the electron beam interacts with crystalline samples in a very specific way. If the sample is crystalline its atoms are geometrically arranged in a periodic pattern which has certain planes with a high density of atoms that act as reflection planes (see Appendix A). Suppose that a coherent electron beam is reflected (or diffracted) from parallel planes of the crystal, each plane reflecting a small fraction of the energy. Any reflected waves, which are in phase with each other, will interfere constructively and form a diffraction pattern. Whereas any scattered waves, which are not in phase, will not be reinforced. The condition for constructive interference is given by Bragg's Law:

$$2d \sin\theta = n\lambda, \tag{4.1}$$

where θ is the incident angle, d is the lattice spacing between crystal planes, n is an integer number and λ is the wavelength of the electron wave. This relation is illustrated in Figure 4.4. It should be noted that the incident and reflected beams form an angle of 2θ with each other.

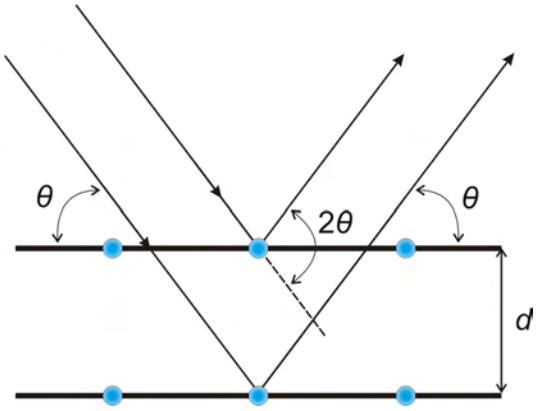

FIGURE 4.4: Bragg's Law of diffraction from parallel planes. The electron beam is reflected from two crystal planes which contain a high density of atoms, the spacing between them is d. If equation 4.1 is satisfied, the beam reflected by the lowest plane reinforces the reflection from the first plane [56].

Consider the case when a collimated electron beam passes through a crystal at a correct angle of incidence for diffraction to occur from a set of lattice planes. The elastically scattered electrons are deviated from the incident beam by an angle 2θ and will result in a bright spot in the diffraction pattern. If a sensitive film is placed at a distance L

from the crystal (Figure 4.5), the diffracted beam hits the screen at A, that is displaced from the unscattered beam by a distance R, such that $R = L\tan(2\theta)$.

As an electron beam is only strongly diffracted from planes that form small angles with it, θ small, the previous relation can be simplified to $R = 2\theta L$. To determine the lattice spacing, the last relationship is combined with Bragg's condition and d can be obtained by

$$d = \lambda L/R, \tag{4.2}$$

for first order of diffraction. Therefore, a single crystal sample, oriented such that various crystal planes are almost parallel to the electron beam, will give rise to a diffraction pattern consisting of a regular array of bright spots.

If the specimen is polycrystalline, individual crystals are randomly oriented and the resulting pattern will be the sum of individual patterns with different orientations. Thus, it will look like rings of radius R around the undiffracted spot. The thickness of the ring is determined by the size of the diffracting crystals. Thin rings are formed by large crystals and, as the crystals become smaller, the ring gets broader and more diffuse.

In the limiting case of amorphous material there are no regularly spaced atomic planes. However, there is short-range order and the diffraction pattern shows a series of diffuse rings.

The essential specimen requirement for TEM analysis is that the sample must have low electron energy loss, so that a sufficient amount of electrons are transmitted and form an image. Therefore, TEM samples must be thin enough in the traveling direction of the electrons to avoid strong inelastic collisions and electron energy loss. Thin films of the order of 100 nm are usually required for good diffraction images. In a bright field image, higher Z elements or thick regions appear darker than low Z elements making it easy to distinguish different materials within the sample.

In order to determine the crystallinity of a sample, the beam is focused onto the selected area of diffraction (SAD). The SAD can be selected by an aperture which limits its size. The identification or orientation determination of a small feature can be obtained in a very small area (400 - 800 nm) with small apertures.

TEM specimens must be mounted on circular metallic grids, ~ 3 mm in diameter and about 15 μm thick. A TEM mesh is usually made of electrolytic copper but may also be made of other metals, e.g. nickel, gold and palladium [159].

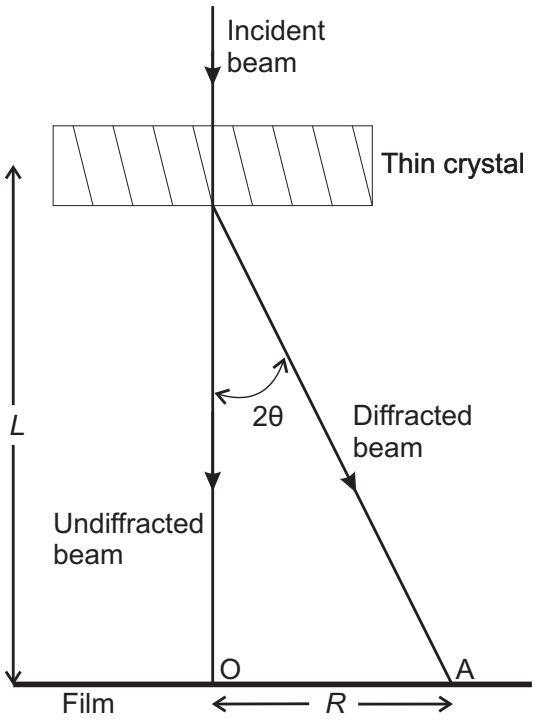

FIGURE 4.5: Basic elements of an electron diffraction camera. Undiffracted electrons travel directly to point O in the photographic screen, while diffracted beams from the sample arrive at A in the screen, from reference [160].

4.1.1.1 Diffraction Patterns of Silicon MOFs

Silicon was deposited in a honeycomb fibre using the HP-CVD method ($\sim$ 14.5 MPa with $\sim$ 750 kPa partial pressure of SiH_4). A SEM cross-sectional micrograph of the resulting fibre is shown in Figure 4.6. This sample was taken from a position along the fibre length 4 cm away from the furnace entrance (see Section 3.5.1 for experimental deposition details). The sample was obtained from very close to the furnace entrance because previous SEM studies revealed that at this position the silicon tubes are very thin. However, the MOF template is much thicker than the 100 nm thickness required for TEM analysis and, thus, before attempting TEM analysis, the semiconductor wires are released from the silica template. The silica cladding of this sample was etched out with HF acid. The free wires were washed with distilled water and chopped into pieces with metallic tweezers. Afterwards, the wires were suspended in isopropanol and picked up with a pipette. They were then drop-cast on TEM copper grids and left to dry out. With this procedure, the probability of finding a tube with a section thin enough for diffraction analysis was low and many grids had to be prepared. The grids were loaded onto a sample holder of the TEM.

A Philips EM 420 TEM microscope with camera length $L = 480$ mm was used. The samples were illuminated with a 120 KeV ($\lambda = 0.03349$ Å) electron beam. Figure 4.7a

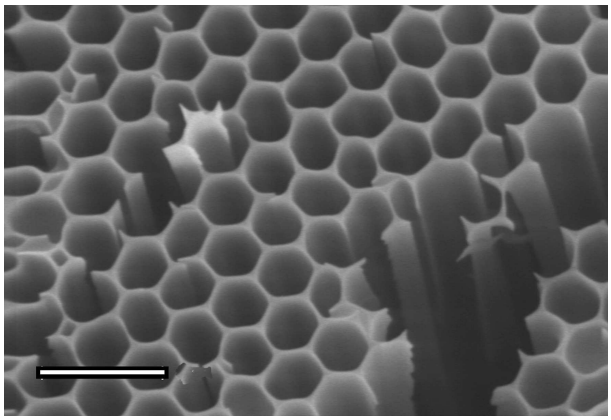

FIGURE 4.6: SEM micrograph of a honeycomb MOF with a thin silicon layer on the walls of the 2 μm holes. The silicon tubes of this fibre were released from the silica matrix and characterised by TEM studies; the scale bar is 5 μm

is a bright field image of a silicon wire. It can be appreciated that this wire has some bright regions that are thin enough for TEM studies. The red and yellow circles indicate the selected areas for diffraction and the patterns are shown in Figures 4.7b and Figure 4.7c respectively. The aperture used in both cases was 400 nm. The SAD enclosed in the red circle led to a set of broad and diffuse concentric rings, which clearly indicate that the silicon in this area is amorphous with some nanocrystal phases.

The diffraction pattern from the area enclosed by the yellow circle in Figure 4.7a is shown in Figure 4.7c. In this region, the diffraction rings are more defined with some bright spots superimposed on them. This indicates that silicon within the selected area is polycrystalline. The rings correspond to different lattice planes and can be assigned to the silicon structure using equation (4.2). The rings indicated in the figure correspond to lattice separations $d = 3.135\,\text{Å}$ and $d = 1.92\,\text{Å}$ and are associated with the (111) and (220) lattice planes of silicon, with lattice constant $a = 5.430\,\text{Å}$.

Therefore, TEM analysis on this particular MOF revealed that the silicon tubes deposited under these experimental conditions contain polycrystalline and amorphous phases. As will be described later, the crystalline structure of silicon is highly dependent on the deposition conditions.

4.1.1.2 Diffraction Patterns of Germanium MOFs

In the first TEM experiments on germanium fibres the procedure used for sample preparation was the same as that described for silicon. Germanium was deposited in a honeycomb fibre using the HP-CVD method ($\sim$ 14 MPa with $\sim$ 750 kPa partial pressure of of GeH_4). A SEM micrograph of this germanium fibre is shown in Figure 4.8. The

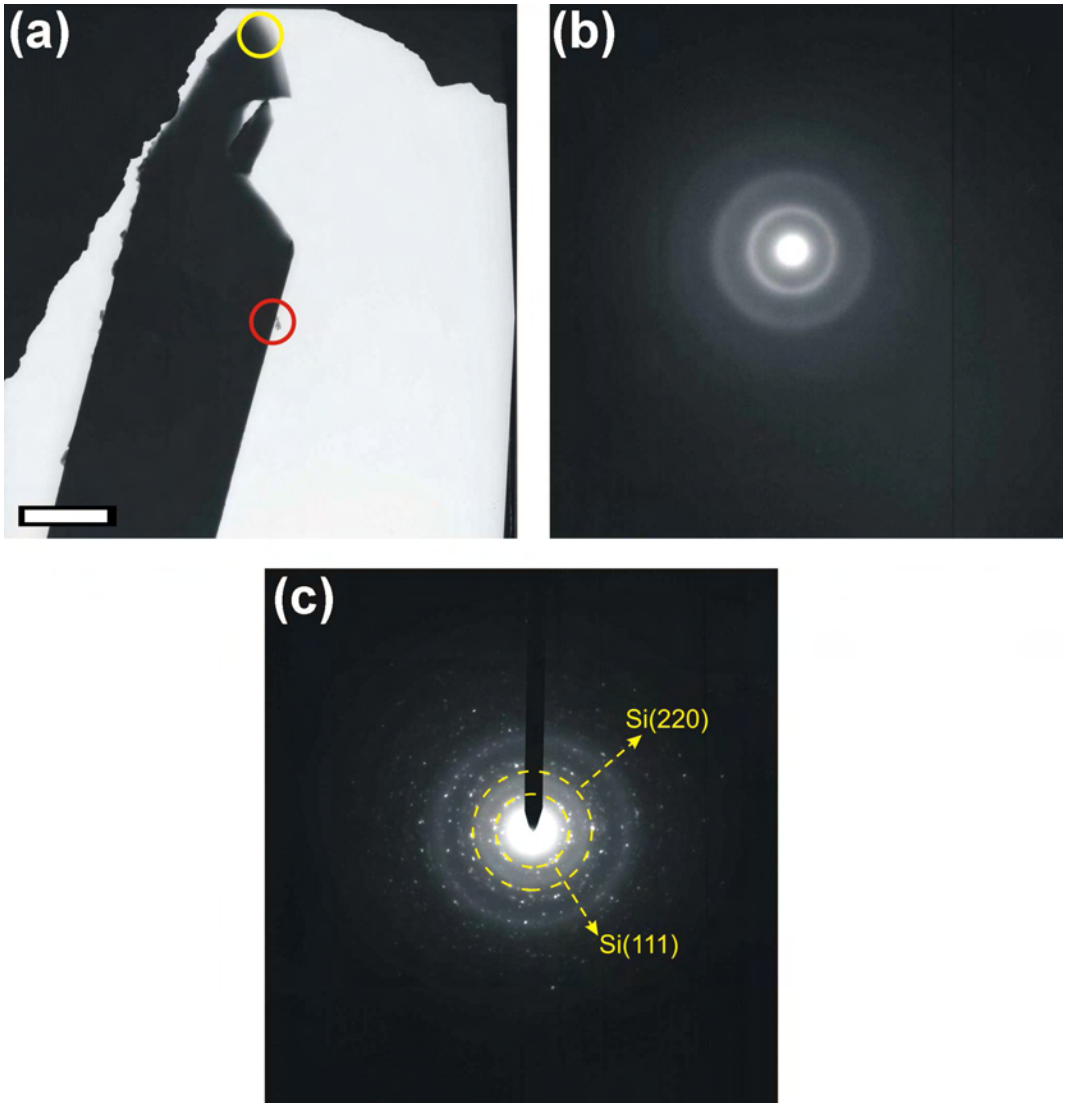

FIGURE 4.7: (a) Bright field image of a 2 μm silicon tube, the circles indicate the SADs; the scale bar is 1 μm. (b) SAD pattern obtained from amorphous silicon with small crystalline phases, obtained from silicon within the red area. (c) "spotty ring" type of diffraction pattern obtained from polycrystalline silicon from the yellow region in (a).

silica fibre template was etched out and the 2 μm germanium tubes were released and mounted on TEM grids.

Figure 4.9a is the bright field image of the deposited germanium and the grey circle is the SAD whose diffraction pattern is shown in Figure 4.9b. The bright spots in the diffraction pattern clearly indicate that the germanium wire is crystalline. Some crystal planes can be identified in the image. Although a 'spotty' diffraction pattern corresponds to single crystal material, the germanium wire is not monocrystalline and, as the SAD is moved to different regions of the sample, the orientation of the planes changes and a different diffraction pattern is obtained. Thus, the wire is composed of

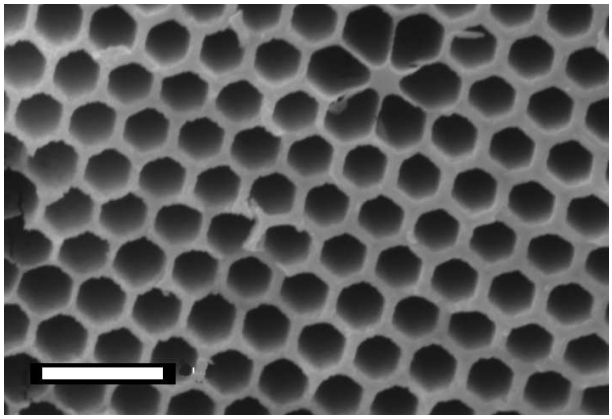

FIGURE 4.8: SEM micrograph of a honeycomb MOF with a 300 nm germanium layer deposited on the 2 μm holes; scale bar is 5 μm

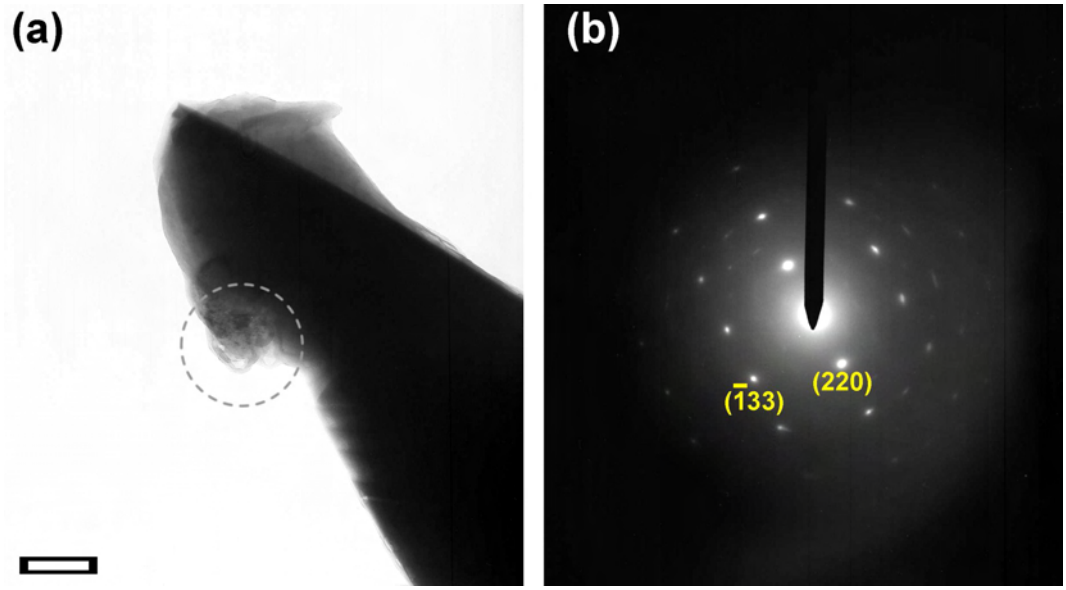

FIGURE 4.9: (a) Bright field image of a 2 μm germanium tube. The circle indicates the SADs; scale bar is 200 nm. (b) diffraction pattern showing crystalline germanium and lattice planes.

polycrystalline material, with big crystal grains, and thus within a SAD there are only a few large crystals.

In order to obtain a better understanding of the orientation and size of the crystals it was necessary to have more control over the sample preparation. For this the silica cladding of a germanium fibre was first removed with HF. Then a focused ion beam (FIB) instrument was used to obtain thin cross sections from the fibres. The thin sample was picked up with micro-manipulators and further thinned with FIB. When the sample was thin enough for TEM analysis, it was mounted on a TEM grid. Some SEM micrographs of the FIB sample preparation procedure are shown in Figure 4.10.

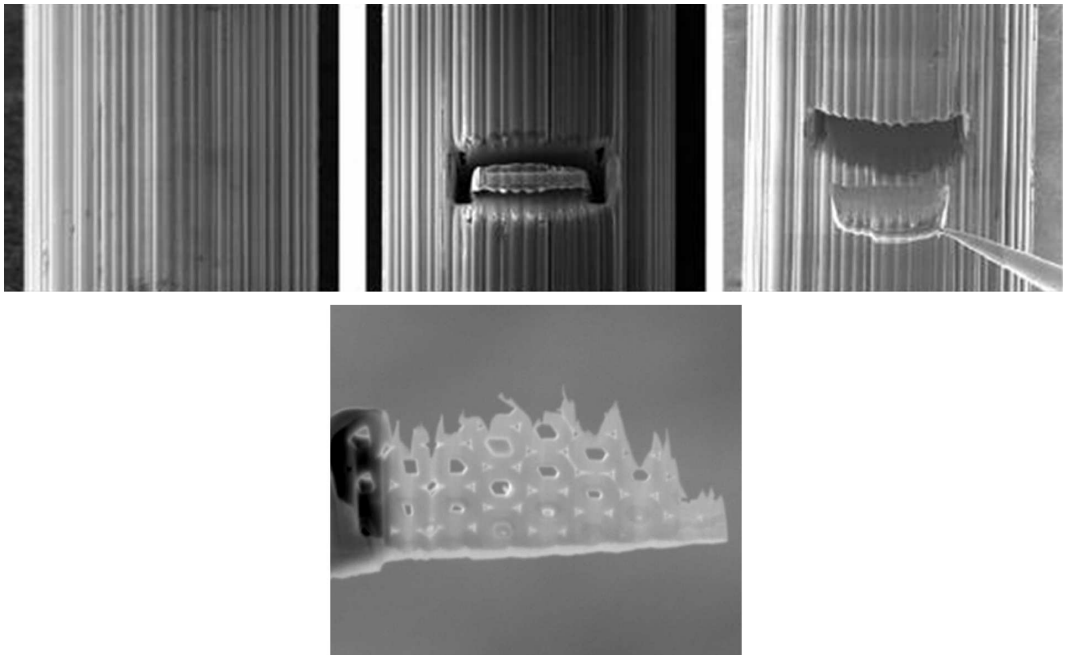

FIGURE 4.10: TEM sample preparation with FIB, images from left to right, 1) SEM image of the germanium-filled fibre after HF etching and prior to FIB. 2) A section of the wires bundle is cut by a FIB. 3) This section is removed with a micromanipulator probe. Bottom image, sample after further thinning with FIB, this sample is ready for TEM (Performed by J. Kulik at the EM facility of the Material Research Institute at Penn State).

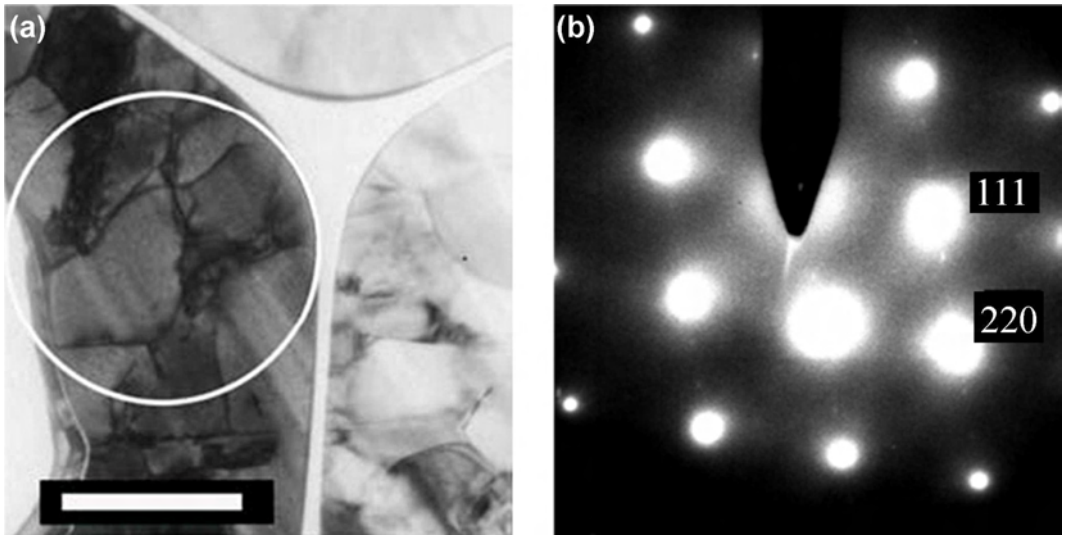

FIGURE 4.11: (a) Cross-sectional bright field image of a germanium-filled honeycomb MOF, showing germanium crystals with hundreds of nanometres scale dimensions. Scale bar 500 nm (b) Selected-area diffraction pattern of the region circled in (a).

Figure 4.11a is the bright field image of a FIB, thinned sample. Even after the FIB process the conformal filling can be appreciated in the image. The uniform annular growth down to very small inner diameters is particularly striking when one considers that the

germanium is polycrystalline, with a grain size as large as 500 nm. The diffraction pattern of the area enclosed in the white circle in Figure 4.11a, is shown is Figure 4.11b. This pattern clearly indicates that the germanium wires are made of crystalline material. For germanium the crystallization is easily achieved upon heating up to 500 °C, at this point the originally amorphous germanium converts into large crystalline grains.

4.1.2 Raman Spectroscopy

Raman spectroscopy is a very useful and non-destructive characterisation technique which quickly provides important information of the structure of semiconductors. The Raman spectra of semiconductor filled fibres were collected in a backscattering configuration, using a Renishaw 2000 Raman spectrometer, using a HeNe ($\lambda = 632.817\,\text{nm}$) laser as the excitation source. When the excitation laser interacts with a sample, a small part of the incoming photons excite lattice vibrations. The remaining energy escapes as light of different frequencies, called Raman radiation. Some of the Raman radiation is slightly lower in frequency than the incident light and is called the Stokes signal and some radiation has a higher frequency than the excitation source and is called the anti-Stokes signal. A Raman spectrum is a plot of the intensity and frequency of the emission; the intensity in terms of emission units and the frequency in terms of the Raman shift from the incident frequency,

$$\text{Raman shift } (\text{cm}^{-1}) = \frac{\nu_{\text{pump}} - \nu_{\text{Raman}}}{100\,\text{c}} \tag{4.3}$$

where ν_{Pump} and ν_{Raman} are the frequencies of the excitation laser and the emitted spectra, and c is the speed of light. A more extensive description of the Raman effect is presented in Chapter 6. The characteristics of the Raman signal depends on the exact composition and the crystalline structure of the sample and therefore it is used to identify crystalline phases in semiconductors.

The natural spectral line shape of a Raman peak follows a Lorentzian curve. However a Raman peak is greatly influenced by other line broadening sources such as molecular collisions. The inherent linewidth is also affected by the spectrometer, by interactions due to the irradiation source or the instrument response factor (instrumental broadening). Experimental Raman peaks are commonly approximated to Voigt line shapes. A Voigt function features a convolution of many interactions causing various broadening features based upon Lorentzian and Gaussian line shapes. Voigt shapes contribute more area to the wings of the peak than a Gaussian, but not to the extent that a Lorentzian peak does. In most experiments the Raman signal of a molecular vibration is better approximated by Voigt functions. The analytical expression of a Voigt peak is given by,

$$V(x) = \frac{\int_{-\infty}^{\infty} \frac{H\exp(-y^2)}{\omega_l^2 + \left[\left(\frac{x-x_0}{\omega_g}\right) - y\right]^2} dy}{\int_{-\infty}^{\infty} \frac{\exp(-y^2)}{\omega_g^2 + y^2} dy}, \tag{4.4}$$

where $V(x)$ is the Voigt function, ω_l and ω_g are the width of the Lorentzian and Gaussian contributions respectively, x_0 is the peak location and H is the peak height. In the following sections the Raman signal of silicon and germanium wires are approximated to Voigt shapes.

4.1.2.1 Raman Spectroscopy of Silicon modified MOFs

In crystalline silicon the momentum conservation rules select only the excitation of optical phonons with zero momentum. This leads to a sharp peak at a specific Raman shift [161, 162]. The Raman spectrum of single crystal silicon comprises a symmetric band at $\sim 521\,\mathrm{cm}^{-1}$ with a band full-width-at-half-maximum (FWHM) of $\sim 3\,\mathrm{cm}^{-1}$ (see Figure 4.12). On the other hand, in amorphous silicon (a:Si) a variety of vibrational modes and energies are allowed. Thus a broad peak centred at $\sim 480\,\mathrm{cm}^{-1}$ is observed, however there are strong variations on the profile from one amorphous sample to another. For example, the amorphous peak has been reported to shift to higher energy when crystals smaller than 10 nm in diameter are present within the amorphous silicon matrix [163, 164].

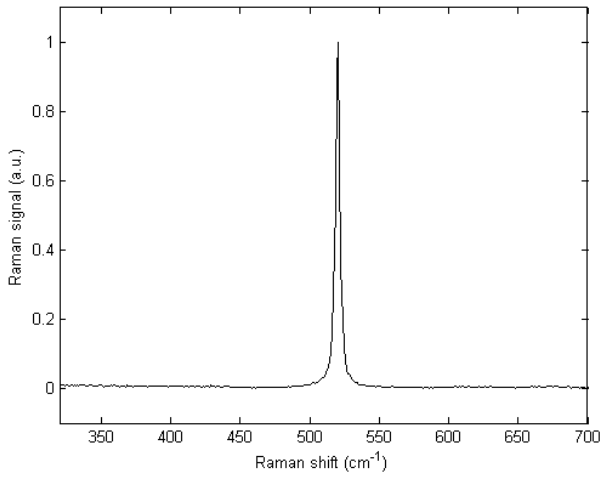

FIGURE 4.12: Typical Raman spectrum of single crystal silicon.

Microcrystalline (μc : Si) silicon can be consider as a mix of disordered crystals, intermediate phase (grain boundaries) and amorphous silicon. The Raman spectrum, however, is not simply the sum of a single crystal and an amorphous silicon spectrum. For polycrystalline silicon the Raman signal is more complex and is determined by the material

characteristics, grain sizes, crystalline fraction, defects, etc. Raman microscopy has been recognized as a valuable method for monitoring changes in the microstructure of polysilicon. For this material the sharp single crystal peak becomes broader and asymmetric with an extended tail at low wavenumbers. The peak becomes more and more asymmetric and broader for smaller crystallite sizes [165]. The deformation of the spectrum is attributed to disordered crystallities [166, 164], bond dilation at grain boundaries [167] and amorphous silicon regions. Peak broadening is indicative of increased phonon relaxation times due to the presence of defects, impurities or small or variable grain sizes [166].

Using the HP-CVD method, a silicon tube was formed inside a silica MOF capillary with an internal diameter of 5 μm and an external diameter of 125 μm. The capillary was heated in a tube furnace from room temperature to 750 °C, at a ramp rate of 4 °C/min, while silane was flowing. Optical microscope images revealed that a continuous tube of silicon was annularly deposited onto the inside of the fibre with a high filling fraction. Raman spectra of this silicon tube, and single crystal wafer as control, were collected with a 633 nm laser at an incident power sufficiently low to avoid heating. The collected spectra were approximated by a single Voigt profile which includes a instrumental broadening of 1.5 cm^{-1} Gaussian contribution. The Raman spectrum of a single crystal silicon wafer was approximated by a single Voigt peak located at 520.1 cm^{-1}, with 3 cm^{-1} FWHM. The Raman signal of the in-fibre silicon is located at 517.5 cm^{-1}, with 5.5 cm^{-1} FWHM including instrumental broadening. The Raman signal and Voigt approximations are shown in Figure 4.13.

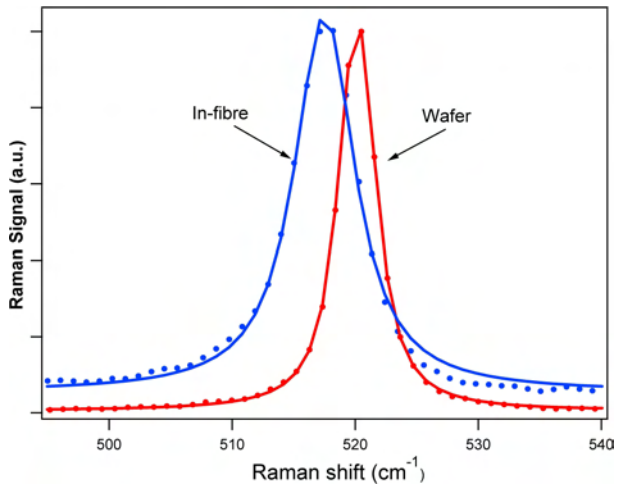

FIGURE 4.13: Raman spectra of in-fibre silicon wire and single crystal silicon wafer (dotted plots). Solid lines through the data are Voigt fits including a 1.5 cm^{-1} Gaussian instrumental component. Each spectra is normalized to its maximum.

It may be recognized from Figure 4.13, that the Raman mode of the silicon tube deposited at 750 °C is asymmetric, broadened, and redshifted (517.5 cm^{-1}) from the single

crystal silicon (520.1 cm^{-1}) peak. Asymmetry is given by the ratio of the half maximum width on the low frequency side of the peak to the maximum width on the high frequency side of the peak. Asymmetry is a characteristic of microcrystalline silicon due to the presence of disordered crystallities and amorphous phases between grains.

Red-shifting of silicon Raman spectra can be due to both the effects of tensile strain [168] and the presence of micro-nanocrystalline and/or amorphous material phases. To separate the effects of strain on the Raman spectra, that might be present at the silica/silicon interface, from spectra broadening that is intrinsic to the microcrystalline silicon sample itself, the silicon tubes were etched out of the silica fibre with HF acid. A few hundred micrometres of the silica cladding were removed and micro-Raman spectrum was collected from both etched and unetched regions, which were close to each other. A microscope image of an etched fibre is shown in Figure 4.14.

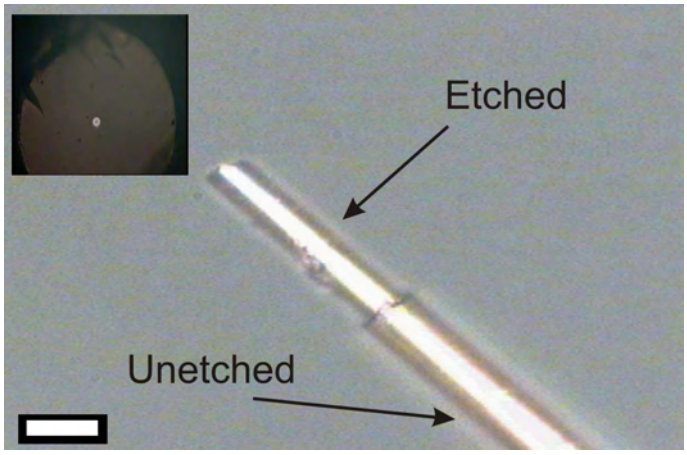

FIGURE 4.14: Microscope image of a silicon filled fibre partially etched from one end. The silicon tube has been released from the silica MOF by HF etching; the scale bar is 5 μm. The inset is a microscope image of the transverse deposition profile before etching.

Micro-Raman spectra collected on the etched tube also exhibit an asymmetric peak, but the peak center is now at 519.6 cm^{-1}, indicating that removal of the tube from the silica template has relieved strain (see Figure 4.15). This clearly confirms that the red-shift observed for the in-fibre silicon tube is entirely due to strain induced at the silica-silicon interface upon cooling from the annealing temperature of 750 °C by the difference in thermal expansion between the silicon tube and the silica fibre. The transfer of shear stress is large enough to redshift the Raman mode by $\sim 2.5\,cm^{-1}$ to the silicon at this silica interface and indicates that the bonding between the two materials is strong. The asymmetry and broadening of the Raman peak confirms the previous results obtained with TEM which indicate that silicon tubes growth at 750 °C are composed of polycrystalline silicon with microcrystalline silicon, disordered micro/nano crystals and amorphous material.

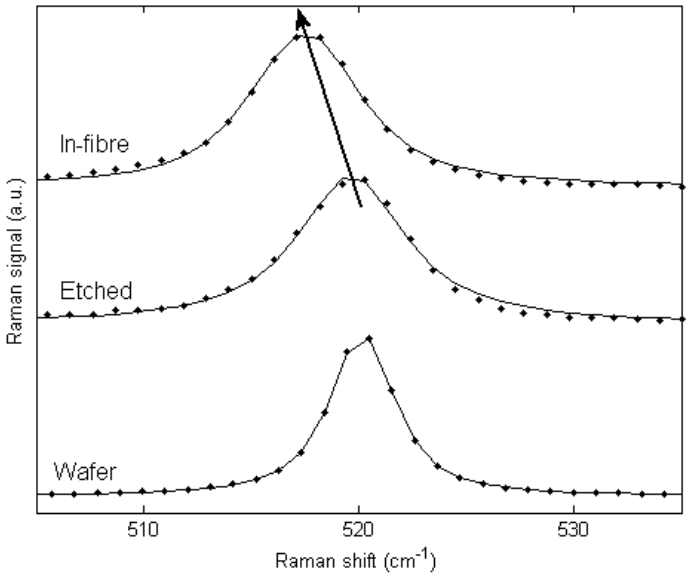

FIGURE 4.15: Micro-Raman spectra of a silicon tube inside a MOF (top), silicon tube etched out of the fibre template (middle), and a single crystal silicon wafer (bottom). The spectra were fitted with a single Voigt peak, including $1.5\,\mathrm{cm}^{-1}$ Gaussian instrumental broadening (solid lines). For in-fibre silicon the peak is centred at $517.5\,\mathrm{cm}^{-1}$ with $5.5\,\mathrm{cm}^{-1}$ FWHM. The etched wire peak is at $519.6\,\mathrm{cm}^{-1}$ with $5.5\,\mathrm{cm}^{-1}$ FWHM, and the single crystal peak is at $520.1\,\mathrm{cm}^{-1}$ with $3\,\mathrm{cm}^{-1}$ FWHM. Each curve has been normalized to the maximum of the peak.

Figure 4.15 shows the Raman signal of the etched and unetched silicon wires and that of single crystal silicon. It can be appreciated that the peak of the in-fibre wire is redshifted from the other two peaks. The asymmetric Raman peak of the in-fibre and etched silicon tubes cannot be "perfectly" approximated by a single Voigt peak, as may be seen from Figure 4.15. The approximations (solid lines) show a deviation from the experimental data at the low and high frequency bands of the peak. In contrast, the single crystal Voigt fit matches the experimental data accurately. The Raman spectrum of polycrystalline silicon can thus be deconvoluted into two peaks, one referring to the Raman contribution of the amorphous material located at $480\,\mathrm{cm}^{-1}$, and the other due to the crystalline phase at $\sim 520\,\mathrm{cm}^{-1}$ [163, 169, 170]. However, it has been shown that, in some cases, the data is best fitted with three peaks [167, 170, 171]. The third peak at $\sim 510\,\mathrm{cm}^{-1}$ arises due to the presence of defective regions and grain boundaries.

In order to get a better approximation to the Raman spectrum of the etched silicon wire, its Raman spectrum was fitted by a sum of two or three Voigt profiles and continuous background so that the structural composition of the sample can be understood. The Igor® curve fitting software was used to decouple the spectrum. It is important to

note that the peak fitting is very sensitive to the choice of starting parameters and the conditions of the fitting procedure.

In the fitting process the amorphous contribution peak was fixed at $480\,\mathrm{cm}^{-1}$. The other two peaks, attributed to micro/nanocrystals, grain boundaries and crystalline silicon were left free to change in position, intensity, width and shape [172]. Then, several fits were performed with different starting points; until a good approximation was obtained. The coefficient $r^2 = 1 - \chi^2$ is a measure of the goodness of fit; an r^2 of 1.0 is perfect fit an r^2 of 0.0 is complete lack of fit [173],

$$\chi^2 = \frac{SSE}{SSM}\,. \tag{4.5}$$

SSE is the sum of squared residuals,

$$SSE = \sum_i (\hat{y}_i - y_i)^2\ , \tag{4.6}$$

where $\hat{y}_i$ is the fitted value for a measured point y_i. SSM is the deviation for y_i from the mean of the y data ($\bar{y}$).

$$SSM = \sum_i (y_i - \bar{y})^2\ , \tag{4.7}$$

The fit obtained of the Raman spectra was only considered to be satisfactory when $r^2 \geq 0.99$. When the Raman spectrum of the etched silicon wire was approximated by a single Voigt peak the $r^2 = 0.97$ value, whereas using two peaks (at $480\,\mathrm{cm}^{-1}$ and $\sim 520\,\mathrm{cm}^{-1}$) improved the value of the fitting procedure to $r^2 = 0.98$. The use of three peaks provided an excellent fit $r^2 = 0.99$.

Figure 4.16 shows the results of the three peaks fitting procedure. The Raman spectrum of the etched silicon wire is plotted in the figure and the inset shows a three Voigt peaks approximation. The first peak is located at a $480\,\mathrm{cm}^{-1}$ with FWHM of $\sim 60\,\mathrm{cm}^{-1}$ attributed to amorphous silicon, the second peak at $517\,\mathrm{cm}^{-1}$ with a $11.1\,\mathrm{cm}^{-1}$ FWHM attributed to boundary regions, defective silicon and small grain sizes. A third peak is located at $519.6\,\mathrm{cm}^{-1}$ with a FWHM of $5.5\,\mathrm{cm}^{-1}$ due to crystallized grains of hundreds of nanometres in diameter. The FWHM of the $519.6\,\mathrm{cm}^{-1}$ peak ($5.5\,\mathrm{cm}^{-1}$) versus that of the single crystal sample $3\,\mathrm{cm}^{-1}$, including instrumental broadening, together with the presence of the two weaker peaks, is consistent with a mixed phase of silicon with both amorphous and crystalline components of varying crystallite sizes [166].

The amorphous and microcrystalline portions of the sample will affect its electrical and optical properties considerably. Voids and grain boundaries might contain a high

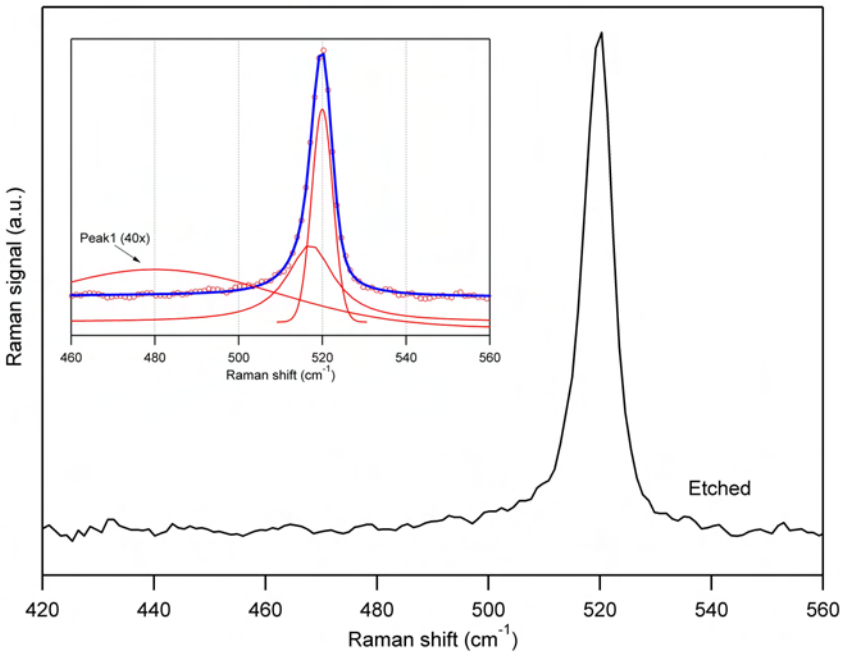

FIGURE 4.16: Raman data of a silicon tube removed from the MOF template. The inset shows the three Voigt peaks approximation (solid blue line through the data). The red lines are the three decoupled peaks. Voigt peak 1 centred at $480\,\mathrm{cm}^{-1}$ is shown magnified 40× for clarity because it is sufficiently broad and weak as to appear as nearly a straight line in the figure at the normal figure scale.

density of recombination centres, whereas a high crystalline fraction is likely to increase the mobility of the charge carriers. The degree and nature of material structure is highly dependent upon the deposition parameters especially the starting material, the anneal temperature and time. In order to improve the material quality of silicon wires/tubes and maximize the grain sizes, the silicon may be deposited inside the fibre and crystallized during a post-deposition temperature treatment [166]. A silicon-annealing process may result in a bigger grain sizes and lead to better electrical and optical properties. In order to obtain better quality material the crystalline structure of wires deposited at different temperatures was investigated. Silicon tubes were grown inside MOFs at 450 °C, 700 °C, 750 °C and finally a sample was subject to a thermal annealing process at 1450 °C after the deposition at 750 °C. The Raman spectra of these silicon tubes is shown in Figure 4.17.

It may be observed from Figure 4.17 that the Raman spectra of the wires becomes more similar to that of single crystal silicon as the deposition temperature increases. This indicates that, as the deposition temperature increases the silicon is composed of bigger crystal grains. In this experiment three distinct varieties of silicon tubes may be recognized, first the tube deposited at 450 °C shows a broad peak located at $\sim 480\,\mathrm{cm}^{-1}$ characteristic of amorphous silicon with no detectable crystalline silicon peak. Tubes

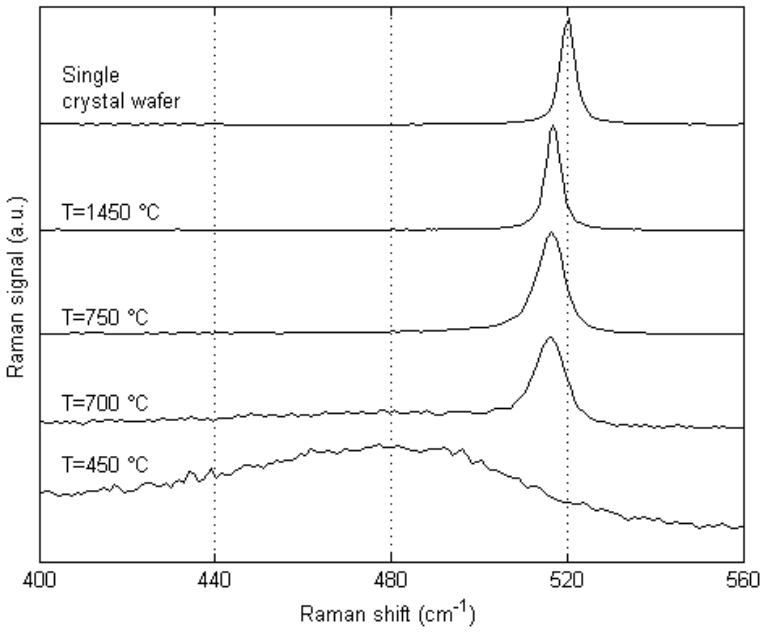

FIGURE 4.17: Raman spectra of silicon wires deposited at different temperatures, of T= 450 °C, 700 °C, 750 °C, and fibre annealed at 1450 °C after deposition. The spectrum of single crystal silicon is included as a reference. Each Raman spectra is normalized to its maximum.

deposited at 700 °C exhibit an asymmetric Raman band with a broad feature overlapping the main peak which indicates that the silicon deposited at this temperature has a high portion of amorphous and defective material. The samples deposited at 750 °C exhibit a less asymmetric and narrower peak located at 516.4 cm^{-1}, compared to the sample deposited at 700 °C. Finally the tubes annealed at 1450 °C show a symmetric peak at 516.86 °C, its peak FWHM is very similar to that of a single crystal which indicates that at this temperature silicon has crystallized and formed grains of hundreds of nanometres in diameter. The redshift of the 520 cm^{-1} peak, characteristic of single crystal silicon to $\sim$ 516 cm^{-1}, observed in these samples is due again to strain at the silicon-silica interface.

The samples deposited at 700 °C, 750 °C and the one annealed at 1450 °C, were used for further analysis. Spectra from these tubes were again fitted by Voigt peaks using Igor® curve fitting software and revealed the existence of various "categories" of polysilicon. The Raman spectrum of the silicon tube, deposited at 700 °C, is shown in Figure 4.18 together with the Raman spectrum of the sample deposited at 450 °C. From this figure it can be observed that the Raman signal of the 700 °C is composed of a sharp peak and the broad peak characteristic of the amorphous tube. In the inset, the Raman spectrum of the 700 °C was fitted with the sum of three Voigt peaks; (1) a broad peak at 471.7 cm^{-1}

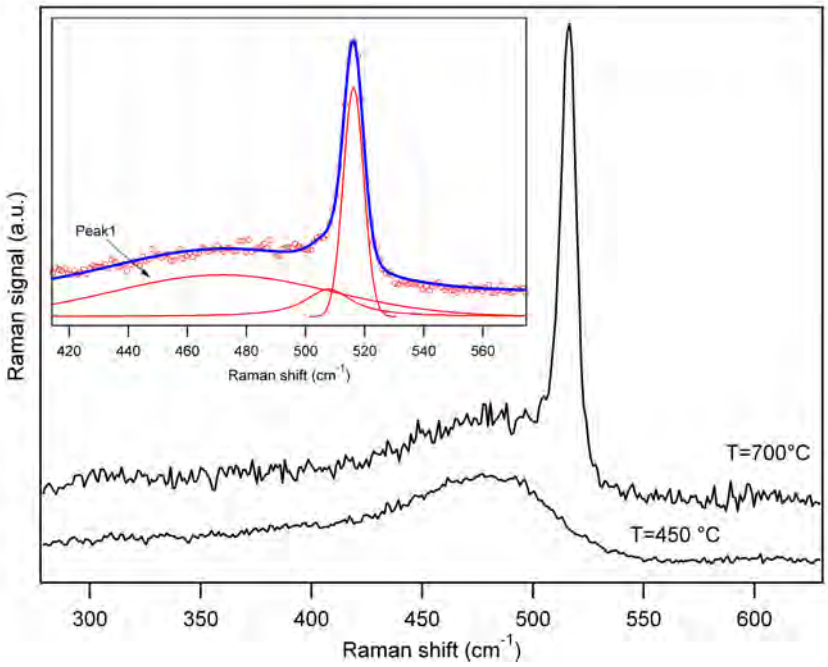

FIGURE 4.18: Raman spectra of silicon tubes deposited at 700 °C and 450 °C. The blue plot through the data in the inset is the three Voigt approximation of the 700 °C sample. The fitted is decoupled into three peaks, shown in red. Peak 1, located at 471.7 cm^{-1} with $\sim$ 86 cm^{-1} FWHM, peak 2 at 507 cm^{-1} with FWHM of 13.88 cm^{-1} and peak 3 at 516.2 cm^{-1} with 7.7 cm^{-1} FWHM. The high contribution of the amorphous peak to the spectrum indicates that the silicon is "just" begining to become crystalline at this deposition temperature.

characteristic of amorphous silicon, (2) at 507 cm^{-1} due to defective crystalline silicon and one located at 516.2 cm^{-1} indicative of crystalline silicon.

Subtle differences between 700 °C samples and 750 °C samples were detected. Tubes deposited at 750 °C are also composed of category 1, 2 and 3 peaks, but the intensity of the amorphous peak is lower than that exhibited by 700 °C tubes, as illustrated in Figure 4.19. Annealing has caused the amorphous silicon to crystallize and some of the polycrystalline grains are now larger. The orientation, however, is random and there are defective silicon crystals and amorphous phases in the sample. The diffraction pattern from tubes deposited at this temperature also confirmed the disordered orientation of crystals and the presence of amorphous phase regions (Chapter 4.1.1.1).

The Raman spectrum of the tube annealed at 1450 °C is shown in Figure 4.20, the inset is the Voigt approximation, and in this case only a single peak centred 516.84 cm^{-1} was required to obtain a good fit. The FWHM of the peak, (3.43 cm^{-1}) including instrumental broadening, is somewhat broader than that of single crystal silicon 3 cm^{-1} due to the random orientation of the crystals. After annealing at 1450 °C, the silicon tube consists of polysilicon with randomly orientated grains 200 – 700 nm in size. The

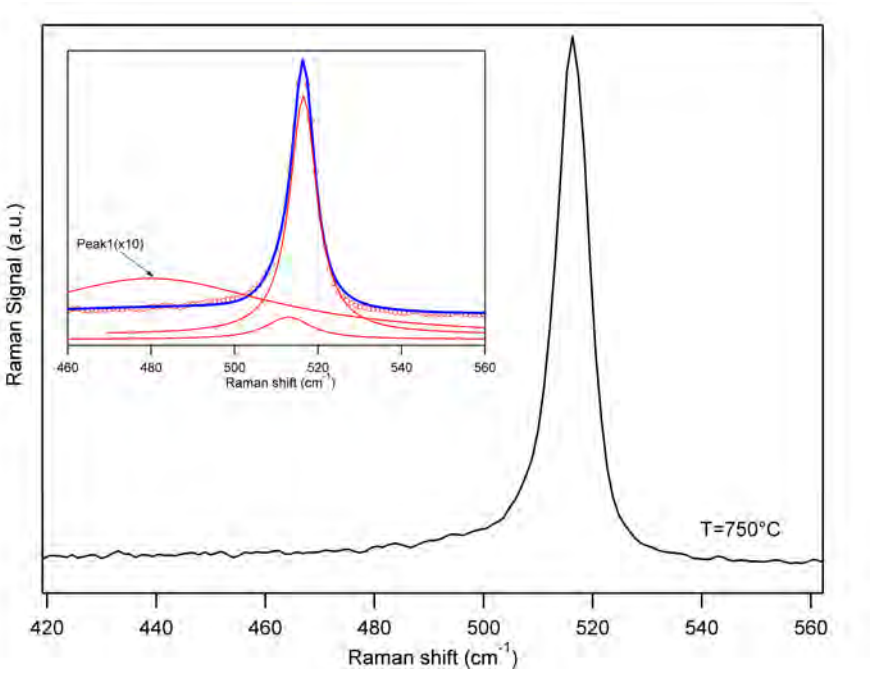

FIGURE 4.19: Raman spectrum of silicon tubes deposited at 750 °C. The blue line through the data in the inset is the three Voigt approximation of the Raman spectrum. Each decoupled peak is shown as a red line. Peak 1, located at 480 cm^{-1} with $\sim$ 81 cm^{-1} FWHM, peak 2 at 511.1 cm^{-1} with FWHM of 15.3 cm^{-1} and peak 3 at 516.4 cm^{-1} with 6.7 cm^{-1} FWHM.

material appears to be dominated by highly crystallized silicon which is likely to improve its electrical and optical properties [172].

The peak areas of the crystalline and the amorphous parts of the Raman spectra correlate to the amount of crystalline and amorphous silicon in the tubes. The fitted Raman profiles enables the crystalline volume fraction (χ_c) of polysilicon to be calculated to give a qualitative measure of the material quality. Although it is not possible to obtain absolute values because the detection efficiency is usually not known, the ratio of the two crystalline peaks and amorphous peak areas, corresponds to the ratio of the amount of crystalline to the amount of amorphous silicon present [174, 170, 171]. χ_c is calculated by considering the contribution of the amorphous phase, the grain boundaries, the intermediate phase, and the crystalline phase,

$$\chi_c = \frac{I_c + I_m}{I_c + I_m + \sigma I_a} \ , \tag{4.8}$$

where I_c is the integrated intensity of the crystalline peak at $\sim$ 520 cm^{-1}, I_m is the integrated intensity of the intermediate phase, grain boundaries and defective crystalline silicon at $\sim$ 510 cm^{-1}; I_a is the integrated intensity of the amorphous peak at $\sim$ 480 cm^{-1} and σ is the ratio of integrated Raman cross section of the amorphous phase to the

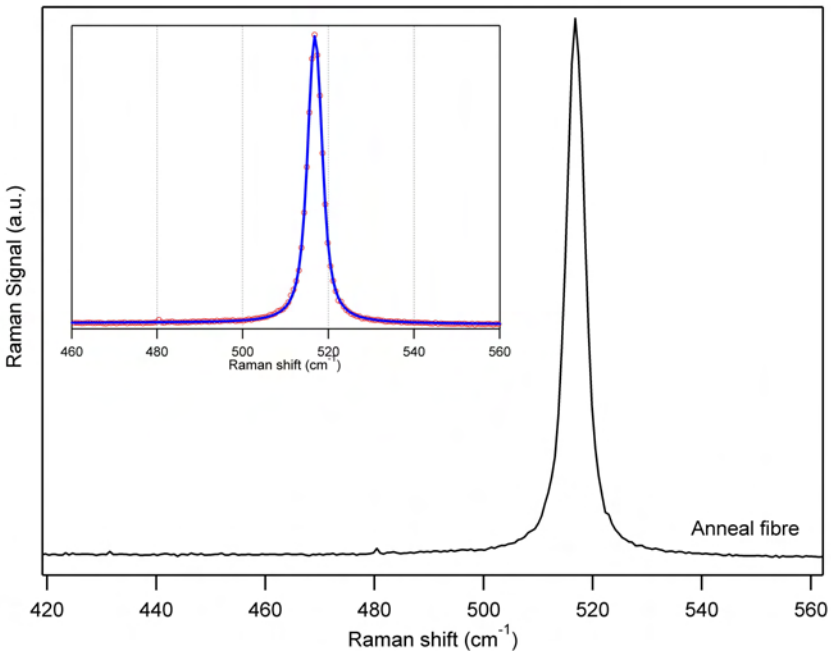

FIGURE 4.20: Raman spectrum of a silicon tube annealed at 1450 °C. Inset, the Raman data was fitted by a single Voigt peak (blue line) including a 1.5 cm^{-1} Gaussian contribution. The peak is located at 516.86 cm^{-1} with a FWHM of 3.43 cm^{-1}. Fitting with two or three peaks did not improve the r^2 value of the overall fitting.

crystalline phase (usually is set between 0.8-1 [172, 170, 171]), for the calculation herein $\sigma = 1$.

The silicon tubes deposited at 450 °C show only a broad amorphous peak, therefore $\chi_c \approx 0\%$. For the tube deposited at 700 °C, in addition to the principal amorphous peak at $\sim 480\,cm^{-1}$, two crystalline peaks arise. The crystalline volume fraction of this sample is only $\approx 39\%$. At the next higher step of deposition temperature, i.e. 750 °C , the intensity of the peak at 516 cm^{-1} increases while the intensity of the amorphous peak decreases. The presence of the grain boundary is still notable in this case, since the peak at 512 cm^{-1} highly contributes to the spectral intensity. The crystalline volume fraction increases and a value of $\approx 87\%$ is obtained for this tube. The tubes annealed at 1450 °C do not have amorphous peaks thus $\chi_c \approx 100\%$. These calculations demonstrate that by thermal treatment the quality of the silicon tubes can be improved and the grain size can be maximized. This is of great importance for future devices because the optical and electrical characteristics that determine polysilicon's usefulness for photonic and electronic devices are established by the crystalline volume fraction and quality of grains.

The redshift observed in the Raman peak of in-fibre silicon, further suggest that it is possible to use optimized fibre geometries to tailor the conformally induced strain in

silicon. Strain induced changes in silicon may lead to desirable changes in the electronic properties such as increased carrier mobility. Moreover, strain breaks silicon's centrosymmetric inversion symmetry and makes it an ideal electro-optic material [175].

4.1.2.2 Raman Spectroscopy of Germanium

Germanium tubes were also deposited inside 5 μm silica capillaries. During the HP-CVD, the capillaries were heated in a tube furnace from room temperature to 500 °C, at a ramp rate of 2 °C/min, while a GeH_4 precursor at 2 MPa partial pressure in argon carrier was flowing at a total pressure of 40 MPa. The characteristic Raman spectra of these tubes is show in Figure 4.21.

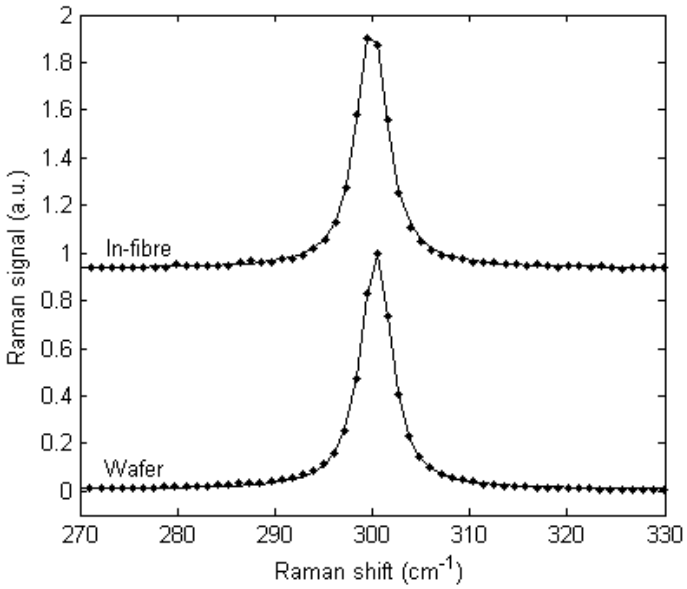

FIGURE 4.21: Micro-Raman spectrum of a germanium tube inside a fibre and that of germanium single crystal wafer. Lines through the data are single Voigt fits including 1.5 cm^{-1} Gaussian component due to instrumental broadening.

Voigt fits, which included a 1.5 cm^{-1} Gaussian instrumental contribution, gave 3.31 cm^{-1} FWHM for the germanium wire in comparison to 3.1 cm^{-1} for single crystal germanium. As in silicon, germanium Raman modes can be broadened by the presence of stress, microcrystalline or nanocrystalline grains, and/or amorphous phases. Amorphous and/or nanocrystalline germanium phases typically exhibit Raman spectra at lower wavenumbers than bulk single crystal material. The germanium wire Raman spectra are symmetric and do not exhibit any low frequency tailing characteristic of the presence of such phases. The somewhat broader (3.31 cm^{-1}), but still symmetric, Raman mode observed for the wire as compared with the wafer (3.1 cm^{-1}) suggests that the sample is crystalline, but not single crystalline. This was confirmed by transmission electron

microscopy, TEM measurements, showed that there are microcrystalline, randomly oriented, grains $\sim 500\,\text{nm}$ in diameter (Chapter 4.1.1.2). There was little difference in the position of the Raman modes for the wires in the fibre and the wafer, $299.8\,\text{cm}^{-1}$ and $300.3\,\text{cm}^{-1}$ respectively, indicating that there is little or no strain induced in the wires upon cooling from the annealing temperature of $500\,^{\circ}\text{C}$.

4.2 Electrical Characterisation

A field effect transistor (FET) is a 3-terminal electronic device, configured like a parallel plate capacitor with one of the electrodes replaced by a semiconductor. By controlling the voltage on one plate (gate), the distribution of charges in the semiconductor are modified. These charges are injected from the source electrode and collected across the semiconductor channel at the drain contact by applying a voltage between both [176]. Figure 4.22 shows a schematic cross-section of a metal-oxide field effect transistor(MOSFET), which are the most commonly used FETs in microelectronic circuits. If the semiconductor between the source and the drain is n-type, a positive voltage applied in the gate contact, leads to accumulation of electrons in the semiconductor (below the gate) and enhances its conductivity. Conversely, $V_{gate} < 0$ depletes the holes in the semiconductor and suppresses conductivity.

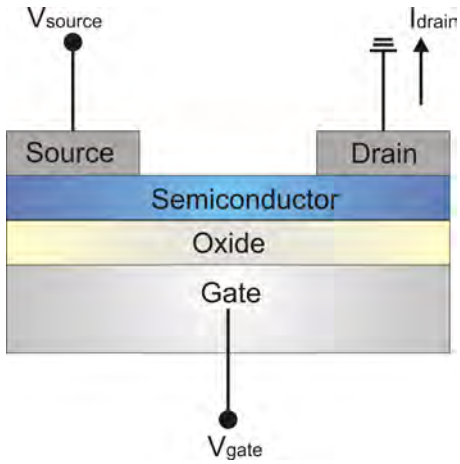

FIGURE 4.22: A schematic view of a FET. In this model electrons are injected from the source and collected at the drain.

The current-voltage ($I-V$) operation of a FET is typically displayed by plots of the drain current I_{drain} as a function of the source-drain voltage V_{source}, at fixed gate voltages V_{gate} are called the output characteristic of the transistor. The I_{drain} vs. V_{gate} dependance for a fixed V_{source} are the transfer characteristics and show how efficiently the gate voltage can switch the device "on" or "off". Due to the FET's digital nature, today there are

millions of them in the processors used in personal computers, cellular phones, and many other microelectronic devices.

Besides their numerous technological applications, FETs can be used to measure the electronic transport of solid materials; this is because the device gives direct access to the carrier type, concentration and mobility. To this end, germanium and silicon tubes were deposited inside MOF capillaries with an internal diameter of 5 μm. The deposition temperature for the silicon tubes was 750 °C and 500 °C for germanium. The samples were etched at both ends with HF acid to expose the semiconductor tube inside. These were then mounted onto glass slides and masked off in the centre. The samples were then evaporated with a 250 nm thick layer of aluminium, which is the classic ohmic contact material for silicon and germanium. A contact is say to be ohmic when it has been prepared so that the current-voltage characteristic of the contact is linear and symmetric. After annealing at 435 °C for 35 min under an inert argon atmosphere, the samples were finished off by removing the central mask [177]. This will reveal two electrically isolated halves of the glass slide. The exposed ends of the capillaries were covered with some Ga-In eutectic to form good electrical contacts with the sintered aluminium on the etched ends of the fibre samples. These two end contacts become the source and drain contacts, as in standard two-terminal *I-V* measurements. An additional capacitatively coupled coaxial gate was also constructed by placing a drop of the In-Ga eutectic onto a section of silica cladding $\sim$ 1 mm in length in the middle of the fibres. By applying a bias voltage to this contact, it was possible to apply a radial electric field to the semiconductor core, thus using the silica cladding as a gate insulator in a similar fashion to that seen in conventional FET devices.

The capacitance of the samples is determined using a simple co-axial approximation, with the semiconductor core being treated as the central conductor and the silica cladding being the cylindrical dielectric spacing between core and outer conductor (the eutectic gate contact). The capacitance per unit length is therefore given by the standard expression for co-axial capacitors [178]

$$C/L = \frac{2\pi\epsilon\varepsilon_0}{\ln(h/r)}\,, \tag{4.9}$$

where C is capacitance, L is the length of the gate (eutectic in the middle), ϵ is the relative dielectric permittivity of the silica cladding, h is the cladding radius and r is the radius of the semiconductor core. All of the electrical measurements were carried out on a probe station using an Agilent 4155C semiconductor parameter analyzer. A representation of the electric circuit is shown in Figure 4.23.

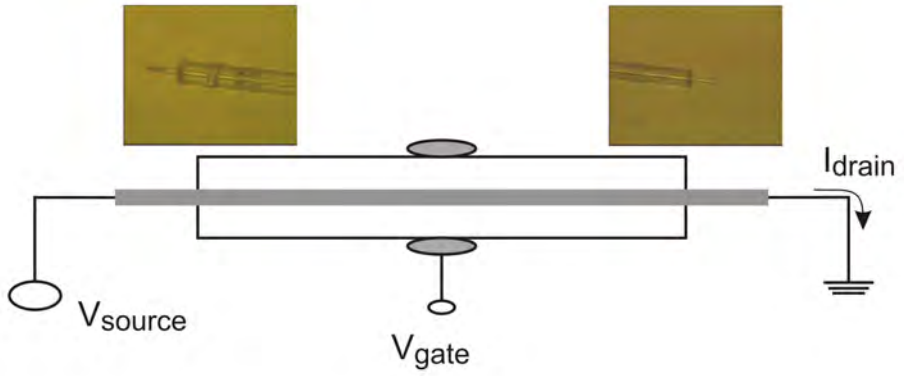

FIGURE 4.23: Schematic of in-fibre FET circuit diagram and microscope images of fibre's etched ends. The semiconductor core protrude out of the silica capillary.

4.2.1 Electrical Properties of Germanium Fibres

Cross-sectional microscope images at both ends of an 11 mm long fibre, completely filled with germanium are displayed in Figure 4.24. Data from room temperature three-terminal electrical characterisation measurements on this 11 mm long fibre are shown in Figure 4.25. With $V_{gate} = 0$, the measurement corresponds to a two-terminal current (I_{drain}) vs voltage (V_{source}) sweep, showing the core to be continuous and electrically conductive with a resistance $R = 2.16 \times 10^9 \Omega$. Taking into account that the germanium core diameter is 5 μm, and the sample length is 11 mm, the resistivity of the sample was calculated to be $5.6 \times 10^{-2} \Omega$cm. The linearity of the V-I curves indicates that the contacts between the germanium core and the probe station are ohmic.

As the gate bias voltage is varied from -100 to +100 V, the gradient of the $I_{drain} - V_{source}$ curve increases significantly, which not only demonstrates that the device operates as a FET but also indicates that transport through the semiconducting wire is dominated by n-type carriers. By setting the $V_{source} = 10$V and measuring the I_{drain} as a function of V_{gate}, the transconductance of the sample was calculated as being $\partial I_{drain}/\partial V_{gate} \approx 5 \times 10^{-11}$ A/V.

The inset to Figure 4.25 shows how I_{drain} varies as a function of V_{gate} for a similar device; the transconductance of the sample begins to be "pinched off" at voltages in the range of -90 to -100 V, emphasizing the operation of this sample as a fibre-based depletion-mode FET switch. Although the experimentally available range of applied gate voltages limits the characterisation of the "off" regime of the FET, the on/off current ratio of the device can be estimated to be 10^4 or better.

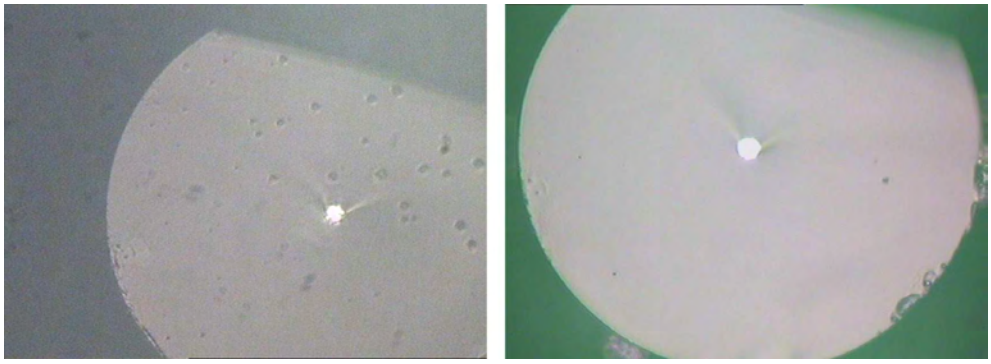

FIGURE 4.24: Cross section of both ends of a germanium fibre used for electrical characterisation, the sample is 11 mm long. The semiconductor material fills completely the 5 μm capillary hole.

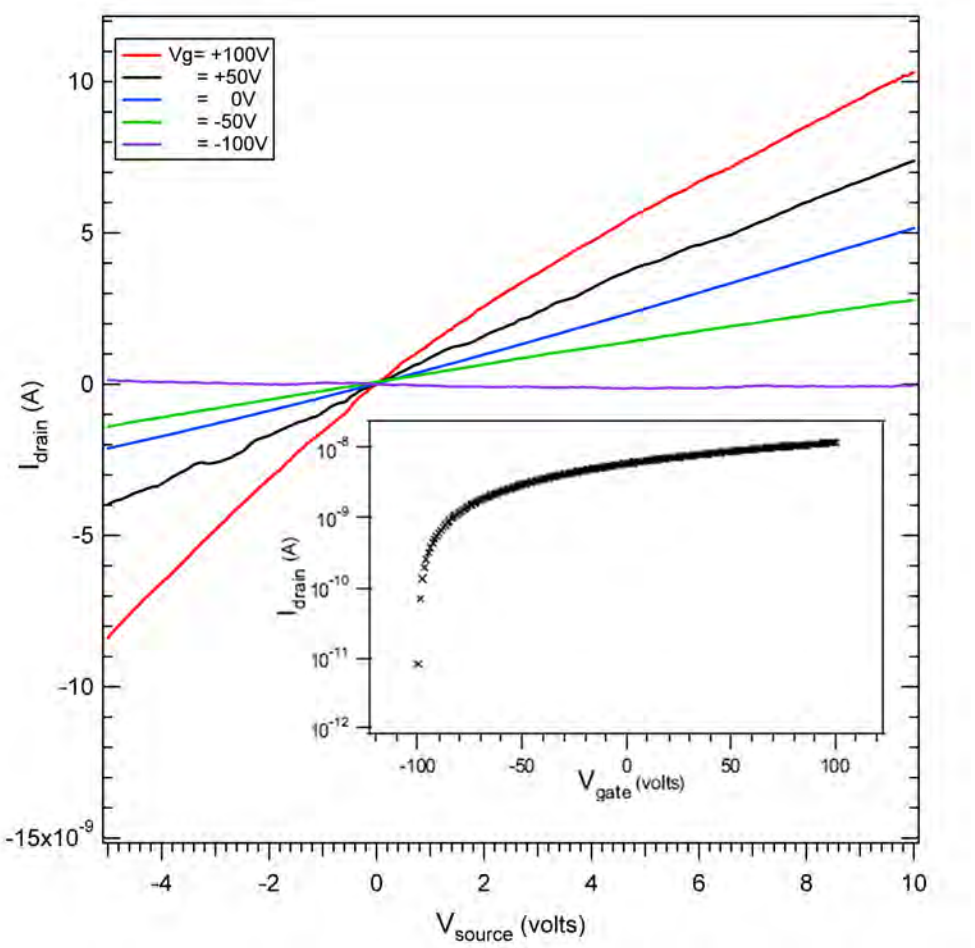

FIGURE 4.25: Three-terminal electrical measurement on an 11 mm long 5 μm capillary completely filled with germanium. The I_{drain} vs V_{gate} characteristics are plotted. The transconductance $(\partial I_{drain}/\partial V_{gate})$ was measured to be $\approx 5 \times 10^{-11}$A/V, at $V_{source} = 10$ V. The inset shows the pinch-off behavior of the device at $V_{gate} \approx -100$ V, at $V_{source} = 10$ V. The on-off operation ratio of the FET is $> 10^4$.

By interpolating the linear slope of $\partial I_{drain}/\partial V_{gate}$ for a given V_{source}, the majority carrier mobility may also be estimated from the three-terminal data, depending on the sample capacitance and the length of the gate contact according to the equation [178, 179]

$$\frac{\partial I_{drain}}{\partial V_{gate}} = \mu \cdot \left(\frac{C}{L^2}\right) V_{source} \tag{4.10}$$

The silica dielectric cladding used in equation (4.9) to calculate the capacitance for the germanium sample was 94 μm in diameter and 1.5 mm long, resulting in a capacitance per unit length of $\sim 6 \times \mathbf{1}0^{-11}\mathrm{Fm}^{-1}$. Using equation (4.10), the calculated device mobility is 1.05 cm^2/Vs at room temperature, as compared with typical room temperature electron mobilities of 100 cm^2/Vs in bulk polycrystalline germanium devices [180]. As mobility is defined as the velocity with which charge carriers move under the application of an electric field, the low mobility measured in our samples clearly reflects the fact that charge transport occurs with high scattering of carriers at impurity sites, grain boundaries and lattice dislocations.

By considering the gate voltage at which "pinch-off", and hence depletion of the material occurs, it was possible to estimate the carrier concentration in these n-type Ge-fibre FETs. The electron carrier density was estimated from the total charge $Q_{tot} = CV_{pinch-off}$ required to deplete the FET. The concentration of free carriers may be calculated by using the following equation [178, 181]

$$n = \frac{CV_{pinch-off}}{e \cdot L\pi r^2}\,, \tag{4.11}$$

where e is the electron charge. Considering that the "pinch-off" occurs at $V_{gate} \approx -100$ V, the free carrier concentration is calculated to be $n = 2.1 \times 10^{15}\,\mathrm{cm}^{-3}$ for this Ge-fibre FET.

4.2.2 Electrical Properties of Silicon Fibres

A 5 μm silicon filled fibre capillary, with cladding thickness of 125 μm and sample length of 18 mm was electrically characterised. The capillary hole was partially filled with silicon, forming a smooth silicon tube with a filling fraction of $\sim 50\%$, as illustrated in Figure 4.26. Figure 4.27 shows a set of typical current vs source-drain voltage data obtained from a silicon-fibre FET at different gate voltages. The two-terminal $I_{drain} - V_{source}$ curves are all linear, thus indicating that the metal electrodes make ohmic contacts to the silicon tube. The gate-dependence of the $I_{drain} - V_{source}$ curves again indicate that the majority of the carriers are again n-type, with a sample resistivity of 0.21 Ωcm and

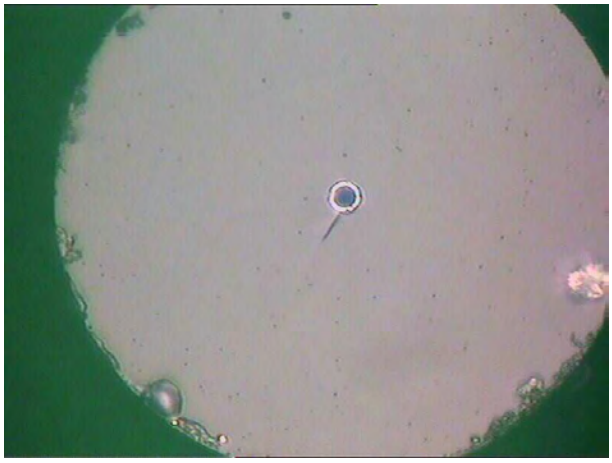

FIGURE 4.26: Cross-sectional view of the silicon fibre used in electrical measurements, the sample is 18 mm long. The silicon tube covers ≈ 50% of the 5 μm capillary hole area.

a carrier mobility of $1.4 \times \mathbf{10}^{-2}\,\mathrm{cm}^2/\mathrm{Vs}$ (bulk crystalline silicon is usually of the order of $10^2 - 10^3\,\mathrm{cm}^2/\mathrm{Vs}$ and amorphous silicon $\sim 1\,\mathrm{cm}^2/\mathrm{Vs}$). By extrapolation of the effect of V_{gate} on the transconductance, the $V_{pinch-off}$ was estimated to be at around -320 V in this case, giving a free-carrier concentration of $6.6 \times 10^{15}\,\mathrm{cm}^{-3}$.

The mobility of the silicon samples is found to be insensitive to temperature (inset Figure 4.27), indicating the predominance of extrinsic scattering mechanisms, such as grain boundaries and surface and charge traps, as is typically characteristic of polycrystalline semiconductors [182, 183]. In the inset of Figure 4.27, the conductivity versus temperature data for a polycrystalline-Si sample is shown to satisfactorily fit a function of the form

$$\sigma(T) = \frac{A}{T^{1/2}} \exp\left(-\frac{\varepsilon}{kT}\right) , \tag{4.12}$$

where σ is the conductivity, A is a semi-empirical constant, ε is an activation energy of the grain-barrier potential and k is Boltzmann's constant. This is an expression which has previously been derived for the variation of conductivity with temperature in the regime of grain-boundary limited transport [184]. While there is no exact information about the dopant concentrations in the n-type silicon sample, the value obtained for the barrier activation energy ($\varepsilon = 3.3\,\mathrm{meV}$) is broadly consistent with the range expected in heavily doped polycrystalline Si [184], but is also heavily compensated due to the trapping state density, in agreement with the relatively low free carrier concentration of $6.6 \times 10^{15}\,\mathrm{cm}^{-3}$ derived from the FET experiments.

For the germanium wires, TEM and Raman measurements show that the material is microcrystalline with grains of the order of 500 μm in diameter, and a crystalline fraction

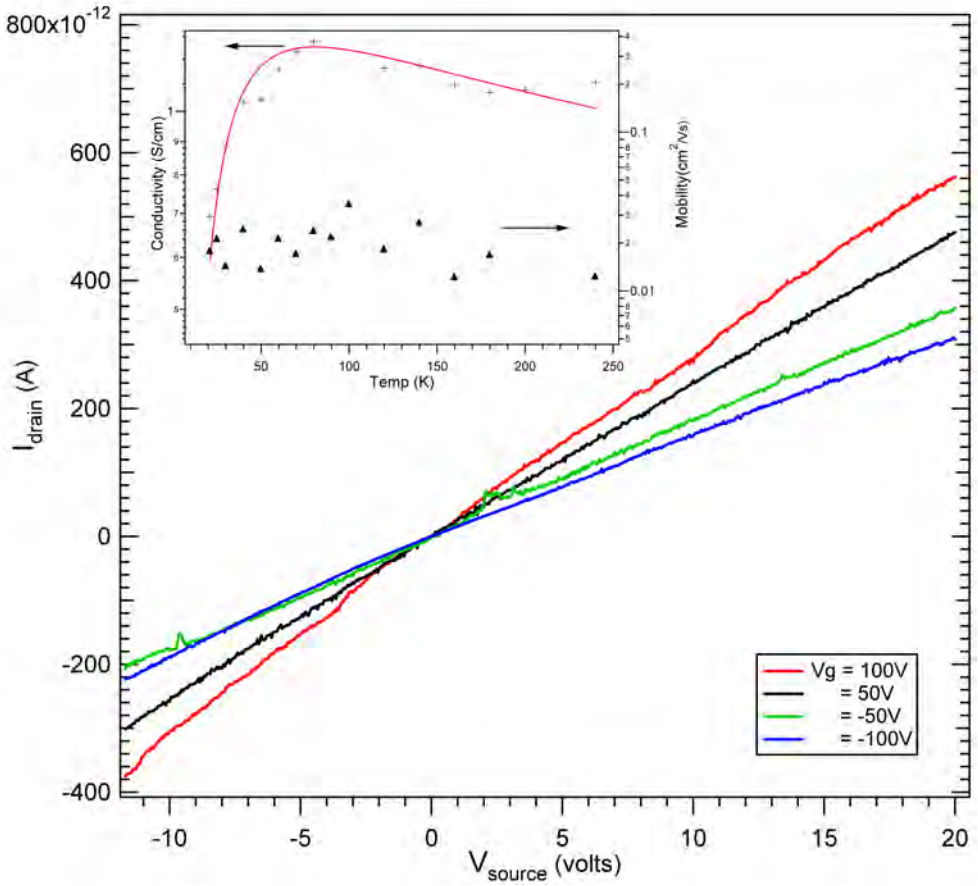

FIGURE 4.27: Three-terminal electrical measurement on a 18 mm length of a 5 μm Si-filled capillary. The I_{drain} vs V_{source} characteristics are plotted for different V_{gate} values. The transconductance ($\partial I_{drain}/\partial V_{gate}$) was determined as being $\approx 1 \times 10^{-12}$A/V, with $V_{source} = 20$ V. The inset shows how the conductivity (+) and mobility (▲) values of such a fibre change as a function of temperature. The conductivity data is also fitted by a technique of least squares to equation (4.12) (red line through the data). This approximation yields a value of 3.3 meV for the grain-barrier activation energy (ε).

$\chi_c \approx 100\%$. The electrical properties reflect the high quality of the polycrystalline semiconductor. In contrast, for the silicon wires deposited at 750 °C, the Raman data indicates a crystallinity of $\chi_c \sim 87\%$. TEM data indicate the presence of a distribution of grain sizes, including nanocrystalline and amorphous materials. Thus, the silicon wires exhibit a mobility about three orders of magnitude less than typical for device quality polycrystalline silicon [185]. However, the germanium wires have a mobility only about two orders of magnitude less than polycrystalline germanium. This one order of magnitude difference in the ratio sample/reference between the materials can be attributed to the differences in the grain structure between silicon and germanium, which can be annealed for grain growth at significantly lower temperatures than for silicon. The present results indicate that reducing the magnitude of the grain-boundary scattering within semiconductor tubes encased in optical fibres is key to further improvements

in electronic transport properties. Annealing of silicon wires at higher temperatures and optimization of the time-temperature ramps used for such annealing, as well as the amount of strain, should allow for a reduction of the amount of amorphous and nanocrystalline silicon along with giving an enhanced grain growth and thus fewer grain boundaries. The Raman signal of silicon wires, annealed at 1450 °C, indicates that $\chi_c \approx$ 100% and that no amorphous material was detected, therefore the electrical properties of wires annealed at this temperature are expected to be higher than those shown by the silicon samples presented in this section. Future experiments will be focused on the electrical characterisation of silicon in-fibre wire/tubes annealed at 1450°C.

Finally, it is worth mentioning that this is the first time that operation of FETs or any other electronic device has been demonstrated within optical fibres filled with crystalline semiconductors. This suggest that the high pressure CVD technique provides an attractive platform for the development of a wide array of next generation, fibre-based optoelectronics.

4.3 Optical Characterisation of Silicon MOFs

During the last decades, silicon photonics has created great interest with research groups all over the world. The high transparency and high nonlinearity of silicon at communications wavelengths, combined with the well-developed silicon top-down processing techniques, renders, silicon as an excellent material for photonic device miniaturization and the future generation of optoelectronic integrated circuits.

Silicon-on-insulator (SOI) waveguides consists of a single crystal silicon layer separated from the silicon substrate by SiO_2. The silica layer provides the low index cladding and light is confined to travel in the high refractive index silicon layer. SOI compared with other integrated optics platforms provides tight optical confinement, due to the large refractive index of silicon which minimizes radiation leakage into the silica substrate. SOI has become as promising platform material and has led to several reports of integrated waveguides [186, 187, 188], beam splitters, add-drop filter, attenuators [189]. Although passive devices with high performance have been fabricated in SOI, adding optical functionality to a silicon chip is one of the most challenging problems of materials research. Silicon is a centro-symmetric material and so second order nonlinear effects in silicon are negligible. Consequently, the need for active devices, such as modulators and switches, has motivated researchers to explore other mechanisms to induce refractive index change in silicon [98]. In the last few years thermo-optic effects [190] and free carrier injection have been used to demonstrate high performance modulators and switches [191, 192, 193]. Recently, strain on silicon planar waveguides was used to break

the crystal symmetry so that significant electro-optic effect could be induced [175] and an optical modulator was demonstrated.

In addition, a major limitation of this material for optoelectronic applications is that silicon is an indirect bandgap semiconductor, which makes it an inefficient emitter of light. Many different effects have been investigated to overcome this limitation and, only recently, stimulated Raman scattering has emerged as the most promising mechanism for achieving in-chip lasing from silicon [194, 195, 196]. Both devices, silicon modulators and lasers, have opened up new promising opportunities for silicon photonics.

Although single crystal silicon has lower optical loss ($\sim 1\,\mathrm{dB/cm}$) and better electrical properties than polycrystalline and amorphous silicon, these phases can be useful for certain devices. The main reason for this is their ease of deposition which allows flexibility in the design and multilevels of interconnection. They also offer the possibility of a wider range of cladding and core thicknesses on a variety of substrates and cheaper processing cost as compared to single crystal devices. In 1996, Agarwal *et al.* [197] reported on the fabrication of a poly-Si waveguide with optical loss of $16\,\mathrm{dB/cm}$. Later on, by improving the surface morphology and decreasing bulk absorption, the same research group reported a further reduction in the bulk loss of poly-Si material to $9\,\mathrm{dB/cm}$ [198]. More recently, the Intel silicon photonics group reported on the fabrication of a fast all-silicon optical modulator in which the active material was poly-Si [192]. The $6.7\,\mathrm{dB}$ on-chip loss of their device was mainly attributed to the doped poly-silicon phase shifter and undoped poly-Si waveguide.

4.3.1 Silicon Optical Fibres

The impregnation of poly-silicon within MOFs voids offers new possibilities with silicon photonics. Devices such as in-fibre silicon modulators, short fibre Raman lasers and optical switches may be envisaged.

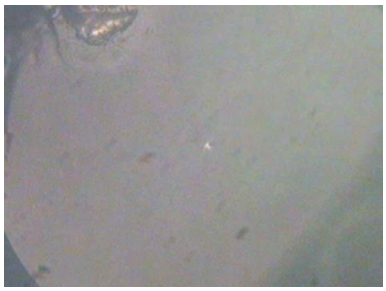

FIGURE 4.28: Microscope image of a $2\,\mu\mathrm{m}$ capillary fibre filled with silicon. This fibre was used in optical experiments. The cladding diameter is $125\,\mu\mathrm{m}$.

For optical transmission experiments, silicon was deposited by means of the HP-CVD process at 750 °C into a 2 μm silica capillary (Figure 4.28). SEM micrographs revealed that a $\sim$ 600 nm thick silicon layer was formed inside the 2 μm diameter hole. This silicon tube was deposited within the capillary hole very evenly over a 7 cm length. With the aim of calculating the optical mode distribution, an approximation of the structure's refractive index profile was input to a computer programme (BeamProp®) which uses a beam propagation method (BPM) to solve Maxwell's equations. Figure 4.29 is the refractive index profile used to compute the optical modes.

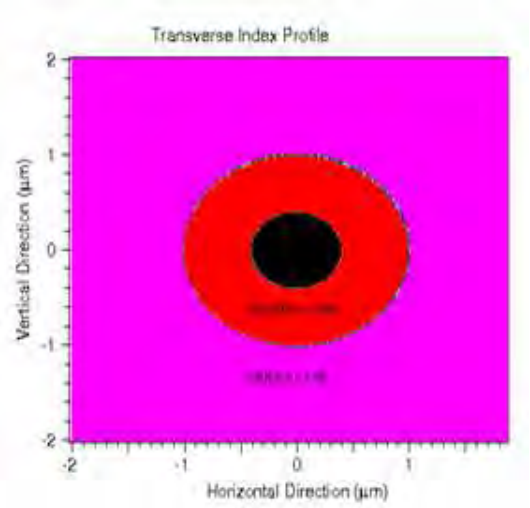

FIGURE 4.29: Transverse index profile of 2 μm diameter silicon-filled MOF used in optical experiments. The red ring is a 600 nm silicon tube $n_{Si} = 3.46$ at 1.55 μm. Silica is displayed with a pink colour with $n_{SiO_2} = 1.46$. The black region is air $n_{air} = 1$.

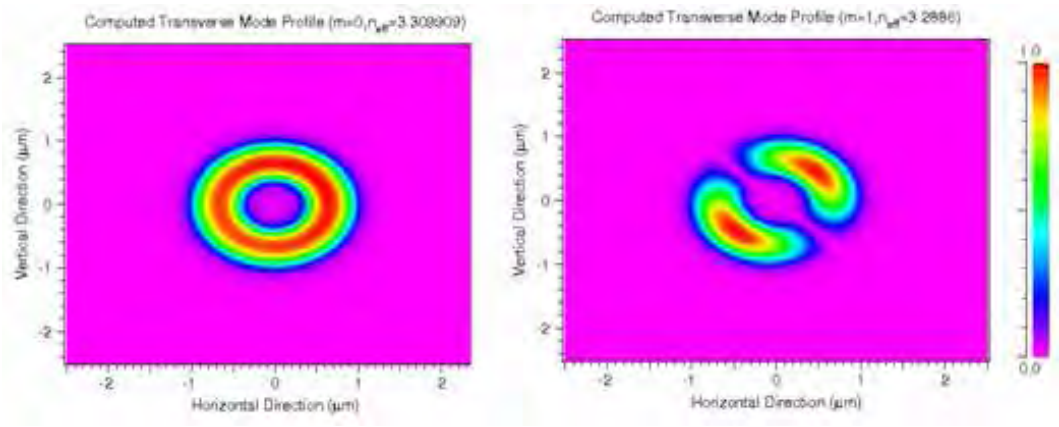

FIGURE 4.30: Energy distribution of the first two guided modes supported by the silicon fibre shown in Figure (4.29) as calculated by a full-vector imaginary distance BPM. The red colour represents high power concentration while the pink regions are low concentration. The effective refractive index of the modes is written at the top of each image.

Figure 4.30 shows the first two guided modes supported by the structure, as calculated with BPM. The simulations indicate that this fibre is highly multimode and 15 degenerate modes are allowed to propagate in the silicon core. In contrast to conventional silica fibres, in this fibre the electromagnetic fields are tightly concentrated in the small silicon ring, as expected for the high refractive index contrast between silicon and silica $\Delta n \approx 2$.

A high power continuous wave (CW) laser diode was used to launch up to 100 mW of $\lambda = 1.55\,\mu$m radiation into the fibre core. A 0.65 numerical aperture (NA) 3.1 mm focal length IR aspheric lens was used to focus the beam waist onto the core. The fibre alignment was controlled using xyz nanometer precision stages with piezo-electric actuators. The coupled light was guided by a 5 cm silicon fibre whose end faces were mechanically cleaved. The output near-field was collimated with a 40× objective and focused onto a Electrophysics IR vidicon camera, in order to image the mode profile. For transmission measurements the output power was collected by a germanium photodiode attached to a Newport 2832C power meter and compared to the input power which was monitored simultaneously.

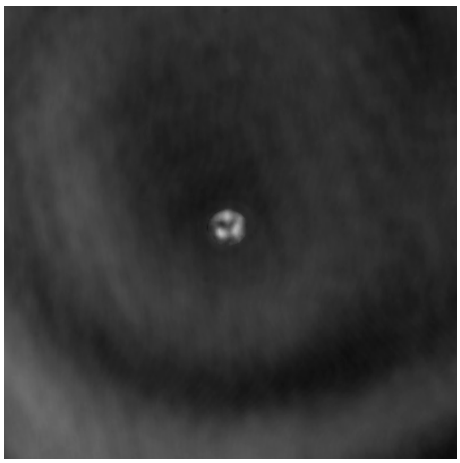

FIGURE 4.31: Near field image of the transmitted light through the 2 μm silicon MOF.

Due to the short fibre length and small core dimensions, it was not possible to entirely decouple the light in the cladding from that transmitted in the core, even though index matching fluid was applied. Other problems encountered during optical characterisation experiments included the low coupling efficiency, caused by the high Fresnel reflection at the air-silicon interfaces (R $\approx$ 30%) and small core. Figure 4.31 is the near-field output of the transmitted mode, obtained with an IR camera. It can be appreciated that the laser radiation has been confined into the silicon core but a lot energy remains in the cladding. Although this experiment clearly indicated that light was guided by the silicon core, it was very convenient to remove the cladding light to do reliable loss measurement and to verify the structure's guiding properties. Approximately 2 mm of

the 125 μm diameter silica cladding was thus chemically etched away at one end of the fibre to allow its optical characteristics to be decoupled from those of the 2 μm diameter silicon core. The etched silicon core was imaged perpendicular to the fibre axis using a IR or visible camera attached to a stereo microscope. A 633 nm laser light launched into the other unetched input-face of the composite fibre did not propagate beyond the cladding region. No light is seen in the etched silicon core (Figure 4.32a and Figure 4.32b) because silicon absorbs strongly at visible wavelengths. However, for near infrared light at energies below the silicon bandgap (1.07 eV), the core is transparent. Therefore, 1.55 μm radiation launched into the core propagated all the way down to the fibre's end (see Figure 4.32c). By measuring the output power waveguided through the isolated silicon core, (for 100 mW launch an output of 0.03 mW was observed) an upper bound of ~ 7 dB/cm was placed on the loss limit, comparing favorably to losses of 4 to 9 dB/cm reported, thus far, for optimized planar polycrystalline silicon waveguides [198, 192].

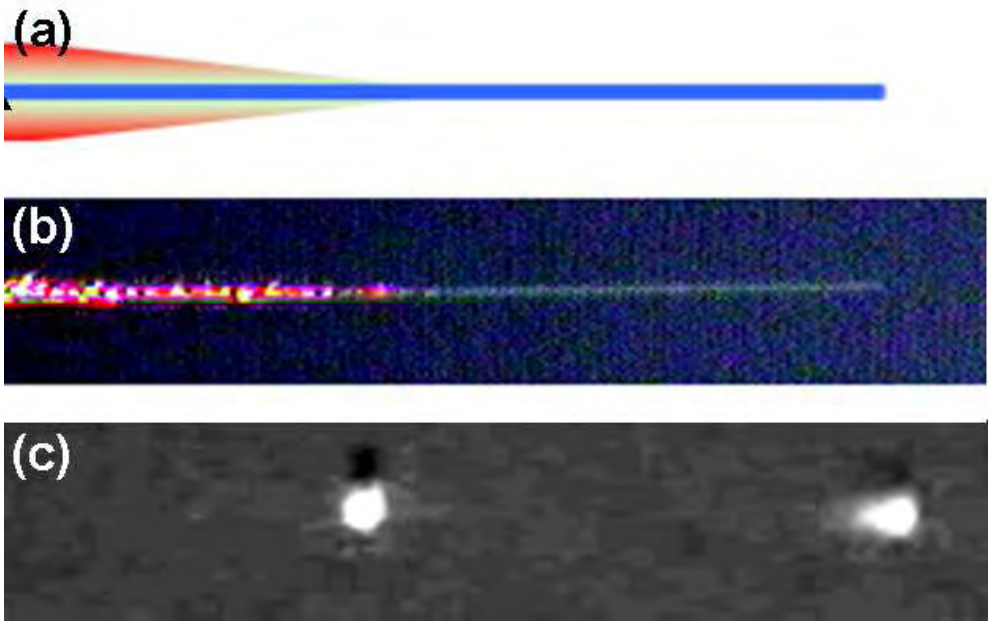

FIGURE 4.32: Schematic of light guiding experiment. (a) The end of a filled fibre is etched to completely expose 2 mm of the central silicon core (blue) and taper a portion of the silica cladding (red). (b) 633 nm light is guided in the tapered silica cladding but not in the exposed silicon. (c) 1.55 μm light propagating through the same etched fibre. The light is scattered at the end of the silica cladding but continues to propagate the full length of the silicon core.

The optical loss in semiconductor devices is a strong function of the surface roughness [199], which can limit the performance of lithographically defined rectilinear silicon waveguides because they have an exposed upper surface. However, as material deposits inside a MOF, the area of the exposed growth surface decreases linearly with the inner diameter and becomes zero in the limit of a fully filled pore. In addition, the outer surface of the fibre integrated semiconductor waveguide is defined by the extremely smooth

silica surface of the MOF pore (0.1 nm root mean square roughness [200]). Therefore, boundary scattering from both inner and outer surfaces is minimized. It is expected that the main mechanisms of optical losses in poly-Si filled fibres are the scattering and absorption within the crystals and crystal boundaries and improvement of the crystal quality will improve the optical properties of the fibres. Currently, optical characterisation of annealed silicon samples has revealed lower optical loss than that measured for 750°C silicon fibres. The guiding properties of optimized silicon fibres, will allow us to exploit the high nonlinearity of silicon, $10^3 - 10^4$ times larger than that of silica [194, 201, 202], to create very short and efficient nonlinear fibre devices, such as IR supercontinuum sources, signal regenerators, Raman fibre lasers, optical frequency converters, etc.

Although, up to now, silicon fibres have been the focus of most our optical investigations owing to their compatibility with the 1.5 μm communication wavelength band, currently, the optical properties of germanium fibres are under investigation.

Finally, the propagation of visible light in etched semiconductor fibres results in nice visual effects, like Figure 4.33 which shows a photograph of a germanium MOF illuminated with blue light. Approximately 2 mm length of silica cladding of a honeycomb fibre filled with germanium was etched away. Then blue light from an argon ion laser was focused onto the unetched end of the fibre. The laser radiation is guided in the silica cladding and light propagation is immediately stopped in the etched region where a bundle of germanium wires protrudes.

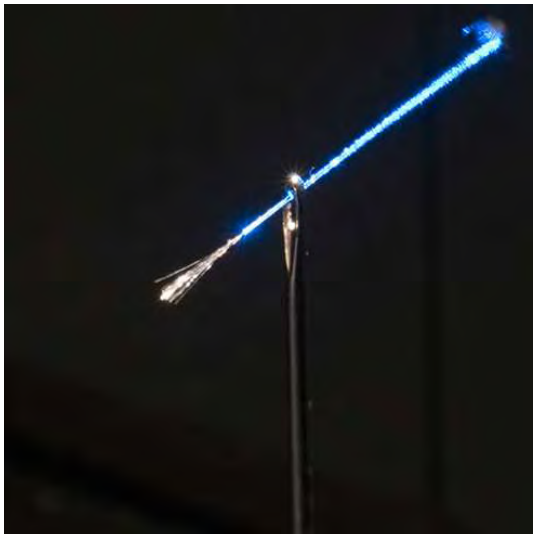

FIGURE 4.33: A germanium-broom: Bundle of 2 μm diameter germanium wires emanating from a honeycomb MOF. Visible light propagation is prohibited in germanium due to its high absorption at these wavelengths [17], photograph by Neil Baril.

4.3.2 In-Fibre Silicon Modulator

As was mentioned before, i.e. the free carrier plasma dispersion effect, the change of refractive index and absorption caused by the concentration variation of free carriers has been used widely in planar silicon modulators and active devices. As a proof of principle, Don-Jin Won a member of the group in PSU has carried out light modulation experiments on amorphous silicon-filled MOFs. Although, the author of this thesis has not directly participated in these experiments the first optical measurements of these fibres were done in Southampton and have been the basis for future experiments.

Despite the fact that amorphous silicon contains more point defects than crystalline silicon and the optical absorption in amorphous silicon can be substantial, these point defects can be passivated to some extent by the incorporation of hydrogen. Hydrogenated a:Si has shown good electrical properties and low optical absorption [203]. Hydrogenated amorphous silicon wires were fabricated inside a 6 μm diameter silica capillary by the HP-CVD method, using 5% silane diluted in the mixture of 10% hydrogen and 85% helium at a total gas pressure of 38 MPa. The MOFs were then heated at 480 °C in a tube furnace to induce thermal decomposition of silane, while the gas precursor flowed through the fibre. The initial hole was completely filled with hydrogenated amorphous silicon over several centimetres of length [204].

The change of refractive index and absorption caused by the concentration variation of free carriers in semiconductors may be used to modulate the intensity of guided light in the silicon core. The density change of carriers modifies the transmission loss due to free carrier absorption [98]. This effect can be induced by either carrier-injection with p-n junctions [205, 192] or photo excitation by light [206]. The a:Si fibre was used as an all-optical modulator of guided 1.55 μm laser radiation using the free-carrier plasma-dispersion effect generated by a 514 nm pump laser in the silicon core [204]. The schematic diagram of the optical in-fibre modulator is shown in Figure 4.34. In the experiments 20 mW of CW laser radiation at 1.55 μm is coupled into the core using free space optics. The transmitted light is focused into a collection fibre which is connected to an ultrafast photodetector. Nanosecond pulses from a Nd:YAG laser are doubled in frequency to generate 532 nm pulses of $\sim$ 17.5 ns at 10 Hz repetition rate. In order to excite electron and hole pairs into the extended states of a:Si, the pump pulses are laterally focused onto the silicon core using a cylindrical lens [204].

When free carriers are generated the refractive index and the loss of the silicon core increases. The change in the amplitude of the detected signal allows us to identify the intensity modulation depth M which reflects the optical bistability, defined by

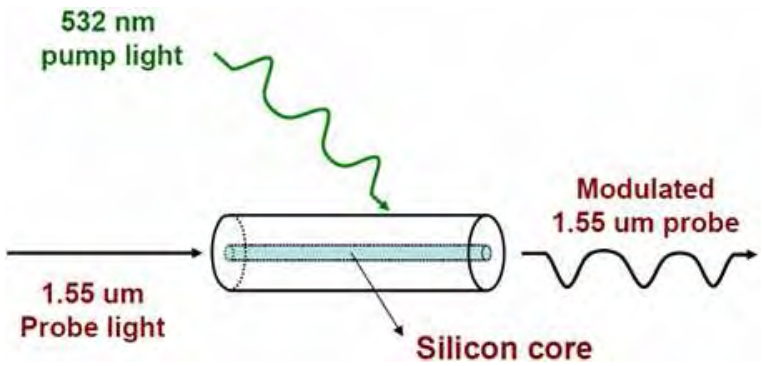

FIGURE 4.34: Schematic diagram of an all-optical in-fibre light modulator. The probe signal at 1.55 μm is guided by the fibre's a:Si core. The pump pulses excite free carriers that change the optical properties of the silicon core, and modulate the amplitude of the probe signal (from reference [204])

$$M = \frac{I_{max} - I_{min}}{I_{max}} \ , \tag{4.13}$$

where I_{min} and I_{max} are the power of the probe signal during photoexcitation and ground states, respectively. For pulses of 65 μJ the M value was measured to be as high as 85%. This prototype a:Si MOF modulator is a major step towards high-speed in-fibre devices. With the successful synthesis of devices like this one, based on semiconductor fibres, the opportunities of replacing planar optoelectronics with more compatible in-fibre semiconductor devices will enter a new era.

Chapter 5

Optical Properties of Metal Nanoparticles

The previous chapter has described the characterisation of semiconductor-modified microstructured optical fibres. SEM, TEM and micro-Raman analysis was used to study the material properties of these fibres. Silicon and germanium in-fibre wires were configured as FET to determine the material conductivity and carrier mobility. Finally, semiconductor-fibres were used as IR optical waveguides and by the photo-excitation of free carriers light modulation was achieved. This chapter is an introduction to the field of plasmonics and provides a theoretical background to Chapter 6 which describes Surface-Enhanced Raman Scattering, and to Chapter 7 where the optical and SERS characterisation of metal-modified microstructured optical fibres is presented.

5.1 Introduction

Metals have played an important role in the development of modern civilisation and have formed the subject of one of the most ancient themes of scientific research. Nowadays, they are the main materials used for guiding electromagnetic radiation at microwave frequencies but, due to their high conductivity in the optical regime, they show strong absorption in the visible and infrared wavelengths which has limited their extension as optical waveguides. However, the optical properties of metals change when their structural dimensions are smaller than the wavelength of light. Nanoscale metallic structures have led to an exponentially increasing number of applications in the context of emerging plasmonics and nanosciences.

Evidence suggest that colloidal metals may have appeared as early as 5^{th} century B.C. in Egypt, and since then they have fascinated people and especially scientists because of their intense and brilliant colours. One of the most famous examples of exploiting the optical properties of metal nanoparticles in ancient times is the Lycurgus Cup, that was manufactured by the Romans. The cup is ruby in transmitted light but green in reflected light due to the presence of silver and gold nanoparticles (see Figure 5.1). During the Middle Ages, gold and silver nanoparticles were again used as a pigment of stained glass windows in Medieval churches.

The interest in understanding the optical properties of metal nanoparticles dates back to Faraday's experiments [207]. In these experiments, Faraday noticed the remarkable dependence of the colour of gold nanoparticles on their size. Also he observed reversible colour changes of thin films prepared from dried colloidal solutions of gold upon mechanical compression.

FIGURE 5.1: Lycurgus glass cup, demonstrating the bright red and green colours, in transmitted and reflected light of gold nanoparticles. Inset: scanning electron microscopy (SEM) image of a characteristic nanocrystal embedded in the cup's glass, from the British Museum website [208].

The optical characteristics of colloidal gold and silver are due to the interaction between the conduction electrons and light. When light interacts with conduction electrons that are confined in a very small volume they can perform a collective oscillation with respect to the positive-ion nuclei, creating a negative charge distribution at the surface. This electron oscillation is therefore called a surface plasmon. The excitation of surface plasmon resonances is what produces a very selective absorption and strong scattering of light.

In order to tailor the next generation of micro/nano metallo-dielectric devices and materials, novel ways to organize the nanoparticles into controlled architectures must be found. This chapter will explore the optical properties of metals and focus on a method

to organize nanoparticles in microstructured optical fibres to exploit their plasmonic properties.

5.2 Classical Optics of Metals

The propagation of electromagnetic waves in a metal may be described by considering a metal as a homogeneous isotropic medium having a high conductivity (σ). With these considerations Maxwell's equations can be written as follows

$$\nabla \times \vec{E} = -\mu \frac{\partial \vec{H}}{\partial t}\,, \tag{5.1a}$$

$$\nabla \times \vec{H} = \varepsilon_m \frac{\partial \vec{E}}{\partial t} + \sigma \vec{E}\,, \tag{5.1b}$$

$$\nabla \cdot \vec{H} = 0\,, \tag{5.1c}$$

$$\nabla \cdot \vec{E} = 0\,. \tag{5.1d}$$

Equation (5.1d) represents the fact that free charges are absent in the interior of an homogeneous metal. This can be easily demonstrated by taking the divergence of equation (5.1b), which then takes the form

$$\varepsilon \nabla \cdot \frac{\partial \vec{E}}{\partial t} + \sigma \nabla \cdot \vec{E} = 0\,. \tag{5.2}$$

Substituting $\nabla \cdot \vec{E} = \rho$ in the previous equation,

$$\frac{\partial \rho}{\partial t} + \frac{\sigma}{\varepsilon}\rho = 0\ . \tag{5.3}$$

Solving this equation by integration yields,

$$\rho = \rho_0 \exp(-t/\tau)\ , \tag{5.4}$$

where $\tau = (\varepsilon_m/\sigma)$. Thus the charge density ρ in a medium is seen to fall exponentially with time. The relaxation time $\tau \simeq 10^{-18}\,\mathrm{s}$ is exceedingly small for metals that have an appreciable conductivity. In addition, this time is much shorter than the period of an optical wave and so an electrostatic equilibrium is established faster than a variation of the field. Consequently, for a highly conductive medium it is appropriate to say that $\rho = 0$ [209, 210] and, thus, $\nabla \cdot \vec{E} = 0$.

The system of equations (5.1) determines the propagation of electromagnetic waves in a conducting material. To explore the propagation of electromagnetic waves, again, one can introduce an electric field of the form $\vec{E} = \vec{E}_0 \exp i(\vec{k} \cdot \hat{z} - \omega t)$. This represents a monochromatic plane wave and is a solution of the following wave equation,

$$\nabla^2 \vec{E} = \mu \left(\varepsilon + i \frac{\sigma}{\omega} \right) \frac{\partial^2 \vec{E}}{\partial t^2} \,. \tag{5.5}$$

If a complex dielectric function is defined as $\varepsilon' = \varepsilon_m + i(\sigma/\omega) = \varepsilon_1 + i\varepsilon_2$, the equation above can easily be reduced to the wave equation of a transparent material

$$\nabla^2 \vec{E} + k^2 \vec{E} = 0 \,, \tag{5.6}$$

where $k^2 = \omega^2 \mu \varepsilon' = \omega^2 \mu \left(\varepsilon + i \frac{\sigma}{\omega} \right)$. Likewise, a complex refractive index may be defined as, $n' = \sqrt{\varepsilon'/\varepsilon_0} = \sqrt{\epsilon_1 + i\epsilon_2}$, $n' = n + i\kappa$,

$$n = \sqrt{\frac{\sqrt{\epsilon_1^2 + \epsilon_2^2} + \epsilon_1}{2}} \quad \text{and} \quad \kappa = \sqrt{\frac{\sqrt{\epsilon_1^2 + \epsilon_2^2} - \epsilon_1}{2}} \quad , \tag{5.7}$$

where n is the refractive index and κ is the absorption coefficient. The wavevector k can now be written as $k = (\omega/c)(n + j\kappa)$ so that the electric field becomes

$$\vec{E} = \vec{E}_0 \; e^{i\omega\left(\frac{zn}{c} - t\right)} e^{-z\omega\left(\frac{\kappa}{c}\right)} \,. \tag{5.8}$$

So far in this and in the previous chapters, the dielectric properties of a matter have been considered as constants but, in practice, matter cannot respond immediately to an excitation field. The optical response of a material results from its interaction with the electromagnetic wave within some characteristic time. This temporal response leads to a time dependence of the dielectric permittivity of materials, and therefore on the frequency (dispersion) of the incident electric field. In order to understand the dispersion of the medium it is necessary to carry out a microscopic analysis of the interaction between light and the atomic structure of the material. Fortunately, it is possible to make a simplified model of the atom by considering a fixed heavy particle (the nucleus) surrounded by light particles (electrons) which can move around the central nucleus. A convenient way of discussing the dispersion relations of metals is to divide their electronic structure in two classes, bound and free electrons.

5.3 Optical Response of Bound Electrons (Lorentz Model)

In a dielectric material the electrons are bound to the atomic nuclei by quasi-elastic forces and when an electromagnetic wave interacts with the bound electrons they oscillate and generate a periodic dipole moment. The Lorentz model describes the behavior of the electrons joined to the atomic nuclei by quasi-elastic forces. Movement of bound electron by an electromagnetic field of a linearly polarised wave is described by

$$m\frac{d^2r}{dt^2} + m\gamma\frac{dr}{dt} + Cr = -eE_0\exp^{(-i\omega t)}\,, \tag{5.9}$$

where e and m are the charge and mass of the electron, respectively. C is a spring constant describing restoring forces due to electrostatic attraction. Since the dielectric dipole moment of the system is dependent on the distance r between the nuclei and the vibrating electrons, the oscillating electrons will emit electromagnetic waves which carry energy away (scattering). Therefore, a damping constant, (γ), must be introduced into the motion equation to describe losses due to scattering and other dissipation mechanisms (e.g. because of collisions between the atoms). Solving the Lorentz equation 5.9 and considering the relations between the dielectric dipole moment ($\vec{p} = -e\vec{r}$), the polarisability of the medium ($\vec{P} = N_b\vec{p}$) and its dielectric properties, it can be shown that the permittivity of a dielectric follows the next relations

$$\epsilon_1 = 1 + \frac{\omega_p^2(\omega_0^2 - \omega^2)}{(\omega_0^2 - \omega^2)^2 + \gamma^2\omega^2} \quad \text{and} \quad \epsilon_2 = \frac{\omega_p^2\gamma\omega}{(\omega_0^2 - \omega^2)^2 + \gamma^2\omega^2}\,, \tag{5.10}$$

where $\omega_0 = \sqrt{\frac{C}{m}}$ is the natural frequency of the electron oscillations and $\omega_p = \sqrt{\frac{N_b e^2}{m\varepsilon_0}}$ is known as the plasma frequency and N_b is the density of bound electrons. The previous equations, know as Lorentz relations, describe the dispersion and absorption for bound electrons (Figure 5.2).

5.4 Optical Response of Free Electrons (Drude Model)

In the case of a perfect conductive medium the electrons are free to move between the molecules and are said to be free electrons. Metals are know as free-electron metals if most of their optical and electronic properties are due to their conduction electrons

[211]. The optical properties of metals can be explained by assuming the existence of an electron gas moving between the positive ions which form the crystal lattice of the metal and can be well described by the Drude model [212]. This model assumes a gas of independent electrons that can freely move with a common average relaxation time τ. The drift-motion of free electrons due to an external electric field $\vec{E} = \vec{E_0}\exp^{(-i\omega t)}$ can be obtained by solving the following equation

$$m\frac{d^2r}{dt^2} + m\gamma\frac{dr}{dt} = -eE_0\exp^{(-i\omega t)}\,, \tag{5.11}$$

where the coefficient $\gamma = 1/\tau$ is the electron relaxation rate which is a phenomenological damping coefficient that quantifies the dissipation of energy due to electron-photon interactions, collisions of the electron gas with the lattice ions, lattice defects and impurities.

The current density $J(\omega) = -N_f e\frac{dr}{dt}$ and the conductivity of a metal can be obtained by solving the equation (5.11),

$$J(\omega) = \frac{N_f e^2}{m}\frac{E(\omega)}{(\frac{1}{\tau} - i\omega)} \quad \text{and} \quad \sigma(\omega) = \frac{\sigma_0}{(1 - i\omega\tau)}\,, \tag{5.12}$$

where $\sigma_0 = \frac{N_f e^2 \tau}{m}$. Using the previous result in equation (5.5), the dielectric function $\epsilon(\omega) = \epsilon_1(\omega) + i\epsilon_2(\omega)$ of a system with N_f free electrons per unit volume, may be written as

$$\epsilon_1 = 1 - \frac{\omega_p^2}{\omega^2 + \gamma^2} \quad \text{and} \quad \epsilon_2 = \frac{\omega_p^2\gamma}{\omega(\omega^2 + \gamma^2)} \tag{5.13}$$

for highly conductive metals at visible frequencies, $\omega_{vis}^2 \gg \gamma^2$, the dielectric function can be approximated to

$$\epsilon_1 = 1 - \frac{\omega_p^2}{\omega^2} \quad \text{and} \quad \epsilon_2 = i\frac{\omega_p^2\gamma}{\omega^3} \tag{5.14}$$

where $\omega_p = \sqrt{\frac{N_f e^2}{m\varepsilon_0}}$ is the plasma frequency. Figure(5.2) shows the real and imaginary parts of the dielectric constants of a free-electron metal calculated with equation (5.14).

In Figure 5.2 one can identify three regions with different optical properties. First an absorbing region which extends from zero to $\omega \sim \gamma$, light in this window is highly absorbed. Secondly, a reflective region corresponding to a metallic reflection. At a certain frequency $\omega = \omega_p$, the dielectric function is equal to zero and the electron

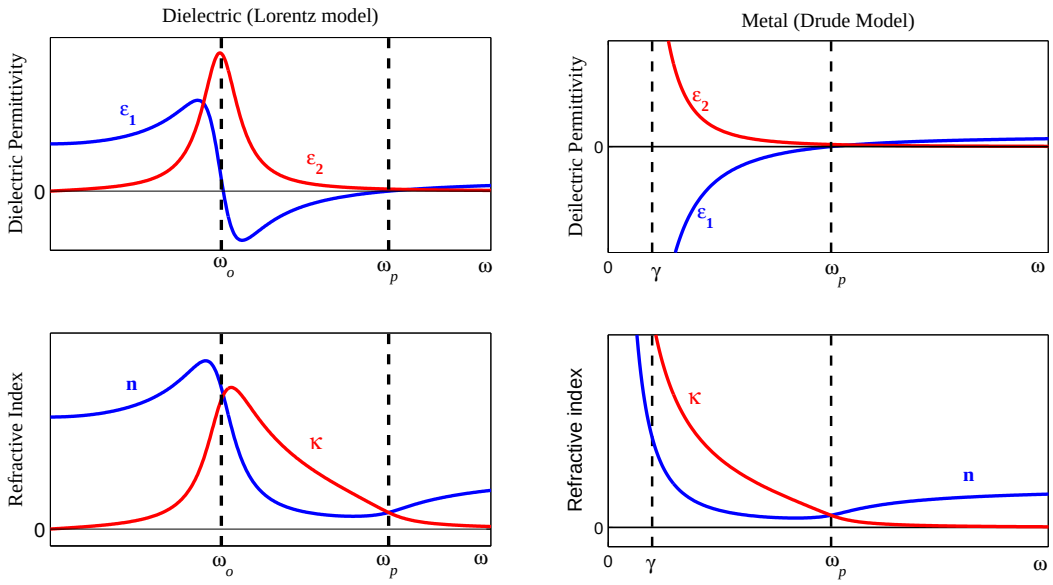

FIGURE 5.2: Plots of the dielectric function of a dielectric (left) and a free-electron metal (right) calculated using the Lorentz relations (5.10) and Drude relations (5.14), respectively. The complex refractive index was obtained using equation (5.7).

density fluctuation is longitudinal. At this frequency it is possible to consider all the oscillating electrons as a single entity known as a volume plasmon. For most metals the plasma frequency is in the UV, however, as will be described in the following sections, the plasmon frequency in a metal can be shifted to the visible range when the material is structured. The last frequency region $\omega > \omega_p$ corresponds to the transparent regime. Because the electrons cannot respond fast enough to screen the electric field for high frequencies, metals are transparent to light.

Some alkaline metals, like sodium, have nearly free-electron behavior and their optical properties are well described by Drude's model [213]. However, for metals like silver or gold the electrons in deeper levels contribute to their dielectric function and Drude's theory fails to accurately describe their properties, especially at visible frequencies.

5.5 Real Metals

Noble metal atoms like Cu, Ag or Au have completely filled 3d, 4d, and 5d shells and just one electron in the 4s, 5s, and 6s bands, respectively. The d-band electrons are very close to the Fermi level and interband transitions between occupied bands into conduction band can be excited by photons with energies corresponding to visible and

ultraviolet frequencies. At these frequencies, both the free electrons plus the interband transitions will contribute to the dielectric function [214].

For silver, the interband transitions do not occur until a threshold energy of $\sim 3.9\,\text{eV}$ [215]. For lower energies, silver shows nearly free electron optical properties and the Drude model closely matches its optical behavior. Whereas, for higher energies, where interband transitions are allowed, an analysis combining Lorentz and Drude's model with quantum theory must be considered in order to accurately describe its optical properties. Due to the difficulties in these calculations it has been more convenient to carry out reflection and absorption experiments to obtain the optical coefficients of noble metals [211, 215, 216]. The most commonly used data from literature are the tables by Johnson and Christy [216]. As an example, Figure 5.3 shows the real and imaginary part of the dielectric function of silver and gold as a function of photon energy.

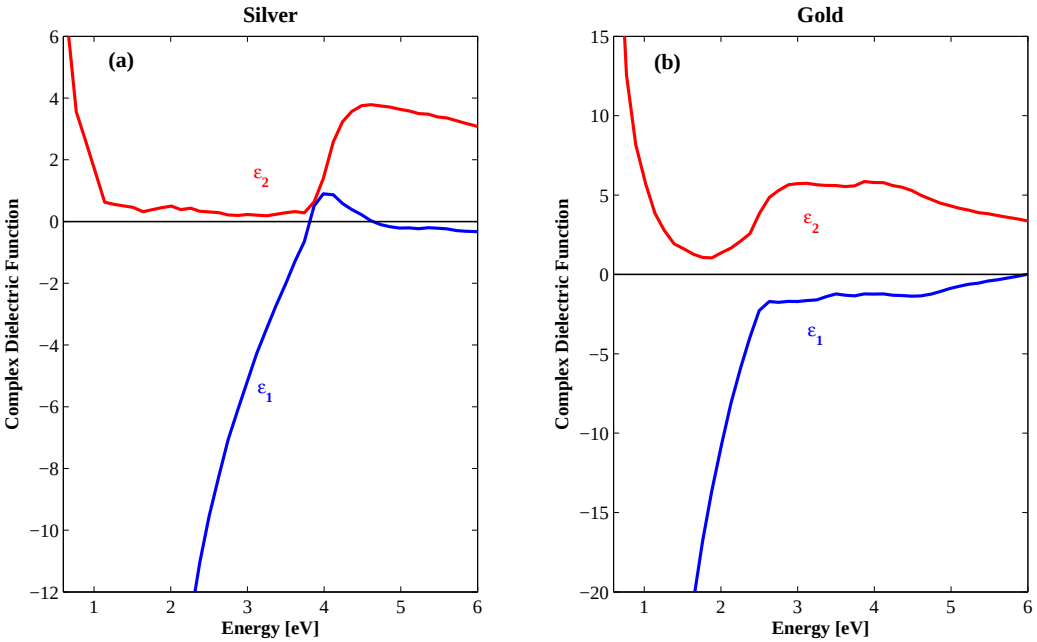

FIGURE 5.3: Spectral dependance of the dielectric constant for (a) silver and (b) gold. The data was obtained experimentally by absorption and reflection measurements. All the experimental values of the dielectric constants of the metals used in this work are taken from [216]

.

It can be seen from Figure 5.3 that for both metals ϵ_2 falls off rapidly in the free electron region and approaches a value close to zero before the interband transitions threshold, which are $\sim 3.9\,\text{eV}$ and $\sim 2.5\,\text{eV}$ for silver and gold, respectively. When using thin metal films to experimentally obtain the optical properties of the metals, scientists observed high absorptions at frequencies that were not present when studying the bulk material. These results attracted a lot of interest and led to the discovery of surface plasmons.

5.6 Surface Plasmons Polaritons

Ritchie [217] noticed that when the geometry of a conductive material is restricted by a boundary there exist a volume plasma oscillation at the frequency ω_p, and an additional charge density fluctuations may occur at other frequencies. These plasmons waves are strictly confined to the boundary and named thereafter as surface plasmons (SPs) [218]. SP waves can propagate along the interface, with a broad spectrum of frequencies from $\omega = 0$ up to $\omega = \omega_p/\sqrt{2}$ (assuming perfect free electron metal behavior and metal/air interface), making an important extension of plasmon physics.

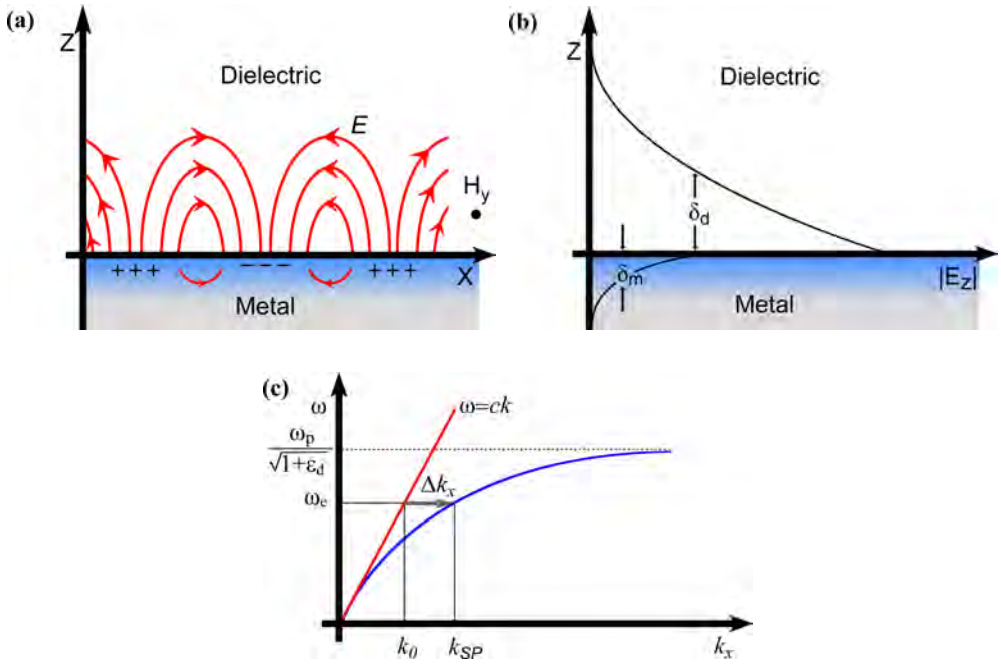

FIGURE 5.4: SPPs on a metal-dielectric interface. (a) Schematic diagram of the charge and electric field distributions at the interface. (b) The intensity of the electric field which reaches its maximum at the surface and decays exponentially with distance away from it. (c) Curves showing the dispersion relation of SPPs (plotted in blue), given by the real part of equation (5.15) and the dispersion relation of light propagating in the dielectric medium (red curve). The blue line is always lying below the light line indicating the non radiative nature of SPP modes. The grey arrow shows the momentum mismatch, Δk_x, between the two waves at a certain excitation frequency ω_e.

As the variation in charge density near the surface acts like dipoles that generate electromagnetic waves, SPs consist of combined surface electromagnetic and charge density waves (Figure 5.4a). SPs are usually called surface plasmon polaritions (SPPs) to reflect their hybrid nature of oscillating electrons along conductor/dielectric boundaries linked with electromagnetic waves. The electric field accompanying the plasma oscillation is normal to the surface and its intensity decays exponentially in the direction perpendicular to it, with a maximum in the surface, see Figure 5.4b. Solving Maxwell's equations for

electromagnetic waves with frequency ω, propagating along a metal/dielectric interface, shows that only TM modes can exist and yields the dispersion relation

$$k'_{SP} = k_0 \sqrt{\frac{\epsilon_d \epsilon'_m}{\epsilon_d + \epsilon'_m}}\,, \tag{5.15}$$

where $k'_{SP} = k_{SP1} + ik_{SP2}$ is the complex propagation constant of the SPPs in the direction parallel to the interface, ϵ'_m and ϵ_d are the frequency-dependent permittivity of the metal and the dielectric material respectively. The real and imaginary part of k'_{SP} are

$$k_{SP1} = k_0 \sqrt{\frac{\epsilon_d \epsilon_{m1}}{\epsilon_d + \epsilon_{m1}}} \quad \text{and} \quad k_{SP2} = k_0 \left(\frac{\epsilon_d \epsilon_{m1}}{\epsilon_d + \epsilon_{m1}} \right)^{3/2} \frac{\epsilon_{m2}}{2\epsilon_{m1}^2}\,. \tag{5.16}$$

The dispersion relation of SPP, plotted in Figure 5.4c, shows that their momentum $\hbar k_{SP1}$ is greater than that of a free-space photon of the same frequency $\hbar k_0$. This increase in momentum is linked with the binding of the electromagnetic wave to the surface and describes the non-radiative nature of SPP.

In contrast to the propagating nature of the SPP along the surface, the electric field E_z decays exponentially into both media, preventing energy propagation away from the surface. In the dielectric medium its decay length is of the order of half the wavelength of light, whereas the penetration distance into the metal is determined by the skin depth. Figure 5.4c, shows that for low frequency plasmons their properties closely match those of an electromagnetic wave indicating that the field concentrates most of its energy in the dielectric medium. Additionally, this figure shows a resonant effect when the plasmon frequency approaches $\omega_p/\sqrt{1+\epsilon_d}$. Near the resonance, large wavevector SPPs exhibit a greater concentration of the field at the interface. Their energy becomes independent of the wavevector and their properties closely resemble those of a volume plasmon.

When light is incident upon a planar metal surface, it cannot be directly transformed into SPP since the wavevector parallel to the surface of the SPP is greater than that of the incident radiation. If light is to be converted into SPP, at a certain photon frequency ω, its wave vector $\hbar k_0$ has to be increased by a value of Δk_x, as illustrated in Figure 5.4c. There are three main techniques by which the missing momentum can be provided. The first one makes use of periodic dielectric structures, with period Λ. In this configuration the light wavevector is increased by integer values of the lattice vector $G = 2\pi/\Lambda$. The periodic media couples light waves for which $\Delta k_x = m\vec{G}$ and strong coupling between the incident light and the SPP may occur when the wave vector condition $k_{sp1} = k_{||air} \pm mG = k_0 \sin\theta \pm mG$ is satisfied (see Figure 5.5a). This technique has been an important means for the study of SPPs [219, 220, 221, 222, 223].

The coupling principle of the second technique is similar to the grating method but involves the scattering of light from a small defect on the surface. The spatial Fourier transform of the defect contains a significant contribution of Δk_{dot} with values up to $2\pi/l$, where l is the size of the defect. If Δk_x is within this range, the defect effectively couples incident radiation into SPP. Strong coupling is observed when the condition $k_{SP1} = k_{||air} \pm \Delta k_{dot}$ [224, 225, 226] is satisfied.

Finally, the prism coupling technique enhances the momentum of the incident light by excitation through a high index medium. Light is totally internally reflected off a high refractive index prism which is either in touch with a thin metal layer, Kretschmann-Rather geometry (Figure 5.5b), or in close proximity to a metal surface, Otto geometry (Figure 5.5c). In the total internal reflection region, the evanescent light wave propagating along the prism base, with increased momentum k_{glass}, can transfer its momentum to SPPs on the air/metal interface if tuned to an appropriate angle ($k_{||glass} = \sqrt{\varepsilon_d}\frac{\omega}{c}\sin\theta = k_{SP1air}$). However, the evanescent waves do not interact with the SPPs on the glass/metal interface because their momentum is higher. This coupling technique has also been called attenuated-total-reflection method [227] and has been widely used for many plasmonic applications, especially for sensors.

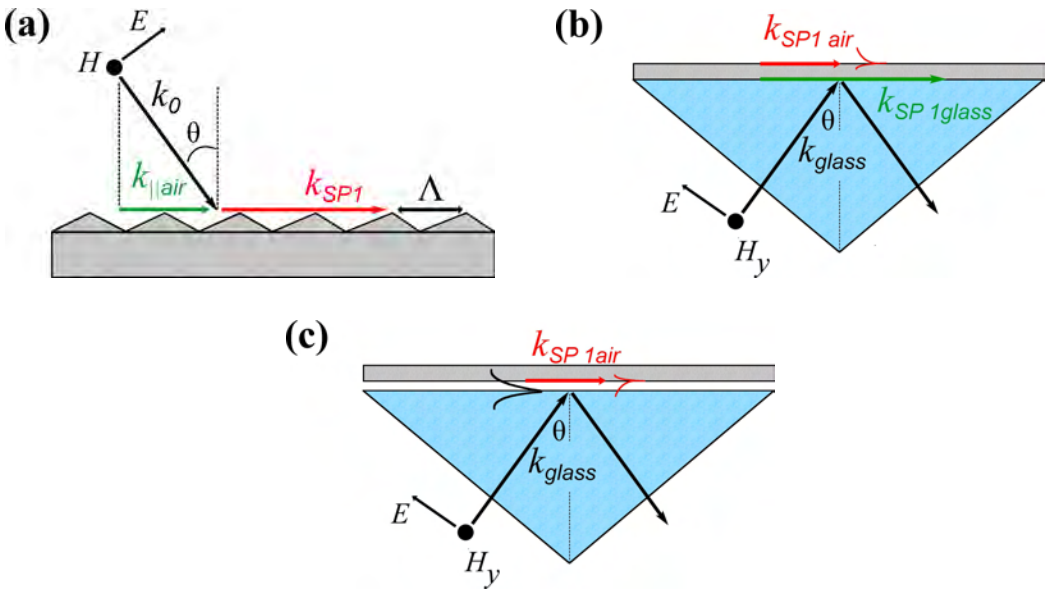

FIGURE 5.5: Techniques used to couple light into surface plasmons. (a) Grating coupling geometry. (b) Kretchmann geometry, makes use of a high refractive index prism which is in contact with a metal surface. This method enables excitation of SPPs at the air/metal interface but SPPs at the metal/glass interface cannot be excited. (c) Otto geometry, the metal surface is in close proximity to the prism.

It is important to note, that the reverse processes also allow SPPs propagating along a periodic structure or interacting with a defect, to lose momentum and be transformed into light [228, 229].

The imaginary part of the SPP's wave vector, k_{SP2} in equation (5.16), corresponds to ohmic loss in the metal. The SPP field intensity decays exponentially during propagation along the surface, its propagation distance, $\delta_{SP} = 1/2k_{SP2}$, is of the order of micrometres at visible frequencies, increasing to millimetres in the near-infrared region. Although the short propagation distance of SPP has been a major limitation to consider plasmonic/photonic components, recently SPP devices shorter than δ_{SP}, have been demonstrated [230, 231, 232].

5.7 Localized Surface Plasmons

In addition to SPP on a plane surface, in other geometries involving major spatial confinement, such as metallic nanoparticles, localized surface plasmons (LSP) can be excited. As it is characteristic of a enclosed system, SPPs will propagate within the metal particle and the reflected wave will interfere with itself leading to standing charge density waves. LSP resonances are present at discrete frequencies which depend on the size and shape of the object to which the plasmon is confined [233]. In contrast to volume plasmons and SPP which have a single resonant frequency, 3D confined structures have an infinite number of plasmon resonances of different symmetry. If the size of the system L is small compared with the wavelength of light $L \ll \lambda$, the standing wave will follow the time dependence of the incident light, and the particles will take a dipole form, as illustrated in Figure 5.6. With an increase in the particle size ($L \sim \lambda$) higher symmetry modes (multipoles resonances) become more important. The resonance conditions of a small metal particle are given by

$$\epsilon_{m1}(\omega) = -\epsilon_d \left(\frac{l+1}{l} \right) , \tag{5.17}$$

where $l = 1, 2, 3 \ldots$. Except for the first resonance $l = 1$, which is dipolar, the others have symmetries corresponding to higher multipoles and therefore are non-radiative [234]. The dipole resonance can be excited with incident light of the resonant frequencies, independent of the wavevector.

The numerical basis for describing the absorption, scattering properties of spherical metal particles are again the Maxwell equations. The Mie-Lorentz theory provides solutions for the scattering of a plane wave by an isotropic sphere-ellipsoid embedded in a homogeneous medium. In this formulation, the incident plane wave and the scattering field are expanded into spherical Bessel and Hankel functions. The internal field is also expanded into spherical functions. By enforcing the boundary condition on the particle surface, the electromagnetic field inside and outside the particle can be computed [212].

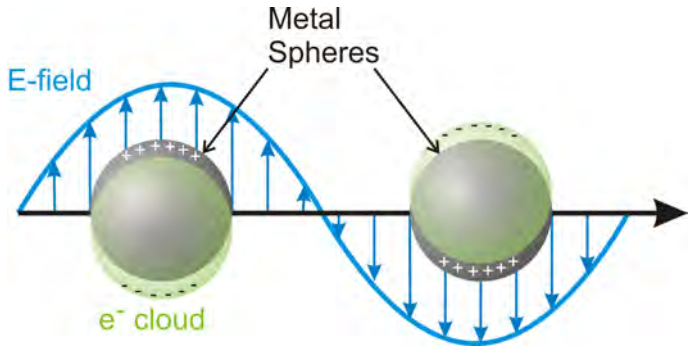

FIGURE 5.6: Schematic representation of the interaction between a metal sphere and a plane wave. The sphere diameter is smaller than the wavelength of light and thus, the charge distribution takes a dipole form.

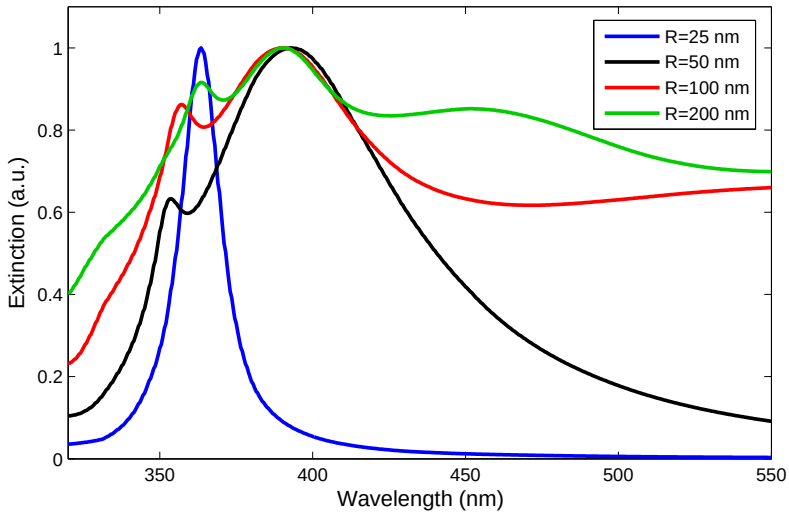

FIGURE 5.7: Extinction ratio for silver nanospheres, of different radii R as given by Mie-Lorentz theory.

Figure 5.7 shows the extinction ratio of silver nanospheres in air. At the resonance frequency strong absorption of light and high a concentration of the field is observed. As the particle size increases the number of plasmon resonance supported by the sphere increase, the band of the dipolar mode shifts towards the red, its bandwidth increases and thus the enhancement of the electromagnetic field decreases.

Although, the spherical geometry yields to an exact solution to Maxwell's equations, any deviation from this symmetry makes the electromagnetic problem far more complicated. For complex geometries (eg. prisms, nanorods, nanocubes, etc.) numerical methods must be applied in order to accurately describe the optical properties of metal nanoparticles [235]. The LSP resonances are highly related to the composition [236], size [237, 238, 239, 240], shape and external dielectric environment. In fact, by tuning the geometrical properties of the nanoparticles it has been possible to move the position

of the LSP resonance across the visible and near-IR spectra [241, 242]. The unique tunability of metallic nanoparticles offer the opportunity of placing the plasmon resonances at a desired wavelength for a particular application, as it is shown in Figure 5.8.

FIGURE 5.8: Solution of metallic nanoshells, as the shell thickness is increased the plasmon resonance is tunned from the visible to infrared wavelengths, taken from reference [243]

5.8 Plasmonic Devices and Applications

The topic of surface plasmons polaritons has a history going back more than a hundred years, but it has recently attracted renewed interest for a variety of reasons. In part, this is because there are now well developed nanoscale fabrication techniques such as electron-beam lithography, ion-beam milling, and self assembly that allow suitable metal/dielectric structures to be fabricated as a way of controlling SPPs. Another motivation for their study is because the field of plasmonics has great potential in a number of fundamental physics and practical applications. Plasmon devices find widespread use in present day commercial industries and in different areas of science and technology. For example, they have been used as bio-molecular sensors, for the characterisation of the optical properties of matter, and they show good prospects for the development of subwavelength lithography techniques and optics. This section describes some of the work that has been done in the field of plasmonics with practical applications.

5.8.1 Sensors and Biosensors

Sensing is probably the most attractive and widely studied application of plasmon waves and a great deal of work has been done in the exploitation of SPPs for biochemical sensing. When in resonance, plasmon structures serve as a local probe of the dielectric medium within a few nanometres of the metal boundary. The enhanced evanescent field near the metal structure allows for a variety of sensing applications and techniques. There are two main types of plasmon sensors. The first one is based on the excitation of

SPPs waves in thin metal films and the second relies on the excitation of LSPs in metal nanostructures.

SPPs sensors have been used since the late seventies and the early eighties saw the first demonstration of gas and biomolecule detection systems [244] based on plasmon-mater interactions. Because the resonance frequency of the plasmon waves depends on the refractive index of the dielectric environment (equation (5.15)), any changes in the optical properties of the region close to the metal boundary modifies the resonance frequency of the SPPs and can be detected with simple devices. SPPs in thin metallic films sensors are excited by prisms or grating coupling mechanisms. The shift in the resonant frequency due to the surrounding environment manifests as a shift in the angle of maximum optical absorption [245]. The sensitivity of the SPP resonance to its immediate environment offers great opportunities to characterise thin metallic films, detect molecules attached to the surface, study biomolecular bounding, environmental changes, etc. For example, by functionalising a metal film by antibodies, specific for single or multiple antigens, and by monitoring the shift of the resonant frequency upon interaction of the binding molecules, it is possible to measure the rates of reactions, the strength of biomolecular binding and the concentration of antigens [246]. The SPR sensor technology has been commercialized by several companies [246, 247, 248] and has become the main label-free technology for the study of real-time biomolecular interactions. As the resonance frequency of LSPs in metal nanostructures depends notably on the refractive index of its immediate environment, metal nanostructures have also been used for sensing applications [249, 250, 251]. However, because of the difficulties in the production of reproducible structures it has not been so widely used as its planar counterpart.

The second kind of plasmon sensors are based on the enhancement of spectroscopy techniques due localized surface plasmon resonance. These sensors take advantage of the fact that LSPs are radiative and provide even higher field enhancements than SPPs (on smooth surfaces) due to the strong three dimensional localization of the electromagnetic fields. Therefore, the matter-light interactions and optical nonlinear effects associated with the environment in close proximity to the surface can be studied with low light intensities. It has been demonstrated that LSPs can greatly amplify the signal of several optical spectroscopy techniques. LSPs are the basis of powerful phenomena such as Surface Enhanced Fluorescence Spectroscopy [252, 253, 254], Surface Enhanced Infrared Absorption Spectroscopy [255, 256] and Surface Enhanced Raman Scattering (SERS) [234, 257, 258] to mention a few. In SERS the molecules attached to the surface of metal nanostructures interact with the high field intensity of LSPs and induce enhanced Raman photons. SERS has recently received great interest, and reports of new and more stable SERS substrates can constantly be found in scientific literature as well as being

used in commercial devices [259, 260]. The SERS effect is discussed in the following chapter and the development of novel SERS substrates based on the deposition of silver nanoparticles within microstructured optical fibres is described in Chapter 7.

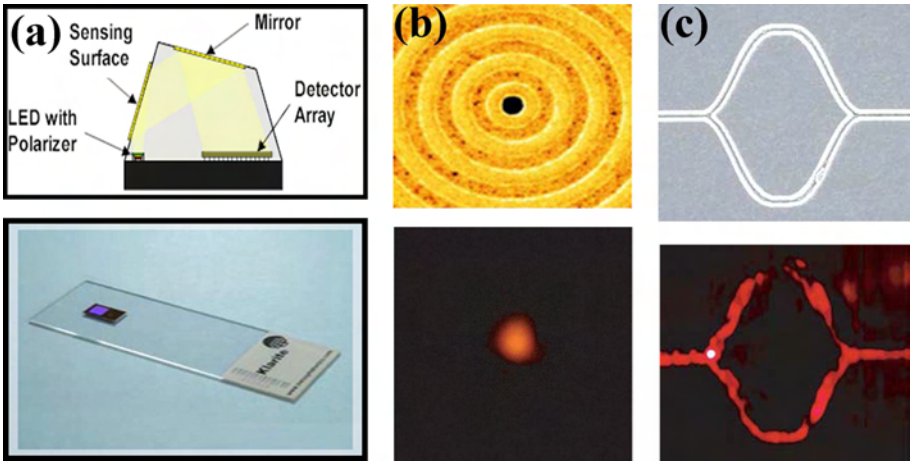

FIGURE 5.9: (a) Commercially available plasmon sensors. Top: biosensor based on SPP resonances in smooth gold films, taken from reference [247]. Bottom: the high localization of EM fields at the surface of nanostructured metal film has been exploited for Surface Enhanced Raman Scattering sensing, from reference [260]. (b) Top: SEM image of silver nanostructure used for enhanced transmission experiments. Bottom: Image of transmitted light, from reference [261]. (c) Top: SEM micrograph of a subwavelength plasmonic Mach-Zehnder interferometer. Bottom: Near field image of the propagating plasmon waves. Taken from reference [262].

5.8.2 Extraordinary Optical Transmission

In 1998 Ebbesen and co-workers [263] reported that the intensity of light transmitted through a metal film with an array of subwavelength apertures is much higher than expected. High transmission of light through nanoholes promises exciting opportunities for subwavelength optical lithography using conventional photoresist and UV lasers [261, 264] leading to great interest in the microelectronics and optoelectronics industries. It is believed that the structuring of the metal surface excites SPPs waves that can travel around the holes and, when both SPPs waves on each side of the film are in phase, the resonant transmission occurs. However, the explanation of this phenomenon in terms of SPPs has been questioned and many theories involving diffraction and near field optics can be found in the literature [265, 266].

5.8.3 Photonic Integration

The areas of computing and communications have boosted a tremendous progress in the development of faster and smaller microelectronic components and during the last few decades we have seen a tremendous miniaturization of electronic circuits. However, electronic devices based on CMOS technology are approaching their limits both in the level of integration and the operational frequency. Quantum effect devices such as single electron transistors, quantum well and quantum dot structures have been considered as a possible approach in computer design. Another alternative is developing all-optical processing devices where the information is processed and transfered in the form of photons. In recent years there has been a strong interest in replacing electronic circuits with faster photonic devices within microchips. Photonic devices are superior to electronic ones in terms of operational bandwidth and speed, but the diffraction limit of light represents a significant challenge to the miniaturization and high density integration of optical elements. Scaling photonic devices down to nanoscale dimensions and their integration in microchips requires electromagnetic energy to be generated, guided and processed in structures smaller than the diffraction limit. The way in which SPPs concentrate light in subwavelength metal structures suggests them to be promising candidates for photonic integration and an attractive platform for all-optical signal processing with structural elements smaller than the diffraction limit. As SPPs concentrate their energy on the surface, this makes it technologically possible to fabricate two dimensional plasmonic structures using conventional material processing techniques.

To date, there have already been break-throughs in subwavelength SPP active [267, 268] and passive devices [269] such as waveguides [270, 271, 230], interferometers, Bragg reflectors [272], ring resonators [262], mirror, lenses, etc. However, the realization of plasmon devices with a loss sufficiently low for practical applications has been a major limitation for practical devices.

Chapter 6

Surface Enhanced Raman Scattering

The change in wavelength of light scattered by a molecule, known as Raman scattering is attributed to the excitation (or relaxation) of vibrational states of the molecule. As different functional groups have different vibrational energies, every molecule has a unique Raman spectrum thus this effect can be exploited as a powerful spectroscopic technique. Moreover, as a vibrational spectroscopy technique, Raman spectroscopy gives much more information about the molecular structure than electronic spectroscopic techniques, such as fluorescence. Other important characteristics of Raman scattering are that it is not quenched by adding species and can be used to simultaneously identify different compounds. the major limitation of Raman spectroscopy is the small cross section of Raman scattering making it an extremely weak effect. The high field localization at resonant frequencies caused by the excitation of surface plasmons has been exploited to amplify the Raman signal of molecules placed on the surface of a nanoscale roughened noble-metal substrate. Surface Enhanced Raman Scattering (SERS) has shown promise to overcome the extremely low sensitivity problem of Raman scattering and has become among the most studied surface probe techniques.

The basic theory of Raman scattering and SERS will be introduced in this chapter. This then leads into Chapter 7 where by the deposition of metal nanoparticles inside the microscale holes of MOF a new kind of in-fibre SERS substrate are characterised experimentally.

6.1 Raman Effect

The scattering of light from a molecule can either occur elastically, Rayleigh scattering, or inelastically whereby the molecular motion modifies the incoming radiation, Raman scattering. This was first observed in 1928 by C.V. Raman who did a series of experimental studies of light scattering in liquid media and noticed the generation of weak radiation at wavelengths different from the incident light [273]. A schematic representation of the energy transitions involved in Raman and Rayleigh scattering is shown in Figure 6.1.

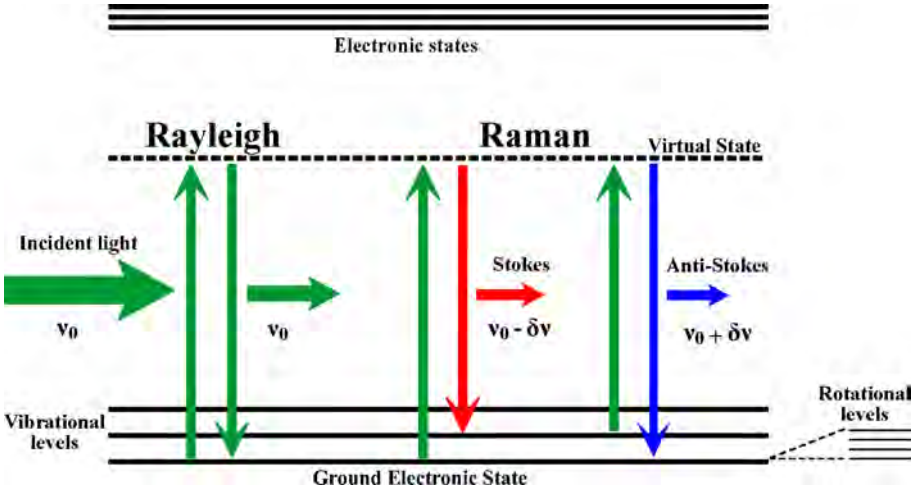

FIGURE 6.1: Diagram for Raman and Rayleigh scattering showing the energy levels involved in the processes. Note that all the scattering processes involve a virtual state. Vibrational absorptions usually occur at infrared wavelengths while rotational absorptions occur in the microwave regime. Therefore, the energy difference (ΔE) between two vibrational states is higher than that between two rotational transitions.

When light interacts with a molecule around 10^{-5} of the incident photons may undergo Rayleigh scattering, the scattered light leaves the molecule with the same frequency as the incident light but will be radiated in random directions. In Raman scattering, approximately 10^{-7} of the of the incident light transfer its power to another optical field whose energy can be shifted up (anti-Stokes) or down (Stokes) by an amount determined by the vibrational modes of the molecule. As shown in Figure 6.1, the Raman scattered photons lose or gain energy causing the molecule to undergo a quantum transition to higher or lower vibrational energy, depending on whether the photons interact with a molecule in the vibrational ground state or an excited vibrational state. It is important to note that in both scattering mechanisms the excitation and scattered photons are not in resonance with any real molecular transitions and the transitional state is said to be virtual. On the other hand, in absorption mechanisms such as fluorescence, the upper state is a real electronic state.

Rayleigh and Raman scattering can be described by an elementary classical theory as follows. When an electric field $\vec{E}$ is incident on a molecule the charge of that molecule is displaced and the molecule becomes polarised. An induced electric dipole momentum $\vec{P}_{ind}$ is created

$$\vec{P}_{ind} = \alpha \vec{E}\,, \tag{6.1}$$

where α is the polarisability of the molecule.

In Rayleigh scattering the molecular polarisability (α) is regarded as having no time dependance [274]. The incident electric field will force the electron cloud to oscillate symmetrically around the nuclei. Therefore, the generated electric momentum will oscillate with the same frequency (ν_0) as the incident light. The molecule will radiate an optical field of the same frequency (see Figure 6.2a).

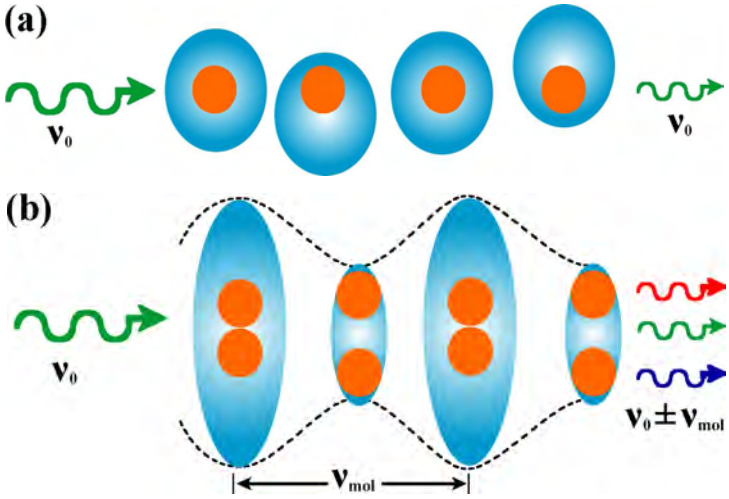

FIGURE 6.2: General polarisability models of (a) Rayleigh and (b) Raman scattering. (a) For a non-rotating and vibrationless molecule, the induced electric dipole has the same spectral components as the incident light. (b) The atomic vibrations "modulate" the induced electric dipole thus, in this case the induced dipole has a richer spectrum.

However, as depicted in Figure 6.2b, the nuclei can perform periodic movements with some nuclear frequency ν_{mol} which may be independent from the incident light. Furthermore the molecular polarisability may change as the molecular vibrations displace the constituent atoms from their equilibrium position. If the optical frequency ν_0 is large in comparison with the nuclear frequencies, only the light electrons will be able to follow the incident field (a condition well satisfied at visible frequencies). For visible light, the electron cloud surrounding the nuclei will oscillate at the frequency of the incident light, but the nuclear positions will also affect the molecular polarisability in

such a way that the amplitude of the electron cloud oscillation will be modulated by the slow nuclear oscillations. Therefore the polarisability has a time dependence of the nuclear frequencies. It follows that the scattered light contains frequency components corresponding to the incident light ν_0 as well as the frequencies corresponding to the nuclear vibrations $\nu_0 \pm \nu_{mol}$. These new optical frequencies correspond to the Raman scattered fields. Moreover, if the molecule is in a stationary state, each atom will feel different forces from the oscillating electrons. This will excite the molecule to a vibrational state and therefore will also radiate Raman frequencies. It is clear that, if the intensity of the incident light is increased, the molecule will oscillate with higher amplitude, equation (6.1), and this will increase the probability of molecular transitions. However, the probability of inducing vibrational transitions is low because the electrons oscillate much faster than the heavy atoms. Thus, the Raman scattering is weaker than Rayleigh scattering; the probability of Raleigh scattering is 1 in 10^5 while the probability of one photon suffering Raman scattering is 1 in 10^7.

As described by the Boltzmann, the population in the excited state differs from that of the ground state by approximately the factor $\exp(-\Delta E/kT)$. Thus the intensity of the anti-Stokes and Stokes Raman signals is generally not the same. Since ΔE is generally large for vibrational transitions (see Figure 6.1) the anti-Stokes vibrational bands are very weak in comparison to the Stokes bands. On the other hand, for rotational transitions, $\Delta E/kT$ is often small and therefore the Stokes and anti-Stokes rotational bands are often of comparable intensity. With this simple classical description of the Raman effect, it is easy to understand that the Raman signal is independent of the exciting frequency and depends on the normal vibrational frequencies of a molecule which are determined by the kind of atoms, bonds strength and configuration of the molecule. Therefore it is commonly said that the Raman spectrum provides a structural "fingerprint" of the molecule.

6.1.1 Theory of the Raman Effect

Although a classical description of the Raman process gives an important qualitative explanation of the effect, it does not provide quantitative information. In order to obtain a quantitative explanation of the Raman effect a quantum mechanical description of the process is required. Although such an analysis is out of the scope of this thesis, the form of the final expressions for the intensity of the Raman fields will be briefly discussed. The quantum mechanical treatment considers the perturbation of the wave-functions of the molecule by the incident electrical field; it calculates the induced transition moment associated with a transition between the initial state (n) and the final state (m), which may be written as follows [275]:

$$P_{nm} = \int \psi_m^* P \psi_n d\tau \ , \tag{6.2}$$

where P is the induced transition dipole moment and ψ_n and ψ_m are the wave functions of the independent states n and m. Solving the previous integral over the whole space leads to the following result,

$$P_{nm} = \frac{1}{h} \sum_r \left(\frac{M_{nr} M_{rm}}{\nu_{rn} - \nu_0} + \frac{M_{nr} M_{rm}}{\nu_{rn} + \nu_0} \right) E \ , \tag{6.3}$$

where h is the Planck's constant, r denotes any energy level of the unperturbed molecule. M_{nr} and M_{rm} are the corresponding transition moments between the states denoted by the subscripts, ν_{rn} and ν_{rm} are the frequency differences between these states, and E is the intensity of the electric field of the incident light. The intensity of the scattered light associated with transition $n \rightarrow m$ is proportional to the square of P_{nm}, according to the relation:

$$I_{nm} = N_n C \left(\nu_0 + \nu_{nm}\right)^4 P_{nm}^2 \ . \tag{6.4}$$

Here N_n is the number of molecules in the initial state, C is a proportionality constant and the frequency $(\nu_0 + \nu_{nm})$ is that of the scattered radiation. When $n = m$ the states of the molecule remains unchanged and Rayleigh scattering occurs, whilst Raman scattering is characterized by $n \neq m$. If the transition is to higher energy,

$$\nu_{nm} = (En - Em)/h \ , \tag{6.5}$$

is negative (Stokes frequency); if the transition is to lower energy $\nu_{nm} > 0$ (anti-Stokes frequency). Equation (6.3) indicates the linear relation between P_{nm}^2 and E^2 and equation (6.4) indicates the proportionality between the Raman intensity and the intensity of the incident field. P_{nm} involves a summation of the transition moments (M_{nr}) from the initial state n to all states r of the unperturbed molecule multiplied by the transition moments from all molecular states to the final state. Although this summation considers all possible molecular transitions, it does not mean that all transitions in fact occur in the scattering process. It is only a mathematical representation of the process which leads to the calculation of the virtual molecular state shown in Figure 6.1.

As mentioned before, the cross-section of the Raman effect is very low, typically 14 orders of magnitude below those of fluorescence. Due to the inherent small magnitude of the Raman effect the applicability of Raman spectroscopy has been restricted for

many years although this has become less of an issue since the development of high power lasers and high sensitivity photodetectors. However, further to this, there are two main techniques that can be exploited for increasing the Raman cross, and section these are resonance Raman scattering (RRS) and surface enhanced Raman scattering (SERS).

6.2 Resonance Raman Scattering

An increase in the intensity of the Raman spectra is observed when the excitation frequency approaches the region of electronic transitions of the material. The enhancement is well described by equation (6.3). If $\nu_0 \sim \nu_{rn}$ the term containing the factor $1/(\nu_{rn}-\nu_0)$ will increase and tend to become important in determining the intensity of the Raman signal. Although, the incident photon will excite the molecule to a real energy level (see Figure 6.3), the process is still not an absorption process and is much weaker than fluorescence. Resonance Raman Scattering usually provides an enhancement of the Raman peaks of a factor up to 10^4. Since the resonance Raman scattering is dominated by molecular vibrations which are related to the part of the molecule responsible for the electron transition, an advantage of RRS is that resonance spectra usually exhibit higher specificity than conventional Raman scattering. This means that for large molecules only the Raman peaks due to vibrational modes of the groups in resonance are enhanced while the Raman signal from the rest of the molecule remains low. This specificity, makes RRS very useful in analyzing big molecules, such as proteins. Furthermore, as will be discussed in greater detail in the following sections, RRS is an important mechanism in SERS.

6.3 Surface Enhanced Raman Scattering

The field of SERS was born in 1974 when Fleishmann *et al.* [276] observed a strong Raman signal from pyridine, absorbed from aqueous solution onto a silver electrode roughened by means of oxidation and reduction cycles. In this publication the authors attributed the strong signal to the large surface area of the roughened substrate and therefore to the increased number of absorbed molecules. This discovery attracted considerable attention in many research groups and later experiments gave evidence that the strong Raman signal could not be accounted for a large number of molecules on the surface, but due to a real enhancement of the Raman effect. Van Duyne [277] and Creighton [278] recognized independently that the enhancement that could be obtained

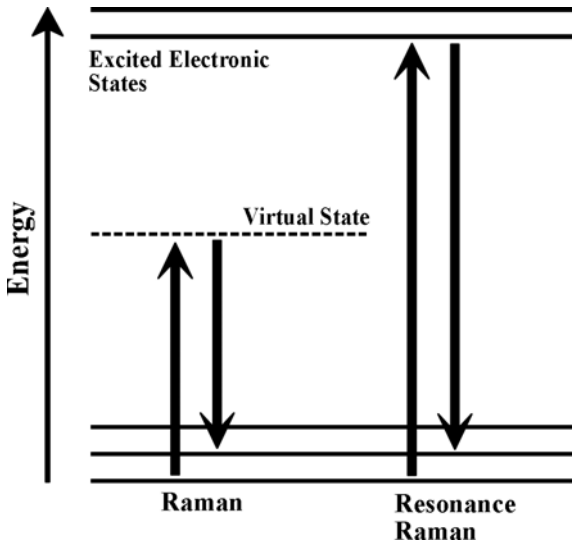

FIGURE 6.3: Schematic diagram showing electron energy levels involved in Raman and resonance Raman scattering.

by the increase of surface area alone was only a factor of 10 while the enhancement observed in Fleishmann's experiments was $10^5 - 10^6$ fold.

Since its discovery, SERS has progressed from studies of pyridine on roughened electrodes to the engineering of metal nanostructured substrates which provide large enhancement factors and certain signal reproducibility, thus making SERS practical. To date the SERS effect has been observed with many different analyte molecules and on a variety of roughened metallic surfaces including Au, Ag, Cu, as well as some alkaline metals. Recently, SERS has been used as a surface analysis technique for biological and chemical characterisation. There are many examples of SERS detection of pesticides, bacteria, cancer cells, glucose, nuclear waste, explosives, etc. In the last few years, due to the advent of nanofabrication techniques and the development of accurate electromagnetic modeling methods, SERS research has accelerated dramatically and there is an extraordinary amount of interest in exploring new nanoscale substrates and fundamental theory. SERS experiments have now achieved unimaginable sensitivity even demonstrating single molecule detection [279].

6.3.1 Enhancement Theories

Over the years, there has been a great deal of work carried out to understand the precise nature of the SERS effect. In 1977, Jeanmarie and Van Duyne [277] attributed the enhancement to an increase in the electromagnetic field at roughened surfaces whereas Albrecht and Creighton [278] described it as a charge transfer absorption band between the adsorbate and the surface. These ideas evolved and gave origin to two theories

which describe the mechanisms of the enhancement; the electromagnetic theory and the chemical theory. Although, there has been much discussion on the role and significance of each contribution, it is generally agreed that the electromagnetic mechanism is the major contributor to the intensity amplification and that both mechanisms act in parallel, i.e. multiplicatively. These two theories are discussed in greater detail in the following sections.

6.3.1.1 Electromagnetic Mechanism

The electromagnetic model is based on the response of nanoscale metallic particles to light waves. As stated in Chapter 5, the geometrical and material characteristics of metallic nanoscale particles determine the resonant frequency of the surface plasmons. Excitation of LSP resonances result in high concentration of the electromagnetic fields at the surface and selective absorption and scattering of the incident electromagnetic wave. The electromagnetic enhancement relies on molecules being located within these large electromagnetic fields. The presence of the nanoparticle electromagnetically modifies the Raman response of the molecule in such a way that the incident field acting on the molecules and the emitted Raman light intensities are increased by the polarised surface. The dipole moment induced in a molecule in close proximity with a metallic feature will be due to both the incident wave and the Lorentz-Mie elastically scattered field by the metal particle. In the same way, the Raman radiation at the observer position consists of the Raman emission of the dipole plus the Raman signal that is re-radiated by the metal particle causing an enhancement factor of $10^4 - 10^6$.

In 1980 Kerker *et al.* [280, 281] proposed a, now-classical, way of investigating the electromagnetic contribution in SERS. In this model they consider a molecule to behave as a classical dipole which is located at an arbitrary position (r') outside a metal sphere of radius a. When a plane electromagnetic wave of frequency ω_0 interacts with the system, the dipole momentum induced in the molecule will radiate at the Raman frequency ω,

$$\vec{p} = \alpha_r \vec{E}_p(r', \omega_0) \ , \tag{6.6}$$

where α_r is the Raman polarisability of the molecule and $\vec{E}_p(r', \omega_0)$ is the electric field at r' and frequency ω_0. Because the metal particle acts as a scatterer of the incident field, $\vec{E}_p$ is composed of the incident field $\vec{E}_i(r', \omega_0)$ plus the field scattered by the particle $\vec{E}_{LM}(r', \omega_0)$, as calculated by Lorentz-Mie theory

$$\vec{E}_p(r', \omega_0) = \vec{E}_i(r', \omega_0) + \vec{E}_{LM}(r', \omega_0) \ . \tag{6.7}$$

The Raman radiation at the observation point r is given by

$$\vec{E}_R(r,\omega_0) = \vec{E}_{DIP}(r,\omega_0) + \vec{E}_{SC}(r,\omega_0) \ , \tag{6.8}$$

where $\vec{E}_{DIP}$ is the field that would be radiated by the oscillating dipole $\vec{p}$ if the sphere was not present and $\vec{E}_{SC}$ is the secondary scattered field by the sphere. All four fields must be calculated by solving the appropriate boundary-value problem and they are given as linear combinations of the Bessel and Hankel functions [280].

The Raman scattering intensity in the radiation zone ($r >> r'$), is the square of the far-field amplitude of E_R, i.e.,

$$I_R = \lim_{kr\to\infty} \left| E_R(r,\omega) \frac{\exp(ikr)}{r} \right|^2 \ . \tag{6.9}$$

The electromagnetic enhancement factor G may now be defined as

$$G = \frac{I_R}{I_R^0} \ , \tag{6.10}$$

where I_R^0 is the Raman intensity in the absence of the metal sphere. In this case the dipole will only be excited by the incident field $E_p = E_i(r',\omega_0)$ and the Raman field is only due to the oscillating dipole $E_R = E_{DIP}(r,\omega)$.

This theoretical model can be applied to determining the enhancement of Raman scattering by a molecule on or near the surface of a metal particle of any size. The model shows high dependence of the enhancement upon the particle size and the excitation frequency. For small particles, enhancement values of $\sim 10^6$ are predicted and they show a sharp resonance due almost exclusively to the excitation of the first order dipole-like plasmon resonance. While, the enhancement factor expected from larger particles is $10^2 - 10^4$ and shows broader excitation spectra due to the excitation of high order multipole plasmon resonances which causes the decrease of both the local field and the scattered field. The relation between the enhancement to the excitation of surface plasmons can be easily appreciated for a molecule near a sphere whose size is optically small ($a << \lambda_0$). In this limit, the calculation of the SERS enhancement is rather simple and is given by

$$G_{em}(\omega) \approx \left| \frac{\varepsilon_m(\omega) - \varepsilon_d}{\varepsilon_m(\omega) + 2\varepsilon_d} \right|^2 \left| \frac{\varepsilon_m(\omega_0) - \varepsilon_d}{\varepsilon_m(\omega_0) + 2\varepsilon_d} \right|^2 \left(\frac{a}{a+d} \right)^{12} \ , \tag{6.11}$$

in which ε_m is the frequency-dependent dielectric constant of the metal composing the sphere, and ε_d is the dielectric constant of the local environment around the sphere. The equation predicts a fast decrease in the enhancement with distance d away from the metal sphere. Assuming the configuration when the molecule is on the sphere's surface ($d = 0$), the enhancement factor is given by [280]:

$$G_{em}(\omega) \propto \left|\frac{\varepsilon_m(\omega) - \varepsilon_d}{\varepsilon_m(\omega) + 2\varepsilon_d}\right|^2 \left|\frac{\varepsilon_m(\omega_0) - \varepsilon_d}{\varepsilon_m(\omega_0) + 2\varepsilon_d}\right|^2 . \tag{6.12}$$

According to this model the magnitude of G_{em} becomes very large when $\mathrm{Re}(\varepsilon_m) \approx -2\mathrm{Re}(\varepsilon_d)$, which is the surface plasmon resonant condition. Therefore, the electromagnetic enhancement is induced by the LSPR concentration of the electric field at the surface of the sphere. The model reveals large SERS signals for metals such as silver or gold, that can achieve the condition $\mathrm{Re}(\varepsilon_m) \approx -2\mathrm{Re}(\varepsilon_d)$ and have low loss at visible frequencies.

Although the fields about a spherical particle can be calculated in close form, this is not the case for particles of arbitrary shape. Thus theoretical models using computational methods have been used to studying complex nanoparticle geometries and for determining the LSP resonances. Several researchers have exploited the LSP resonances in SERS experiments by attaching molecules around metal nanoparticles. This is possible when using colloid solutions or alternatively the particles can be deposited on supporting substrates.

Moskovitz [282, 234] proposed that a rough surface may be idealized as a set of elliptical particles placed on a flat substrate. The model assumes that neighbouring particles are sufficiently well separated so that their interaction may not be accounted for. Thereafter, it is expected that rough surfaces will have electromagnetic properties in between those of an isolated particle and a flat surface. Flat metallic surfaces have non-radiative SPPs which propagate along the surface. For an air/metal interface, the allowed values of ω span in the continuous range $\omega_{SPP} < \omega_R$, with $\omega_R = \omega_p/\sqrt{2}$ being the only resonance frequency. On the other hand, isolated spheres support infinite number of LSP resonances whose frequencies are given by $l\mathrm{Re}[\varepsilon_m(\omega_R)] + (l+1)\mathrm{Re}(\varepsilon_d) = 0$ (here $l = 1, 2, 3, \dots$). However, only the dipole like resonance ($l = 1$) is optically active (may be excited by light waves and radiate light), as the others have higher order symmetries and are therefore not optically active. As an isolated sphere is moved in close proximity to the surface, the dipole resonance may excite the surface plasmon and the two waves interact with each other. Therefore, the surface plasmon resonance frequency ($\omega_p/\sqrt{2}$) is blue shifted and the LSP resonance ($\omega_p/\sqrt{3}$) is red shifted. As the particle moves even closer to the surface, it provides the momentum necessary to couple light waves into SPP. Likewise, the surface acts as a mirror of the sphere dipole. The image dipole acts

on the sphere exciting multipolar modes which are otherwise not optically accessible. The resonance spectrum of the system as a whole thus becomes richer than in the case when the two objects are independent.

In addition, consider the case in which two particles are close to each other, the system will present extra plasmon resonances due to electromagnetic coupling between the particles. Presumably the energy concentrated in the gap between them will be high and therefore will produce even higher enhancements. By calculating the electromagnetic fields at various points in a system comprising more than one particle, there have been some extensions to the theory to treat more realistic SERS substrates. In general, the fields located between two nanoparticles are even higher than those near isolated structures, implying further SERS enhancements [283, 284].

The electromagnetic theory has been able to account for a large number of features of SERS. These include, the observation of an enhancement at some distance of the scatter molecule from the surface, the high sensitivity of the enhancement to the degree of surface roughness, the fact that only coinage metals produced large effects, the angular dependance of the enhancement, and the negligible enhancement at a flat surface, etc. Many of the surface treatments used to fabricate SERS substrates produce a surface covered with particles fairly similar to ellipsoids, so that the Mie theory has been able to qualitatively predict many of their features. However, the particles in general have a wide distribution of sizes and shapes which makes the exact analysis of the optical properties of SERS substrates very difficult. Therefore for "complex" SERS substrates, consisting of many particles (more than 4), it has been more fruitful to turn to experiments to obtain appropriate descriptions of the electromagnetic properties. Indeed, this is the case for our fibre SERS substrates (to be described in the Chapter 7), that consist of many particles of different sizes and distributions so that, combined with the complex 3D fibre geometry, make it very challenging to obtain an appropriate description of their electromagnetic properties.

6.3.1.2 Chemical Enhancement

It has been proved that the electrodynamic model alone cannot completely describe all the experimental evidence of SERS. For example, the fact that certain types of molecules, such as pyridine and piperidine, which contain electrons available for bonding with the surface, displayed enhancement factors greater than other molecules that are not adsorbed [285], the observation of voltage-dependent SERS intensity of molecules adsorbed on electrodes, and many other observations [234, 257], seem to be in conflict with the electromagnetic theory. However, these effects can be explained in terms of chemical mechanisms which involve first layer metal-molecule interactions. Although

many possible chemical enhancement theories have been investigated, most of them have a common theme; resonance Raman scattering via accessible charge transfer between intermediate states.

Figure 6.4 illustrates how the initial, intermediate and final state of resonance Raman scattering are modified for adsorbed molecules. The molecular orbitals of chemisorbed molecules are broadened by the interaction with the free metal electrons and the continuum of metal states can act as intermediate states for lower energy resonance scattering processes.

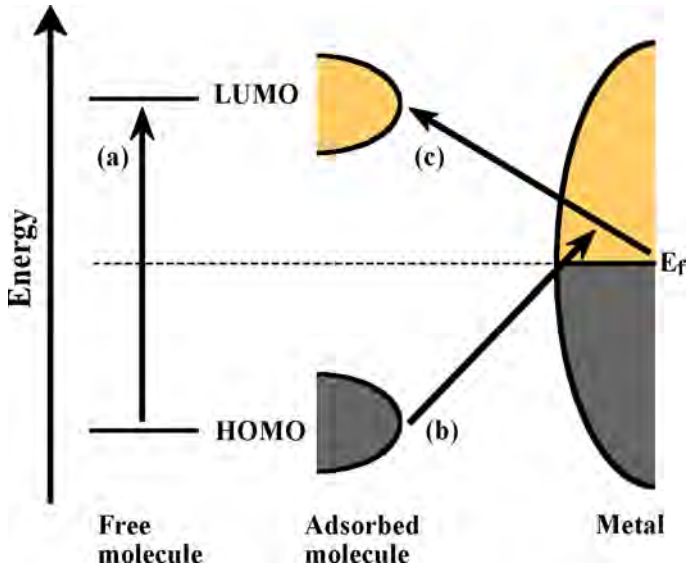

FIGURE 6.4: Energy levels scheme for molecule-metal complex. The discrete molecular levels of the free molecule are changed due to chemisorption effects. The metal's Fermi energy lies approximately in the middle between the higher occupied molecular (HOMO) and the lower unoccupied molecular orbitals (LUMO) of the molecule. The possible charge transfer paths are shown.

Resonance Raman scattering, attributed to electron transitions in a free molecules (path (a) in Figure 6.4), can only be excited by ultraviolet photons, however, when considering the molecule-metal system as a whole, charge transfer transitions may be possible at lower energies in the visible region of the spectrum. Two new possibilities of charge transfer could be envisioned in the system. Electrons can be excited from the molecule HOMO to unfilled metal orbitals above the Fermi energy (molecule-metal charge transfer, path (b)), or transitions in which free electrons are transferred from the metal conduction band to the LUMO in the molecule (metal-molecule charge transfer, path (c)). This chemical theory has been strengthened by the observation of low energy electronic absorption bands in mono layer metal-molecule systems [286, 287, 288] by means of electron energy loss spectroscopy. Moreover, spectrochemical experiments have proved that the metal-molecule charge transfer excitation is red shifted upon making the electron potential more negative (increasing the Fermi level). Even though the chemical

enhancement may be observed on atomically smooth metal surfaces, the presence of nanoscale features on the film provides an easier route for the hot electrons to the adsorbed molecule and facilitates the generation of hot electrons in the metal. Therefore the chemical model predicts that the enhancement is more effective when the surface is rough, whereas for electromagnetic enhancement, nanoscale roughness is essential.

In general it is thought that the chemical mechanisms can amplify the Raman scattering cross section by a factor of 10-100 and although this is small compared to electromagnetic mechanisms, the effects multiply so that the chemical contribution is of great importance if high enhancement factors ($> 10^6$) are to be obtained.

Chapter 7

Metal Modified Optical Fibres

The previous two chapters have provided an introduction to the field of plasmonics and one of its most fruitful applications; SERS. This chapter focuses on the optical characterisation of MOFs coated with silver nanoparticles. These fibres allow the excitation of surface plasmons by optical guided modes. The fibre geometry offers significant benefits over conventional plasmonic planar structures in that it simplifies the coupling to the plasmon modes and, due to the waveguiding capabilities of MOFs, the optical guided modes offer extended electromagnetic interaction lengths to excite multiple plasmon resonances along the fibre. Investigations of the SERS capabilities of these structures have shown large enhancements in the Raman spectra of target molecules absorbed on the metal surface. The novelty and practicability of the metal-functionalised MOFs substrates opens up new possibilities for the next generation of in-fibre photonic/plasmonic devices.

7.1 Introduction

The incorporation of metals into a MOF geometry enables the integration of photon transport with the active plasmonic region to yield completely integrated devices with unique excitation and detection capabilities. All-fibre devices offer a number of advantages over conventional planar plasmonic structures in that they are cheap, compact, robust, flexible and are compatible with existing optical fibre systems.

Due to the momentum mismatch between light and plasmons propagating along the metal/air interface of thin films, plasmonic devices based on a 2D geometry typically require the use of a prism or coupling elements to phase match the incoming radiation with surface plasmon waves adding bulk and complexity (see Chapter 5). By exploiting

the unique guiding geometry of MOFs, the silica core can be thought of as a matching device, which increases the momentum of a photon and permits the coupling between guided optical modes and plasmons on the air/metal interface. Based on this approach, a number of theoretical studies have been conducted to investigate the transmission properties of metal-dielectric MOF, ranging from fibres with thin-smooth coatings on the capillary walls to solid nanowire inclusions [289, 290, 291]. The results have shown that, by carefully choosing the fibre structure and metal coating, it is possible to tune the wavelength and the number of plasmon resonances, as well as to control the fibre loss. Because the modal properties of MOFs can be tailored, the problem of phase matching can be easily circumvented by engineering the fibre geometry. By having a multimode fibre, which allows the propagation of higher order modes each with a different propagation constant, the coupling to the plasmon modes is even easier. However the fibres used in the following experiments have been impregnated with granular coatings rather than smooth-thin coatings. Thus localized surface plasmons resonances rather than surface plasmon waves are expected to exist in these structures, as will be described in the following section. However, future experiments will be devoted to investigate the plasmonic properties of MOFs with smooth coatings.

MOFs with metal coatings on the internal capillary walls offer a number of advantages over earlier investigations of plasmon-photon interaction in optical fibres. In these previous studies, the interaction between the core guided light and plasmons was achieved by depositing metal films on the outside of either a tapered fibre or on a window etched into the cladding [292, 293, 294, 295, 296, 297, 298, 299]. Metal-modified MOFs are not only more robust and easier to fabricate but also the active region is isolated, via the silica walls, from the surrounding environment.

The fibres used in this chapter are functionalised using the high pressure chemical deposition technique, described in Section 3.7. During the deposition processes the fibres were heated to $\sim 200\,^{\circ}\mathrm{C}$, with the organometallic silver precursor dissolved in high-pressure heptane. A variety of MOFs structures are investigated and control of the deposition profiles in these fibres is obtained by tuning the experimental parameters such as the temperature, precursor concentration, flow rate and deposition time to yield a range of particle sizes, from tens to hundreds of nanometres, and profiles that vary from sparse nanoparticles to thin granular films [300]. For example, the SEM micrographs shown in Figure 7.1 reveal that a thin film with silver particles is annularly deposited inside the fibre capillaries and that, by changing the silver precursor concentration and the deposition time, silver nanoparticle coating thicknesses of (a) $\sim 200\,\mathrm{nm}$, (b) $\sim 300\,\mathrm{nm}$ and (c) $\sim 500\,\mathrm{nm}$ are also formed. SEM micrographs taken at section intervals along $5\,\mathrm{cm}$ samples show a similar deposition profile along their length.

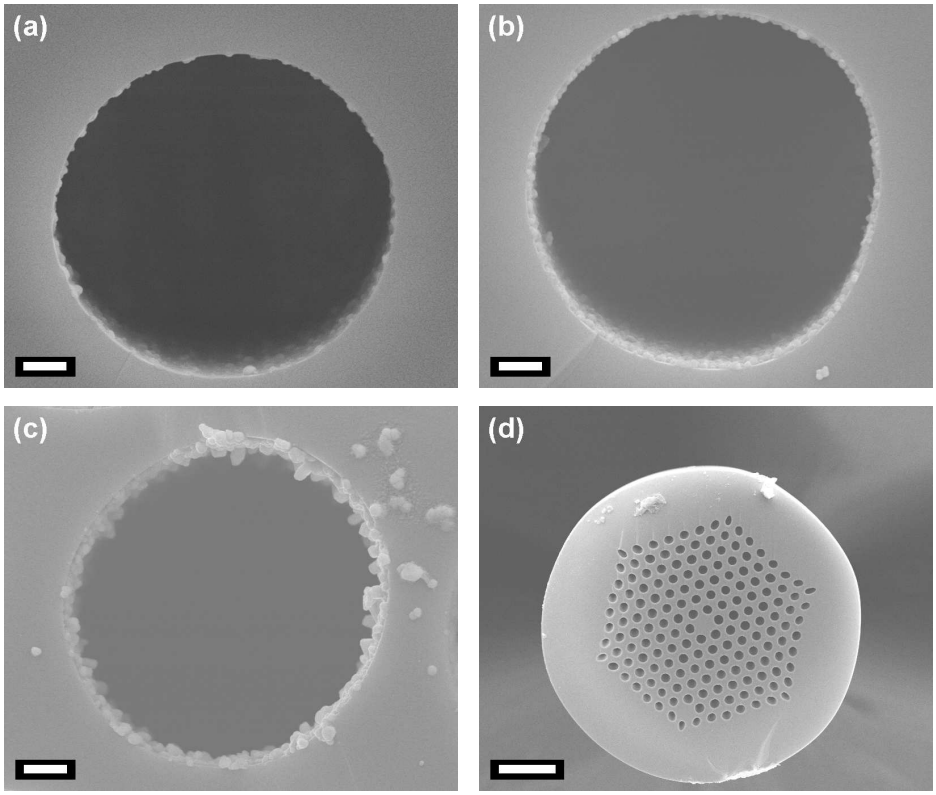

FIGURE 7.1: Silver deposition within the holes of a honeycomb fibre with a hexagonal lattice, the hole size is $\sim 7\,\mu$m in diameter and the pitch is $\sim 12\,\mu$m. (a) Thin deposition fibre, scale bar $1\,\mu$m. (b) Medium deposition, scale bar $1\,\mu$m. (c) Thick deposition, scale bar $1\,\mu$m. (d) Empty fibre template, scale bar is $40\,\mu$m

7.2 Transmission Properties of MOFs with Metal Inclusions

One of the major problems of plasmonic devices incorporating optical waveguides is how to couple optical energy from guided modes into surface plasmon modes, which exist on the air/metal interface. If the metal is deposited as a smooth film then this requires phase matching of the two modes. However, the strict phase matching requirements can be relaxed if instead the metal is deposited as nanoparticles, as described in Chapter 5. Under these conditions the plasmon modes will be localized on the surface of the particles and can be excited simply by launching light on or near the resonant wavelength, independent of the wavevector of the guided mode. Significantly, localized surface plasmon modes can generate even higher electromagnetic enhancements owing to the strong 3D confinement. The silver profiles achieved in the fibres, shown in Figure 7.1, are granular rather than smooth which suggests that indeed only localized surface plasmon modes will be excited. Efficient coupling to these modes can be ensured by

choosing fibre geometry. By exploiting the long interaction lengths of the guided modes it is expected that many plasmonic resonances can be excited along the fibre.

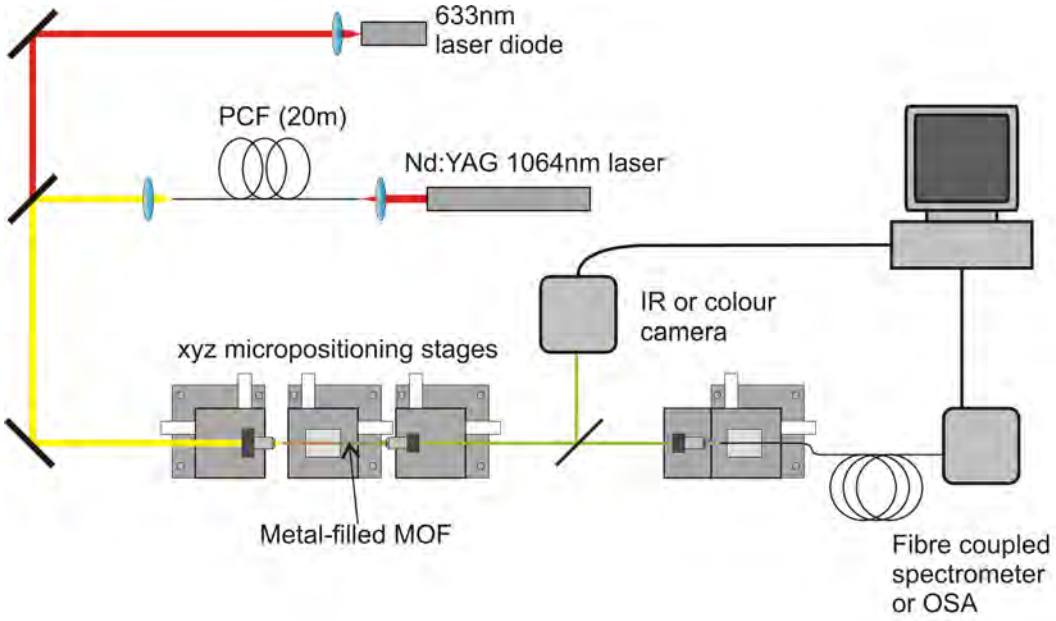

FIGURE 7.2: Experimental setup (not to scale) for transmission measurements of silver nanoparticles-filled MOF.

To study the optical properties of the silver nanoparticle impregnated MOFs, a visible supercontinuum laser has been used as the excitation source. A Q-switched solid state laser operating at 1064 nm and 1 ps pulse duration (from Teem photonics) is launched into 20 m of highly nonlinear MOF, with zero dispersion at the pump wavelength, (from Crystal Fibre). The nonlinear effects in the fibre broaden the spectral components of the pump pulses, generating up to 10 mW of supercontinuum light spanning from ~ 500 nm to $\sim 1.6\,\mu$m. To measure the optical losses at a wavelength which will be used in the SERS measurements, light from a 633 nm diode laser can also be coupled into the fibres. The experimental set up used in these experiments is shown in Figure 7.2.

Optical characterisation of MOFs with a hexagonal lattice of 168-holes with a diameter of $\sim 7\,\mu$m and $\Lambda \sim 12\,\mu$m is performed over the spectral range of 500 nm to 850 nm, where the long wavelength limit is restricted due to the operational range of the spectrometer. The light is launched via free space coupling with a 40× microscope objective lens into the cleaved end of the silver impregnated MOFs. The fibre is aligned with piezoelectrically controlled xyz micro-positioning stages. The transmitted light is collected by a second objective and focused onto a colour video camera. Figure 7.3 shows the near field mode profiles for (a) an empty silica control fibre, and two silver fibres corresponding to the deposition extremes where (b) is the thin deposition (Figure 7.1a) and (c) is the thick deposition (Figure 7.1c). Due to the short length of the fibres (~ 5 cm lengths) transmission of the lossy cladding modes can be observed, as seen in the top images. As

expected, there is a clear increase in the absorption of the light in the cladding as we move to thicker silver depositions as well as some wavelength selective absorption.

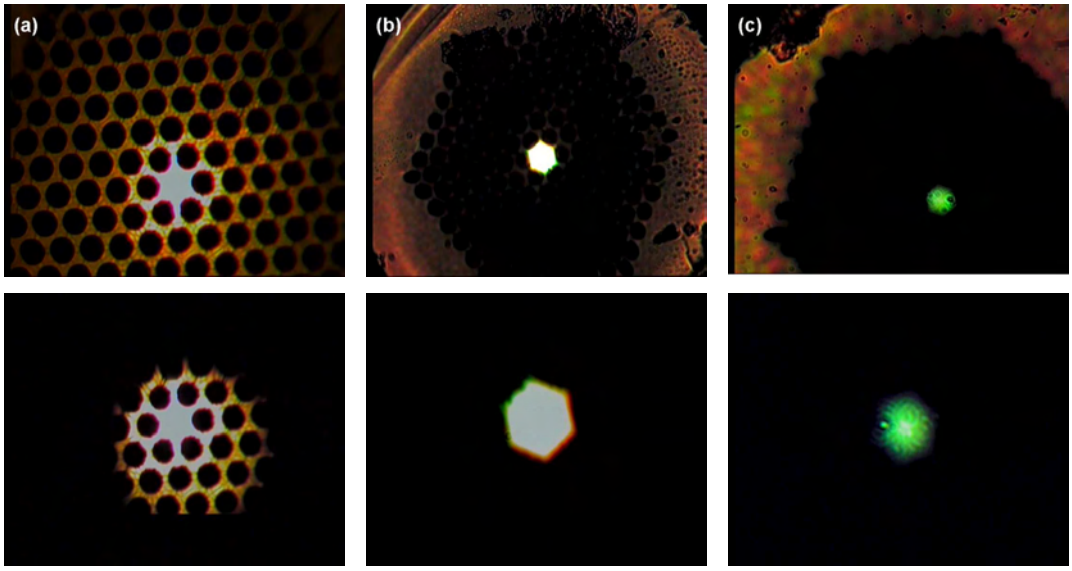

FIGURE 7.3: Near field images of the fundamental mode of (a) an empty silica fibre, (b) a thin silver coated fibre and (c) a thick silver coated fibre. Top images are without filtering to show the cladding modes, bottom images are taken after a pinhole to isolate the core guided light.

For the spectral measurements the guided core modes were isolated from those of the lossy cladding modes using a pinhole and the filtered modes are shown in the bottom images (Figure 7.3). The yellow colour of the light transmitted through the empty fibre is simply that of the supercontinuum source, confirming that there is no preferential absorption of the control MOF at any wavelength. Moving to the fibre with a thin silver deposition, the mode now has hints of colour around the edges suggesting that the silver absorption has altered its transmission properties. This is even more evident in the fibre with a thick deposition where there is clearly a strong absorption at the red end of the spectrum so that the mode looks bright green. To quantify the observations, the transmitted light is then focused into a collection fibre attached to an Ocean Optics 2000 spectrometer, with a detection range from 340 nm to 1000 nm. The resultant spectra obtained from the two silver fibres, normalized to the light transmitted through the control fibre, are plotted in Figure 7.4.

The noticeable lack of any strong resonant absorptions, typically associated with localized surface plasmon excitations, is attributed to the averaging over many particle sizes, interparticle separations and film thicknesses which can be excited due to the long interaction distance. The transmission spectrum for the thin deposition fibre shows an absorption that increases for longer wavelengths. This is in contrast with that of the thick deposition fibre where now there is a very strong absorption of the red end of the wavelength range which accounts for the green colour of the mode. The dramatic shift

of the absorption to longer wavelengths is not unexpected as it is well known that when the silver particle size increases the localized plasmon resonances are shifted from blue to red. Furthermore, when the particle spacings are of the order of nanometres then the interparticle interactions can shift the absorptions even further to the near infrared [301].

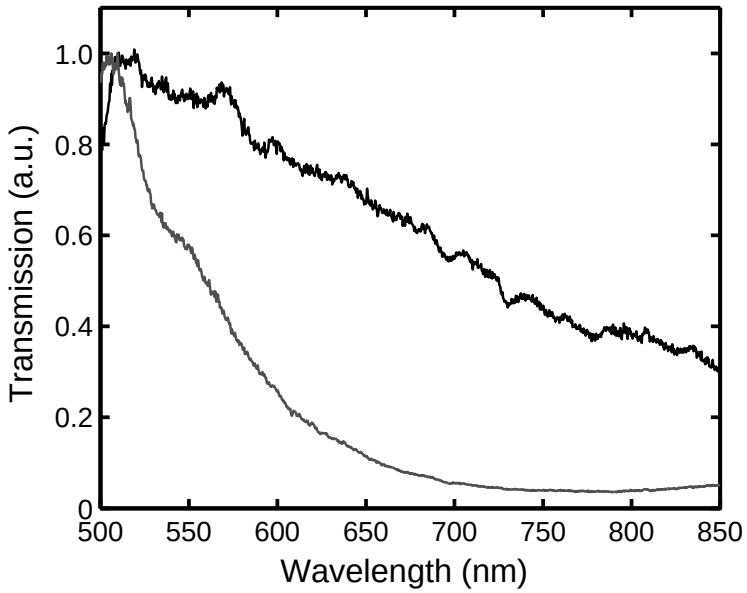

FIGURE 7.4: Transmitted spectra corresponding to silver impregnated MOFs with a thin deposition (black line) and a thick deposition (grey line), normalized to the transmission through an empty MOF.

One of the major obstacles to integrating plasmonic waveguiding devices within existing photonics infrastructures is the large inherent losses associated with surface plasmon waves, which typically limits device lengths to order of millimeters [289, 270]. However, by ensuring that most of the guided light is confined to the low loss silica core of MOFs it is possible to reduce the optical loss of the structures and thus push device lengths out to the centimetre lengths used in the above measurements. To quantify the losses corresponding to the various deposition profiles of the silver MOFs shown in Figure 7.1, cut-back measurements using a 633 nm continuous wave (CW) 2 mW laser were performed. As before, the light is free space coupled into the fibres using a 40× objective, with a second objective being used to collimate the transmitted light. The output power is measured with a Newport 2832C power meter with a silicon detector head. The transmission losses for the three fibres were measured to be: (a) ~ 0.6 dB/cm, (b) ~ 2.5 dB/cm and (c) ~ 5 dB/cm. This increase in loss for increasing silver thickness is as expected, and we attribute the notable low loss of the thin deposition fibre to the sparseness of the particle deposition. By assuming a 3 dB device loss tolerance, realistic length scales for these silver fibres are in the range $0.6 - 5$ cm, which are sufficiently long to be manageably handled. In general, conventional planar plasmon waveguides exhibit

lower losses for infrared frequencies than in the visible as reflected in the increased plasmon propagation lengths at IR wavelengths [302]. This is not the case in our MOFs geometry, as the longer wavelengths interact more strongly with the silver in the holey cladding, greatly increasing the propagation losses. Consequently, this highlights the importance of the design of the MOF structure to minimize the device losses for the required wavelength of operation.

7.3 SERS Characterisation

Since the discovery of SERS more than 30 years ago [276], there have been tremendous developments in the surface sciences and nano-processing techniques that have permitted the fabrication of SERS substrates with appropriate feature sizes. For example, using conventional semiconductor processing techniques, SERS templates have been produced via electron beam lithography [303], focused ion beam patterning [304], thermal evaporation [305] and chemical colloid reactions [306]. Although these substrates can provide high SERS signals, their fabrication can be costly, time consuming and is restricted to planar geometries that limit the interaction length over which plasmons can be excited along the device. On the other hand, templates ranging from polymer nano-spheres [307, 308, 309], to porous silicon [310] have been used for bottom-up fabrication of metallic SERS substrates. Conventional planar SERS substrates do not have any optical guiding mechanism therefore the interaction area between the electromagnetic field and the analytes is restricted to the spot size of the laser beam. The fibre templating technique, described in this thesis, circumvents these limitations by combining the very long interaction length of optically guided modes with a template whose size and shape can be precisely controlled without lithography and that is extremely robust.

Although adding a metal nanoparticle coating into the holes of the MOF increases the optical loss, due to the high absorption of metals at optical frequencies, centimetre long fibres enable the exploitation of plasmonic effects with acceptable optical loss. Previous attempts at fabricating fibre-based SERS substrates have exploited the immobilization of solution-based colloidal metal nanoparticles onto the silica walls [311] of silica capillaries. It is clear that this method does not provide control over the deposition thickness, the particle size is determined by the colloidal solution and, in order to achieve sufficient fluid flow, these devices have been restricted to internal dimensions of the order of $50\,\mu$m or greater which does not allow for engineering the optical-plasmonic properties of the resulting fibres. Moreover these devices do not support optical guided modes, which limits the photon-plasmon interaction to the short propagation distance of lossy capillary modes. Another example of previous fibre-based SERS substrates, is based on the thermal evaporation of metal nanoparticles onto the external walls of conventional

step-index fibres [295, 297]. Although, these fibres provide long interaction distances of the guided modes with the deposited particles, it has the disadvantage that the metal surface is exposed to the external environment which makes the system unstable and it must be handled with care. Whereas, MOFs with metal-nanoparticle inclusions, can be engineering to obtain the desirable optical-plasmonic properties, the silver coatings can be precisely controlled and are robust. Therefore they represent a promising platform technology for fully integrated surface enhanced Raman scattering (SERS) sensors.

The metal-nanoparticle fibre substrates were tested for SERS activity using benzenethiol as the target molecule. Benzenethiol is a suitable molecule for investigating SERS due to its distinct Raman features, strong affinity for coinage-metal surfaces, and formation of self-assembled monolayers. The measurements were conducted using a conventional Renishaw 2000 Raman spectrometer with a 785 nm Ti:sapphire laser excitation source, operating at an average power of 20 mW, and using a 20× microscope objective which produces a spot size of approximately 5 μm in diameter. In all the experiments only the Stokes signal was measured, as the anti-Stokes process is hundreds of time weaker.

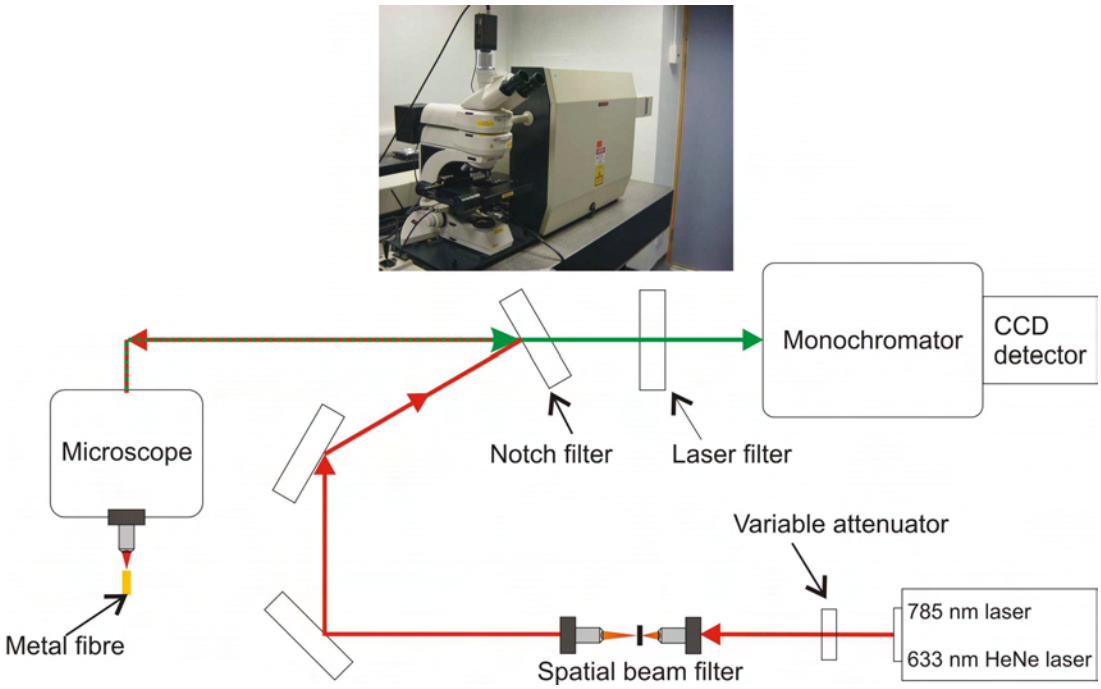

FIGURE 7.5: Schematic diagram and photograph of the Renishaw 2000 Raman spectrometer. A 633 nm HeNe laser was also used in SERS experiments.

Figure 7.5 shows a schematic diagram of the Raman spectrometer. As indicated by the red arrow the excitation laser light is directed into the spectrometer. The light is then directed through the spatial beam filter. The collimated beam is then reflected onto the notch filter, where it is directed into the microscope and it is focused onto the fibre's cleaved end. The Raman and Rayleigh scattered light and, reflected laser light are collected by the microscope and directed to the notch filter and through to the laser

filter where the remaining laser light and Rayleigh scattering are eliminated. The Raman scattering then goes through to the monochromator whose entrance slit is set to $50\,\mu m$ for all the measurements reported in this thesis. The diffracted beam is collected by the CCD detector. The Renishaw 2000 system can perform static or extended scans. A static scan records a spectrum from a narrow range of wavenumbers and the monochromator grating assembly remains still. Extended scans require movement of the grating and a spectrum can be recorded over a much broader range of wavenumbers, however the minimum integration time is 10 s for one scan. In order to normalize the intensity of the SERS signal obtained in different experiments, the intensity of the SERS spectra presented in this chapter is measured in counts/power/second where the photon counts detected by the CCD detector are divided by the power of the excitation laser and the integration time used in the experiment.

The SERS responde of two fibre template designs was investigated, an hexagonal array containing $18 \times 5\,\mu$m diameter air holes with a $20\,\mu$m silica core and a hexagonal array with $168 \times 12\,\mu$m holes and a $15\,\mu$m core. Samples from the resulting metal-filled fibres were prepared in ~ 15 mm lengths. Thus, for a 15 cm long silver coated fibre ~ 10 SERS substrates were obtained so that the individual fabrication cost of the substrates is low whilst the production rate is high. The sectioned samples were then treated with a drop of 1 mM benzenethiol solution in ethanol (purity $> 98\%$ Aldrich and HPLC-grade Aldrich, respectively). After the solvent had evaporated, the fibres were rinsed and then soaked in ethanol for 30 minutes. This procedure ensures that, at most, a monolayer of benzenethiol was present on the silver coating inside the fibres during the Raman measurements. In this process the sulphur atom chemisorbs onto the metal surface and the hydrogen atom is released thus changing the vibrational modes of the molecule.

Figure 7.6 compares a typical SERS spectrum from (a) a metal functionalised MOF with that of (b) a bulk Raman spectrum of neat benzenethiol. The distinctive characteristics of both spectra can be assigned to the aromatic ring vibrations. The bands at $1586\,\mathrm{cm}^{-1}$ and $1000\,\mathrm{cm}^{-1}$, in the Raman spectra of neat benzenethiol are redshifted to $1574\,\mathrm{cm}^{-1}$ and $997\,\mathrm{cm}^{-1}$ for the SERS spectra of a monolayer of benzenethiol, due to the adsorption of the target molecule to the metal surface as shown in the inset of Figure 7.6(a). The SERS detection of a monolayer of benzenethiol in the silver-nanoparticle coated fibres is verified from the absence of the bands at $2567\,\mathrm{cm}^{-1}$ and $918\,\mathrm{cm}^{-1}$ in the SERS spectra, which are attributed to the stretching and bending vibrations of S-H molecular bond, as expected if all the molecules are attached directly to the silver surface [312].

To illustrate the uniformity of the deposition over the cross-section of the 168-holes MOFs, the SERS spectra was measured at different positions across the structured cladding. Under these launch conditions, the fibre modes that are excited are the lossy cladding modes that exist in the MOF templates because of the large silica fraction of

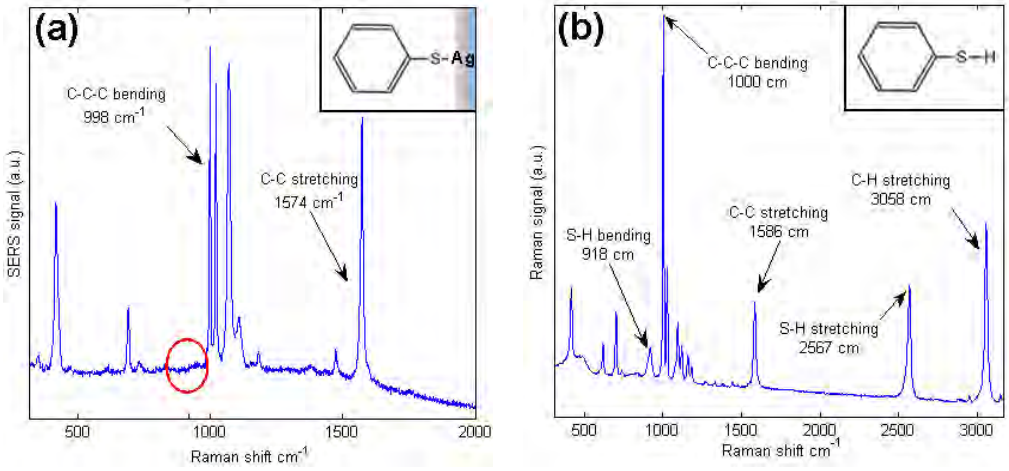

FIGURE 7.6: (a) SERS signal of benzenethiol on a silver impregnated fibre substrate, the absence of the S-H bond in the spectrum verifies that all the molecules are attached to the surface, areas enclosed by the red circles. (b) Typical Raman spectra of neat benzenethiol with a schematic of the molecule shown in the inset.

the cladding (see Figure 7.7a and Figure 7.8c). The benzenethiol molecules that are absorbed onto the silver nanoparticles within the fibre couple to the LSP modes, thus releasing Raman scattered photons. The generated Raman photons are collected with the same objective lens used to focus the incident pump beam. Figure 7.7c shows the collected spectra corresponding to the coloured positions marked on the SEM micrograph of Figure 7.7a. A strong signal is observed in all cases and the main vibrational modes of the target molecule can be assigned as reported in the literature [313] and again, detection of a monolayer is verified. Additionally, no Raman peaks were observed in a control fibre where 1 mM benzenethiol was impregnated into an empty (silica only) MOF. For the control fibre, the typical Raman spectra of silica, consisting of a series of broad peaks separated by $440\,\mathrm{cm}^{-1}$, was observed [314].

A significant feature of the spectra, presented in Figure 7.7c, is that the relative intensity is higher for the positions which are closer to the core of the fibre. To investigate this, the incident beam was focused onto the silica cores of the two different fibre templates (168-holes and 18-holes) to excite low loss guided modes. Figure 7.7b is a SEM micrograph of the 18-holes fibre. Figure 7.7d shows the measured SERS spectra for the two samples, together with a control spectrum obtained from a fibre that has no silver impregnation, clearly illustrating the intense signal detectable in this configuration. Although the optical guided modes concentrate most of their energy in the core of the fibre, a small part of the energy is located in the air regions surrounding the core as evanescent fields which interact with the silver coating and excite surface plasmon along the fibre length [311]. For the choice of pump wavelength, the fibres used in the experiments are multimode so that various LSP modes may be excited on a range of silver particles sizes.

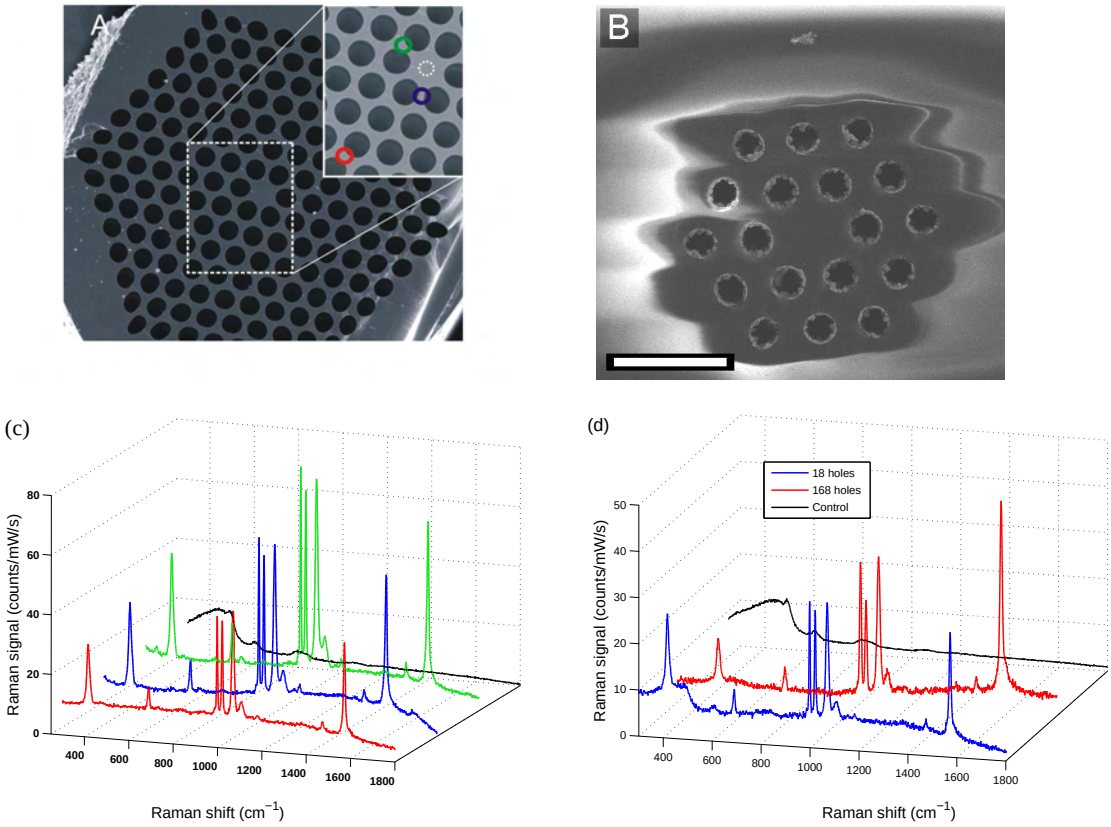

FIGURE 7.7: (a) SEM micrograph of the cleaved face of a low silver filling-fraction 168-hole MOF. A magnified view of the sampled area is shown in the inset. (b) SEM micrograph of the cleaved face of an 18-holes MOF, scale bar is 20 μm. (c) Colour coded SERS spectra across the cleaved face of a 168-hole MOF corresponding to the coloured positions marked on the micrograph inset. (d) SERS spectra obtained from the 18 and 168-hole templates, with the incident excitation beam focused onto the silica cores as indicated by the dotted circle in the micrograph. In both spectra the Raman response from a control MOF with no silver filling is overlaid in black. To facilitate comparison, the SERS spectra have not been background corrected, but have all been shifted to have a baseline close to zero (counts/mW/s).

As measured in Section 7.2, the losses of silver impregnated fibres with moderate particle sizes and film thicknesses are typically $\sim 2\,$dB/cm at 633 nm. This indicates that the 15 mm long fibres used in our experiments can provide a much larger interaction area compared to a planar substrate where the area is determined solely by the spot size of the pump laser. Furthermore the mode guiding mechanism allows for averaging over the various particle sizes and spacings thus moderating the effects of "hot spots". Owing to the unusual 3D geometry of the MOF SERS substrate the calculation of a precise SERS enhancement factor, following the conventional methods presented in the literature, is nontrivial [258]. However, given a number of assumptions a lower bound on the SERS enhancement factor may be calculated. In particular a single monolayer coverage, with

a packing density of 6.8×10^{14} molecules/cm^2 [315], over the entire 15 mm length was assumed and the percentage of the fundamental guided mode in the air to was used to estimate the power in the excitation field. Comparing the SERS measurements to a standard Raman measurement on neat benzenethiol, the resulting enhancement factor is estimated to be greater than 10^4, which compares favourably to enhancements reported elsewhere in the literature.

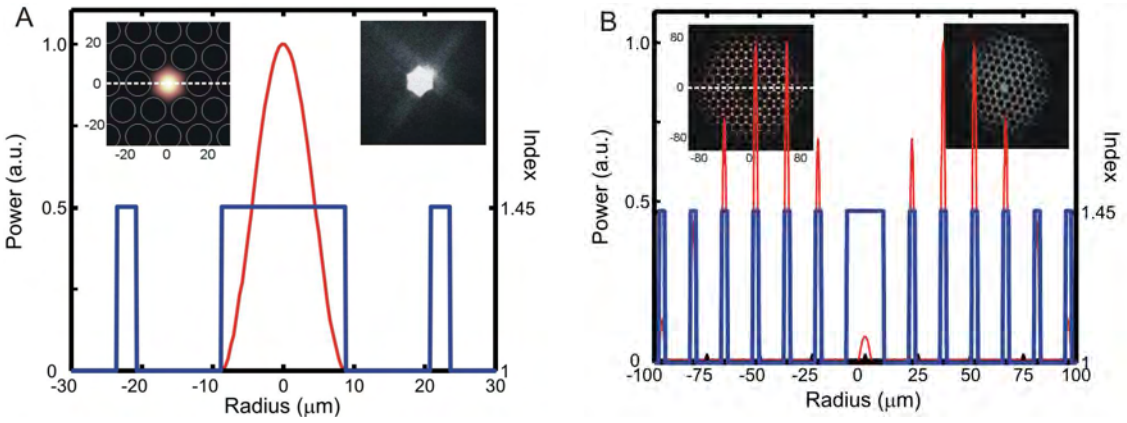

FIGURE 7.8: Calculated mode profile of the 168-hole MOF showing (a) the fundamental guided mode and (b) the cladding filling mode at an excitation wavelength of 785 nm. The figures show the normalized power distribution across the silica MOF as a function of radial position, as indicated by the dotted lines across the 2D intensity plots shown in the top left insets. The top right insets show the distributed modes generated by launching a 633 nm laser into the control silica (i.e. no silver) fibre as imaged by an Electrophysics 7290A Vidicon IR camera.

Using the FEM software, the propagation constant and field distribution of the fundamental and higher order modes of an empty MOF were calculated. As shown in Figure 7.8a, the low loss fundamental guided mode in the core has only a small fraction of the overall power propagating in the air, resulting in relatively low excitation of nanoparticle plasmon resonances per unit (cross-sectional) area when silver is deposited inside the MOF. However, this is compensated by the long propagation length of the fundamental mode so that a large number of nanoparticle resonances can be excited adjacent to the core. Raman photons generated along the fibre are thus efficiently collected and guided by the high numerical aperture silica core and detected by the spectrometer. Conversely, in Figure 7.8b an example of a lossy cladding mode is shown which is far more delocalized across the periodic hole array and has a larger component propagating in the air with little or no power in the core. This results in substantially different behavior as the area of plasmonic interaction is larger, and many more silver nanoparticles will be excited per unit area; however, this increased excitation efficiency is offset by the lossy mode's shorter propagation distance, resulting in fewer plasmon resonances throughout the length of the fibre. In addition, the generated Raman photons are not well coupled

and localized by the high NA core, resulting in low detection efficiency for this particular setup. In either scenario, the detected SERS signals obtained with the 168-fibre are approximately equivalent in magnitude as can be seen by comparing the graphs of Figure 7.7c and Figure 7.7d (showing the SERS response from various positions on the cladding and core respectively), suggesting that the relative trade-offs of both modal excitation conditions roughly balance each other out, for this particular fibre template.

Given the conflicting criteria of many nanoparticle plasmon excitations per unit area, versus long optical propagation distances and efficient Raman photon collection and detection, it would at first appear that further improvements to the optical fibre based substrates will have to operate within these opposing constraints. However, the 168 and 18−hole MOFs used in these experiments are early stage designs and are thus relatively simple proof-of-principle structures with large, non-optimized feature sizes. Indeed, for the laser wavelength used in these experiments (785 nm), the large 20 μm diameter core results in very few guided modes with any significant penetration of the optical power into the air holes. This suggests that in order to combine the desirable properties of large excitation areas with long propagation distances and efficient collection/detection, the ideal optical fiber characteristics would exhibit a large NA together with low loss guided modes that have a large optical component propagating in the voids. These criteria can be satisfied by a MOF design that has a small core diameter and a large air fraction honeycomb cladding [316] as this retains the high core-cladding refractive index contrast required for large NA, but at the same time requires the guided modes to propagate with a large amount of power in the air due to the small core size.

An important consideration into the practicality of a SERS substrate is its temporal stability. Silver is regarded as having superior plasmonic properties to gold at visible wavelengths [216] due to the larger real (negative) part of its dielectric constant and its smaller imaginary (loss) component. However, as silver is prone to oxidation resulting in the strong suppression of surface plasmons, it has been largely neglected as a material for fabricating SERS substrates with high reproducibility. Despite this potential problem, the fibre structures demonstrated here have been shown to generate efficient SERS signals months after they were fabricated, without special storage considerations, highlighting the temporal stability and mechanical robustness of the substrates.

7.3.1 Fibres with Different Geometries

In order to investigate the above claim of optimised excitation with a small core geometry, a new fibre template was impregnated with silver nanoparticles. A MOF template based on a $126 \times 1\,\mu$m hole structure with a small $\sim 1\,\mu$m diameter silica core (see Figure 7.9) was chosen due to its small dimensions. This fibre structure has a larger overlap

between modes guided in the core and the silver particles surrounding the core. Thus a higher enhancement of the SERS signal of molecules attached to the metal surface is expected when light is launched into the core. The propagation of light launched into the cladding will be restricted to very short distances due to the high loss of the cladding modes. Samples from both fibre geometries ($168 \times 12\,\mu$m holes and $126 \times 1\,\mu$m holes) were tested for SERS activity. In these experiments aminothiophenol was chosen as the target molecule due to its lower toxicity than benzenethiol. As for benzenethiol, aminothiophenol can easily form monolayers when its S-H group forms a S-metal bond onto coinage metal surfaces. Again the SERS spectra of aminothiophenol monolayers, attached to the metal surface, present characteristic features which differ from the Raman peaks of the bulk material [317].

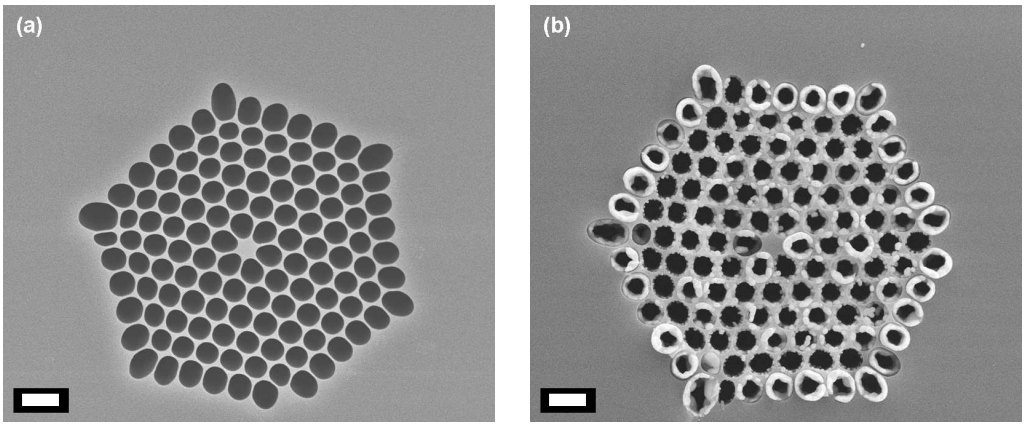

FIGURE 7.9: SEM micrographs (a) of the small core fibre template and (b) a silver-filled fibre, scale bars are $2\,\mu$m in both images.

In these experiments the silver-filled fibres were again sectioned in ~ 15 mm long samples but this time treated by soaking them overnight in a 1 mM solution of aminothiophenol in ethanol. Following this the samples were washed then soaked in ethanol for 2 hrs. This procedure removes all molecules not attached to the metal surface [318]. Finally the fibre ends were hand cleaved leaving a clean surface. Figure 7.9 shows SEM micrographs of a small core fibre (a) before and (b) after silver impregnation, where in this case the deposition thickness is ~ 200 nm, slightly less than that of the large core fibre shown in Figure 7.1b.

In the following experiments the SERS signals were collected with a Renishaw 2000 Raman microscope, similar to that used in the previous experiments, but now using a 633 nm HeNe laser excitation source. The excitation laser was focused with a $50\times$ objective to a spot size of $\sim 2\,\mu$m onto the cleaved ends of the sample. The SERS spectra obtained from the small core fibre, plotted in Figure 7.10a, show a clear difference, with the signal of the core being $\sim 10\times$ larger than that obtained from the microstructured cladding. However, the SERS signal obtained from the core of the large structured fibre,

shown in Figure 7.10a, is similar to that from the holey cladding, as expected from Figure 7.7. Furthermore, owing to the greatly improved interaction between the light and the silver nanoparticles, the small core fibre exhibits SERS signals more than an order of magnitude stronger than the large structure when focused in the core. This finding highlights the possibility of tailoring the plasmon-photon interaction within metal-filled MOFs via modal overlap engineering.

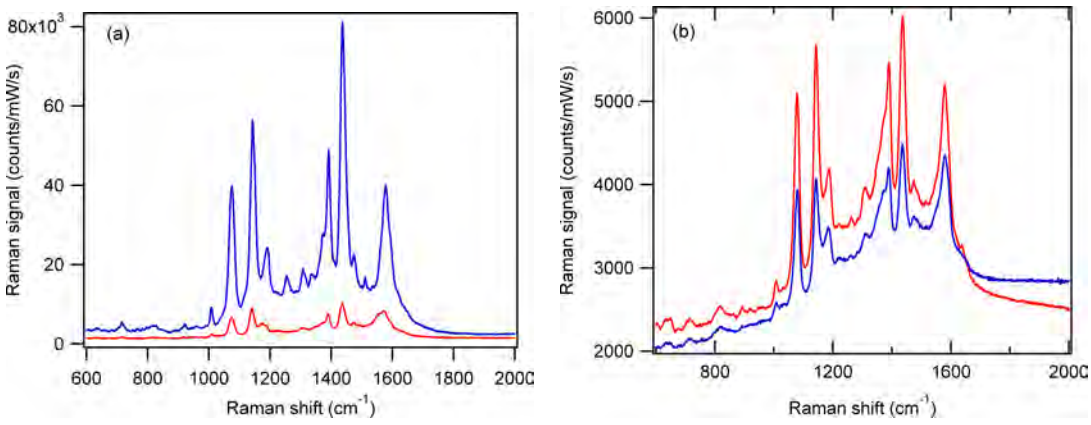

FIGURE 7.10: SERS spectra of aminothiophenol obtained from silver impregnated MOFs. (a) Spectra from small core MOF template and (b) from large MOF template. The blue spectra are obtained with the excitation laser focused onto the silica cores. The spectra plotted in red are the signals obtained with the incident light focused onto the structured claddings.

7.3.2 Remote SERS Sensing

Following the successful optimisation of the core guided excitation mechanism, the small core fibre was tested for potential use in remote sensing applications. For this experiment silver was deposited in the last three centimetres of a 15 cm long fibre. Thus the SERS active region was confined to the tip of the MOF. The silver end of the fibre was treated with aminothiophenol using the procedure described previously. The pump laser was then launched into the fibre core at the empty end, using a 50× objective. The light propagating down the fibre interacts with the metal modified end, where the SERS signal of aminothiophenol is excited, and some of the scattered light is guided back to the input end where it is collected by the same lens. The collected SERS signal is displayed in Figure 7.11.

Although the SERS signal obtained from the remote sensing experiments presents a high background such that its intensity is larger than the intensity of the measured vibrational peaks, definite features of the SERS spectra of aminothiophenol can be recognized as indicated in Figure 7.11. It is expected that improvements on the deposition profile and fibre geometry will result in more efficient and sensitive remote SERS sensing devices.

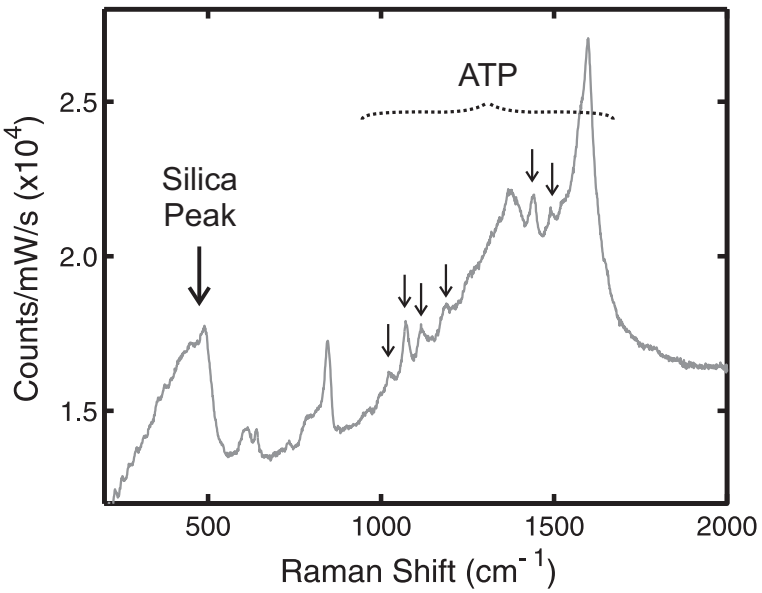

FIGURE 7.11: SERS signal of aminothiophenol obtained in a remote sensing configuration.

7.4 Efficient Electrical Characterisation of the SERS Substrates

In addition to examining their optical properties, silver impregnated MOFs can also be electrically characterised to establish both the homogeneity and quantity of deposition. Similarly the SERS signal, detected when analyte molecules are infiltrated within the structures, can be directly correlated to the deposition profile of the nanoparticles within the MOFs. Therefore, by assuming a direct correlation between electrical measurements and SERS response it is possible to use this method as a fast and non-destructive method of scanning quickly through a number of SERS fibres to find those with optimized deposition profiles.

Electrical resistivity measurements on two 18-hole fibres with different silver filling fractions were performed. The fibres were prepared by placing indium-gallium eutectic onto cleaved ends, with the polymer coating removed. This provided a low resistance contact between the fibre and the probe station, as illustrated in the inset of Figure 7.12a. Figure 7.12 shows the current vs. voltage curves with silver filling fractions (defined as filled cross-sectional area of each pore) of approximately (a) 40% and (c) 10%, for different sample lengths. For the fibre with a higher silver filling fraction, the resistance per millimeter of a 23 mm long sample increased slightly from 33.4 Ωmm to 36.2 Ω/mm after recleaving to 6 mm (Figure 7.12a), whereas for the lower silver filling fraction fibre the resistance per millimeter decreased from 46.30 MΩ/mm at 27 mm, to 17.61 MΩ/mm at 18 mm and 19.11 MΩ/mm at 9 mm lengths (Figure 7.12b). This variation of the I-V

behavior along the fibre length suggests that the deposition profile is not homogeneous for the low filling fraction sample.

These electrical measurements can then be related to the SERS response of the fibre where an inverse correlation between the electrical resistance properties of optical fibres and the signal strength was observed. This is illustrated in Figures 7.12b and 7.12d where the signal from the low filling fraction (high resistance) fibre is 3× higher than the (low resistance) sample with a high filling fraction, which can be attributed in part to the higher loss in the high filling fraction fibre. This very convenient electrical characterisation method thus allows us to quickly scan through a number of samples to establish which deposition profiles are likely to provide a strong Raman response, and to obtain samples with reproducible SERS response.

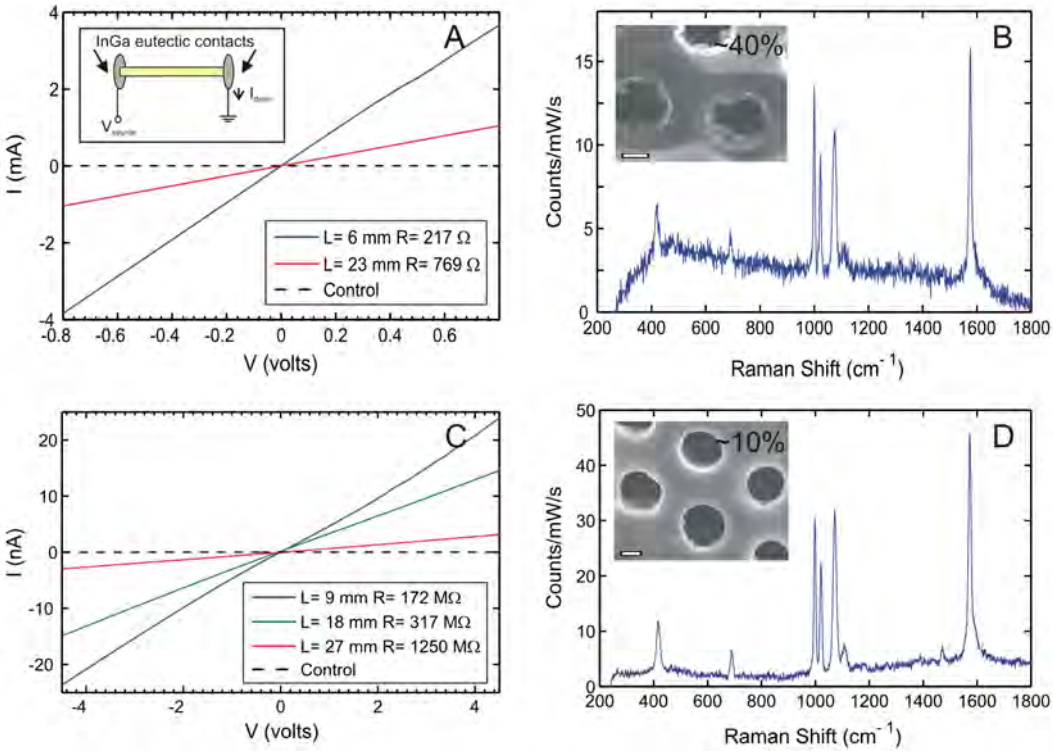

FIGURE 7.12: Current/voltage measurements on various lengths of two 18-hole silver filled MOFs with filling fractions of (a) ∼ 40% and (c) ∼ 10%. The samples had been cleaved at the ends and electrical contacts made with InGa eutectic (circuit diagram in top inset of (a)). The lengths corresponding to each spectrum are given in the insets, together with the calculated sample resistances based on an Ohmic model together with control measurements on an unfilled silica MOF (dashed lines). (b) and (d) display the corresponding SERS response of the different filling fractions shown in the micrograph insets.

Chapter 8

Semiconductor Quantum Dots

The previous chapters have described different material processing techniques that have resulted in the functionalisation of MOFs with silicon, germanium, polymers, metals and silver nanoparticles. As the quantum confinement effects in low-dimensional semiconductors results in superior material properties such as: small lasing threshold, modified electrical and optical properties [319], the development of fibres with semiconductor quantum inclusions has been relevant to this research, this chapter is the starting point for future functionalisation of MOF with semiconductor quantum dots. With this purpose in mind, work was carried out for the development of a chemical process that has resulted in the fabrication of colloidal PbSe quantum dots which exhibit luminescence at communication wavelengths. Colloidal quantum dots synthesized in solution can be coated onto the silica walls of MOFs by simply using the capillary action. The final experiments outlined in this thesis are focused on the synthesis and characterisation of the absorption and photoluminescence properties of PbSe nanocrystals.

8.1 Introduction

An important characteristic of macroscopic size matter is that its physical properties are fully independent of the dimensions. An example of this is the energy gap that separates the conduction from the valence energy bands of a semiconductor. In bulk semiconductors the width of this bandgap is a fixed parameter, which is determined by the material structure. However, this situation changes in the case of nanoscale particles, with size of the order of $\sim$ 10 nm (few atoms, 100s to 1000s). Within this size regime the properties of materials can be tuned through their physical dimensions rather than by the traditional way of varying composition. In a nanoscale system, the surface atoms constitute a major part of the structure and due to the close proximity between central

atoms to the surface, the particle boundary affects the overall properties of the system. Almost all properties seem to be tunable by the size, from luminescence to melting temperature. This phenomenon is called the quantum size effect and is observed in both metals and semiconductors [100, 320]. In the case of semiconductors, quantum size effects are remarkable [319], for example the bandgap of CdSe can be tuned between deep red ($\sim$ 1.7eV) to blue ($\sim$ 3eV) as the size is varied from approximately 2 nm to 5 nm, this can be seen in Figure 8.1. As the QD size decreases, the bandgap increases which results in a blue shift of the emission wavelength (see Appendix A).

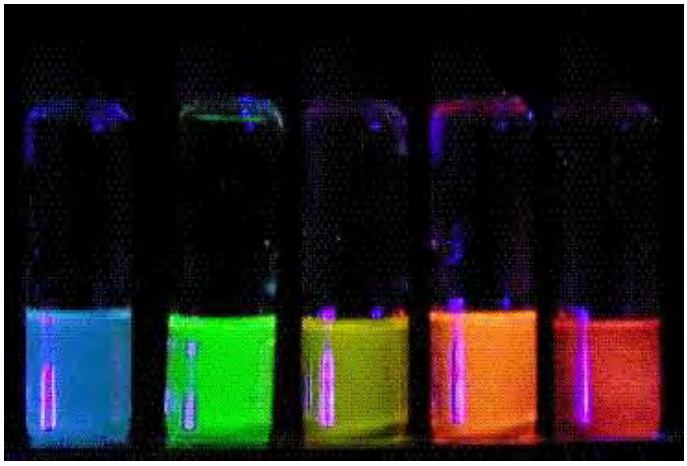

FIGURE 8.1: Photoluminescence of a series of different sized core-shell CdSe/ZnS quantum dots. All illuminated simultaneously with a hand-held ultraviolet lamp. From reference [321]

The confinement of electrons transforms the size-invariant continuum of electronic states of bulk materials into size-dependent electronic states in quantum systems. To understand how quantum size effects modify the electronic density of states (DOS) of the conduction and the valence bands of conductors and semiconductors, the Schrödinger wave equation is solved for a particle in a "box" having either 1, 2, or 3 spatial dimensions of the order of the Bohr radius of the electron, hole or exciton. As the dimensionality of quantum confined matter changes from that of a 2D quantum well, to a 1D quantum wire, and finally to a 0D quantum dot (QD), the density of states changes from the classical parabolic shape of the bulk system, first to a 2D stepped parabola, then to a 1D inverse stepped parabola and finally to a 0D discrete form. A schematic illustration of the transformation of the density of states in semiconductors from bulk to quantum dots is shown in Figure 8.2.

In a semiconductor QD the 3D quantum confinement produced by the particle border restricts carrier motion in all directions, and the intraband scattering and relaxation processes seen in bulk semiconductors are strongly modified by quantum effects. The electronic spectrum of QDs consists of separated peak states with energy spacing that increases as the dot size is reduced. The unique possibilities for tailoring the physical,

electronic and optical properties of zero dimensional systems have attracted a diverse range of potential applications for semiconductor QDs, most notably in precise wavelength light-emitting diodes [322], optical gain media [323], biological fluorescence labeling [324], full color displays, electronic switches and recording media [325]. CdSe and CdS quantum dots systems have been successful characterised for photonic applications at visible wavelengths. Klimov and co-workers have demonstrated optical gain phenomena, such as amplified spontaneous emission in thin films of infrared-emitting PbSe nanocrystals [326]. PbSe quantum dots are among the few materials that can provide size-quantized exciton transitions at telecommunications wavelengths. In addition, they have relatively large Bohr radii that can readily provide access to the quantum confinement regime at room temperature [327]. Research into applications of colloidal quantum dots has largely focussed on optoelectronic planar devices. However, due to the interesting optical properties of PbSe quantum dots in the telecommunications windows, it is motivating to introduce these nanostructures into MOFs for the development of QDs based optoelectronic fibre devices.

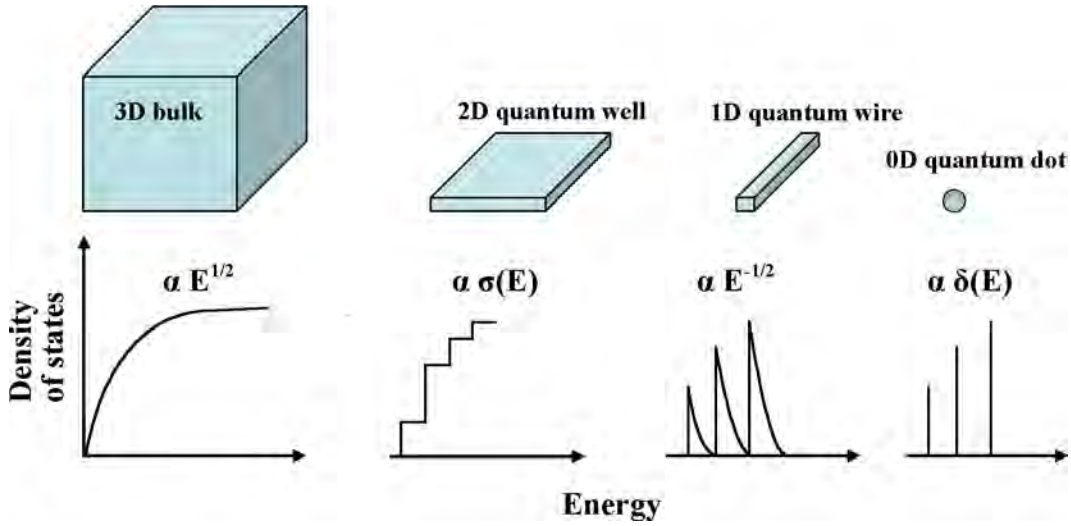

FIGURE 8.2: Density of states as a function of energy of quantum-confined semiconductor structures. As the degree of confinement increases the carriers occupy increasingly fewer energy levels. QDs have a peak-like density of states enabling a higher concentration of carriers to contribute to the band-edge optical material emission. This provides important applications for quantum systems, in principle, ultralow threshold laser diodes [328]. $\sigma(E)$ and $\delta(E)$ denotes the step and Dirac-delta functions respectively.

8.2 Synthesis of PbSe Quantum Dots

Although the size dependence of the optical properties of metals has been studied since the 19^{th} century (see Chapter 5), this is not the case for semiconductor nanocrystals. It

was not until the last two decades that intense research aimed at making monodisperse semiconductor quantum dots, in order to study the size evolution of their chemical and physical properties, has been carried out. The fabrication of these QDs has been approached by two different techniques. The first and most common and conventional, is a physical top-down approach in which the dimension of bulk material is physically reduced. Some examples include lithography and molecular beam epitaxy. The second, is the wet-chemical technique in which a quantum dot is formed by self-assembly of the constituent atoms [319]. The most widely used wet-chemistry method is often referred to as arrested nucleation and growth. This process is based on chemical replacement reactions between chemical compounds providing metal ions (Cd^{2+}, Zn^{2+}, Pb^{2+}, etc.) and those containing chalcogenide ions (S^{2-}, Se^{2-}, Te^{2-}, etc.). The general reaction scheme, for the example of PbSe, reads as [329]

$$N(Pb^{2+}+Se^{2-}) \rightarrow (PbSe)_N \tag{8.1}$$

The chemical synthesis of semiconductor QDs usually results in small nanoclusters capped by an organic monolayer which are rapidly nucleated and then slowly grown in solution. It allows for the fabrication of dots down to the truly atomic regime of 1 nm to about 20 nm, thus providing easy access to quantum size effects. Due to the organic capping layer, these QDs have numerous superior attributes compares to lithography synthesised QDs. For instance, the organic capping layer provides the nanocluster with solubility properties in a wide range of nonpolar and polar solvents, control over surface functionality and chemical passivation of the surface. In addition, the dots can be processed much faster and cheaper than with MBE, or any other top-down lithographic method and for the purposes of this thesis QDs in solution can be deposited inside MOFs.

Following on from a series of experiments concerning the organometallic synthesis of capped semiconductor nanocrystals by wet-chemistry [330, 331, 332], several different synthesis strategies have been reported for narrow band-gap II-VI infrared emitters. The most notable of these being the work of Wehrenberg *et al.* [333] and Du *et al.* [327]. The basic idea behind the synthesis is to rapidly create a large number of viable PbSe seeds, from suitable precursors at saturation, and then allow these seeds to grow at the same rate and end up with TOP capped PbSe nanoclusters (TOP, trioctylphosphine, is a surfactant-ligand-solvent). The most commonly used process, as described by Wehrenberg, requires the synthesis of stable precursors of lead and selenium, which are then combined at room temperature under an inert atmosphere. This stock solution is then rapidly injected into a comparable volume of a coordinating solvent, or surfactant, at a high temperature, which has the effect of stripping away the protective organic components of the precursors, allowing them to react, giving rise to Pb(II)Se which

forms a black insoluble solid and precipitates out of solution. In this research, our group have explored a more convenient "one-pot" method of thermo-solvolytic precipitation, which offers greater control over important parameters, such as reaction temperature and component concentration.

In the synthesis of PbSe QDs, high-quality starting materials, ACS grade Pb(II) acetate trihydrate and elemental selenium pellets were used. Firstly, the required organometallic lead component Pb(II) oleate was prepared by suspending Pb(II) acetate $\cdot 3H_2O$ (0.76 g, 2 mmol) and oleic acid (2.82 g, 10 mmol) in a 100 ml round-bottomed flask containing 40 mL of diphenyl ether. This suspension was placed on a rotary mantle oven for 2 hours at a temperature of 135 °C. The process replaces acetic acid with oleic acid, thus stabilizing the Pb(II) cation. The process additionally distils off the displaced acetic acid and any residual water of crystallization from the original salt. When the process is finished the solution looks yellow and the temperature is decreased to 100 °C

The selenium precursor, trioctylphosphine selenide (TOPSe), was prepared by dissolving selenium pellets directly into trioctylphosphine (TOP) to provide a 1 molar solution. Rapid stirring over the course of several hours ($\sim$ 24hrs) was required to dissolve the pellets and care was taken to maintain an inert environment.

Once the organometallic precursors are ready, a typical experimental procedure involves placing freshly prepared Pb(II) oleate solution (2 mmol of lead), with a large stirrer bar, into a three-necked flask under a constant flow of nitrogen. This flask is then placed into a temperature-feedback controlled heating mantle at the required reaction temperature ($\sim$ 100 °C) and allowed to equilibrate.

The reaction is initiated by rapidly injecting 6 mL of TOPSe (6 mmol selenium) into the hot flask, whilst maintaining inert conditions, by injection through a septum. If carried out effectively, this step should produce a rapid nucleation of PbSe QDs and, as they grow, the solution's colour changes from yellow to brown/black. This is characteristic of the absorption spectrum of PbSe nanocrystals in the IR. Aliquots (about 1 ml) of the proceeding reaction are taken at noted time intervals to permit the later examination of the time course of the nanoparticle growth. Colloidal QDs are then directly injected into a flask with an excess volume of methanol at room temperature, to inhibit further growth and to dissolve out the undesired solvent, unbound coordinating molecules and unreacted precursors. As the newly synthesized nanocrystals are coated in TOP, they are very insoluble in polar solvents such as methanol. Hence they are precipitated out of solution and may be recovered by centrifugation.

As was mentioned before, the synthesis is essentially a three-step process of nucleation, growth and ripening. Suitable experimental conditions and control of component stoichiometry allows for each of these steps, to some extent, to be controlled independently.

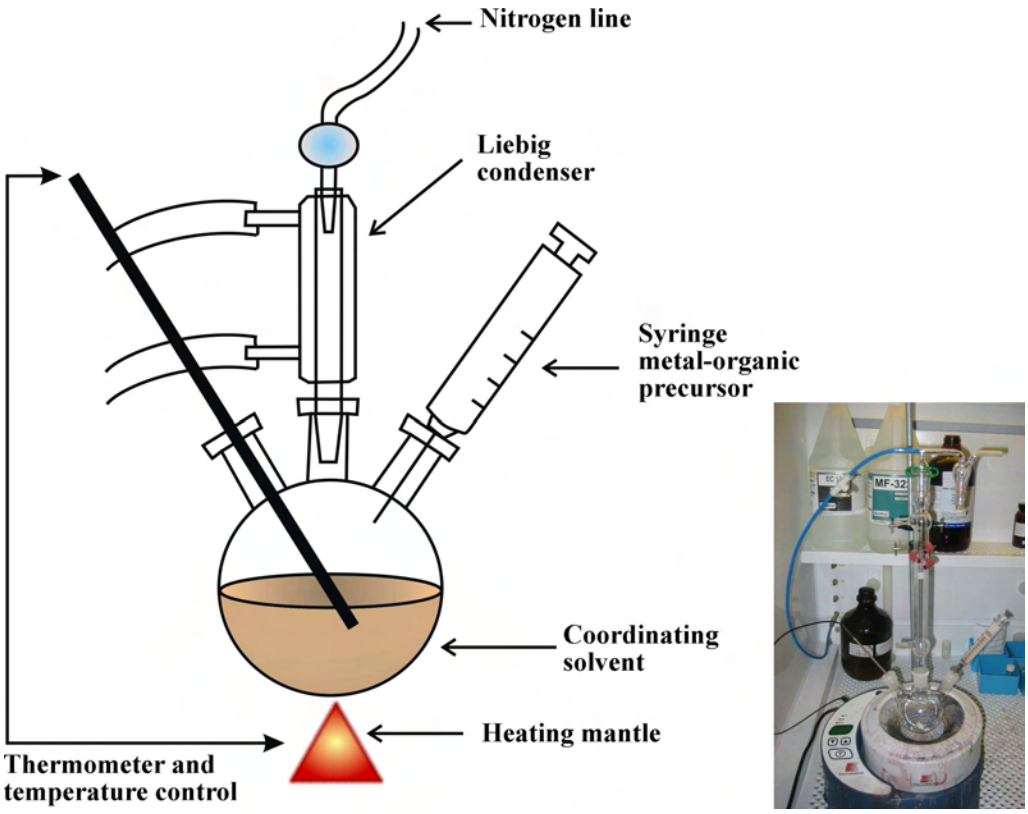

FIGURE 8.3: Schematic diagram of the experimental setup for colloidal synthesis of PbSe QDs. The reactions take place in 3-necked flask with a Liebig condenser attached to the middle neck and rubber septa for the introduction of reagents and a thermometer on the other two necks. The vessel is heated by a mantle, with temperature control via feedback. The entire apparatus is purged with nitrogen and kept at a slight overpressure by attaching the nitrogen line and a bubbler to the condenser. Inset photograph of the set-up.

The nucleation phase is primarily influenced by the temperature of the reaction vessel. Higher temperatures cause rapid and complete nucleation of the available precursors, resulting in little or no growth from solution, whereas lower temperatures result in low reaction rates due to increased precursor stability. In practice, reaction temperatures in the range of $90 - 110\,^{\circ}\mathrm{C}$ were used.

The growth phase is critically dependent on the lead:selenium ratio. Clearly, the lead and selenium precursors always react with the ratio 1:1; however, the different binding strengths of the oleic acid and TOP ligands have important consequences for the availability of free lead and selenium atoms during the dynamic phase of crystalline growth. It was possible to experiment with these factors by varying the concentrations of TOP (soft Lewis base) and oleic acid (hard base) in standardized reactions and also observe that this affects not only the growth rate but also the size distributions of the resultant nanoparticle ensembles. Most interestingly, it was found that any uncoordinated TOP from the TOPSe precursor plays a pivotal role in the growth stage and this may be due

to the premature stabilization of the surfaces of nascent nanocrystals, rather than an issue surrounding precursor stability. Perhaps, high concentrations of TOP within the reaction vessel may cause a high fraction of the nanocrystal surface sites to become TOP coordinated rather than solvent coordinated, leading to a retardation of the growth rate and a departure from the desired "size-focusing" regime [332]. This problem may be exacerbated by the disproportionate quantities of TOPSe used in many reported methods. On a related issue, it was also found that the reaction is sensitive to the purity of the TOP used. The rapid rates of reaction seen if freshly distilled high-purity TOP is used are not, in fact, conducive to the effective control of particle growth. However, in common with other alkyl phosphines, TOP will gradually oxidize to trioctylphosphine oxide (TOPO) if exposed to air and a large concentration of TOPO can potentially build up before any physical signs, such as the formation of solid crystals of TOPO, are noticeable. An ideal TOPO impurity concentration, where reaction rates and control over growth are optimal, is often seen some days or weeks after distillation of the TOP and the commercially available tech-grade TOP often produces satisfactory results. This synthesis does not appear to yield any useful product if the TOPO impurity content is subsequently allowed to increase still further over time. The effects of the ripening phase should be an increase in nanocrystal size, with a corresponding red shift in the relevant spectral peaks, as smaller particles coalesce (Ostwald ripening [334]). However, the ripening stage is difficult to isolate and in this context is effectively subsumed into the growth phase.

When the required nanocrystal size is reached, the reaction may be terminated by removal of the heat and the addition of a large excess of methanol into the vessel. The reaction product samples were treated by centrifuging ($\sim$ 5000 rev/min), which facilitated precipitation of the brown/black quantum dots. The methanol solution was decanted away and the product dried under a stream of nitrogen. The resultant oleic acid capped PbSe nanocrystals were stored under nitrogen and wrapped in aluminium foil until required. Subsequent spectroscopic analysis was carried out using samples dispersed into hexanes. The longevity of PbSe stored dissolved in hexane, or any other solvent, was not explored, however, we note that commercially available material is routinely stored and delivered in hexane.

8.3 Optical Characterisation of Semiconductor Nanocrystals

The absorption and photoluminescence (PL) spectra of PbSe QDs of different sizes were experimentally obtained. The growth temperature was 100°C. The absorption

spectra of solutions of QDs in hexane were taken using a Hewlett Packard dual-beam ultraviolet/visible/near-infrared spectrometer and using a hexane-only reference cell. The optical transmittance of light through samples is measured, after reference correction, as a function of wavelength. The absorbance,A, can be calculated as a function of wavelength by

$$\frac{I}{I_0} = 10^{-A}\,, \tag{8.2}$$

where I is the intensity through the sample at a particular wavelength. I_0 is the intensity through the reference hexane cell.

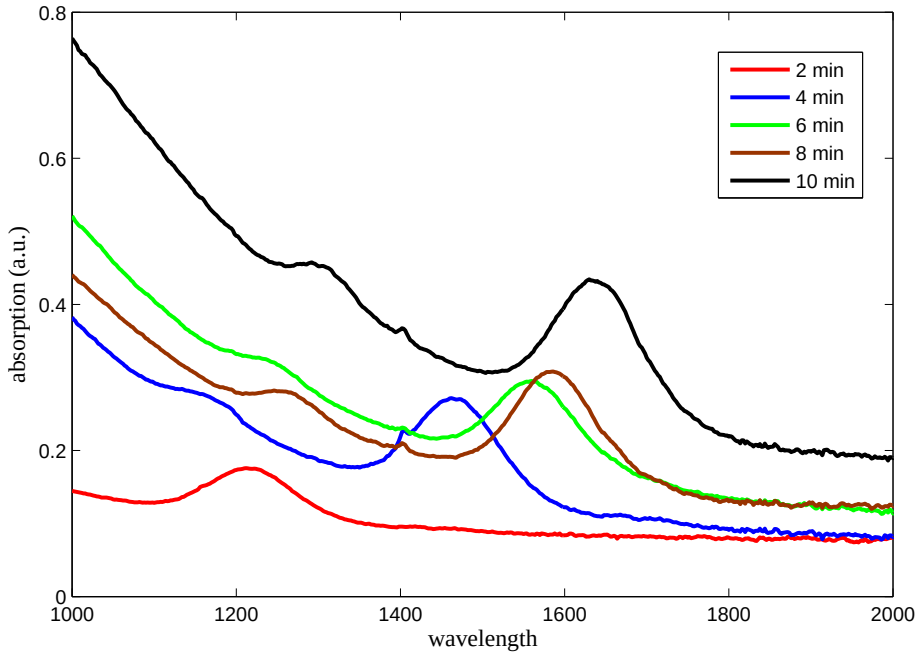

FIGURE 8.4: The above graphs display the absorption of PbSe quantum dots from a representative synthesis for different growth times from 2 to 10 minutes, after injection. The plots show the absorption peak tuning as the particle size (time) increases. The broadening of the absorption peak is mainly related to inhomogeneous size distribution.

As expected from quantum confinement effects, Figure 8.4 shows the absorption shift towards the blue of the bulk band gap of 0.28 eV (4.42 μm), locating the absorption spectra in IR telecommunications wavelengths. Also, the spectra show the principal transition ($\mathbf{1S(h)-1S(e)}$) absorption peak of the PbSe nanocrystals which is size tuned from $\lambda = 1200$nm to 1600nm between 2 and 10 min after injection. This demonstrate how the principal absorption peak may be effectively tuned across the $\sim 1.3 - 1.55\,\mu$m telecommunications window wavelengths, and thus allows for the use of these QDs in a

number of potential applications. The second exciton absorption peak (**1P**(**h**) − **1S**(**e**)) can also be seen at shorter wavelengths in some of the larger QDs absorption spectra. The relatively large electron, hole and exciton Bohr radii of PbSe (~ 23, 23 and 46 nm respectively) allows strong quantum confinement effects in relatively large structures and a very wide range of absorption wavelengths, from the visible up to around $4\,\mu$m, that may be sampled by tuning the particle size in the $1 - 40$ nm regime.

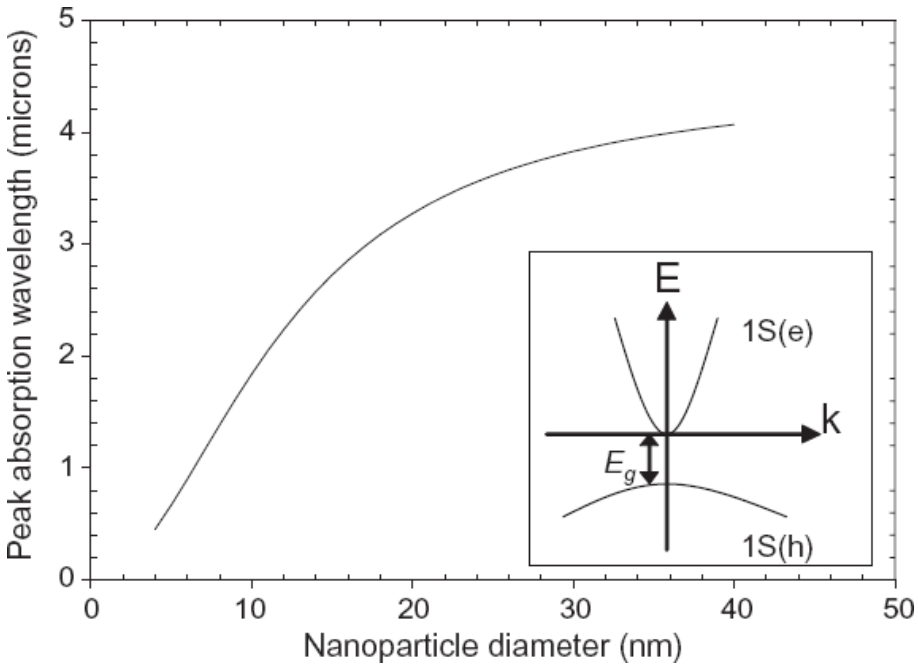

FIGURE 8.5: A two-level effective-mass model, predicting the variation in absorption peak wavelength with nanocrystal diameter, for spherical PbSe nanoparticles (see Appendix A). The parameters used in this model were $Eg = 0.28$ eV, $m^*(e) = 0.084m$ and $m^*(h) = 0.70m$, where Eg is the bulk band-gap energy and m is the electron rest mass. The inset shows a schematic band diagram for the **1S(e)** and **1S(h)** states of the PbSe quantum dot.

In order to correlate the absorption features of the experimental data with the particle size, an effective-mass model of the **1S(h)** and **1S(e)** band transitions has been developed for spherical particles of PbSe nanoparticles [335]. This model considers a semiconductor sphere with diameter (D) surrounded by an infinitely high potential barrier, and by using appropriate values for the conduction-electron and valence-electron effective masses and taking the bulk band-gap energy of PbSe to be 0.28 eV, the shift in energy of the **1S** levels can be calculated, as shown in Appendix A. The spacing between the **1S(e)** and **1S(h)** levels then defines the band-gap energy of the PbSe nanocrystal. Figure 8.5 shows the predicted band-gap energy as funtion of the particle diameter. This indicates that principal absorption wavelengths are expected to vary as the particle diameter changes and that diameters in the approximate range $7.7 - 8.5$ nm are requires to access the telecommunication-window wavelengths. Relating the absorption spectra in Figure 8.4 to the particle in a box model indicates that the mean particle diameter was

tuned from $\sim 7.3\,\text{nm}$ through to $\sim 9.4\,\text{nm}$ in that particular synthesis. Again by applying the particle-in-a-box model, the absorption peak broadening observed in Figure 8.4 can be related to an inhomogeneous particle size distribution. For example, in Figure 8.4 for the 4 min nanocrystals, the observed full width at half-maximum of the peak is $\Delta\lambda \approx 146\,\text{nm}$, the exciton absorption peak is centred at $\lambda \approx 1460\,\text{nm}$ and the mean diameter D is calculated to be $D = 8.32\,\text{nm}$. Assuming a Gaussian size distribution and the FWHM gives a ΔD of 0.54 nm which implies a $\Delta D/D$, size distribution of 6.5%. Therefore, it can be inferred that the colloidal synthesis used for the fabrication of the QDs yields a particle size distribution of approximately 5-10% [336].

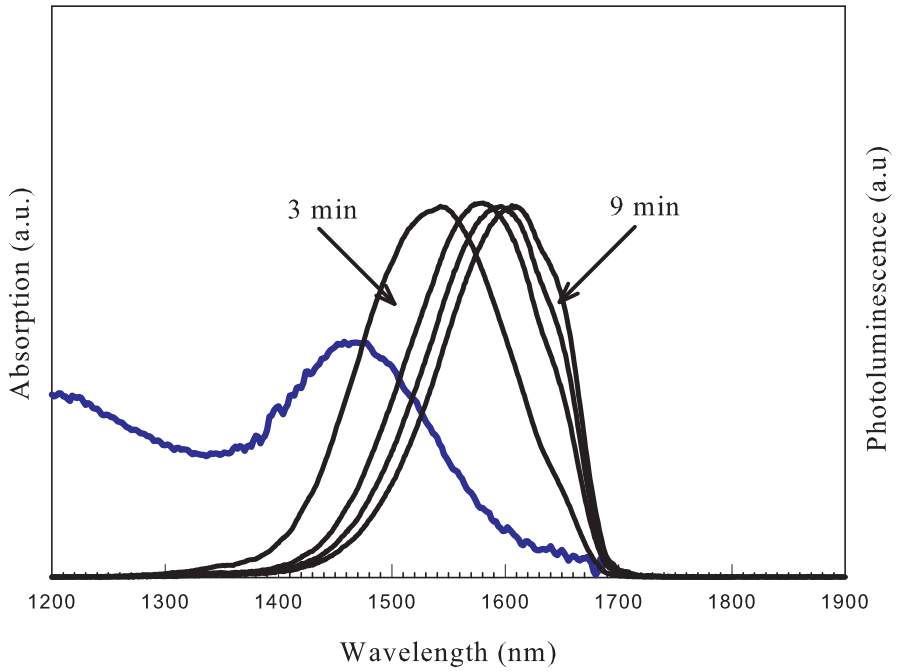

FIGURE 8.6: Normalized room-temperature photoluminescence spectra of PbSe quantum dots from a representative synthesis for different growth times 3, 5, 7 and 9 minutes after injection. The plots clearly show the size tuning of the PL peak with increased growth time. The QDs sizes were calculated by the parabolic bands and effective mass approximation, using the position of the absorption peak obtained in each experiment [335]. The diameter was calculated to be $D = 8.07\,\text{nm}$, $D = 8.4\,\text{nm}$, $D = 8.45\,\text{nm}$ and $D = 8.46\,\text{nm}$, respectively. The broadening of the features is due to larger size distribution as the synthesis time increases. The graph also shows the absorption of the 3 min QDs for reference (blue line).

In order to investigate the room temperature photoluminescent properties of the PbSe quantum dots, solutions of the samples in hexanes were placed into fluorimetry-grade silica cuvettes and excited with a $\lambda = 808\,\text{nm}$ pulsed laser diode. The photoluminescence was collected at a right angle to the excitation and was analyzed using a standard collimation and monochromator arrangement and an infrared detector, with lock-in amplification. Figure 8.6 shows typical PL spectra of different diameters PbSe quantum

dots. Growth times of 3, 5, 7, 9 minutes after injection were used to tune the nanocrystal size. In common with previous reports in the literature, the PL is somewhat ($\sim 40\,\text{meV}$) Stokes shifted from the absorption peak, owing to a fine-structure splitting of hole states, that is not accounted for in the simple effective-mass model described in Appendix A [337], the absorption of the 3 min quantum dots is also plot in the figure as reference. The spectral bandwidth of the luminescence is comparable to that of the absorption peaks, which suggests that the bandwidth is a consequence of the particle-size distribution. The ability to size-tune the absorption features of the PbSe nanocrystals across the telecommunications window also implies that it is possible to size-tune the PL in a similar fashion, as shown in Figure 8.6.

Of particular importance to the use of these materials in future applications is the issue of achieving high quantum yields (or PL efficiency) and the ability to measure and calculate this accurately. A technique of quantitative comparison between the QDs PL and that from an infrared dye of known quantum yield was used to accurately calculate the sample PL efficiency. The commercially available dye used was 'indocyanine green' which has a 12% quantum yield in dimethylsulphoxide (DMSO). For this trial, the optical densities of the sample and reference solutions were matched as closely as possible at the wavelength of the diode laser excitation source (808 nm), with both solutions placed into fluorimetry cuvettes of identical geometries and path lengths. Care was taken not to exceed an optical density of 0.1 in either cuvette, as this might lead to problems of self-absorption. Next, their PL was detected using the same detection set-up as described above. The geometries and circumstances of excitation and detection were therefore identical for sample and reference. Lastly, the PL spectra were compared in order to calculate an accurate PL efficiency for the PbSe nanocrystal sample. Using the definition of quantum yield

$$QY = \frac{\text{Number of photons emitted}}{\text{Number of photons absorbed}} \tag{8.3}$$

and by considering both the photon energy and the sensitivity response of the detector as functions of wavelength, it is possible to establish an accurate relation between the two PL irradiance spectra with the known dye PL efficiency. In order to determine the QDs quantum yield, the formula used in all PL efficiency calculations was

$$QY = \frac{\eta \int \lambda I_{sample}(\lambda) R(\lambda) d\lambda}{\int \lambda I_{ref}(\lambda) R(\lambda) d\lambda}\,, \tag{8.4}$$

where I_{sample} and I_{ref} are the irradiance spectra of the PL of the quantum dot and reference dye respectively, $R(\lambda)$ is the detector response function and η is the nominal quantum yield of the reference dye.

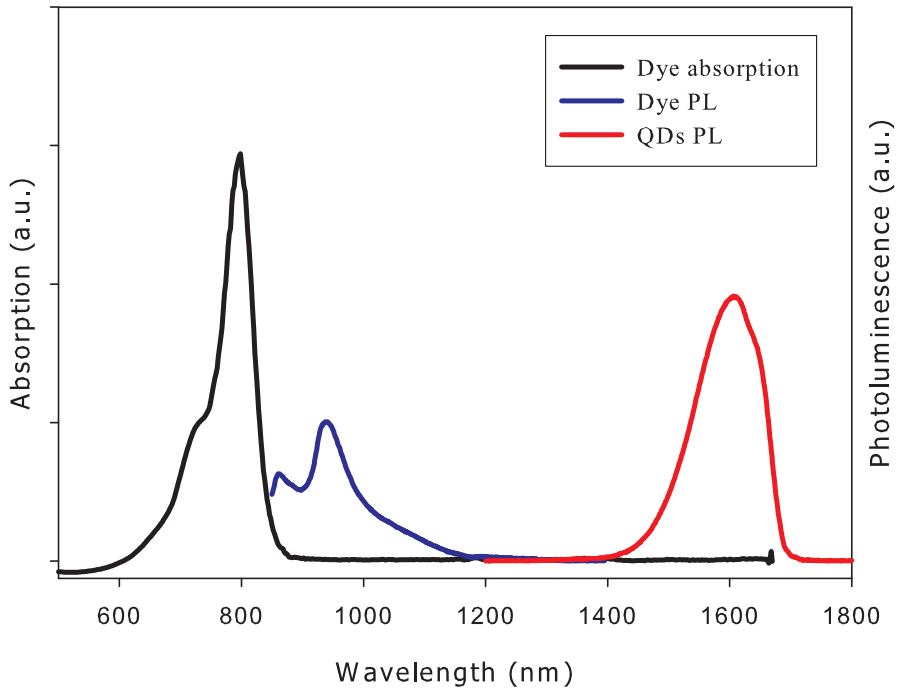

FIGURE 8.7: Absorption and photoluminescence spectra of the cyanine dye, indocyanine green in DMSO are shown together with the PL spectrum of a representative synthesis of PbSe nanocrystals. In order to make a correct "photons out-photons in" calculation of the PL quantum yields, the areas under the two PL spectra was calculate and the variations in detector response and photon energy with wavelength was taken into account.

Figure 8.7 shows the spectra from an experiment to determine the PL efficiency of a typical PbSe sample. The measured quantum efficiencies were as high as 60%, which compares favorably with other reported values [333]. Table 8.1 displays values of PL efficiency as a function of growth time (particle size). The results show a clear trend of the efficiency decreasing at longer growth times. This effect may be due to extrinsic factors during the fabrication process, such as the residual presence of moisture or oxidizing agents in the reaction vessel during the dynamic phase of crystal growth. Alternatively, variations in luminescence, "blinking" effects, due to size-dependent Auger recombination effects, as commonly seen in quantum-dot systems [338], may also play a role.

Growth time (min)	PL efficiency(%)
3	61
5	36
7	27
9	23

TABLE 8.1: Variation of the measured PL efficiency of PbSe as a function of the growth time.

Table 8.1 shows that the photoluminescence quantum yields at room temperature ranges between 23 and 61% and it is important to note that no inorganic surface passivation, such as capping with a semiconductor shell was required to obtain these high quantum efficiencies. The high quantum efficiencies observed in these experiments, combined with the high PL stability and photon energy tuneability of PbSe nanocrystals, open up the possibility to consider the inclusion of PbSe QDs within holey fibres as an active medium. To achieve this it is necessary to investigate the PL properties of the QDs when they are forming solid compounds. It should be considered that, although high PL efficiencies in solution have been observed, such values are not likely from solid films of the nanocrystals. This is due to the much smaller distances between nanocrystals in such films relative to solutions and, hence, the much higher probability of energy transfer of excitons between particles [339] and the increased likelihood of sampling a non-radiative centre or "trap" in the structure.

In conclusion, these experiments reveal that colloidal PbSe QDs synthesized following the method described here exhibit excellent properties: their emission can be tuned over $1.2-2\,\mu$m, they can be made to be very monodisperse and offer high photoluminescence quantum yields. By coating the inner surface of large diameter capillaries ($>75\,\mu$m in diameter), solution processed nanocrystal fibre structures have already demonstrated optical gain and lasing in a whispering gallery mode configuration [340, 341]. Future work will focus on the deposition of PbSe nanocrystals inside MOFs in order to add semiconductor functionalities to MOFs. For example, fibre laser devices will be fabricated by coating the inner wall of a capillary with a thin film of nanocrystals and by filling the core with a high index fluid to guide the excitation and emission light. Feedback to induce lasing will be achieved by incorporating the PbSe quantum dot modified fibre into a loop.

Chapter 9

Conclusions

In this thesis MOF have been successfully used as microfluidic vessels for the synthesis of materials within the fibre voids, by means of high-pressure chemical deposition techniques. Two main techniques, high-pressure CVD and supercritical fluid deposition were explored as potential routes towards the fabrication of hybrid fibre devices combining semiconductors, metals and dielectrics.

9.1 Summary of Results

This research has identified different experimental conditions for the conformal deposition of amorphous and polycrystalline silicon and germanium films. It was found that in order to obtain conformal deposition inside high aspect ratio capillary voids of MOFs, the semiconductor must be deposited at low temperatures, in the amorphous phase, and crystallization is then achieved by means of a post-deposition annealing process. The resulting silicon and germanium structures were thoroughly characterised with SEM, TEM and Raman studies, as well as by electrical transport and optical transmission measurements. When it was necessary to have access to the semiconductor material itself, HF etching was used to release the semiconductor wires and tubes from the MOF silica template. These free standing structures are the highest aspect ratio semiconductor wires/tubes fabricated to date by any known method.

SEM analysis showed that, by means of our HPCVD process, conformal tubes with uniform internal diameter are formed over centimetre lengths inside the capillary holes of MOFs. Capillary holes ranging from hundreds of nanometres to tens of microns in diameter can be either partially or completely filled with silicon and germanium.

TEM was used to extract qualitative information regarding the material structure and the crystallite size. TEM analysis shows that germanium wires grown at 500 °C are polycrystalline with crystallite sizes of the order of 500 nm in diameter. In contrast, the diffraction pattern of silicon wires grown at 700 °C, are featureless with broad rings and diffuse spots which implies that the material is polycrystalline, with amorphous and small crystallite phases.

The evolution of the structural composition of silicon tubes, grown at different processing temperatures, was studied using Raman spectroscopy. It was found that the material goes through many phases before reaching a polycrystalline structure. At low deposition temperatures (450 °C), the material produced is amorphous and its Raman spectrum shows a broad peak located at $\sim 480\,\mathrm{cm}^{-1}$. As the deposition temperature is increased to 700 °C, the material starts to crystallize and small crystallites are formed. Three Voigt peaks were used to decouple the spectra and to calculate the crystallinity fraction of the material, which was calculated to be $\sim 37\%$. At higher temperatures (750 °C), the crystallites grow and polycrystalline silicon with fewer defective and amorphous regions is obtained. The crystallinity fraction of silicon tubes deposited at this temperature is $\sim 87\%$. Subsequently, with an annealing process at 1450 °C larger crystals are formed and the crystallinity fraction of these tubes is $\sim 100\%$.

In comparison, the Raman spectra of germanium tubes shows that polycrystalline material with a crystallinity fraction of $\sim 100\%$ is deposited at much lower temperatures (500 °C). In addition, the results of the Raman study show that in-fibre silicon tubes are subject to tensile strain which is reflected as a redshift of the Raman peak of $\sim 2\,\mathrm{cm}^{-1}$. Once the tubes are etched out of the MOF template the strain is released. This suggest that it is possible to design fibre geometries to induce strain in semiconductors that may lead to desirable changes in the electronic and optical properties of the material. Further studies will focus on introducing additional stress during deposition either longitudinally, by compressing or stretching, or radially, by twisting or bending the fibres.

In-fibre silicon and germanium wires were configured as FETs. These transistors are the first example of in-fibre electronic devices and established the potential of this technology to create an new class of optical fibres with both photonic and electronic capabilities. In addition, in-fibre FETs served as valuable characterisation tools which provided information about the carrier type, carrier concentration and mobility of the semiconductor material. The carrier mobility of germanium tubes was one order of magnitude better than that of silicon. This can be attributed to the difference in the crystalline structure between silicon and germanium tubes. Therefore, results of Raman, TEM and electrical studies indicate that optimization of the annealing process should allow for a reduction of the amount of amorphous and defective material along with larger grain sizes. Higher crystallinity fraction and larger crystals should reduce the magnitude of

the grain-boundary scattering in semiconductor modified MOFs and will improve their electronic and optical properties.

This thesis has also characterised the light guiding properties of silicon-filled MOFs. The transmission loss of a silicon fibre was measured to be $\sim 7\,\mathrm{dB/cm}$ at $\lambda = 1550\,\mathrm{nm}$, which is comparable to the value of $3 - 7\,\mathrm{dB/cm}$ reported for poly-silicon planar waveguides. Scattering due to sidewall roughness is a critical component of the loss in planar silicon waveguides because of the high index contrast between the core and the cladding. In-fibre tubes/wires are fabricated inside a very smooth template, which should make their outer diameter also very smooth. Scattering at the inner surface becomes relatively unimportant because its area is so small as the silicon tube grows inwards. We can conclude that the measured loss of poly-silicon fibres is mainly due to intrinsic absorption and grain boundary scattering, and therefore further improvements on the material quality will result in better waveguides. Work was then conducted to demonstrate an in-fibre optical modulator based on a silicon-filled MOF. Photoexcitation of free carriers was used to modulate light with light. The modulation concept relies on the fact that the concentration variation of free carriers modifies the absorption of silicon. Therefore by exciting free carries with a pulsed laser, one can drive the system from a low absorption state to a lossy state and modulate the amplitude of light guided in the silicon core. Optical pulses of $65\,\mu\mathrm{J}$ in the control channel were sufficient to achieve a ten fold modulation of the probe signal.

Another advantage of MOF templates is their transparency, allowing for structuring of the deposition within them via photolysis. Laser-assisted supercritical fluid deposition was used to deposited gold seeds at specific locations inside the fibre. Then, single crystal silicon wires were successfully formed via a high-pressure version of vapour-liquid-solid growth.

Supercritical fluid deposition was employed for the deposition of metals and polymers inside MOFs. This thesis has investigated the optical transmission properties of MOFs with silver-nanoparticle inclusions with a range of deposition profiles. These fibres exhibit low optical loss ($\sim 2\,\mathrm{dB/cm}$), compared to planar plasmon waveguides at visible wavelengths. The extended interaction over centimetre lengths that is associated with the guided core modes, makes possible the excitation of plasmon resonances on various particle sizes, interparticle separations and film thicknesses along the fibre which resulted in a broad absorption band across the red end of the visible spectrum. The low optical losses that were measured when visible light is guided in the core, demonstrate the potential for the silver impregnated MOFs to be integrated with conventional photonic devices. The ability to control the loss at longer or at specific wavelengths simply via the metal deposition profile and the choice of MOF designs is currently under investigation.

Silver-modified MOFs have been characterised using Raman measurements, demonstrating SERS detection of a single molecular layer of target molecules. The SERS data obtained, when light is coupled into the fibre at different positions (core and cladding), has been extremely useful for understanding the SERS process in fibre-based substrates. A qualitative explanation of the interaction between the optical modes and the metal nanoparticles has identified two excitation mechanisms.

In the first regime, when the pump laser is coupled into the fibre core, guided modes are excited and can propagate over centimetre lengths (due to their relatively low loss). During the interaction between guided modes and the silver particles near the core, SERS photons are excited and may be efficiently collected by the high refractive index core. As guided modes concentrate most of their energy in the core, in this mechanism the excitation efficiency of Raman photons per until length is considered low.

The second mechanism is relevant when light is launched onto the structured cladding and lossy modes are excited. Cladding modes highly interact with the metal particles then exciting plasmon modes in more silver particles. The excitation efficiency per unit length is greater than in the first case. However cladding modes' propagation is restricted to shorter lengths and the collection of SERS photons is less efficient than in the first mechanism.

The ability to engineer the fibre geometry gives us the unique opportunity to control photon/plasmon interactions via these two excitation mechanisms which can result in fibres with large SERS enhancements. Finally, MOF SERS substrates have exceptional temporal and mechanical stability, providing strong signals at least one year after fabrication. While, in contrast, planar SERS substrates may provide enhancements for about one month and must be handled with extreme care to avoid damaging the active area.

9.2 Future Devices and Work

Many possible active and passive devices in which the transport, generation, modulation, processing and detection of light is fully integrated into optical fibres can now be envisioned. The performance of such devices will depend critically on the quality and crystalline structure of the materials within the fibre. Thus, as presented here, successful realisation of these devices will rely on further improvements in the deposition methods and the ability to deposit semiconductors in any crystalline phase. Deposition of direct bandgap semiconductors, such as GaAs and ZnSe whose non-centrosymmetry yields electrooptical effects, is a major step forward for in-fibre lasers and modulators. Experiments are currently underway to improve the properties of silicon and germanium structures as well as to demonstrate compound and direct bandgap semiconductor

deposition inside MOFs. It is anticipated that such a broad range of materials can deposited by extending existing chemical vapor deposition precursors to high-pressure CVD method.

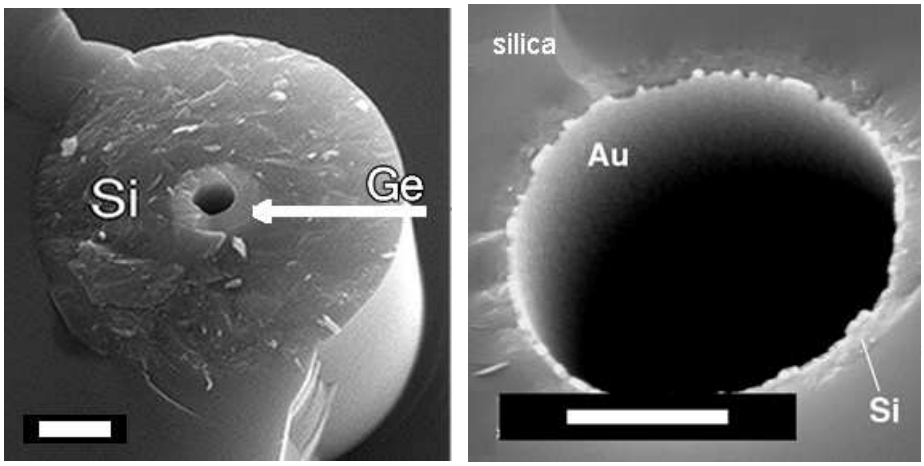

FIGURE 9.1: (Left) Silicon-germanium radial heterojunction integrated into a 6 μm MOF capillary, scale bar is 1 μm. (Right) 80 nm thick gold layer sequentially deposited onto a silicon tube, scale bar is 2 μm.

Of particular interest is the development of semiconductor Raman lasers and nonlinear devices. The high nonlinearity of silicon means that large Raman gains and nonlinear effects can be achieved in short lengths, resulting in extremely compact devices. Furthermore, the transparency of silicon and germanium at infrared wavelengths offers great potential to push Raman lasing wavelengths out to the mid infrared. Using optimized silicon and germanium impregnated fibres, stimulated Raman amplification and four wave mixing will be investigated for the purposes of developing all-fibre frequency converters in the infrared.

Figure 9.1 shows SEM micrographs of cylindrical heterojunctions that have been fabricated by sequential deposition. Structures like these bring the possibility of incorporating multiple layers of semiconductors and metals. Semiconductor/semiconductor and semiconductor/metal heterojunctions can be exploited to engineering the optoelectronic properties of in-fibre semiconductor devices. In-fiber detectors that are compact, and integrate with existing fibre infrastructure, may be possible. Heterojunctions combining direct bandgap semiconductors and metals may result in optically or electrically pumped fibre lasers, which are another attractive future application.

The sequential deposition of a silicon cladding and a germanium core might result in infrared fibre waveguides with low loss. As the refractive index of amorphous silicon at near infrared wavelengths is higher than that of crystalline silicon [342, 343], the sequential deposition of these materials, could also result in efficient IR waveguides.

Silicon and germanium fibre FETs are a starting point for future work. The electrical properties of high temperature annealed wires and heterojunctions are currently under investigation. Doping strategies for p-n heterojunctions is also a major target of the ongoing research.

There has been an increasing theoretical interest in MOFs that incorporate metallic thin films and nanoparticles, to yield a new kind of in-fibre plasmonic devices with applications in sensors, subwavelength optics and plasmon physics [14, 289, 290, 344, 291, 344, 345, 346]. An experimental demonstration of these theoretical predictions is another major target of the current research. Currently investigation of the optical properties of silver and gold impregnated MOFs, with coating profiles ranging from smooth thin films to granular films is being carried out. The applicability of smooth coating as resonant plasmon structures for bio/chemical sensors has been planned as future work. Although investigation of the optical properties of fibres with metal nanoparticles has been presented in this thesis, more detailed optical studies will be carried out in the near future.

Finally, the ability to integrate plasmonic materials such as silver and gold within MOF templates makes it possible to use these fibre devices for remote SERS sensing. Remote SERS sensors is another exciting future application of metal-modified MOFs, which is again currently under investigation.

Appendix A

Quantum Confinement Effects

On a simple level quantum confinement effects may be understood by considering Heisenberg's uncertainty relationships between the momentum and spatial position of both free and confined particles. For a particle in the periodic potential of a bulk crystal, its energy and momentum can both be precisely defined but simultaneously the particle position is not defined. As the crystal size decreases, the particle becomes more and more localized, this results in an increase in the position certainty but in a decrease in the momentum certainty. As will be shown, from the Schrödinger equation, for a free particle the dependence of energy on the wavevector is quadratic, whereas for a particle confined within a small volume its wavefunction has to obey boundary conditions along the direction of confinement, producing a series of discrete energy eigenvalues. Given the relation between energy and momentum in the bulk solid, one can see how a series of nearby transitions, occurring at slightly different energies in the bulk, will be compressed by quantum confinement into a single, intense transition in a quantum dot.

A.1 Crystal Structure

Bulk crystals are formed by the infinite repetition of identical groups of atoms (the crystal *basis*). The set spatial positions where the basis are located is known as the crystal *lattice*. The number of atoms or molecules in the crystal basis may be one or it may be more than one. A 3D crystal may be constructed as a linear combination of three lattice vectors, $(\vec{a}_1, \vec{a}_2, \vec{a}_3)$, such that the crystal looks identical at the points $\vec{r}$ and $\tilde{\mathrm{r}}_0$ [56, 347]:

$$\vec{r}(x, y, z) = \vec{r}_0 + u_1\vec{a}_1 + u_2\vec{a}_2 + u_3\vec{a}_3 \tag{A.1}$$

where u_1, u_2, u_3 are any integer. The complete crystalline lattice is defined by all the set of points $\vec{r}$.

The smallest possible lattice (minimum-volume cell in 3D and minimum-area cell in 2D) that can build up the complete structure is known as the primitive lattice and the vectors $\vec{a}_1$ which define it are known as the primitive lattice vectors which are used to define the crystal axes. The crystal axes are used to define the crystal planes which are atom-rich planes. The crystal planes are identified by a set of three numbers in the form (hkl), called *Miller Indices*, where h, k, l are integers. These numbers can be regarded as reciprocals of the intercepts which the plane makes on the primitive lattice vectors [56], as shown in Figure A.1.

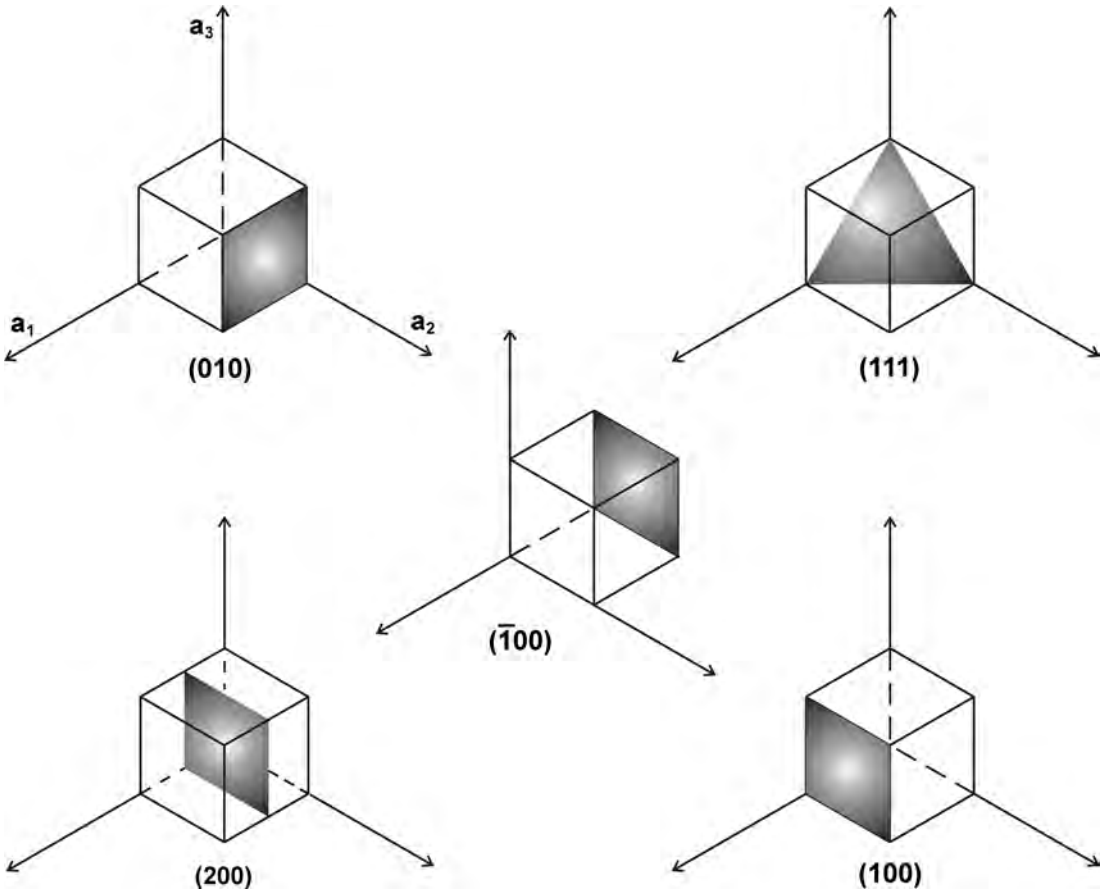

FIGURE A.1: Views of important planes in a cubic Bravais lattice. The plane index is conventionally enclosed in parenthesis. The planes (100), (200), ($\bar{1}$,0,0) are parallel to each other and perpendicular to the lattice vector $\vec{a}_1$.

A crystal lattice must define it selves by translations or rotations about an axis and there are not an infinite number of lattice structures that can be used to make a periodic crystal. In 2D dimensions for example, there are only five especial lattices that result in an infinite crystal and in 3D there are fourteen different types. These especial crystal lattices are known as Bravais lattices. In 2D these are the hexagonal, square, rectangular,

centered rectangular and oblique lattices. In 3D the 14 Bravais lattices are grouped in seven types of primitive cells, which are cubic, tetragonal, trigonal, hexagonal, triclinic, monoclinic and orthorhombic. Some of these have more than one lattice; for example the cubic system presents three Bravais lattices: simple cubic (SC), body-centered cubic (BCC), and the face-centered cubic (FCC) lattices.

The crystal structure of diamond is equivalent to a face-centred cubic lattice, with a primitive basis of two identical carbon atoms: one at $\vec{r} = (0, 0, 0)$ and the other at $\vec{r} = (1/4, 1/4, 1/4)$, where the coordinates are given as fractions along the cube sides. This is the same as two interpenetrating FCC lattices, offset from one another along a body diagonal by one-quarter of its length. Each atom in the diamond lattice has a covalent bond with four adjacent atoms which together form a tetrahedron. The diamond structure is the crystalline structure of silicon and germanium and other technological important semiconductors. The diamond structure is formed by covalent bonding formed in group IV materials, carbon, silicon, germanium and tin.

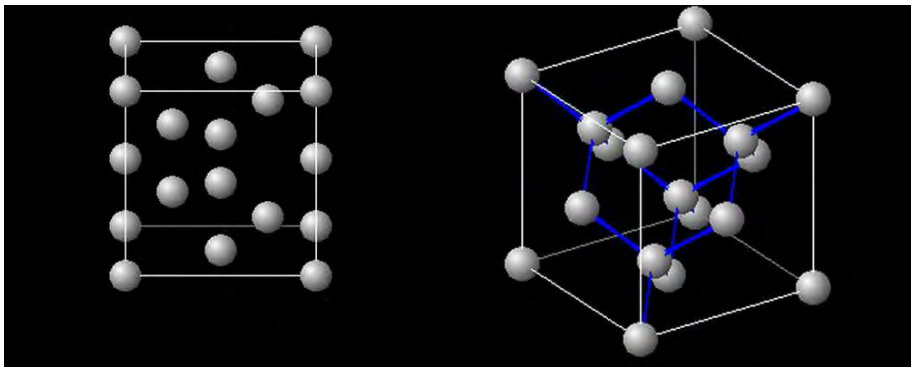

FIGURE A.2: 3D views of the crystal structure of silicon from two different angles. The image on the right also show the atomic bonds. The lattice constant of silicon is 5.43 Å which is the distance between the atoms located in the cube vertices (white lines). The blue lines correspond to 2.35 Å, from reference [348].

A.2 Electron Diffraction by Crystals

In TEM analysis the crystal structure of materials is studied through the diffraction of electrons. When and electrons waves interact with a solid they are scattered by the crystal atoms. The resulting diffraction pattern is used to determine the crystalline structure of the material, its lattice constants, orientation, etc. Fourier analysis tell us that the diffraction pattern from a periodic structure can be expressed in terms of the Fourier transform of the crystal lattice which is known as the reciprocal lattice. The reciprocal lattice is also a Bravais lattice in the Fourier space and may be build up by

a set of primitive vectors known as the reciprocal lattice vectors, $\vec{b}_1,\ \vec{b}_2,\ \vec{b}_3$, which are defined as follows [56]:

$$\vec{b}_1 = 2\pi\frac{\vec{a}_2 \times \vec{a}_3}{\vec{a}_1 \cdot \vec{a}_2 \times \vec{a}_3}\,, \qquad \vec{b}_2 = 2\pi\frac{\vec{a}_3 \times \vec{a}_1}{\vec{a}_1 \cdot \vec{a}_2 \times \vec{a}_3}\,, \qquad \vec{b}_3 = 2\pi\frac{\vec{a}_1 \times \vec{a}_2}{\vec{a}_1 \cdot \vec{a}_2 \times \vec{a}_3}\,. \tag{A.2}$$

Any point in the reciprocal lattice can expressed as a linear combination of the primitive reciprocal vectors,

$$\vec{G} = v_1\vec{b}_1 + v_2\vec{b}_2 + v_3\vec{b}_3\,. \tag{A.3}$$

The Brillouin zone is defined as the primitive cell in the reciprocal lattice. All the concepts studied this appendix can be extended to photonic crystals with the only difference being the scale of the periodic structure. In solid state crystals the distance between atoms is a few Angstroms whereas in photonic crystals the distance between regions with varying refractive index is of the order of the wavelength of light.

A.3 Quantum Confinement Effects

In bulk crystalline solids, the arrangement of atoms causes a periodic potential barrier to the electron and holes motion. The electron and hole states allowed within the crystal may be obtained by solving the stationary Schrödinger equation of a particle moving in a periodic potential,

$$\left[-\frac{\hbar^2}{2m}\nabla^2 + V(\vec{r})\right]\Psi(\vec{r}) = E\Psi(\vec{r})\,, \tag{A.4}$$

where m is the effective mass of the particle. The potential $U(\vec{r})$ has the periodicity of the crystal's Bravais lattice

$$V(\vec{r}) = V(\vec{r} + \vec{R})\,, \tag{A.5}$$

for all lattice vectors $\vec{R}$. According to Bloch's theorem, the eigenvectors of equation A.4, the electronic wave functions in a bulk crystal can be written as

$$\Psi_{\nu k}(\vec{r}) = u_{\nu k}(\vec{r})e^{i\vec{k}\cdot\vec{r}}\,, \tag{A.6}$$

and

$$u_{\nu k}(\vec{r}) = u_{\nu k}(\vec{r} + \vec{R})\,, \tag{A.7}$$

where $\vec{k}$ is the wave vector reduced to the first Brillouin zone and ν is the band index (conduction or valence band). The allowed energy levels of the electron carriers are distributed into bands with a finite energy bandgap (E_g) between the valence and conduction bands. In parabolic band approximation the energy eigenvalues for the electron and hole are then given by

$$E_e(k) = E_g + \frac{\hbar^2 k^2}{2m_e} \quad \text{and} \quad E_h(k) = \frac{\hbar^2 k^2}{2m_h}\,. \tag{A.8}$$

where m_e and m_h are the effective mass of the electron or hole respectively. In this approximation the carriers behave as free particles with an effective mass which attempts to incorporate the periodic potential feel by the carrier in the lattice. This approximation allows the atoms in the lattice to be ignored and the electron and hole to be treated as if they were free particles, but with a different mass [320].

In order to describe the consequences of quantum confinement on the allowed electron and hole states, one can consider the *particle-in-a-box model*. In this model the charge carriers with effective mass m are confined in all three dimensions inside an spherical potential well of radius a. The confinement potential in spherical coordinate (r, θ, ϕ) is given by

$$V = \begin{cases} 0 & \text{for } r < a \\ \infty & \text{for } r > a \end{cases} \tag{A.9}$$

Outside the quantum dot, the solution to the Schrödinger equation (A.4) is trivial and gives a wavefunction equal to zero. Inside of the well ($r < a$), the Schrödinger equation (A.4) takes the form

$$\left(\nabla^2 + k^2\right) \Psi(r, \theta, \phi) = 0\,. \tag{A.10}$$

where k is the wavenumber corresponding to $k^2 = 2mE/\hbar$ and the Laplacian in spherical coordinates is given by

$$\nabla^2 = \frac{1}{r^2}\frac{\partial}{\partial r^2}\left(r^2 \frac{\partial}{\partial r^2}\right) + \frac{1}{r^2 \sin\theta}\frac{\partial}{\partial \theta}\left(\sin\theta \frac{\partial}{\partial \theta}\right) + \frac{1}{r^2 \sin\theta}\frac{\partial^2}{\partial \phi^2} \tag{A.11}$$

The solutions to equation (A.10) are obtained using a separation of variables approach

$$\Psi_{lmn}(\vec{r}) = R_{ln}(r)Y_l^m(\theta,\phi)\,, \tag{A.12}$$

where $Y_l^m(\theta,\phi)$ are the spherical harmonics and the quantum numbers, $n = 1, 2, 3, \ldots$, $l = 0, 1, 2, \ldots$ and $m = 0, \pm1, \pm2, \ldots, \pm l$. In addition, the spherical harmonics have the especial property of being eigenfunctions of the Laplacian in spherical coordinates

$$\nabla^2 Y_l^m(\theta,\phi) = \frac{-l(l+1)}{r^2} Y_l^m(\theta,\phi)\,. \tag{A.13}$$

The Laplacian of the product of two functions F and G is given by

$$\nabla^2(FG) = \left(\nabla^2 F\right) G + 2\left((\nabla F)\cdot(\nabla G)\right) + F\left(\nabla^2 G\right)\,. \tag{A.14}$$

Since $R_{ln}(r)$ is a radial function and $Y_l^m(\theta,\phi)$ is a spherical harmonic. The gradient of R_{ln} is a radial vector which is tangent to the gradient of $Y_l^m(\theta,\phi)$, therefore

$$2\left((\nabla R_{ln}(r))\cdot(\nabla Y_l^m(\theta,\phi)\right) = 0\,. \tag{A.15}$$

Then

$$\nabla^2\left(R_{ln}(r)Y_l^m(\theta,\phi)\right) = \left(\nabla^2 R_{ln}(r)\right) Y_l^m(\theta,\phi) + R_{ln}(r)\left(\nabla^2 Y_l^m(\theta,\phi)\right)\,, \tag{A.16}$$

by substitution of equation (A.13) into the previous equation,

$$\nabla^2\left(R_{ln}(r)Y_l^m(\theta,\phi)\right) = \frac{1}{r^2}\frac{d}{dr}\left(r^2\frac{dR_{ln}}{dr}\right) Y_l^m + R_{ln}\left(\frac{-l(l+1)}{r^2}\right) Y_l^m \tag{A.17}$$

The previous equation is introduced into equation (A.10) in order to separate the radial and spherical harmonic parts. The radial part of the wavefuntion satisfies the radial Schrödinger equation

$$\frac{d}{dr}r^2\frac{dR_{ln}}{dr} + \left(k^2r^2 - l(l+1)\right) R_{ln} = 0\,. \tag{A.18}$$

The linearly independent solutions to the radial Schrödinger equation which are regular in the origin are given by the Bessel function of the first kind J_l. Thus, the radial wavefunctions may be described in terms on the Bessel funtions, such that

$$R_{ln}(r) = AJ_l(kr)\,, \tag{A.19}$$

where A is a constant. The discrete nature of the energy levels follows from boundary conditions imposed by the "box" which requires the radial wavefunctions to vanish at $r = a$, requiring $J_l n(ka) = 0$. This restricts the allowed k values to those where the $ka = \chi_{ln}$. Where χ_{ln} denotes the n^{th} zero of the Bessel function of order l. The complete solution to the spherical problem can now be expressed as,

$$\Psi_{lmn}(\vec{r}) = Y_l^m(\theta, \phi) J_l \left(\frac{\chi_{ln} r}{a} \right) \tag{A.20}$$

The allowed energies of electrons and holes for a given values of l, n are

$$E_{nl}^e = E_g + \frac{\hbar^2}{2m_e} \frac{\chi_{nl}^2}{a^2} \quad \text{and} \quad E_{nl}^h = \frac{\hbar^2}{2m_h} \frac{\chi_{nl}^2}{a^2}, \tag{A.21}$$

where E_g is the bandgap energy of the respective bulk semiconductor. It can be seen from equation (A.21) that as the semiconductor QD size decreases, the electronic excitation shifts to higher energy; in inverse proportion to the square of the radius $1/a^2$. The particle-in-a-box states may be labelled according to the principal quantum number and symmetry, in a similar fashion to nuclear states. The four lowest lying states are therefore, **1S**$(n = 0, l = 1)$, **1P**$(n = 1, l = 1)$, **1D**$(n = 1, l = 2)$ and **2S**$(n = 2, l = 0)$. In a semiconductor quantum dot the electronic states are conventionally denoted as, for example, **1S(e)** and **1P(e)** similarly a hole state is **1S(h)**.

Appendix B

List of Publications

Journal Publications

1. **Transmission measurements of microstructured optical fibers with metal-nanoparticle inclusions.**
   A. Amezcua-Correa, A. C. Peacock, J. Yang, P. J. A. Sazio and S. M. Howdle
   In preparation.

2. **Surface-enhanced Raman scattering using microstructured optical fiber substrates.**
   A. Amezcua-Correa, J. Yang, A. C. Peacock, C. E. Finlayson, J. R. Hayes, P. J. A. Sazio, J. J. Baumberg and S. M. Howdle
   Advanced Functional Materials, **17**, 2024, (2007).

3. **Electrical and Raman characterization of silicon and germanium-filled microstructured optical fibers.**
   C. E. Finlayson, A. Amezcua-Correa, P. J. A. Sazio, N. F. Baril and J. V. Badding,
   Applied Physics Letters **90**, 132110, (2007).

4. **Microstructured optical fibers as high-pressure microfluidic reactors.**
   P. J. A. Sazio, A. Amezcua-Correa, C. E. Finlayson, J. R. Hayes , T. J. Scheidemantel, N. F. Baril, B. R. Jackson, D. J. Won, F. Zhang, E. R. Margine, V. Gopalan, V. H.Crespi and J. V. Badding,
   Science **311**, 1583, (2006).

5. **Infrared emitting PbSe nanocrystals for telecommunication window applications.**
   C. E. Finlayson, A. Amezcua-Correa, P. J. A. Sazio, P. S. Walker, M. C. Grossel,

R. J. Curry, D. C. Smith and J. J. Baumberg,
Journal of Modern Optics **52**, 955, (2005).

Conference Publications

1. **Deposition of electronic and plasmonic materials inside microstructured optical fibres.**
   A. Amezcua-Correa, A. C. Peacock, N. F. Baril, J. Calkins, D. J. Won, V. Gopalan, J. V. Badding and P.J.A. Sazio, in *Electro-Active Materials*, Cranfield, 2007.

2. **Electronic and plasmonic materials inside microstructured optical fibres.**
   P. J. A. Sazio, A. Amezcua-Correa, C. E. Finlayson, J. R. Hayes , T. J. Scheidemantel, N. F. Baril, B. R. Jackson, D. J. Won, F. Zhang, E. R. Margine, V. Gopalan, V. H.Crespi and J. V. Badding,, in *Frontiers in Optics*, San Jose, 2007, Invited Paper.

3. **Highly efficient SERS inside microstructured optical fibres via optical mode engineering.**
   A. C. Peacock, A. Amezcua-Correa, P. J. A. Sazio, J. J. Baumberg, J. Yang and S. M. Howdle, in *ECLEO*, Munich, 2007.

4. **Microstructured optical fibres as micro/nano materials templates for optoelectronic and surface enhanced Raman scattering applications.**
   A. Amezcua-Correa, A. C. Peacock, C. E. Finlayson, N. F. Baril, D. J. Won, V. Gopalan, J. V. Badding, J. Yang, S. M. Howdle, J.J. Baumberg and P. J. A. Sazio, in *Nanoscale Physics and Technology*, Southampton, 2007.

5. **Integrated optoelectronics in an optical fiber.**
   J. V. Badding, P. J. A. Sazio, V. Gopalan, A. Amezcua-Correa, T. J. Scheidemantel, C. E. Finlayson, N. F. Baril, B. Jackson and D. J. Won, in *SPIE Photonics West*, San Jose, 2007, Invited Paper.

6. **Surface enhanced Raman scattering using metal modified microstructured optical fibre substrates.**
   A. Amezcua-Correa, A. C. Peacock, C. E. Finlayson, J. J. Baumberg, J. Yang, S. M. Howdle and P. J. A. Sazio, in *ECOC*, Cannes, 2006.

7. **High Pressure CVD inside Microstructured Optical Fibres.**
   P. J. A. Sazio, A. Amezcua-Correa, C. E. Finlayson, J. R. Hayes, T. J. Scheidemantel, N. F. Baril, B. R. Jackson, D. J. Won, F. Zhang, E. R. Margine, V. Gopalan, V. H. Crespi, and J. V. Badding, in *ECOC*, Cannes, 2006, Invited Paper.

8. **Surface enhanced Raman scattering using metal modified microstrucured optical fiber substrates.**
   J. Yang, A. Amezcua-Correa, A. C. Peacock,, C. E. Finlayson, J. J. Baumberg, S. M. Howdle and P. J. A. Sazio, in *Optics East: Industrial Sensing Technologies*, Boston, 2006, Invited Paper.

9. **Microstructured optical fibers as high-pressure microfluidic reactors.**
   A. Amezcua-Correa, C. E. Finlayson, J. R. Hayes, N. F. Baril, D. J. Won, V. Gopalan, J. V. Badding and P. J. A. Sazio, in *SET for Britain*, London, 2006.

10. **Fabrication of extreme aspect ratio wires within photonic crystal fibers.**
    J. V. Badding, P. J. A. Sazio, A. Amezcua-Correa, T. J. Scheidemantel, C. E. Finlayson, N. F. Baril, D. J. Won, H. Fang, B. Jackson, A. Borhan and V. Gopalan, in *Proceeding of SPIE*, 2005.

11. **Microstructured Optical Fibres Semiconductor Metamaterials.**
    A. Amezcua-Correa, P. J. A. Sazio, C. E. Finlayson, H. Fang, D. J. Won, T. J. Scheidemantel, B. Jackson, N. F. Baril, V. Gopalan and J. V. Badding, in *LEOS*, Sydney, 2005, Invited Paper.

12. **Microstructured optical fibres semiconductor metamaterials.**
    A. Amezcua-Correa, C. E. Finlayson, P. J. A. Sazio, H. Fang, D. J. Won, T. J. Scheidemantel, B. Jackson, N. F. Baril, V. Gopalan and J. V. Badding, in *PREP2005*, Lancaster, 2005.

13. **Microstructured optical fibres semiconductor metamaterials.**
    A. Amezcua-Correa, C. E. Finlayson, P. J. A. Sazio, H. Fang, D. J. Won, T. J. Scheidemantel, B. Jackson, N. F. Baril, V. Gopalan and J. V. Badding, in *ASSP*, Vienna, 2005.

14. **Infrared emitting PbSe nanocrystals for telecommunication window applications.**
    C. E. Finlayson, A. Amezcua-Correa, R. J. Curry, P. J. A. Sazio, P. S. Walker, M. C. Grossel, D. C. Smith and J. J. Baumberg, in *ASSP*, Vienna, 2005.

15. **Lithography-free fabrication of high index contrast, extreme aspect ratio semiconductor structures**
    H. Fang, D. J. Won, A. Sharan, T. J. Scheidemantel, B. Jackson, N. F. Baril, V. Gopalan, A. Amezcua-Correa and P. J. A. Sazio, in *Symposium on Infrared Materials and Technologies*, Pennsylvania, 2004, Invited Paper.

16. **Lithography-free fabrication of high index contrast, extreme aspect ratio semiconductor structures**

H. Fang, D. J. Won, A. Sharan, T. J. Scheidemantel, B. Jackson, N. F. Baril, V. Gopalan, A. Amezcua-Correa and P. J. A. Sazio, in *MRS Fall Meeting*, Boston, 2004.

17. **Infrared emitting PbSe nanocrystals for telecommunication window applications.**
C. E. Finlayson, A. Amezcua-Correa, R. J. Curry, P. J. A. Sazio, P. S. Walker, M. C. Grossel, D. C. Smith and J. J. Baumberg, in *PhotonQEP*, Glasgow, 2004.

Bibliography

[1] http://www.corning.com.

[2] E. Yablonovitch. Inhibited spontaneous emission in solid-state physics and electronics. *Physical Review Letters*, 58(20):2059–2062, 1987.

[3] S. John. Strong localization of photons in certain disordered dielectric superlattices. *Physical Review Letters*, 58(23):2486–2489, 1987.

[4] J. D. Joannopoulos, Robert D. Meade, and Joshua N. Winn. *Photonic crystals : molding the flow of light*. Princeton University Press, Princeton, N.J., 1995.

[5] O. Painter, R. K. Lee, A. Scherer, A. Yariv, J. D. O'Brien, P. D. Dapkus, and I. Kim. Two-dimensional photonic band-gap defect mode laser. *Science*, 284(5421):1819–1821, 1999.

[6] S. Y. Lin, E. Chow, V. Hietala, P. R. Villeneuve, and J. D. Joannopoulos. Experimental demonstration of guiding and bending of electromagnetic waves in a photonic crystal. *Science*, 282(5387):274–276, 1998.

[7] T. Baba, N. Fukaya, and J. Yonekura. Observation of light propagation in photonic crystal optical waveguides with bends. *Electronics Letters*, 35(8):654–655, 1999.

[8] T. A. Birks, P. J. Roberts, P. S. J. Russel, D. M. Atkin, and T. J. Shepherd. Full 2-D photonic bandgaps in silica/air structures. *Electronics Letters*, 31(22):1941–1943, 1995.

[9] J. C. Knight, T. A. Birks, P. S. Russell, and D. M. Atkin. All-silica single-mode optical fiber with photonic crystal cladding. *Optics Letters*, 21(19):1547–1549, 1996.

[10] T. A. Birks, J. C. Knight, and P. S. Russell. Endlessly single-mode photonic crystal fiber. *Optics Letters*, 22(13):961–963, 1997.

[11] J. C. Knight, J. Broeng, T. A. Birks, and P. S. J. Russel. Photonic band cap guidance in optical fibers. *Science*, 282(5393):1476–1478, 1998.

[12] P. Russell. Photonic crystal fibers. *Science*, 299(5605):358–362, 2003.

[13] J. C. Knight. Photonic crystal fibres. *Nature*, 424(6950):847–851, 2003.

[14] P. S. J. Russell. Photonic-crystal fibers. *Journal of Lightwave Technology*, 24(12):4729–4749, 2006.

[15] T. M. Monro and D. J. Richardson. Holey optical fibres: Fundamental properties and device applications. *Comptes Rendus Physique*, 4(1):175–186, 2003.

[16] P. J. A. Sazio, A. Amezcua-Correa, C. E. Finlayson, J. R. Hayes, T. J. Scheidemantel, N. F. Baril, B. R. Jackson, D. J. Won, F. Zhang, E. R. Margine, V. Gopalan, V. H. Crespi, and J. V. Badding. Microstructured optical fibers as high-pressure microfluidic reactors. *Science*, 311(5767):1583–1586, 2006.

[17] J. V. Badding, V. Copalan, and P. J. A. Sazio. Building semiconductor structures in optical fiber. *Photonics Spectra*, 40(8):80–88, 2006.

[18] A. M. Morales and C. M. Lieber. A laser ablation method for the synthesis of crystalline semiconductor nanowires. *Science*, 279(5348):208–211, 1998.

[19] Y. Huang, X. F. Duan, Y. Cui, L. J. Lauhon, K. H. Kim, and C. M. Lieber. Logic gates and computation from assembled nanowire building blocks. *Science*, 294(5545):1313–1317, 2001.

[20] Y. Cui and C. M. Lieber. Functional nanoscale electronic devices assembled using silicon nanowire building blocks. *Science*, 291(5505):851–853, 2001.

[21] X. F. Duan, Y. Huang, R. Agarwal, and C. M. Lieber. Single-nanowire electrically driven lasers. *Nature*, 421(6920):241–245, 2003.

[22] R. S. Friedman, M. C. McAlpine, D. S. Ricketts, D. Ham, and C. M. Lieber. High-speed integrated nanowire circuits. *Nature*, 434(7037):1085–1085, 2005.

[23] E. Yablonovitch, T. J. Gmitter, and K. M. Leung. Photonic band-structure - the face-centered-cubic case employing nonspherical atoms. *Physical Review Letters*, 67(17):2295–2298, 1991.

[24] Y. A. Vlasov, K. Luterova, I. Pelant, B. Honerlage, and V. N. Astratov. Enhancement of optical gain of semiconductors embedded in three-dimensional photonic crystals. *Applied Physics Letters*, 71(12):1616–1618, 1997.

[25] K. Busch and S. John. Liquid-crystal photonic-band-gap materials: The tunable electromagnetic vacuum. *Physical Review Letters*, 83(5):967–970, 1999.

[26] E. Yablonovitch. Optics - liquid versus photonic crystals. *Nature*, 401(6753):539, 1999.

[27] P. Vukusic and J. R. Sambles. Photonic structures in biology. *Nature*, 424(6950):852–855, 2003.

[28] S. Y. Lin, J. G. Fleming, D. L. Hetherington, B. K. Smith, R. Biswas, K. M. Ho, M. M. Sigalas, W. Zubrzycki, S. R. Kurtz, and J. Bur. A three-dimensional photonic crystal operating at infrared wavelengths. *Nature*, 394(6690):251–253, 1998.

[29] P. G. Kazansky and V. Pruneri. Electrically stimulated light-induced second-harmonic generation in glass: Evidence of coherent photoconductivity. *Physical Review Letters*, 78(15):2956–2959, 1997.

[30] M. Key, I. G. Hughes, W. Rooijakkers, B. E. Sauer, E. A. Hinds, D. J. Richardson, and P. G. Kazansky. Propagation of cold atoms along a miniature magnetic guide. *Physical Review Letters*, 84(7):1371–1373, 2000.

[31] P. S. Westbrook, B. J. Eggleton, R. S. Windeler, A. Hale, T. A. Strasser, and G. L. Burdge. Cladding-mode resonances in hybrid polymer-silica microstructured optical fiber gratings. *IEEE Photonics Technology Letters*, 12(5):495–497, 2000.

[32] C. Kerbage, A. Hale, A. Yablon, R. S. Windeler, and B. J. Eggleton. Integrated all-fiber variable attenuator based on hybrid microstructure fiber. *Applied Physics Letters*, 79(19):3191–3193, 2001.

[33] M. Fokine, L. E. Nilsson, A. Claesson, D. Berlemont, L. Kjellberg, L. Krummenacher, and W. Margulis. Integrated fiber Mach-Zehnder interferometer for electro-optic switching. *Optics Letters*, 27(18):1643–1645, 2002.

[34] T. T. Larsen, A. Bjarklev, D. S. Hermann, and J. Broeng. Optical devices based on liquid crystal photonic bandgap fibres. *Optics Express*, 11(20):2589–2596, 2003.

[35] F. Benabid, F. Couny, J. C. Knight, T. A. Birks, and P. S. Russell. Compact, stable and efficient all-fibre gas cells using hollow-core photonic crystal fibres. *Nature*, 434(7032):488–491, 2005.

[36] F. Benabid, J. C. Knight, G. Antonopoulos, and P. S. J. Russell. Stimulated Raman scattering in hydrogen-filled hollow-core photonic crystal fiber. *Science*, 298(5592):399–402, 2002.

[37] M. Bayindir, F. Sorin, A. F. Abouraddy, J. Viens, S. D. Hart, J. D. Joannopoulos, and Y. Fink. Metal-insulator-semiconductor optoelectronic fibres. *Nature*, 431(7010):826–829, 2004.

[38] D. J. Monk and D. R. Walt. Fabrication of gold microtubes and microwires in high aspect ratio capillary arrays. *Journal of the American Chemical Society*, 126(37):11416–11417, 2004.

[39] N. R. B. Coleman, M. A. Morris, T. R. Spalding, and J. D. Holmes. The formation of dimensionally ordered silicon nanowires within mesoporous silica. *Journal of the American Chemical Society*, 123(1):187–188, 2001.

[40] N. R. B. Coleman, K. M. Ryan, T. R. Spalding, J. D. Holmes, and M. A. Morris. The formation of dimensionally ordered germanium nanowires within mesoporous silica. *Chemical Physics Letters*, 343(1-2):1–6, 2001.

[41] D. P. Long, J. M. Blackburn, and J. J. Watkins. Chemical fluid deposition: A hybrid technique for low-temperature metallization. *Advanced Materials*, 12(12):913–915, 2000.

[42] J. M. Blackburn, D. P. Long, A. Cabanas, and J. J. Watkins. Deposition of conformal copper and nickel films from supercritical carbon dioxide. *Science*, 294(5540):141–145, 2001.

[43] J. J. Watkins, J. M. Blackburn, and T. J. McCarthy. Chemical fluid deposition: Reactive deposition of platinum metal from carbon dioxide solution. *Chemistry of Materials*, 11(2):213–215, 1999.

[44] C. R. Kurkjian, J. T. Krause, and M. J. Matthewson. Strength and fatigue of silica optical fibers. *Journal of Lightwave Technology*, 7(9):1360–1370, 1989.

[45] P. Kaiser, E. A. J. Marcatili, and S.E. Miller. A new optical fiber. *Bell System and Technical Journal*, 52(2):265–269, 1973.

[46] P. Kaiser and H. W. Astle. Low-loss single material fibers made from pure fused silica. *Bell System and Technical Journal*, 53:1021–1039, 1974.

[47] P. Yeh, A. Yariv, and E. Marom. Theory of Bragg fiber. *Journal of the Optical Society of America*, 68(9):1196–1201, 1978.

[48] S. R. Nagel, J. B. Macchesney, and K. L. Walker. An overview of the modified chemical vapor-deposition (MCVD) process and performance. *IEEE Journal of Quantum Electronics*, 18(4):459–476, 1982.

[49] F. Brechet, P. Roy, J. Marcou, and D. Pagnoux. Singlemode propagation into depressed-core-index photonic-bandgap fibre designed for zero-dispersion propagation at short wavelengths. *Electronics Letters*, 36(6):514–515, 2000.

[50] F. Brechet, P. Leproux, P. Roy, J. Marcou, and D. Pagnoux. Analysis of band-pass filtering behaviour of singlemode depressed-core-index photonic-bandgap fibre. *Electronics Letters*, 36(10):870–872, 2000.

[51] B. Temelkuran, S. D. Hart, G. Benoit, J. D. Joannopoulos, and Y. Fink. Wavelength-scalable hollow optical fibres with large photonic bandgaps for CO_2 laser transmission. *Nature*, 420(6916):650–653, 2002.

[52] M. Ibanescu, Y. Fink, S. Fan, E. L. Thomas, and J. D. Joannopoulos. An all-dielectric coaxial waveguide. *Science*, 289(5478):415–419, 2000.

[53] K. Kuriki, O. Shapira, S. D. Hart, G. Benoit, Y. Kuriki, J. F. Viens, M. Bayindir, J. D. Joannopoulos, and Y. Fink. Hollow multilayer photonic bandgap fibers for NIR applications. *Optics Express*, 12(8):1510–1517, 2004.

[54] R. F. Cregan, B. J. Mangan, J. C. Knight, T. A. Birks, P. S. Russell, P. J. Roberts, and D. C. Allan. Single-mode photonic band gap guidance of light in air. *Science*, 285(5433):1537–1539, 1999.

[55] S. John. Electromagnetic absorption in a disordered medium near a photon mobility edge. *Physical Review Letters*, 53(22):2169–2172, 1984.

[56] C. Kittel. *Introduction to solid state physics*. Wiley, New York, 7th edition, 1996.

[57] H. P. Myers. *Introductory solid state physics*. Taylor and Francis, London, 2nd edition, 1997.

[58] G. P. Agrawal. *Nonlinear fiber optics*. Academic Press, San Diego, 3rd edition, 2001.

[59] S. K. Varshney, M. P. Singh, and R. K. Sinha. Propagation characteristics of photonic crystal fibers. *Journal of Optical Communications*, 24, 2002.

[60] M. D. Nielsen and N. A. Mortensen. Photonic crystal fiber design based on the V-parameter. *Optics Express*, 11(21):2762–2768, 2003.

[61] J. C. Knight, T. A. Birks, R. F. Cregan, P. S. Russell, and J. P. de Sandro. Large mode area photonic crystal fibre. *Electronics Letters*, 34(13):1347–1348, 1998.

[62] T. M. Monro, D. J. Richardson, N. G. R. Broderick, and P. J. Bennett. Holey optical fibers: An efficient modal model. *Journal of Lightwave Technology*, 17(6):1093–1102, 1999.

[63] N. A. Mortensen, M. D. Nielsen, J. R. Folkenberg, A. Petersson, and H. R. Simonsen. Improved large-mode-area endlessly single-mode photonic crystal fibers. *Optics Letters*, 28(6):393–395, 2003.

[64] K. Furusawa, T. M. Monro, P. Petropoulos, and D. J. Richardson. Modelocked laser based on ytterbium doped holey fibre. *Electronics Letters*, 37(9):560–561, 2001.

[65] J. Limpert, T. Schreiber, S. Nolte, H. Zellmer, A. Tunnermann, R. Iliew, F. Lederer, J. Broeng, G. Vienne, A. Petersson, and C. Jakobsen. High-power air-clad large-mode-area photonic crystal fiber laser. *Optics Express*, 11(7):818–823, 2003.

[66] W. J. Wadsworth, R. M. Percival, G. Bouwmans, J. C. Knight, and P. S. J. Russel. High power air-clad photonic crystal fibre laser. *Optics Express*, 11(1):48–53, 2003.

[67] N. G. R. Broderick, T. M. Monro, P. J. Bennett, and D. J. Richardson. Nonlinearity in holey optical fibers: measurement and future opportunities. *Optics Letters*, 24(20):1395–1397, 1999.

[68] J. C. Knight, J. Arriaga, T. A. Birks, A. Ortigosa-Blanch, W. J. Wadsworth, and P. S. Russell. Anomalous dispersion in photonic crystal fiber. *IEEE Photonics Technology Letters*, 12(7):807–809, 2000.

[69] W. H. Reeves, D. V. Skryabin, F. Biancalana, J. C. Knight, P. S. Russell, F. G. Omenetto, A. Efimov, and A. J. Taylor. Transformation and control of ultra-short pulses in dispersion-engineered photonic crystal fibres. *Nature*, 424(6948):511–515, 2003.

[70] D. Mogilevtsev, T. A. Birks, and P. S. Russell. Group-velocity dispersion in photonic crystal fibers. *Optics Letters*, 23(21):1662–1664, 1998.

[71] A. Ferrando, E. Silvestre, J. J. Miret, and P. Andres. Nearly zero ultraflattened dispersion in photonic crystal fibers. *Optics Letters*, 25(11):790–792, 2000.

[72] W. H. Reeves, J. C. Knight, P. S. J. Russell, and P. J. Roberts. Demonstration of ultra-flattened dispersion in photonic crystal fibers. *Optics Express*, 10(14):609–613, 2002.

[73] V. Finazzi, T. M. Monro, and D. J. Richardson. Small-core silica holey fibers: nonlinearity and confinement loss trade-offs. *Journal of the Optical Society of America B-Optical Physics*, 20(7):1427–1436, 2003.

[74] P. Petropoulos, T. M. Monro, W. Belardi, K. Furusawa, J. H. Lee, and D. J. Richardson. 2R-regenerative all-optical switch based on a highly nonlinear holey fiber. *Optics Letters*, 26(16):1233–1235, 2001.

[75] J. E. Sharping, M. Fiorentino, P. Kumar, and R. S. Windeler. All-optical switching based on cross-phase modulation in microstructure fiber. *IEEE Photonics Technology Letters*, 14(1):77–79, 2002.

[76] J. H. Lee, P. C. Teh, Z. Yusoff, M. Ibsen, W. Belardi, T. M. Monro, and D. J. Richardson. A holey fiber-based nonlinear thresholding device for optical CDMA receiver performance enhancement. *IEEE Photonics Technology Letters*, 14(6):876–878, 2002.

[77] Z. Yusoff, J. H. Lee, W. Belardi, T. M. Monro, P. C. Teh, and D. J. Richardson. Raman effects in a highly nonlinear holey fiber: amplification and modulation. *Optics Letters*, 27(6):424–426, 2002.

[78] J. E. Sharping, M. Fiorentino, P. Kumar, and R. S. Windeler. Optical parametric oscillator based on four-wave mixing in microstructure fiber. *Optics Letters*, 27(19):1675–1677, 2002.

[79] X. Liu, C. Xu, W. H. Knox, J. K. Chandalia, B. J. Eggleton, S. G. Kosinski, and R. S. Windeler. Soliton self-frequency shift in a short tapered air-silica microstructure fiber. *Optics Letters*, 26(6):358–360, 2001.

[80] M. Fiorentino, J. E. Sharping, P. Kumar, A. Porzio, and R. S. Windeler. Soliton squeezing in microstructure fiber. *Optics Letters*, 27(8):649–651, 2002.

[81] J. K. Ranka, R. S. Windeler, and A. J. Stentz. Visible continuum generation in air-silica microstructure optical fibers with anomalous dispersion at 800 nm. *Optics Letters*, 25(1):25–27, 2000.

[82] J. Herrmann, U. Griebner, N. Zhavoronkov, A. Husakou, D. Nickel, J. C. Knight, W. J. Wadsworth, P. S. J. Russell, and G. Korn. Experimental evidence for supercontinuum generation by fission of higher-order solitons in photonic fibers. *Physical Review Letters*, 88(17):173901, 2002.

[83] A. V. Husakou and J. Herrmann. Supercontinuum generation of higher-order solitons by fission in photonic crystal fibers. *Physical Review Letters*, 8720(20):203901, 2001.

[84] W. J. Wadsworth, A. Ortigosa-Blanch, J. C. Knight, T. A. Birks, T. P. M. Man, and P. S. Russell. Supercontinuum generation in photonic crystal fibers and optical fiber tapers: a novel light source. *Journal of the Optical Society of America B-Optical Physics*, 19(9):2148–2155, 2002.

[85] S. Coen, A. H. L. Chan, R. Leonhardt, J. D. Harvey, J. C. Knight, W. J. Wadsworth, and P. S. J. Russell. White-light supercontinuum generation with 60-ps pump pulses in a photonic crystal fiber. *Optics Letters*, 26(17):1356–1358, 2001.

[86] J. M. Dudley, G. Genty, and S. Coen. Supercontinuum generation in photonic crystal fiber. *Reviews of Modern Physics*, 78(4):1135–1184, 2006.

[87] G. Humbert, W. J. Wadsworth, S. G. Leon-Saval, J. C. Knight, T. A. Birks, P. S. J. Russell, M. J. Lederer, D. Kopf, K. Wiesauer, E. I. Breuer, and D. Stifter. Supercontinuum generation system for optical coherence tomography based on tapered photonic crystal fibre. *Optics Express*, 14(4):1596–1603, 2006.

[88] P. Petropoulos, H. Ebendorff-Heidepriem, V. Finazzi, R. C. Moore, K. Frampton, D. J. Richardson, and T. M. Monro. Highly nonlinear and anomalously dispersive lead silicate glass holey fibers. *Optics Express*, 11(26):3568–3573, 2003.

[89] A. V. Husakou and J. Herrmann. Supercontinuum generation in photonic crystal fibers made from highly nonlinear glasses. *Applied Physics B-Lasers and Optics*, 77(2-3):227–234, 2003.

[90] A. Bjarklev, A. Sanchez Bjarklev, and J. Broeng. *Photonic crystal fibres*. Kluwer Academic Publishers, Boston, 2003.

[91] M. D. Feit and J. A. Fleck. Light-propagation in graded-index optical fibers. *Applied Optics*, 17(24):3990–3998, 1978.

[92] M. D. Feit and J. A. Fleck. Computation of mode properties in optical fiber wave-guides by a propagating beam method. *Applied Optics*, 19(7):1154–1164, 1980.

[93] S. Jungling and J. C. Chen. A study and optimization of eigenmode calculations using the imaginary-distance beam-propagation method. *IEEE Journal of Quantum Electronics*, 30(9):2098–2105, 1994.

[94] R. Scarmozzino, A. Gopinath, R. Pregla, and S. Helfert. Numerical techniques for modeling guided-wave photonic devices. *IEEE Journal of Selected Topics in Quantum Electronics*, 6(1):150–162, 2000.

[95] K. Saitoh and M. Koshiba. Full-vectorial imaginary-distance beam propagation method based on a finite element scheme: Application to photonic crystal fibers. *IEEE Journal of Quantum Electronics*, 38(7):927–933, 2002.

[96] R.T. Bise, R. S. Windeler, K.S. Kranz, B. J. Eggleton, and D.J. Trevor. Tuneable photonic bandgap fiber. In *Optical Fiber Communications*, pages 466–468, Anahaim, 2002.

[97] S. W. Leonard, H. M. van Driel, K. Busch, S. John, A. Birner, A. P. Li, F. Muller, U. Gosele, and V. Lehmann. Attenuation of optical transmission within the band

gap of thin two-dimensional macroporous silicon photonic crystals. *Applied Physics Letters*, 75(20):3063–3065, 1999.

[98] R. A. Soref and B. R. Bennett. Electrooptical effects in silicon. *IEEE Journal of Quantum Electronics*, 23(1):123–129, 1987.

[99] R. Feynman. There is plenty of room at the bottom, 1959.

[100] Geoffrey A. Ozin and Andre C. Arsenault. *Nanochemistry : a chemical approach to nanomaterials*. Royal Society of Chemistry, Cambridge, UK, 2005.

[101] R. Wetherbee. The diatom glasshouse. *Science*, 298(5593):547–547, 2002.

[102] K. H. Jeong, J. Kim, and L. P. Lee. Biologically inspired artificial compound eyes. *Science*, 312(5773):557–561, 2006.

[103] R. A. Pai, R. Humayun, M. T. Schulberg, A. Sengupta, J. N. Sun, and J. J. Watkins. Mesoporous silicates prepared using preorganized templates in supercritical fluids. *Science*, 303(5657):507–510, 2004.

[104] K. P. Johnston and P. S. Shah. Materials science - making nanoscale materials with supercritical fluids. *Science*, 303(5657):482–483, 2004.

[105] George E. Possin. A method for forming very small diameter wires. *Review of Scientific Instruments*, 41(5):772–774, 1970.

[106] R. F. Service. Materials science - throwing-or molding-a curve into nanofabrication. *Science*, 273(5273):312–312, 1996.

[107] Y. N. Xia, E. Kim, X. M. Zhao, J. A. Rogers, M. Prentiss, and G. M. Whitesides. Complex optical surfaces formed by replica molding against elastomeric masters. *Science*, 273(5273):347–349, 1996.

[108] Y. A. Vlasov, X. Z. Bo, J. C. Sturm, and D. J. Norris. On-chip natural assembly of silicon photonic bandgap crystals. *Nature*, 414(6861):289–293, 2001.

[109] C. R. Martin. Membrane-based synthesis of nanomaterials. *Chemistry of Materials*, 8(8):1739–1746, 1996.

[110] T. E. Bogart, S. Dey, K. K. Lew, S. E. Mohney, and J. M. Redwing. Diameter-controlled synthesis of silicon nanowires using nanoporous alumina membranes. *Advanced Materials*, 17(1):114–117, 2005.

[111] O. D. Velev, T. A. Jede, R. F. Lobo, and A. M. Lenhoff. Porous silica via colloidal crystallization. *Nature*, 389(6650):447–448, 1997.

[112] O. D. Velev, P. M. Tessier, A. M. Lenhoff, and E. W. Kaler. Materials - a class of porous metallic nanostructures. *Nature*, 401(6753):548–548, 1999.

[113] S. A. Johnson, P. J. Ollivier, and T. E. Mallouk. Ordered mesoporous polymers of tunable pore size from colloidal silica templates. *Science*, 283(5404):963–965, 1999.

[114] D. J. Norris and Y. A. Vlasov. Chemical approaches to three-dimensional semiconductor photonic crystals. *Advanced Materials*, 13(6):371–376, 2001.

[115] P. N. Bartlett, J. J. Baumberg, P. R. Birkin, M. A. Ghanem, and M. C. Netti. Highly ordered macroporous gold and platinum films formed by electrochemical deposition through templates assembled from submicron diameter monodisperse polystyrene spheres. *Chemistry of Materials*, 14(5):2199–2208, 2002.

[116] S. John and K. Busch. Photonic bandgap formation and tunability in certain self-organizing systems. *Journal of Lightwave Technology*, 17(11):1931–1943, 1999.

[117] G. M. Whitesides and M. Boncheva. Beyond molecules: Self-assembly of mesoscopic and macroscopic components. *Proceedings of the National Academy of Sciences of the United States of America*, 99(8):4769–4774, 2002.

[118] Marc J. Madou. *Fundamentals of microfabrication : the science of miniaturization.* CRC Press, Boca Raton, Fla., 2nd edition, 2002.

[119] Ivor Brodie and Julius J. Muray. *The physics of microfabrication.* Plenum Press, New York, 1982.

[120] N. Agarwal, N. Kane, and R. F. Bunshah. Structure and property relationships of Ni-20Cr produced by high-rate physical vapor-deposition. *Journal of Vacuum Science and Technology*, 12(2):619–623, 1975.

[121] D. H. Boone, Strangma.Te, and L. W. Wilson. Some effects of structure and composition on properties of electron-beam vapor-deposited coatings for gas-turbine superalloys. *Journal of Vacuum Science and Technology*, 11(4):641–646, 1974.

[122] J.J. Tietjen. Chemical vapor deposition of electronic materials. *Annual Review of Materials Science*, 3:317–326, 1973.

[123] W. G. French, J. B. Macchesney, and A. D. Pearson. Glass fibers for optical communications. *Annual Review of Materials Science*, 5:373–394, 1975.

[124] K. L. Choy. Chemical vapour deposition of coatings. *Progress in Materials Science*, 48(2):57–170, 2003.

[125] M. J. Ludowise. Metalorganic chemical vapor-deposition of III-V semiconductors. *Journal of Applied Physics*, 58(8):R31–R55, 1985.

[126] X. H. Hou and K. L. Choy. Processing and applications of aerosol-assisted chemical vapor deposition. *Chemical Vapor Deposition*, 12(10):583–596, 2006.

[127] F. T. Wallenberger and P. C. Nordine. Strong, pure, and uniform carbon-fibers obtained directly from the vapor-phase. *Science*, 260(5104):66–68, 1993.

[128] T. H. Baum and C. R. Jones. Laser chemical vapor-deposition of gold. *Applied Physics Letters*, 47(5):538–540, 1985.

[129] H.M. Manasevit. Single-crystal gallium arsenide on insulating substrates. *Applied Physics Letters*, 12:156–159, 1968.

[130] P. D. Dapkus. Metalorganic chemical vapor-deposition. *Annual Review of Materials Science*, 12:243–269, 1982.

[131] C.R. Martin. Nanomaterials: A membrane-based synthetic approach. *Science*, 266:1961–1966, 1994.

[132] S. A. Sapp, D. T. Mitchell, and C. R. Martin. Using template-synthesized micro- and nanowires as building blocks for self-assembly of supramolecular architectures. *Chemistry of Materials*, 11(5):1183, 1999.

[133] R. M. Penner. Mesoscopic metal particles and wires by electrodeposition. *Journal of Physical Chemistry B*, 106(13):3339–3353, 2002.

[134] A. M. Kressin, V. V. Doan, J. D. Klein, and M. J. Sailor. Synthesis of stoichiometric cadmium selenide films via sequential monolayer electrodeposition. *Chemistry of Materials*, 3(6):1015–1020, 1991.

[135] J. D. Klein, R. D. Herrick, D. Palmer, M. J. Sailor, C. J. Brumlik, and C. R. Martin. Electrochemical fabrication of cadmium chalcogenide microdiode arrays. *Chemistry of Materials*, 5(7):902–904, 1993.

[136] S. A. Sapp, B. B. Lakshmi, and C. R. Martin. Template synthesis of bismuth telluride nanowires. *Advanced Materials*, 11(5):402–404, 1999.

[137] K. B. Jirage, J. C. Hulteen, and C. R. Martin. Nanotubule-based molecular-filtration membranes. *Science*, 278(5338):655–658, 1997.

[138] J. C. Hulteen, K. B. Jirage, and C. R. Martin. Introducing chemical transport selectivity into gold nanotubule membranes. *Journal of the American Chemical Society*, 120(26):6603–6604, 1998.

[139] V. P. Menon and C. R. Martin. Fabrication and evaluation of nanoelectrode ensembles. *Analytical Chemistry*, 67(13):1920–1928, 1995.

[140] A. I. Cooper. Polymer synthesis and processing using supercritical carbon dioxide. *Journal of Materials Chemistry*, 10(2):207–234, 2000.

[141] Erdogan Kiran, Pablo G. Debenedetti, Cor J. Peters, and North Atlantic Treaty Organization. Scientific Affairs Division. *Supercritical fluids : fundamentals and applications*. Kluwer Academic Publishers, Dordrecht ; Boston, 2000.

[142] M. Poliakoff and S. Howdle. Supercritical chemistry - synthesis with a scanner. *Chemistry in Britain*, 31(2):118–121, 1995.

[143] Brian N. Hansen, Brooks M. Hybertson, Robert M. Barkley, and Robert E. Sievers. Supercritical fluid transport-chemical deposition of films. 4(4):749–752, 1992.

[144] A. Cabanas, D. P. Long, and J. J. Watkins. Deposition of gold films and nanostructures from supercritical carbon dioxide. *Chemistry of Materials*, 16(10):2028–2033, 2004.

[145] J. M. Blackburn, D. P. Long, and J. J. Watkins. Reactive deposition of conformal palladium films from supercritical carbon dioxide solution. *Chemistry of Materials*, 12(9):2625–2631, 2000.

[146] N. E. Fernandes, S. M. Fisher, J. C. Poshusta, D. G. Vlachos, M. Tsapatsis, and J. J. Watkins. Reactive deposition of metal thin films within porous supports from supercritical fluids. *Chemistry of Materials*, 13(6):2023–2031, 2001.

[147] A. Cabanas, J. M. Blackburn, and J. J. Watkins. Deposition of Cu films from supercritical fluids using cu(i) beta-diketonate precursors. *Microelectronic Engineering*, 64(1-4):53–61, 2002.

[148] E. T. Hunde and J. J. Watkins. Reactive deposition of cobalt and nickel films from their metallocenes in supercritical carbon dioxide solution. *Chemistry of Materials*, 16(3):498–503, 2004.

[149] J. V. Badding, P. J. A. Sazio, A. Amezcua-Correa, T. J. Scheidemantel, C. E. Finlayson, N. F. Baril, D. J. Won, H. Fang, B. Jackson, A. Borhan, and V. Gopalan. Fabrication of extreme aspect ratio wires within photonic crystal fibers. *Proceeding of SPIE*, 2005.

[150] B. R. Jackson. *Template-Directed High-Pressure Vapour-Liquid-Solid Growth of Silicon Micro-Wires within Silica Capillary Microstructured Optical fibres*. PhD thesis, The Pennsylvania State University, 2005.

[151] R.S. Wagner and W.C. Ellis. Vapor-liquid-solid mechanism of single crystal growth. *Applied Physics Letters*, 4(5):89–90, 1964.

[152] Y. Cui, Q. Q. Wei, H. K. Park, and C. M. Lieber. Nanowire nanosensors for highly sensitive and selective detection of biological and chemical species. *Science*, 293(5533):1289–1292, 2001.

[153] X. F. Duan, Y. Huang, Y. Cui, J. F. Wang, and C. M. Lieber. Indium phosphide nanowires as building blocks for nanoscale electronic and optoelectronic devices. *Nature*, 409(6816):66–69, 2001.

[154] J. F. Wang, M. S. Gudiksen, X. F. Duan, Y. Cui, and C. M. Lieber. Highly polarized photoluminescence and photodetection from single indium phosphide nanowires. *Science*, 293(5534):1455–1457, 2001.

[155] J. Xiang, W. Lu, Y. J. Hu, Y. Wu, H. Yan, and C. M. Lieber. Ge/Si nanowire heterostructures as high-performance field-effect transistors. *Nature*, 441(7092):489–493, 2006.

[156] A. San Paulo, N. Arellano, J. A. Plaza, R. R. He, C. Carraro, R. Maboudian, R. T. Howe, J. Bokor, and P. D. Yang. Suspended mechanical structures based on elastic silicon nanowire arrays. *Nano Letters*, 7(4):1100–1104, 2007.

[157] Y. N. Xia, P. D. Yang, Y. G. Sun, Y. Y. Wu, B. Mayers, B. Gates, Y. D. Yin, F. Kim, and Y. Q. Yan. One-dimensional nanostructures: Synthesis, characterization, and applications. *Advanced Materials*, 15(5):353–389, 2003.

[158] B. J. Eggleton, C. Kerbage, P. S. Westbrook, R. S. Windeler, and A. Hale. Microstructured optical fiber devices. *Optics Express*, 9(13):698–713, 2001.

[159] Ian M. Watt. *The principles and practice of electron microscopy.* Cambridge University Press, Cambridge ; New York, 2nd edition, 1997.

[160] Desmond Kay. *Techniques for electron microscopy.* F. A. Davis Co., Philadelphia, 2d edition, 1965.

[161] B. N. Brockhouse and P. K. Iyengar. Normal modes of germanium by neutron spectrometry. *Physical Review*, 111(3):747–754, 1958.

[162] J. H. Parker, D. W. Feldman, and M. Ashkin. Raman scattering by silicon and germanium. *Physical Review*, 155(3):712, 1967.

[163] E. Bustarret, M. A. Hachicha, and M. Brunel. Experimental-determination of the nanocrystalline volume fraction in silicon thin-films from Raman-spectroscopy. *Applied Physics Letters*, 52(20):1675–1677, 1988.

[164] H. Xia, Y. L. He, L. C. Wang, W. Zhang, X. N. Liu, X. K. Zhang, D. Feng, and H. E. Jackson. Phonon mode study of Si nanocrystals using micro-Raman spectroscopy. *Journal of Applied Physics*, 78(11):6705–6708, 1995.

[165] H. Touir, J. Dixmier, K. Zellama, J. F. Morhange, and P. Elkaim. Bimodal crystal size distribution in annealed RF magnetron silicon films: a memory effect of the local order inhomogeneities in the initial amorphous state. *Journal of Non-Crystalline Solids*, 230:906–910, 1998.

[166] A. A. Parr, D. J. Gardiner, R. T. Carline, D. O. King, and G. M. Williams. Structural variations in polysilicon, associated with deposition temperature and degree of anneal. *Journal of Materials Science*, 36(1):207–212, 2001.

[167] S. Veprek, F. A. Sarott, and Z. Iqbal. Effect of grain boundaries on the Raman spectra, optical absorption, and elastic light scattering in nanometer-sized crystalline silicon. *Physical Review B*, 36(6):3344–3350.

[168] A. A. Parr, K. Gill, D. J. Gardiner, J. D. Hoyland, D. Sands, K. Brunson, and R. T. Carline. A comparison of laser- and furnace-annealed polysilicon structure. *Semiconductor Science and Technology*, 17(1):47–54, 2002.

[169] M. H. Brodsky, M. Cardona, and J. J. Cuomo. Infrared and Raman-spectra of silicon-hydrogen bonds in amorphous silicon prepared by glow-discharge and sputtering. *Physical Review B*, 16(8):3556–3571, 1977.

[170] C. Das and S. Ray. Onset of microcrystallinity in silicon thin films. *Thin Solid Films*, 403:81–85, 2002.

[171] T. Kaneko, M. Wakagi, K. Onisawa, and T. Minemura. Change in crystalline morphologies of polycrystalline silicon films prepared by radiofrequency plasma-enhanced chemical-vapor-deposition using SiF_4+H_2 gas-mixture at 350 °C. *Applied Physics Letters*, 64(14):1865–1867, 1994.

[172] C. Smit, R. A. C. M. M. van Swaaij, H. Donker, A. M. H. N. Petit, W. M. M. Kessels, and M. C. M. van de Sanden. Determining the material structure of microcrystalline silicon from Raman spectra. *Journal of Applied Physics*, 94(5):3582–3588, 2003.

[173] WaveMetrics. Curve Fitting, Igor Pro, 2003.

[174] C. Das, A. Dasgupta, S. C. Saha, and S. Ray. Effects of substrate temperature on structural properties of undoped silicon thin films. *Journal of Applied Physics*, 91(11):9401–9407, 2002.

[175] R. S. Jacobsen, K. N. Andersen, P. I. Borel, J. Fage-Pedersen, L. H. Frandsen, O. Hansen, M. Kristensen, A. V. Lavrinenko, G. Moulin, H. Ou, C. Peucheret, B. Zsigri, and A. Bjarklev. Strained silicon as a new electro-optic material. *Nature*, 441(7090):199–202, 2006.

[176] S. M. Sze. *Semiconductor devices, physics and technology.* Wiley, New York, 2nd edition, 2002.

[177] C. E. Finlayson, A. Amezcua-Correa, P. J. A. Sazio, N. F. Baril, and J. V. Badding. Electrical and Raman characterization of silicon and germanium-filled microstructured optical fibers. *Applied Physics Letters*, 90(13):13211, 2007.

[178] R. Martel, T. Schmidt, H. R. Shea, T. Hertel, and P. Avouris. Single- and multi-wall carbon nanotube field-effect transistors. *Applied Physics Letters*, 73(17):2447–2449, 1998.

[179] D. W. Wang, Q. Wang, A. Javey, R. Tu, H. J. Dai, H. Kim, P. C. McIntyre, T. Krishnamohan, and K. C. Saraswat. Germanium nanowire field-effect transistors with SiO_2 and high-κ HfO_2 gate dielectrics. *Applied Physics Letters*, 83(12):2432–2434, 2003.

[180] Z. G. Meng, Z. H. Jin, G. A. Bhat, P. Chu, H. S. Kwok, and M. Wong. On the formation of solid state crystallized intrinsic polycrystalline germanium thin films. *Journal of Materials Research*, 12(10):2548–2551, 1997.

[181] Y. Huang, X. Duan, Y. Cui, and C. M. Lieber. Gallium nitride nanowire nanodevices. *Nano Letters*, 2(2):101–104, 2002.

[182] H. P. Maruska, A. K. Ghosh, A. Rose, and T. Feng. Hall-mobility of polycrystalline silicon. *Applied Physics Letters*, 36(5):381–383, 1980.

[183] C. A. Dimitriadis and P. A. Coxon. Hopping conduction in undoped low-pressure chemically vapor-deposited polycrystalline silicon films in relation to the film deposition conditions. *Journal of Applied Physics*, 64(3):1601–1604, 1988.

[184] J. W. Seto. The electrical properties of polycrystalline silicon films. *Journal of Applied Physics*, 46(12):5247–5254, 1975.

[185] A. Mimura, N. Konishi, K. Ono, J. Ohwada, Y. Hosokawa, Y. A. Ono, T. Suzuki, K. Miyata, and H. Kawakami. High-performance low-temperature poly-Si n-channel TFTs for LCD. *IEEE Transactions on Electron Devices*, 36(2):351–359, 1989.

[186] A. G. Rickman, G. T. Reed, and F. Namavar. Siilicon-on-Insulator optical Rib wave-guide loss and mode characteristics. *IEEE Journal of Lightwave Technology*, 12(10):1771–1776, 1994.

[187] G. Cocorullo, F. G. Della Corte, M. Iodice, T. Polichetti, I. Rendina, and P. M. Sarro. Low loss all-silicon single mode optical waveguide with small cross-section. *Fiber and Integrated Optics*, 20(3):207–219, 2001.

[188] Y. J. Wang, Z. L. Lin, X. L. Cheng, C. S. Zhang, F. Gao, and F. Zhang. Scattering loss in Silicon-on-Insulator Rib waveguides fabricated by inductively coupled plasma reactive ion etching. *Applied Physics Letters*, 85(18):3995–3997, 2004.

[189] B. Jalali and S. Fathpour. Silicon photonics. *IEEE Journal of Lightwave Technology*, 24:4600–4615, 2006.

[190] R. L. Espinola, M. C. Tsai, J. T. Yardley, and R. M. Osgood. Fast and low-power thermooptic switch on thin Silicon-on-Insulator. *IEEE Photonics Technology Letters*, 15(10):1366–1368, 2003.

[191] A. Cutolo, M. Iodice, P. Spirito, and L. Zeni. Silicon electro-optic modulator based on a three terminal device integrated in a low-loss single-mode SOI waveguide. *Journal of Lightwave Technology*, 15(3):505–518, 1997.

[192] A. S. Liu, R. Jones, L. Liao, D. Samara-Rubio, D. Rubin, O. Cohen, R. Nicolaescu, and M. Paniccia. A high-speed silicon optical modulator based on a metal-oxide-semiconductor capacitor. *Nature*, 427(6975):615–618, 2004.

[193] L. Liao, D. Samara-Rubio, M. Morse, A. S. Liu, D. Hodge, D. Rubin, U. D. Keil, and T. Franck. High speed silicon Mach-Zehnder modulator. *Optics Express*, 13(8):3129–3135, 2005.

[194] O. Boyraz and B. Jalali. Demonstration of a silicon Raman laser. *Optics Express*, 12(21):5269–5273, 2004.

[195] H. S. Rong, R. Jones, A. S. Liu, O. Cohen, D. Hak, A. Fang, and M. Paniccia. A continuous-wave Raman silicon laser. *Nature*, 433(7027):725–728, 2005.

[196] H. S. Rong, A. S. Liu, R. Jones, O. Cohen, D. Hak, R. Nicolaescu, A. Fang, and M. Paniccia. An all-silicon Raman laser. *Nature*, 433(7023):292–294, 2005.

[197] A. M. Agarwal, L. Liao, J. S. Foresi, M. R. Black, X. M. Duan, and L. C. Kimerling. Low-loss polycrystalline silicon waveguides for silicon photonics. *Journal of Applied Physics*, 80(11), 1996.

[198] L. Liao, D. R. Lim, A. M. Agarwal, X. M. Duan, K. K. Lee, and L. C. Kimerling. Optical transmission losses in polycrystalline silicon strip waveguides: Effects of waveguide dimensions, thermal treatment, hydrogen passivation, and wavelength. *Journal of Electronic Materials*, 29(12):1380–1386, 2000.

[199] J. S. Foresi, M. R. Black, A. M. Agarwal, and L. C. Kimerling. Losses in polycrystalline silicon waveguides. *Applied Physics Letters*, 68(15):2052–2054, 1996.

[200] P. J. Roberts, F. Couny, H. Sabert, B. J. Mangan, D. P. Williams, L. Farr, M. W. Mason, A. Tomlinson, T. A. Birks, J. C. Knight, and P. S. J. Russell. Ultimate low loss of hollow-core photonic crystal fibres. *Optics Express*, 13(1):236–244, 2005.

[201] D. Dimitropoulos, V. Raghunathan, R. Claps, and B. Jalali. Phase-matching and nonlinear optical processes in silicon waveguides. *Optics Express*, 12(1):149–160, 2004.

[202] M. Dinu, F. Quochi, and H. Garcia. Third-order nonlinearities in silicon at telecom wavelengths. *Applied Physics Letters*, 82(18):2954–2956, 2003.

[203] G. Cocorullo, F. G. Della Corte, I. Rendina, C. Minarini, A. Rubino, and E. Terzini. Amorphous silicon waveguides and light modulators for integrated photonics realized by low-temperature plasma-enhanced chemical-vapor deposition. 21(24):2002–2004, 1996.

[204] D.J. Won. Amorphous silicon-filled microstructure optical fibers for in-fiber light modulation. *Manuscript in preparation*, 2007.

[205] Q. F. Xu, B. Schmidt, S. Pradhan, and M. Lipson. Micrometre-scale silicon electro-optic modulator. *Nature*, 435(7040):325–327, 2005.

[206] S. Stepanov and S. Ruschin. Modulation of light by light in Silicon-on-Insulator waveguides. *Applied Physics Letters*, 83(25):5151–5153, 2003.

[207] M. Faraday. The Bakerian lecture: On the relations of gold and other metals to light. *Proceedings of the Royal Society of London*, 8:356–361, 1856.

[208] http://www.thebritishmuseum.ac.uk/.

[209] M. Born and E. Wolf. *Principles of optics : electromagnetic theory of propagation, interference and diffraction of light*. Cambridge University Press, Cambridge, U.K., 7th expanded edition, 1999.

[210] Anatolii Viacheslavovich Sokolov. *Optical properties of metals*. American Elsevier Pub. Co., New York, 1967.

[211] Uwe Kreibig and Michael Vollmer. *Optical properties of metal clusters*. Springer, Berlin ; New York, 1995.

[212] Craig F. Bohren and Donald R. Huffman. *Absorption and scattering of light by small particles*. Wiley, New York, 1983.

[213] T. Inagaki, L. C. Emerson, E. T. Arakawa, and M. W. Williams. Optical-properties of solid Na and Li between 0.6 and 3.8 Ev. *Physical Review B*, 13(6):2305–2313, 1976.

[214] Maciej Suffczynski. Optical constants of metals. *Physical Review*, 117(3):663, 1960.

[215] H. Ehrenreich and H. R. Philipp. Optical properties of Ag and Cu. *Physical Review*, 128(4):1622, 1962.

[216] P. B. Johnson and R. W. Christy. Optical-constants of noble-metals. *Physical Review B*, 6(12):4370–4379, 1972.

[217] R. H. Ritchie. Plasma losses by fast electrons in thin films. *Physical Review*, 106(5):874, 1957.

[218] E. A. Stern and R. A. Ferrell. Surface plasma oscillations of a degenerate electron gas. *Physical Review*, 120(1):130, 1960.

[219] Ye-Yung Teng and Edward A. Stern. Plasma radiation from metal grating surfaces. *Physical Review Letters*, 19(9):511, 1967.

[220] A. Hessel and A. Oliner. A new theory of Wood's anomalies on optical gratings. *Applied Optics*, 4(10):1275–1297, 1965.

[221] R. H. Ritchie, E. T. Arakawa, J. J. Cowan, and R. N. Hamm. Surface-plasmon resonance effect in grating diffraction. *Physical Review Letters*, 21(22):1530, 1968.

[222] W. L. Barnes, T. W. Preist, S. C. Kitson, and J. R. Sambles. Physical origin of photonic energy gaps in the propagation of surface plasmons on gratings. *Physical Review B*, 54(9):6227–6244, 1996.

[223] I. R. Hooper and J. R. Sambles. Surface plasmon polaritons on thin-slab metal gratings. *Physical Review B*, 67(23):235404, 2003.

[224] I. I. Smolyaninov, D. L. Mazzoni, and C. C. Davis. Imaging of surface plasmon scattering by lithographically created individual surface defects. *Physical Review Letters*, 77(18):3877–3880, 1996.

[225] B. Hecht, H. Bielefeldt, L. Novotny, Y. Inouye, and D. W. Pohl. Local excitation, scattering, and interference of surface plasmons. *Physical Review Letters*, 77(9):1889–1892, 1996.

[226] H. Ditlbacher, J. R. Krenn, N. Felidj, B. Lamprecht, G. Schider, M. Salerno, A. Leitner, and F. R. Aussenegg. Fluorescence imaging of surface plasmon fields. *Applied Physics Letters*, 80(3):404–406, 2002.

[227] A. S. Barker. Optical measurements of surface plasmons in gold. *Physical Review B*, 8(12):5418, 1973.

[228] J. Moreland, A. Adams, and P. K. Hansma. Efficiency of light-emission from surface-plasmons. *Physical Review B*, 25(4):2297–2300, 1982.

[229] P. T. Worthing and W. L. Barnes. Efficient coupling of surface plasmon polaritons to radiation using a bi-grating. *Applied Physics Letters*, 79(19):3035–3037, 2001.

[230] S. I. Bozhevolnyi, J. Erland, K. Leosson, P. M. W. Skovgaard, and J. M. Hvam. Waveguiding in surface plasmon polariton band gap structures. *Physical Review Letters*, 86(14):3008–3011, 2001.

[231] S. I. Bozhevolnyi, V. S. Volkov, and K. Leosson. Localization and waveguiding of surface plasmon polaritons in random nanostructures. *Physical Review Letters*, 89(18):186801, 2002.

[232] J. R. Krenn, B. Lamprecht, H. Ditlbacher, G. Schider, M. Salerno, A. Leitner, and F. R. Aussenegg. Non diffraction-limited light transport by gold nanowires. *Europhysics Letters*, 60(5):663–669, 2002.

[233] K. L. Kelly, E. Coronado, L. L. Zhao, and G. C. Schatz. The optical properties of metal nanoparticles: The influence of size, shape, and dielectric environment. *Journal of Physical Chemistry B*, 107(3):668–677, 2003.

[234] M. Moskovits. Surface-enhanced spectroscopy. *Reviews of Modern Physics*, 57(3):783–826, 1985.

[235] C. Oubre and P. Nordlander. Optical properties of metallodielectric nanostructures calculated using the finite difference time domain method. *Journal of Physical Chemistry B*, 108(46):17740–17747, 2004.

[236] S. Link, Z. L. Wang, and M. A. El-Sayed. Alloy formation of gold-silver nanoparticles and the dependence of the plasmon absorption on their composition. *Journal of Physical Chemistry B*, 103(18):3529–3533, 1999.

[237] R. C. Jin, Y. W. Cao, C. A. Mirkin, K. L. Kelly, G. C. Schatz, and J. G. Zheng. Photoinduced conversion of silver nanospheres to nanoprisms. *Science*, 294(5548):1901–1903, 2001.

[238] T. K. Sau and C. J. Murphy. Seeded high yield synthesis of short Au nanorods in aqueous solution. *Langmuir*, 20(15):6414–6420, 2004.

[239] E. K. Payne, K. L. Shuford, S. Park, G. C. Schatz, and C. A. Mirkin. Multipole plasmon resonances in gold nanorods. *Journal of Physical Chemistry B*, 110(5):2150–2154, 2006.

[240] L. J. Sherry, S. H. Chang, G. C. Schatz, R. P. Van Duyne, B. J. Wiley, and Y. N. Xia. Localized surface plasmon resonance spectroscopy of single silver nanocubes. *Nano Letters*, 5(10):2034–2038, 2005.

[241] S. L. Westcott, J. B. Jackson, C. Radloff, and N. J. Halas. Relative contributions to the plasmon line shape of metal nanoshells. *Physical Review B*, 66(15):155431, 2002.

[242] T. R. Jensen, M. D. Malinsky, C. L. Haynes, and R. P. Van Duyne. Nanosphere lithography: Tunable localized surface plasmon resonance spectra of silver nanoparticles. *Journal of Physical Chemistry B*, 104(45):10549–10556, 2000.

[243] http://www.ece.rice.edu/ halas/index.html.

[244] B. Liedberg, C. Nylander, and I. Lundstrom. Biosensing with surface-plasmon resonance - how it all started. *Biosensors and Bioelectronics*, 10(8):1–9, 1995.

[245] J. Homola, S. S. Yee, and G. Gauglitz. Surface plasmon resonance sensors: review. *Sensors and Actuators B-Chemical*, 54(1-2):3–15, 1999.

[246] http://www.biacore.com/lifesciences/index.html.

[247] http://www.nomadics.com/.

[248] http://www.micro-systems.de/index.htm.

[249] E. Hutter and J. H. Fendler. Exploitation of localized surface plasmon resonance. *Advanced Materials*, 16(19):1685–1706, 2004.

[250] P. Englebienne. Use of colloidal gold surface plasmon resonance peak shift to infer affinity constants from the interactions between protein antigens and antibodies specific for single or multiple epitopes. *Analyst*, 123(7):1599–1603, 1998.

[251] P. Englebienne, A. Van Hoonacker, and M. Verhas. High-throughput screening using the surface plasmon resonance effect of colloidal gold nanoparticles. *Analyst*, 126(10):1645–1651, 2001.

[252] S. A. Levi, A. Mourran, J. P. Spatz, F. C. J. M. van Veggel, D. N. Reinhoudt, and M. Moller. Fluorescence of dyes adsorbed on highly organized, nanostructured gold surfaces. *Chemistry-A European Journal*, 8(16):3808–3814, 2002.

[253] S. Link and M. A. Ei-Sayed. Optical properties and ultrafast dynamics of metallic nanocrystals. *Annual Review of Physical Chemistry*, 54:331–366, 2003.

[254] N. Calander. Theory and simulation of surface plasmon-coupled directional emission from fluorophores at planar structures. *Analytical Chemistry*, 76(8):2168–2173, 2004.

[255] A. Hartstein, J. R. Kirtley, and J. C. Tsang. Enhancement of the infrared-absorption from molecular monolayers with thin metal overlayers. *Physical Review Letters*, 45(3):201–204, 1980.

[256] M. Osawa. Dynamic processes in electrochemical reactions studied by surface-enhanced infrared absorption spectroscopy (SEIRAS). *Bulletin of the Chemical Society of Japan*, 70(12):2861–2879, 1997.

[257] A. Campion and P. Kambhampati. Surface-enhanced Raman scattering. *Chemical Society Reviews*, 27(4):241–250, 1998.

[258] Z. Q. Tian, B. Ren, and D. Y. Wu. Surface-enhanced Raman scattering: from noble to transition metals and from rough surfaces to ordered nanostructures. *Journal of Physical Chemistry B*, 106(37):9463–9483, 2002.

[259] http://www.oxonica.com/.

[260] http://www.mesophotonics.com/.

[261] H. J. Lezec, A. Degiron, E. Devaux, R. A. Linke, L. Martin-Moreno, F. J. Garcia-Vidal, and T. W. Ebbesen. Beaming light from a subwavelength aperture. *Science*, 297(5582):820–822, 2002.

[262] S. I. Bozhevolnyi, V. S. Volkov, E. Devaux, J. Y. Laluet, and T. W. Ebbesen. Channel plasmon subwavelength waveguide components including interferometers and ring resonators. *Nature*, 440(7083):508–511, 2006.

[263] T. W. Ebbesen, H. J. Lezec, H. F. Ghaemi, T. Thio, and P. A. Wolff. Extraordinary optical transmission through sub-wavelength hole arrays. *Nature*, 391(6668):667–669, 1998.

[264] D. B. Shao and S. C. Chen. Surface-plasmon-assisted nanoscale photolithography by polarized light. *Applied Physics Letters*, 86(25):253107, 2005.

[265] H. J. Lezec and T. Thio. Diffracted evanescent wave model for enhanced and suppressed optical transmission through subwavelength hole arrays. *Optics Express*, 12(16):3629–3651, 2004.

[266] G. Gay, O. Alloschery, B. V. De Lesegno, C. O'Dwyer, J. Weiner, and H. J. Lezec. The optical response of nanostructured surfaces and the composite diffracted evanescent wave model. *Nature Physics*, 2(4):262–267, 2006.

[267] A. V. Krasavin, K. F. MacDonald, N. I. Zheludev, and A. V. Zayats. High-contrast modulation of light with light by control of surface plasmon polariton wave coupling. *Applied Physics Letters*, 85(16):3369–3371, 2004.

[268] A. V. Krasavin and N. I. Zheludev. Active plasmonics: Controlling signals in Au/Ga waveguide using nanoscale structural transformations. *Applied Physics Letters*, 84(8):1416–1418, 2004.

[269] A. V. Zayats and I. I. Smolyaninov. Near-field photonics: surface plasmon polaritons and localized surface plasmons. *Journal of Optics A-Pure and Applied Optics*, 5(4):S16–S50, 2003.

[270] P. Berini, R. Charbonneau, N. Lahoud, and G. Mattiussi. Characterization of long-range surface-plasmon-polariton waveguides. *Journal of Applied Physics*, 98(4):043109, 2005.

[271] S. A. Maier, M. L. Brongersma, P. G. Kik, S. Meltzer, A. A. G. Requicha, and H. A. Atwater. Plasmonics - a route to nanoscale optical devices. *Advanced Materials*, 13(19):1501–1505.

[272] H. Ditlbacher, J. R. Krenn, G. Schider, A. Leitner, and F. R. Aussenegg. Two-dimensional optics with surface plasmon polaritons. *Applied Physics Letters*, 81(10):1762–1764, 2002.

[273] C.V. Raman and K.S. Krishnoan. A new type of secondary radiation. *Nature*, 121:501–502, 1928.

[274] Herman A. Szymanski. *Raman spectroscopy : theory and practice*. Plenum Press, New York, 1967.

[275] Richard K. Chang and Thomas E. Furtak. *Surface enhanced Raman scattering*. Plenum Press, New York, 1982.

[276] M. Fleischmann, P. J. Hendra, and A. J. Mcquilla. Raman-spectra of pyridine adsorbed at a silver electrode. *Chemical Physics Letters*, 26(2):163–166, 1974.

[277] D. L. Jeanmaire and R. P. Vanduyne. Surface Raman spectroelectrochemistry: Part 1. heterocyclic, aromatic, and aliphatic-amines adsorbed on anodized silver electrode. *Journal of Electroanalytical Chemistry*, 84(1):1–20, 1977.

[278] M. G. Albrecht and J. A. Creighton. Anomalously intense Raman-spectra of pyridine at a silver electrode. *Journal of the American Chemical Society*, 99(15):5215–5217, 1977.

[279] S. M. Nie and S. R. Emery. Probing single molecules and single nanoparticles by surface-enhanced Raman scattering. *Science*, 275(5303):1102–1106, 1997.

[280] M. Kerker, D. S. Wang, and H. Chew. Surface enhanced Raman-scattering (SERS) by molecules adsorbed spherical-particle: errata. *Applied Optics*, 19(24):4159–4174, 1980.

[281] D. S. Wang, H. Chew, and M. Kerker. Enhanced Raman-scattering at the surface (SERS) of a spherical-particle. *Applied Optics*, 19(14):2256–2257, 1980.

[282] M. Moskovits. Surface-roughness and enhanced intensity of Raman-scattering by molecules adsorbed on metals. *Journal of Chemical Physics*, 69(9):4159–4161, 1978.

[283] N. Liver, A. Nitzan, and J. I. Gersten. Local-fields in cavity sites of rough dielectric surfaces. *Chemical Physics Letters*, 111(4-5):449–454, 1984.

[284] E. Hao and G. C. Schatz. Electromagnetic fields around silver nanoparticles and dimers. *Journal of Chemical Physics*, 120(1):357–366, 2004.

[285] J. R. Lombardi, R. L. Birke, T. H. Lu, and J. Xu. Charge-transfer theory of surface enhanced Raman-spectroscopy: Herzberg-Teller contributions. *Journal of Chemical Physics*, 84(8):4174–4180, 1986.

[286] A. Campion, J. E. Ivanecky, C. M. Child, and M. Foster. On the mechanism of chemical enhancement in surface-enhanced Raman-scattering. *Journal of the American Chemical Society*, 117(47):11807–11808, 1995.

[287] P. Kambhampati, C. M. Child, and A. Campion. On the role of charge-transfer resonances in the chemical mechanism of surface-enhanced Raman scattering. *Journal of the Chemical Society, Faraday Transactions*, 92:4775 – 4780, 1996.

[288] P. Kambhampati, C. M. Child, M. C. Foster, and A. Campion. On the chemical mechanism of surface enhanced Raman scattering: experiment and theory. *Journal of Chemical Physics*, 108(12):5013–5026, 1998.

[289] B. T. Kuhlmey, K. Pathmanandavel, and R. C. McPhedran. Multipole analysis of photonic crystal fibers with coated inclusions. *Optics Express*, 14(22):10851–10864, 2006.

[290] A. Hassani and M. Skorobogatiy. Design of the microstructured optical fiber-based surface plasmon resonance sensors with enhanced microfluidics. *Optics Express*, 14(24):11616–11621, 2006.

[291] C. G. Poulton, M. A. Schmidt, G. J. Pearce, G. Kakarantzas, and P. St. J. Russell. Numerical study of guided modes in arrays of metallic nanowires. *Optics Letters*, 32:1647–1649, 2007.

[292] S. J. Albader and M. Imtaar. Azimuthally uniform surface-plasma modes in thin metallic cylindrical-shells. *IEEE Journal of Quantum Electronics*, 28(2):525–533, 1992.

[293] S. J. Albader and M. Imtaar. Optical fiber hybrid-surface plasmon polaritons. *Journal of the Optical Society of America B-Optical Physics*, 10(1):83–88, 1993.

[294] A. Diez, M. V. Andres, and J. L. Cruz. In-line fiber-optic sensors based on the excitation of surface plasma modes in metal-coated tapered fibers. *Sensors and Actuators B-Chemical*, 73(2-3):95–99, 2001.

[295] D. L. Stokes and T. Vo-Dinh. Development of an integrated single-fiber sers sensor. *Sensors and Actuators B-Chemical*, 69(1-2):28–36, 2000.

[296] D. Monzon-Hernandez, J. Villatoro, D. Talavera, and D. Luna-Moreno. Optical-fiber surface-plasmon resonance sensor with multiple resonance peaks. *Applied Optics*, 43(6):1216–1220, 2004.

[297] D. L. Stokes, Z. H. Chi, and T. Vo-Dinh. Surface-enhanced-Raman-scattering-inducing nanoprobe for spectrochemical analysis. *Applied Spectroscopy*, 58(3):292–298, 2004.

[298] A. K. Sharma and B. D. Gupta. Fiber optic sensor based on surface plasmon resonance with nanoparticle films. *Photonics Nanostructures*, 3:30–37, 2005.

[299] Y. Zhang, C. Gu, A. M. Schwartzberg, and J. Z. Zhang. Surface-enhanced Raman scattering sensor based on D-shaped fiber. *Applied Physics Letters*, 87(12):123105, 2005.

[300] A. Amezcua-Correa, J. Yang, C. E. Finlayson, A. C. Peacock, J. R. Hayes, P. J. A. Sazio, J. J. Baumberg, and S. M. Howdle. Surface-enhanced Raman scattering using microstructured optical fiber substrates. *Advanced Functional Materials*, 17(13):2024–2030, 2007.

[301] K. Kurihara, C. Rockstuhl, T. Nakano, T. Arai, and J. Tominaga. The size control of silver nano-particles in SiO_2 matrix film. *Nanotechnology*, 16(9):1565–1568, 2005.

[302] W. L. Barnes, A. Dereux, and T. W. Ebbesen. Surface plasmon subwavelength optics. *Nature*, 424(6950):824–830, 2003.

[303] L. Gunnarsson, E. J. Bjerneld, H. Xu, S. Petronis, B. Kasemo, and M. Kall. Interparticle coupling effects in nanofabricated substrates for surface-enhanced Raman scattering. *Applied Physics Letters*, 78(6):802–804, 2001.

[304] A. G. Brolo, E. Arctander, R. Gordon, B. Leathem, and K. L. Kavanagh. Nanohole-enhanced Raman scattering. *Nano Letters*, 4(10):2015–2018, 2004.

[305] Tuan Vo-Dinh. Sers chemical sensors and biosensors: new tools for environmental and biological analysis. *Sensors and Actuators B: Chemical*, 29(1-3):183–189, 1995.

[306] E. J. Bjerneld, F. Svedberg, and M. Kall. Laser-induced growth and deposition of noble-metal nanoparticles for surface-enhanced Raman scattering. *Nano Letters*, 3(5):593–596, 2003.

[307] J. C. Hulteen and R. P. Vanduyne. Nanosphere lithography - a materials general fabrication process for periodic particle array surfaces. *Journal of Vacuum Science and Technology a-Vacuum Surfaces and Films*, 13(3):1553–1558, 1995.

[308] S. Coyle, M. C. Netti, J. J. Baumberg, M. A. Ghanem, P. R. Birkin, P. N. Bartlett, and D. M. Whittaker. Confined plasmons in metallic nanocavities. *Physical Review Letters*, 87(17):176801, 2001.

[309] J. J. Baumberg, T. A. Kelf, Y. Sugawara, S. Cintra, M. E. Abdelsalam, P. N. Bartlett, and A. E. Russell. Angle-resolved surface-enhanced Raman scattering on metallic nanostructured plasmonic crystals. *Nano Letters*, 5(11):2262–2267, 2005.

[310] S. Chan, S. Kwon, T. W. Koo, L. P. Lee, and A. A. Berlin. Surface-enhanced Raman scattering of small molecules from silver-coated silicon nanopores. *Advanced Materials*, 15(19):1595–1598, 2003.

[311] W. Q. Xu, S. P. Xu, Z. C. Lu, L. Chen, B. Zhao, and Y. Ozaki. Ultrasensitive detection of 1,4-bis(4-vinylpyridyl)phenylene in a small volume of low refractive index liquid by surface-enhanced Raman scattering-active light waveguide. *Applied Spectroscopy*, 58(4):414–419, 2004.

[312] W. K. Yi, C. W. Park, M. S. Kim, and K. Kim. Vibrational spectroscopic study of benzenethiol on silver surface. *Bulletin of the Korean Chemical Society*, 8(4):291–296, 1987.

[313] S. W. Han, S. J. Lee, and K. Kim. Self-assembled monolayers of aromatic thiol and selenol on silver: Comparative study of adsorptivity and stability. *Langmuir*, 17:6981–6987, 2001.

[314] R. H. Stolen, C. Lee, and R. K. Jain. Development of the stimulated Raman-spectrum in single-mode silica fibers. *Journal of the Optical Society of America B-Optical Physics*, 1(4):652–657, 1984.

[315] C. L. Haynes and R. P. Van Duyne. Plasmon-sampled surface-enhanced Raman excitation spectroscopy. *Journal of Physical Chemistry B*, 107:7426–7433, 2003.

[316] J. H. Lee, W. Belardi, K. Furusawa, P. Petropoulos, Z. Yusoff, T. M. Monro, and D. J. Richardson. Four-wave mixing based 10-Gb/s tunable wavelength conversion using a holey fiber with a high SBS threshold. *IEEE Photonics Technology Letters*, 15(3):440–442, 2003.

[317] Y. L. Wang, H. J. Chen, S. J. Dong, and E. K. Wang. Surface-enhanced Raman scattering of silver-gold bimetallic nanostructures with hollow interiors. *Journal of Chemical Physics*, 125(4):074709, 2006.

[318] Z. H. Zhu, T. Zhu, and Z. F. Liu. Raman scattering enhancement contributed from individual gold nanoparticles and interparticle coupling. *Nanotechnology*, 15(3):357–364, 2004.

[319] A. P. Alivisatos. Semiconductor clusters, nanocrystals, and quantum dots. *Science*, 271(5251):933–937, 1996.

[320] Victor I. Klimov. *Semiconductor and metal nanocrystals : synthesis and electronic and optical properties*. Marcel Dekker, New York, 2004.

[321] C. E. Finlayson. *Optical Characterization of Semiconductor Nanocrystals*. PhD thesis, University of Cambridge, 2001.

[322] M. Achermann, M. A. Petruska, S. Kos, D. L. Smith, D. D. Koleske, and V. I. Klimov. Energy-transfer pumping of semiconductor nanocrystals using an epitaxial quantum well. *Nature*, 429(6992):642–646, 2004.

[323] V. I. Klimov, A. A. Mikhailovsky, S. Xu, A. Malko, J. A. Hollingsworth, C. A. Leatherdale, H. J. Eisler, and M. G. Bawendi. Optical gain and stimulated emission in nanocrystal quantum dots. *Science*, 290(5490):314–317, 2000.

[324] M. Bruchez, M. Moronne, P. Gin, S. Weiss, and A. P. Alivisatos. Semiconductor nanocrystals as fluorescent biological labels. *Science*, 281(5385):2013–2016, 1998.

[325] P. Alivisatos. Colloidal quantum dots. from scaling laws to biological applications. *Pure and Applied Chemistry*, 72(1-2):3–9, 2000.

[326] R. D. Schaller, M. A. Petruska, and V. I. Klimov. Tunable near-infrared optical gain and amplified spontaneous emission using pbse nanocrystals. *Journal of Physical Chemistry B*, 107(50):13765–13768, 2003.

[327] H. Du, C. L. Chen, R. Krishnan, T. D. Krauss, J. M. Harbold, F. W. Wise, M. G. Thomas, and J. Silcox. Optical properties of colloidal PbSe nanocrystals. *Nano Letters*, 2(11):1321–1324, 2002.

[328] A. A. Guzelian, U. Banin, A. V. Kadavanich, X. Peng, and A. P. Alivisatos. Colloidal chemical synthesis and characterization of InAs nanocrystal quantum dots. *Applied Physics Letters*, 69(10):1432–1434, 1996.

[329] Ulrike Woggon. *Optical properties of semiconductor quantum dots.* Springer, Berlin, 1997.

[330] V. L. Colvin, A. N. Goldstein, and A. P. Alivisatos. Semiconductor nanocrystals covalently bound to metal-surfaces with self-assembled monolayers. *Journal of the American Chemical Society*, 114(13):5221–5230, 1992.

[331] C. B. Murray, D. J. Norris, and M. G. Bawendi. Synthesis and characterization of nearly monodisperse CdE (E = S, Se, Te) semiconductor nanocrystallites. *Journal of the American Chemical Society*, 115(19):8706–8715, 1993.

[332] X. G. Peng, J. Wickham, and A. P. Alivisatos. Kinetics of II-VI and III-V colloidal semiconductor nanocrystal growth: "focusing" of size distributions. *Journal of the American Chemical Society*, 120(21):5343–5344, 1998.

[333] B. L. Wehrenberg, C. J. Wang, and P. Guyot-Sionnest. Interband and intraband optical studies of PbSe colloidal quantum dots. *Journal of Physical Chemistry B*, 106(41):10634–10640, 2002.

[334] P. W. Voorhees. Ostwald ripening of 2-phase mixtures. *Annual Review of Materials Science*, 22:197–215, 1992.

[335] L. Bnyai and S.W. Koch. *Semiconductor Quantum Dots.* Series on Atomic, Molecular and Optical Physics. World Scientific, USA, 1993.

[336] C. E. Finlayson, A. Amezcua-Correa, P. J. A. Sazio, P. S. Walker, M. C. Grossel, R. J. Curry, D. C. Smith, and J. J. Baumberg. Infrared emitting PbSe nanocrystals for telecommunications window applications. *Journal of Modern Optics*, 52(7):955–964, 2005.

[337] A. D. Andreev, E. V. Kolobkova, and A. A. Lipovskii. Optical absorption in PbSe spherical quantum dots embedded in glass matrix. *Journal of Applied Physics*, 88(2):750–757, 2000.

[338] M. Kuno, D. P. Fromm, H. F. Hamann, A. Gallagher, and D. J. Nesbitt. Nonexponential "blinking" kinetics of single CdSe quantum dots: a universal power law behavior. *Journal of Chemical Physics*, 112(7):3117–3120, 2000.

[339] C. R. Kagan, C. B. Murray, and M. G. Bawendi. Long-range resonance transfer of electronic excitations in close-packed CdSe quantum-dot solids. *Physical Review B*, 54(12):8633–8643, 1996.

[340] M. Kazes, D. Y. Lewis, and U. Banin. Method for preparation of semiconductor quantum-rod lasers in a cylindrical microcavity. *Advanced Functional Materials*, 14(10):957–962, 2004.

[341] S. Hoogland, V. Sukhovatkin, I. Howard, S. Cauchi, L. Levina, and E. H. Sargent. A solution-processed 1.53 μm quantum dot laser with temperature-invariant emission wavelength. *Optics Express*, 14(8):3273–3281, 2006.

[342] M. Fried, T. Lohner, W. A. M. Aarnink, L. J. Hanekamp, and A. Vansilfhout. Determination of complex dielectric functions of ion-implanted and implanted-annealed amorphous-silicon by spectroscopic ellipsometry. *Journal of Applied Physics*, 71(10):5260–5262, 1992.

[343] G. K. Hubler, C. N. Waddell, W. G. Spitzer, J. E. Fredrickson, S. Prussin, and R. G. Wilson. High-fluence implantations of silicon - layer thickness and refractive-indexes. *Journal of Applied Physics*, 50(5):3294–3303, 1979.

[344] A. Hassani and M. Skorobogatiy. Design criteria for microstructured-optical-fiber-based surface-plasmon-resonance sensors. *Journal of the Optical Society of America B-Optical Physics*, 24(6):1423–1429, 2007.

[345] G. Shvets, S. Trendafilov, J. B. Pendry, and A. Sarychev. Guiding, focusing, and sensing on the subwavelength scale using metallic wire arrays. *Physical Review Letters*, 99(5), 2007.

[346] B. T. Kuhlmey and R. C. McPhedran. Photonic crystal fibres with resonant coatings. *Physica B-Condensed Matter*, 394(2):155–158, 2007.

[347] Neil W. Ashcroft and N. David Mermin. *Solid state physics*. Holt, Rinehart and Winston, New York, 1976.

[348] http://jas.eng.buffalo.edu/education/solid/unitcell/home.html.